[redacted]

PACIFIC NORTHWEST LABORATORY ANNUAL REPORT FOR 1967 TO THE USAEC DIVISION OF BIOLOGY AND MEDICINE

VOLUME II: PHYSICAL SCIENCES

PART 3. ATMOSPHERIC SCIENCES

OCTOBER 1968

[redacted]

AEC RESEARCH & DEVELOPMENT REPORT

BATTELLE NORTHWEST
PACIFIC NORTHWEST LABORATORY

LEGAL NOTICE

PACIFIC NORTHWEST LABORATORY
RICHLAND, WASHINGTON
operated by
BATTELLE MEMORIAL INSTITUTE
for the
UNITED STATES ATOMIC ENERGY COMMISSION UNDER CONTRACT AT(45-1)-1830

PRINTED BY/FOR THE U. S. ATOMIC ENERGY COMMISSION

BNWL-715
Part 3
UC-49 Biology
and Medicine

PACIFIC NORTHWEST LABORATORY
ANNUAL REPORT FOR 1967
to the
USAEC Division of Biology and Medicine
VOLUME II: PHYSICAL SCIENCES
Part 3. Atmospheric Sciences

by
C. L. Simpson, Manager
and
Staff Members of
Atmospheric Sciences Section
Environmental and Radiological Sciences Department

Edited by
D. W. Pearce

October 1968

BATTELLE MEMORIAL INSTITUTE
PACIFIC NORTHWEST LABORATORY
RICHLAND, WASHINGTON

Volume I of this report to the USAEC Division of Biology and Medicine covers work in the biological sciences and is issued as BNWL-714. Volume II of this report covers work in the physical sciences and is issued as BNWL-715 in four parts: Instrumentation, Part 1; Radiological Sciences, Part 2, Atmospheric Sciences, Part 3; Earth Sciences, Part 4.

Printed in the United States of America
Available from
Clearinghouse of Federal Scientific and Technical Information
National Bureau of Standards, U.S. Department of Commerce
Springfield, Virginia 22151
Price: Printed Copy $3.00; Microfiche $0.65

TABLE OF CONTENTS

These reports are drawn principally from personnel of the Atmospheric Sciences Section of the Environmental and Radiological Sciences Department. Contributions and co-authors from other organizations as well as occasional related activities not sponsored by the Division of Biology and Medicine may also be included. Such facts are acknowledged by footnotes.

BNWL-715
Part 3

PACIFIC NORTHWEST LABORATORY
ANNUAL REPORT FOR 1967
to the
USAEC Division of Biology and Medicine
VOLUME II: PHYSICAL SCIENCES
Part 3. Atmospheric Sciences

REAL TIME SAMPLING OF ZINC SULFIDE TRACER IN DIFFUSION STUDIES

W. L. Dotson, P. W. Nickola, and M. A. Wolf

INTRODUCTION

The development of real time samplers (RTS) by the Pacific Northwest Laboratory[1] resulted from the need for time resolution of tracer distribution in the study of diffusion processes. Initial use of RTS in defining the variability of concentration with time at a point was extended by mounting the instrument on a pickup truck. The surfaced, crosswind profiles of the nearly instantaneous tracer distribution thus provided measurement of the lateral variability of tracer distributions as reported by Nickola and Elderkin.[2] The results of this mobile application also provide insight into the manner in which a time-integrated distribution is attained, thereby establishing a more intimate relationship between the distribution and the mechanisms which determine it. A further extension of the real time sampler was its adaptation to airborne use to provide a four-dimensional description of the diffusing tracer. Initial tests with the airborne unit were described by Dotson et al.[3]

TEST SERIES 4D

Some results of the combined surface and airborne real time sampler (ARTS) tests at Hanford, Series 4D, are the subject of this report. The wealth of data, and the extensive reduction and analysis thereby required preclude a complete summary of the eight tests which were performed. Instead, several salient features of four of these tests are presented and discussed. These tests were selected on the basis of their demonstration of the utility of real time samplers rather than for their completeness of data. Indeed, surface real time sampler records have been analyzed only for Test 4D-7, and no filter sampler data are available for Test

4D-4. These four tests demonstrate diffusion under the variety of stabilities shown by Figure 1 and were selected for this contrast also. While the temperature profiles of Tests 4D-2 and 4D-4 are quite similar, it should be noted that wind speeds increased from 16.1 mph to 36.5 mph from bottom to top of the 400 ft tower for Test 4D-4, while for Test 4D-2 winds were about 10 mph over that full height.

DATA INTERPRETATION METHODS

The two modes of sampling in the 4D test series yield initial data not directly comparable. The means for integrating these data requires some discussion. It should be noted also that the ARTS record differs significantly from the RTS record due to the reduced definition resulting from the rate at which the aircraft traverses the tracer. The RTS record reveals

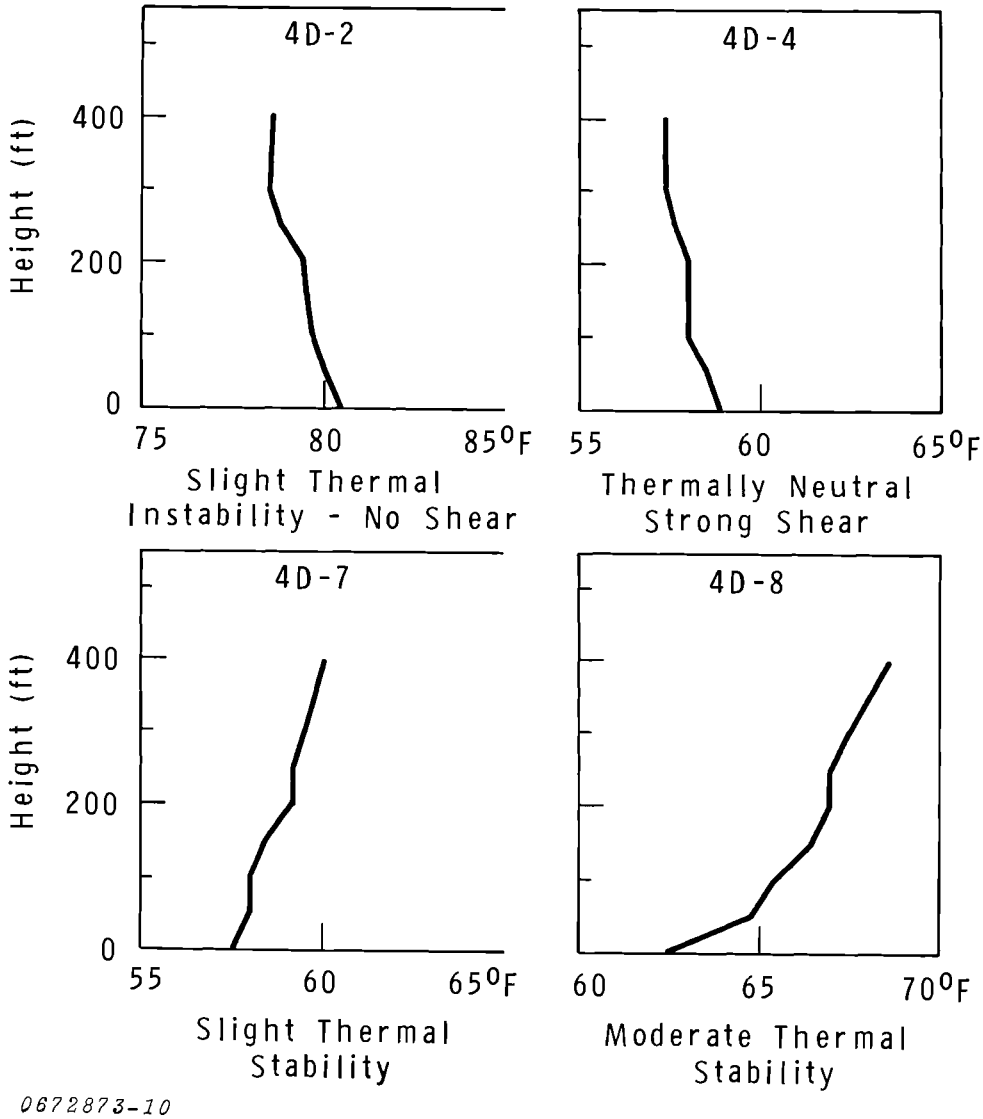

Neg. 0672873-10

FIGURE 1. Temperature Profiles of Test Series 4D

detailed concentration in addition to a crosswind integration of the tracer, while the peak concentration and crosswind integration are the only quantities presently derived from the ARTS record.

The filter assay gives the exposure, or time-integrated concentration, at each position for the passage of the total tracer release. The mean concentration can be derived by dividing the exposure by the duration of tracer passage. The RTS, by virtue of record definition and the precise positioning during each traverse, can provide instantaneous concentrations at each filter. These instantaneous concentrations will be both greater and less than the average concentration of that filter and, if a representative number of traverses is made, the RTS average should equal the filter average. Consequently, the exposures determined in these two ways should also be identical and thus afford a means for directly comparing the RTS with the filters. Indeed, RTS and the ARTS were calibrated in this manner. In addition to this identical function, the RTS provides measurements of the time variation of the instantaneous concentration at each point, or from another viewpoint, the nearly instantaneous distribution of tracer.

The ARTS, due to its present lack of resolution and precise positioning, is capable only of defining instantaneous crosswind integrated concentrations and positions and widths of the tracer plume. Since the ARTS recorded signal is the crossplume time integral of concentration, the desired crosswind integrated concentration (CIC) is determined by dividing the crosswind integrated "exposure" (CIE) by the time to cross the plume and then multiplying this resultant mean concentration by the crosswind width of the plume. The result, of course, is equivalent to multiplying CIE by the aircraft speed. The ARTS CIC can be directly compared with the RTS CIC formed in like manner. For comparison with the filters, there are two methods available. The more straightforward is to compare the time-averaged ARTS CIC with the time-mean CIC of the filter samplers, or the crosswind summed exposure (CSE) multiplied by the filter sampler spacing and divided by the time of total tracer passage. However, comparison of filters and ARTS at a common elevation, as with the RTS, is desirable. The low density of tower samplers in a crosswind direction precludes comparison of the mean CIC and only the mean concentrations, therefore, are available for comparison. Since the ARTS mean concentration always contains the peak concentration at the altitude of a particular traverse, it is reasoned that the greatest tower filter mean concentration at that elevation should be compared.

ARTS data can additionally be compared to the tracer flux which is given at the source by the rate of tracer generation and at another distance by the product of a height interval and the summation of the product of CIC and wind velocity within each height interval.

All comparisons discussed in this section require adequate sampling to obtain reasonable agreement. The deficiencies in practice are apparent,

and the measure of success is similarly qualified. Further discussion of these and other limitations appear in the next section.

DATA REDUCTION

Exposure, the time integral of concentration, is found by dividing the mass found on the filter by the flow rate appropriate to each sampler. For comparison between tests, the exposures are normalized by dividing by the amount of tracer generated.

RTS recorder charts are averaged by 5 sec intervals during cloud traverse. The mean signal level for each interval is readily determined with the aid of the mechanical integrater of the RTS recorder system. Through the prior calibration of the RTS with a filter sampler, the mean chart signals are converted to concentrations and thence to normalized concentrations by dividing by tracer emission rate. These 5 sec mean normalized concentrations are assigned a field location by use of the chart event marker. Units of both the normalized filter exposures, E/Q, and the normalized RTS concentrations, XT/Q, are expressed in $sec\text{-}m^{-3}$. As noted in the preceding section, the mean of the XT/Q values for total tracer passage should equal the filter E/Q at the same arc position provided that sufficient traverses of the RTS result in representative sampling of the time variations of concentration. Individual traverses will record the variability extent of the concentration.

Reduction of the ARTS record consisted of tabulating for each tracer traverse the following:

- Time of initial contact
- Time separation of ground reference and initial point
- Time duration for tracer traverse
- Altitude
- Peak concentration
- CIE determined by the recorder mechanical integrator

Using the previously determined ARTS calibration, the CIE and peak concentration are converted from signal level to units of $g\text{-}sec\ m^{-3}$ and $g\text{-}m^{-3}$, respectively, and mean concentration is determined by dividing the CIE by the traverse time duration.

Meteorological data, summarized in an appropriate manner to show the test history of the various parameters, include vertical profiles taken near the source of wind velocity, temperature, and the lateral component of turbulence to 400 feet.

SERIES 4D RESULTS

The results of this test series can be best presented by focusing on the more complete measurements of Test 4D-7 and their contribution to a fuller understanding of the total diffusion. Figure 2, showing distribution of normalized exposures measured by the surface filter samplers, exhibits a clearly defined peak near 137° and a long, low valued tail extending northward.

Figure 3 presents the manner in which the distribution of Figure 2

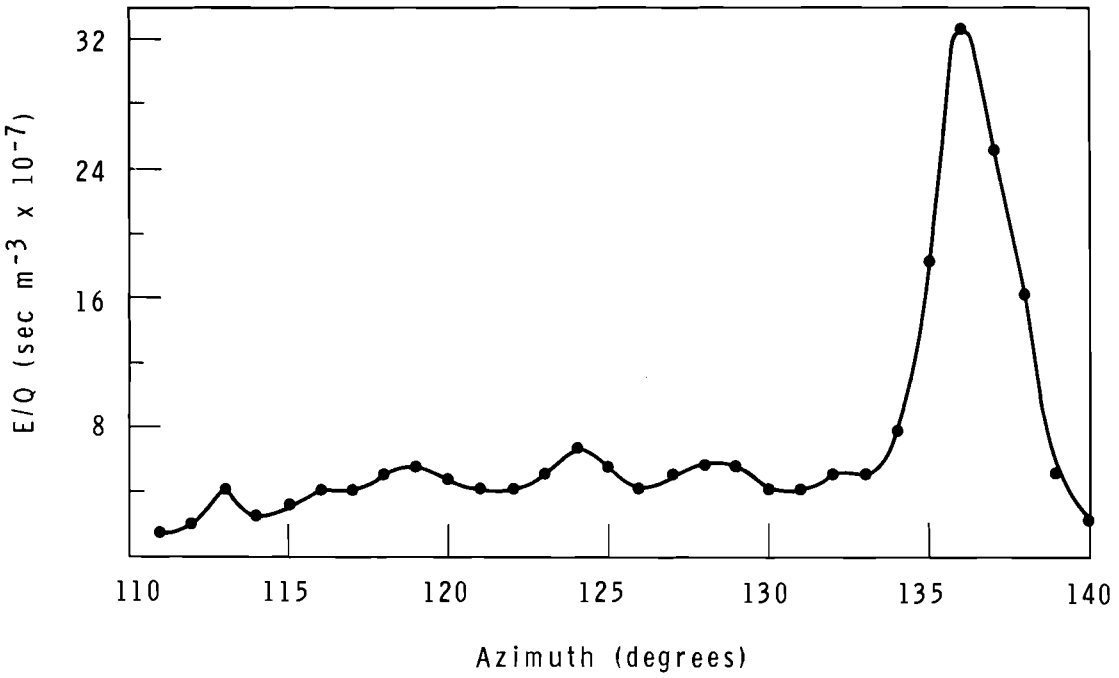

Neg. 0672873-8

FIGURE 2. Surface Distribution of E/Q at 3200 Meter Arc Defined by Filter Samplers of Test 4D-7

was achieved. A striking change in character of the crosswind distribution of concentration took place between traverses 6 and 7. The narrow, symmetrical, high-peak distributions of the first six traverses suddenly gave way to wide, undulating, low-peak distributions for traverses 7 through 14. One would expect to see a concurrent, similar striking change in the meteorology. Strangely, none is evident from the wind and temperature measurements at the source. At all levels of measurement, from 2.5 to 400 ft, wind speeds, wind directions, temperatures, and the variances of all three remained reasonably constant throughout the test. The wind direction at the source was 320°, with upper winds decreasing only to 310 degrees. Thus, the wind direction at the source can explain only that tracer at or near the peak. Unfortunately, no wind measurement was made between the source and the 3200 m arc, for the anomalous tracer distribution is attributed to a low-level crossflow in that region. Such cool air with a southerly component has been observed during other field diffusion experiments. This flow is thought to be drainage from Rattlesnake Mountain, which is oriented NW-SE about six miles southwest of the diffusion site. It is interesting to note that, although this flow did not affect the source, it caused a distribution on the 800 m arc similar to that on the 3200 m arc.

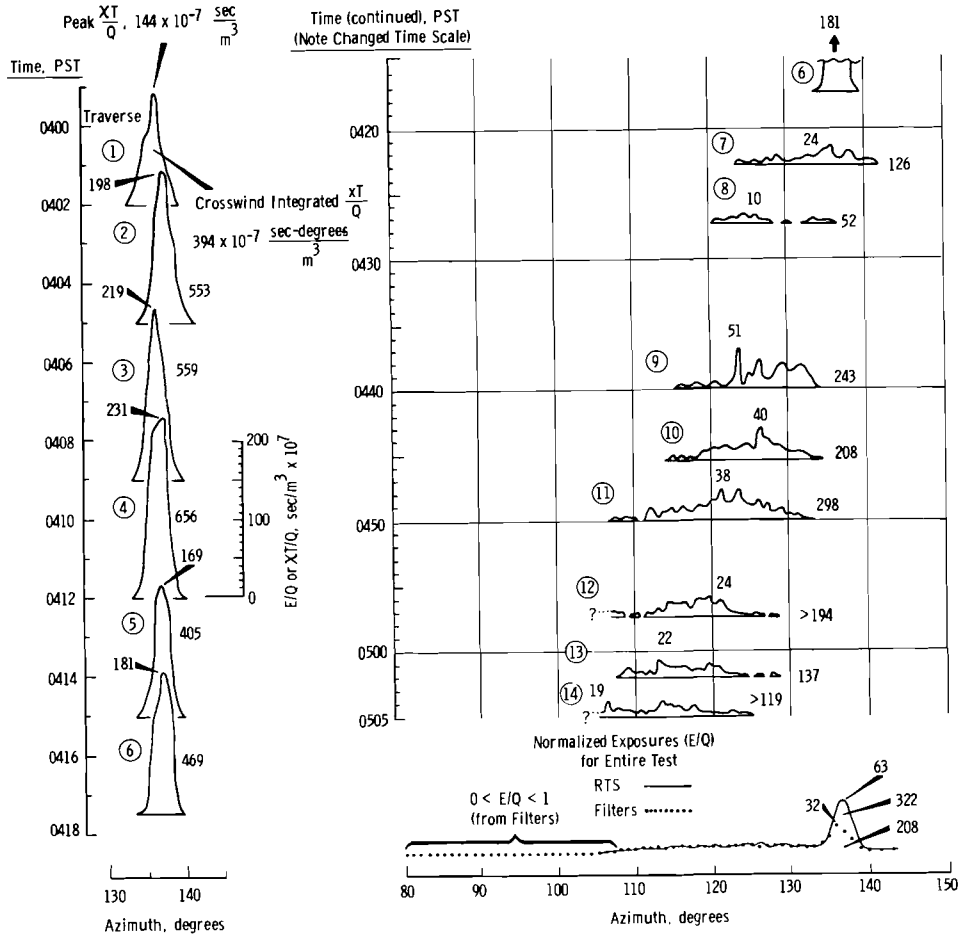

Neg. 0672744-1

FIGURE 3. Tracer Distribution at 3200 Meters During Test A-7 (Tracer Emission 0345 to 0440 PST)

Beyond the RTS capability for documenting the onset of local perturbations to the flow, strikingly demonstrated here, is the capacity for detailed description of the nearly instantaneous plume also clearly shown in Figure 3. The normalized crosswind integrated concentration is given to the right of each instantaneous distribution. These can be compared with the normalized crosswind integrated exposure determined from the filter samplers. This latter value of 208×10^{-7} sec-degrees/m^{-3}, shown in the lower right figure, was equal to the instantaneous value for one traverse, greater for five, and less for eight. Of interest are similar comparisons of crosswind integrated concentrations made during three previous tests in neutral to unstable conditions. In these less stable cases, 16 of 21 of the integrated traverses gave values less than the crosswind integration of the filters. It is proposed that the infrequent high concentration under

unstable conditions is missed by the traversing RTS. Conversely, the infrequent low concentration during stable conditions might also be missed by the RTS.

One discrepancy in the comparison involves the heights of sample collection. The RTS sampled at a height of 3 m on the truck bed, while the filters were exposed at a height of 1.5 meters. The presence of tower mounted filters on the arc presented the opportunity to check the vertical gradient of tracer at this arc distance. The mass of tracer at 3.1 meters was found to average 118% of that at the 1.5 m level. Use of this correction factor would result in equal division of traverses with greater and lesser values.

The comparison of XT/Q for each individual traverse with the filter E/Q was expected only to have equal numbers greater and less; but, if the time period for which each 5 sec mean concentration applies can be specified, the sum of the resulting exposures should compare to filter exposures at corresponding locations. The period for which a measured concentration was considered to be applicable encompassed the time interval from halfway to the preceding traverse to halfway to the succeeding traverse. The solid curve in the lower right plot on Figure 3 was generated in this manner. While azimuth agreement is good, the curve does not match well in magnitude the dotted curve from the filters. This difference is not unexpected in view of the previously mentioned preponderance of relatively high XT/Q values for the individual crosswind traverse. Correction, as before, for the error due to tracer gradient between 1.5 and 3.1 m would reduce the ratio of RTS exposure value to filter exposure value from 1.55 to 1.31. It should be noted, however, that the ratio of 1.18 was determined from exposures which did not encompass the early peaks of concentration. If the vertical gradient of concentration is assumed to vary as the lateral gradient, the vertical gradients occurring with the peaks centered around 137° must result in a ratio greater than 1.18 between the 3.1 and 1.5 m levels. Indeed, reference to the detailed comparison of Figure 4 shows only minor disagreement for lower concentrations in the tail to which the 1.18 ratio should apply.

The ratio of peak concentration to mean concentration is another parameter of interest. Calculation of approximations to this ratio at all points along the sampling arc have been made for Test 4D-7. E/Q values measured by the filter and computed from time-weighted RTS values of XT/Q were both compared to the maximum 5 sec mean XT/Q at each comparable location. The plots of these ratios are shown in Figure 4 below the curve of normalized mean concentration, or E/Q. The difference in the two peak-to-mean ratio curves is due, of course, to the differences in the RTS and filter curves of mean concentration. For the peak RTS to mean RTS curve, central values range from 3 to 5. The high values at either end suggest that the predominant contribution was received from brief peaks of tracer. The peak-to-mean ratio is dependent on the averaging times determining both peak and mean values.

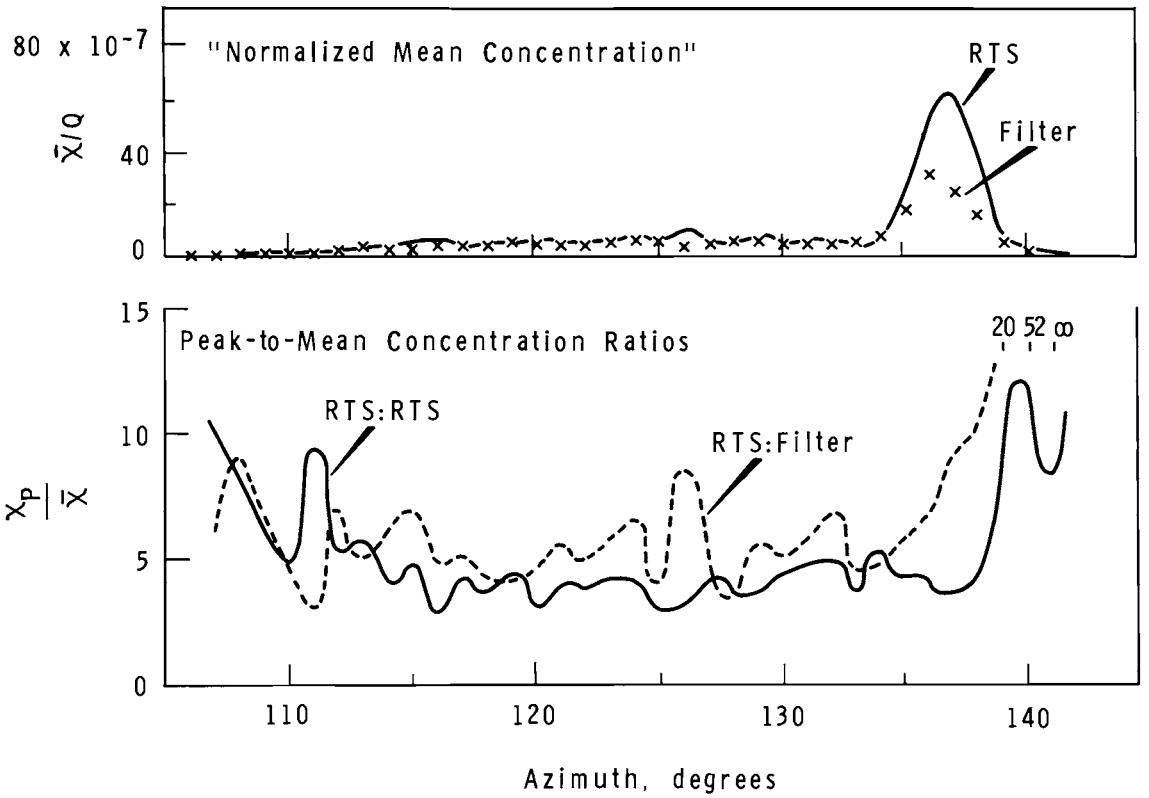

Neg. 0672873-4

FIGURE 4. Peak-To-Mean Concentration Ratios on 3200 Meter Arc Test 4D-7

The striking change of surface tracer distribution shown by the RTS at 0420 PST with reduced values of the crosswind integrated concentration suggests lifting of the tracer cloud by the drainage flow. Filter sampling on the tower nearest the initially peaked center of tracer distribution (some 400 m to the north) shows a definitely higher exposure above 15 m for the total run. The ARTS record of crosswind integrated concentration best demonstrates, perhaps, that this perturbation at the surface was felt as sharply above. Figure 5 demonstrates this effect with the averaged vertical profiles of tracer flux before and after the major surface change. The apparent increase in total flux following the onset of drainage is covered in the following discussion. For the purpose of examining the redistribution of tracer, the distribution during drainage flow normalized to the pre-drainage total flux is shown by the hatched area. Comparison of the curve enclosing the hatched area with the broken curve shows that the reduction at the surface is accompanied with vertical extension of the tracer. The unadjusted curve during drainage shows a total flux double that before the onset of drainage. It is, in fact, 1.7 times greater than the emission rate. The initial flux below emission

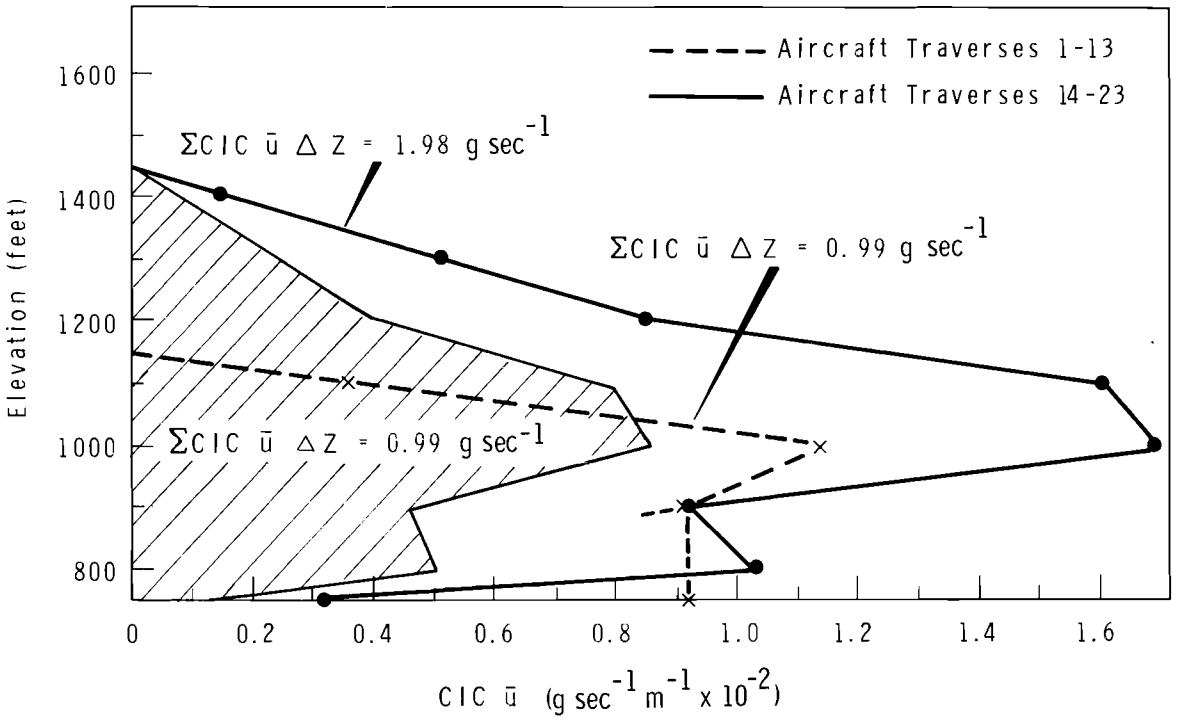

Neg. 0673405-1

FIGURE 5. Test 4D-7 Tracer Flux Distributions

rate is not unreasonable for high deposition rates, but the augmented flux is less easily explained. It must be presumed that the crossflow also had a component opposed to the mean wind measured at the tower and that use of the tower winds for calculation of flux leads to excessive values. The simultaneous lifting and shearing of the main flow must also contribute to the observed error.

The displacement and widening of the tracer plume, so pronounced at the surface for Test 4D-7, was somewhat more subtle aloft. The change in width particularly, was less noticeable possibly because of the tendency to disregard low level signals in the data reduction of the lower resolution ARTS chart. In addition, the generally greater variability displayed by instantaneous plumes aloft, presumably due to less intense mixing after separation from the surface, is shown in Figure 6 where widths and displacements for series 4D tests 2,4,7, and 8 are presented. Only for Test 4D-8 is the variability low. In that test, extreme stability of the surface layer contained the plume below 800 ft and all of the traverses shown were made at that altitude. The shift in the center of the plume aloft during Test 4D-4 is seen to be about 2300 ft, roughly 13°, and comparable to the shift observed on the surface.

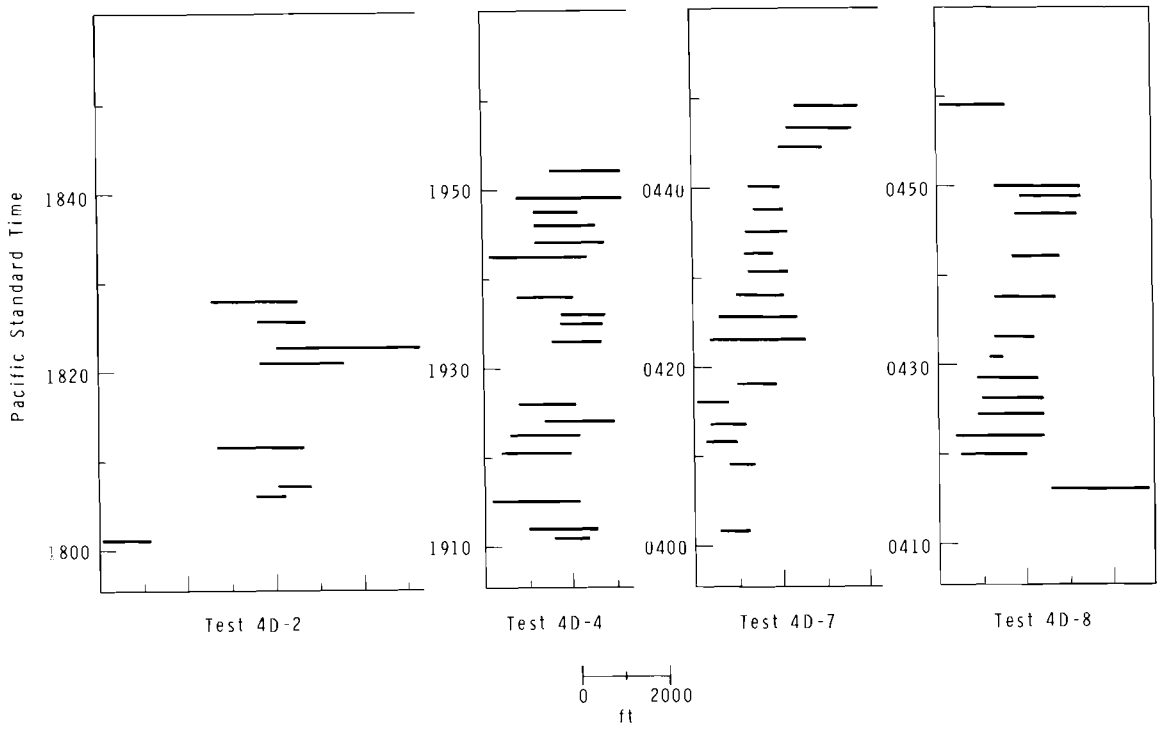

Neg. 0673405-2

FIGURE 6. Instantaneous Widths and Positions of Tracer at 3200 Meters Defined by Airborne Real Time Sampler

Within that time span, however, the shift aloft appears to lag that on the surface.

The comparison of ARTS measurements with RTS measurements was briefly touched upon in Figure 5 where both were used to construct a vertical distribution of flux. The desired comparison of ARTS and filter measurements at a common elevation is available only through tower filter data. Figure 7 shows the normalized mean concentrations determined with towers and ARTS. Test 4D-4, for which tower data were not available, is included only to show a distribution profile under a condition of neutral thermal stability, but with high wind shear. The absence of measurable tracer above 800 ft, and even up to 850 ft accounts for the single ARTS determined point for Test 4D-8. The agreement, perhaps fortuitous, is heartening. Location of the southernmost tower 400 m north of the main tracer passage prevents direct comparison of the ARTS values for Test 4D-7. It is observed, however, that the ARTS-defined profile is compatible with the surface maximum at 136° and with the vertical distribution of tracer at the closest tower. Test 4D-2 requires some additional discussion since the center of the plume was within a degree of the 130° tower. The question of calibration arising for this test is not applicable to subsequent tests. Calibration of the ARTS for all tests

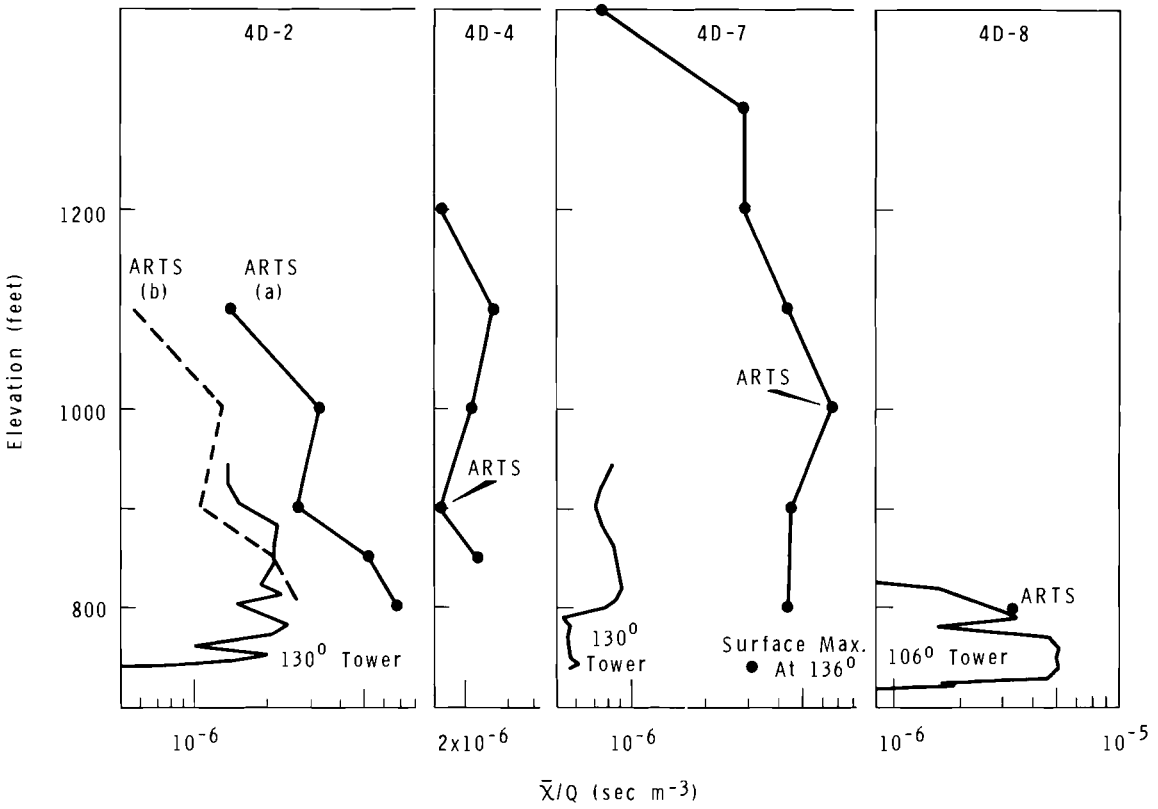

Neg. 0672873-2

FIGURE 7. Comparisons of $\bar{X}/Q$ From Filter and ARTS Samplers For Selected Tests of Series 4D

after 4D-2 was made using an RTS which was, itself, calibrated against filter samplers on March 1 and May 17, 1967. However, the ARTS calibration prior to Test 4D-2 was made with an RTS sampler calibrated over two years earlier. Filter samples exposed during the calibration of the ARTS prior to Test 4D-2 gave the lower conversion constant resulting in the broken curve displaying reasonable agreement with the tower samples. Figure 7, in addition to showing the ability of the ARTS to define the mean concentration, shows also that valid readings of mean concentration can be extended to heights well above conventional samplers.

FURTHER DEVELOPMENT OF THE ARTS SYSTEM

The use of the ARTS has been limited in the past to atmospheric environments free of liquid water and dust since both produce sporadic signals and the former may cause system failure. This limitation, particularly serious with the high sensitivities required at greater distances from the source, resulted in the decision to redesign the system. The redesigned system features:

- Improved flow characteristics through substitution of a new style light trap
- Insensitivity to liquid water through sealing of the entire

flow from contact with the photo-multiplier tube and electronics

- Discrimination between zinc sulfide and other particulates by use of optical filters to:
  - limit the ultraviolet illumination of the tracer to its excitation frequency, and
  - limit the radiation incident upon the photo-multiplier to the peak reradiation frequency of the zinc sulfide
- Increased stability of the system electronics through use of a dual photo-multiplier tube sensing system which provides
  - a constant reference signal
  - compensation for temperature changes, and
  - increased sensitivity by dark current cancellation.

REFERENCES

1. *P. W. Nickola, M. O. Rankin, M. F. Scoggins, and E. M. Sheen. "A System for Recording Air Concentrations of Zinc Sulfide Fluorescent Pigment on a Real Time Scale," J. Appl. Meteor., vol. 6, pp. 430-433. 1967.*

2. *P. W. Nickola and C. E. Elderkin. "Instantaneous Plume Detection," Pacific Northwest Laboratory Annual Report for 1966 in the Physical Sciences, BNWL-481-1. Pacific Northwest Laboratory, Richland, Washington, 1967.*

3. *W. L. Dotson, P. W. Nickola, and M. A. Wolf. "Real Time Sampling of Airborne Tracer with Aircraft," Pacific Northwest Laboratory Annual Report for 1966 in the Physical Sciences, BNWL-481-1. Pacific Northwest Laboratory, Richland, Washington, 1967.*

THE USE OF INSTANTANEOUS PLUME MEASUREMENTS TO APPROXIMATE A MEAN PLUME

J. V. Ramsdell

INTRODUCTION

Traditionally the study of diffusing plumes has been divided into distinct parts consisting of (1) study of mean properties of the plume, and (2) study of instantaneous properties of the plume. There have been few diffusion studies in which both instantaneous and mean properties of the same plume have been examined.

The interrelationship between the mean and instantaneous properties of a plume is important not only theoretically but also practically. An example might be diffusion studies conducted in regions where direct examination of the mean properties of the diffusing plume is not possible over the entire downwind distance of interest. It may be possible in such studies to examine the properties of the instantaneous plume by use of moving instrumentation even though stationary instrumentation for the measurement of the mean plume cannot

be used. If the instantaneous plume properties are measured, then the ability to translate them into mean plume properties will be of value.

A number of diffusion experiments have been conducted at Hanford and in an Air Force study in which both instantaneous and mean measurements of the same plume have been made. The results of an analysis of 12 of these tests are presented here to demonstrate a rudimentary capability to transform instantaneous plume measurements to mean plume properties and to demonstrate a specific application of this capability.

THEORETICAL RELATIONSHIP BETWEEN THE INSTANTANEOUS AND THE MEAN PLUME

While little experimental work has been done on the relationship between instantaneous and mean properties of a plume, the theoretical relationship between the two has been closely examined. One particularly useful approach to this relationship was published by F. A. Gifford.[1] According to Gifford, the variance of the distribution of material within a mean plume should be equal to the sum of the variance of the position of the instantaneous plume centerline about the mean centerline and the average variance of the distribution of the material about the instantaneous plume centerline. This relationship provides a theoretical basis for transforming instantaneous properties of a plume to mean properties.

Six diffusion tests, conducted in unstable air at Hanford, have been analyzed in an attempt to verify Gifford's theoretical relationship. Measurements of the instantaneous properties of the plume were made with a Real Time Sampler (RTS) developed at Hanford.[2] RTS units were mounted on a pickup truck[3] and on a Beechcraft Queen Air airplane[4] which traversed concentric sampling arcs during the period of tracer release in a manner similar to that described by Nickola and Elderkin.[3] The roving RTS units made an average of 12 intercepts of the instantaneous plume at a constant distance from the source in each test. The intercept distance from the source varied from test to test within the range 800 and 3200 meters.

Computation of the variance of the positions of the instantaneous plume centerline was straightforward as the RTS charts were directly correlated with positions on the sampling arc through event markers on the charts. The mean centerline was determined by averaging the positions of the instantaneous centerline, and the variance about the mean centerline was calculated directly from the definition of variance. The variance of material about the instantaneous centerline was estimated from the trace on the RTS chart using the maximum concentration, the minimum detectable concentration, and the width of each plume intercept. As a first approximation, the distribution of material within the instantaneous plume was assumed to be Gaussian, an assumption also made by Gifford. The two variances determined from the RTS data were then summed to approximate variance of the distribution of material within the mean plume.

While the RTS units measured the instantaneous plume, the mean properties of the plume were measured by filters in the usual Hanford manner.[5] The variance of the distribution of material in the mean plume was computed directly from the filter exposures.

The two methods for determining σ_y, the standard deviation (variance$^{1/2}$) of the horizontal distribution for a mean plume, are compared in Figure 1. The relationship between the RTS approximation of σ_y and σ_y as determined from the filter data is:

$$\sigma_y \text{ (filters)} = 0.794\ \sigma_y \text{ (RTS)} + 38.5$$

The relationship has a correlation coefficient of 0.953 which indicates that a mean plume, σ_y, may be usefully approximated by measurement of the instantaneous plume and the tranformation techniques used. The size of the correlation coefficient may be somewhat fortuitous due to the small number of tests analyzed.

Of additional interest are the relative contributions of the meander of the instantaneous plume and diffusion meander within the instantanecus

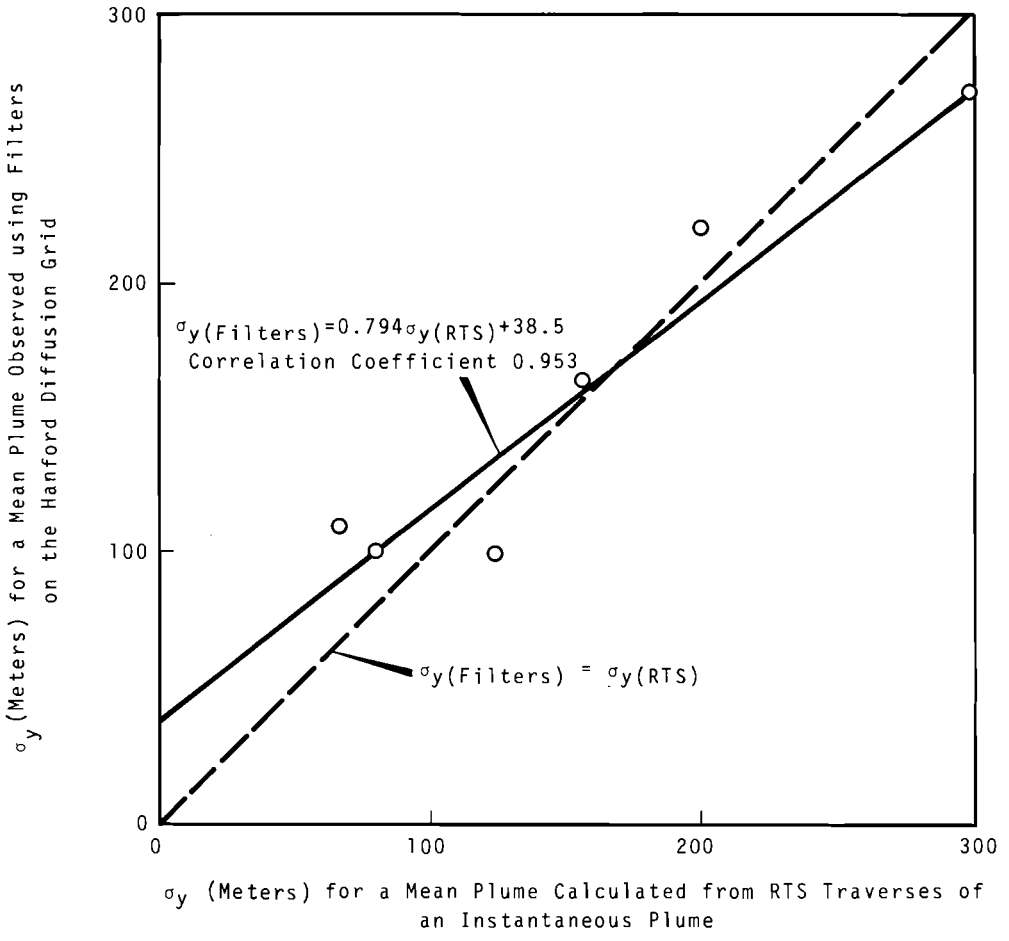

FIGURE 1. Correlation of Measured σy and Approximated σy for a Mean Plume

plume. In the distance range included in these tests, the contribution of the meander of the instantaneous plume centerline to the variance of the distribution of material about the mean centerline is three to ten times larger than the contribution of the distribution within the instantaeous plume.

APPLICATION OF INSTANTANEOUS PLUME MEASUREMENTS TO APPROXIMATE A MEAN PLUME

A series of diffusion tests for the Air Force presents an opportunity to apply the techniques developed for approximating the mean properties of a plume from measurement of its instantaneous properties in a practical manner. The tests were conducted over mountainous coastal terrain. The prevailing wind carried the tracer off shore about 3000 m from the source. Stationary sampling arcs were constructed at 500, 1000, and approximately 2100 meters. To gather data beyond the fixed sampling grid, an RTS unit mounted in the Queen Air was used. During the tracer releases, the aircraft made intercepts of the plume at approximately 3, 6, and 9 miles from the source, and occasionally at distances of 12 miles and beyond. The instantaneous plume measurements from the 3, 6, and 9-mile intercepts have been transformed into forms compatible with measurements of the mean plume with the same techniques used to verify Gifford's model, and with a method similar to that reported by Nickola and Elderkin.[3] The results of these manipulations are presented with the data from the sampling grid in Figures 2 and 3.

The growth of σ_y of the mean plume with increasing distance from the source is shown in Figure 2. The growth of the average σ_y over land is much as would be expected from the results of other diffusion studies ($\sigma_y \propto x^{0.8}$). The noticeable decrease in the growth rate of σ_y off shore ($\sigma_y \propto x^{0.4}$) is reasonable and has been reported in the literature by several writers.[6] Of particular interest is the rapid growth of σ_y indicated between 2100 m, the end of the sampling grid, and 5000 m, the beginning of the aircraft sampling area. To better examine this rapid change in σ_y, both growth rates have been projected to a common distance, 3000 m, the approximate distance from the source to the coastline. The σ_y derived from the RTS data is a factor of about 3.7 larger than that computed from the sampling grid, a difference too large to be explained by projection of lines of unequal slopes.

The rate of decrease in exposure as distance from the source increases casts some light on this discontinuity. In Figure 3, the RTS data (transformed to approximate mean plume properties) and the sampling grid data for the Air Force study show the decrease in maximum exposure with distance. A definite difference in the rate of decrease in exposure from the filter data, over land, and the RTS data, over water, indicates (not unexpectedly) that diffusion is more rapid over land than over a body of water. When the slopes of the two curves are again projected to 3000 m, the maximum exposure developed by the extrapolation of the RTS data is about 0.22 of that developed by the extrapolation of the sampling

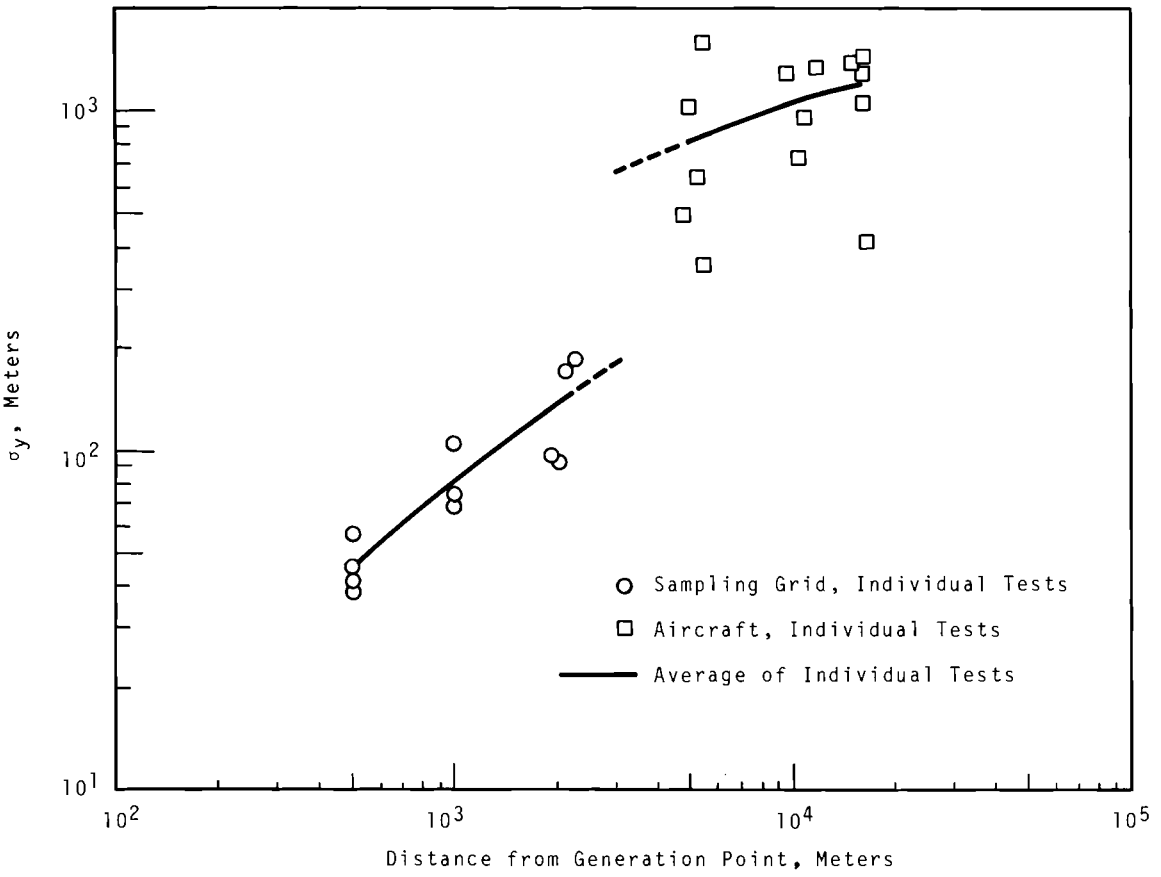

FIGURE 2. Growth of Lateral Dispersion of a Mean Plume with Distance

grid data. It is significant that about 80% of this decrease in exposure can be accounted for by the rapid increase in σ_y discussed earlier and that the contribution of other factors, notably σ_z, is therefore relatively small.

Both Figures 2 and 3 indicate the region of rapid diffusion between the end of the sampling grid and the beginning of the aircraft sampling area. This indication is felt to result from the air flow at the coastline rather than to the differing methods of determining the mean properties of the diffusing plume. To substantiate this reasoning, two plausible mechanisms for the rapid diffusion at the coastline can be postulated. The increased diffusion could be caused by an extreme wind direction shear resulting from the joining of separate air flows over and around the point of land on which the source was located. The rapid diffusion could also be caused by downwash and wake effects created by the downslope flow of air toward the coast and the flow of air over the

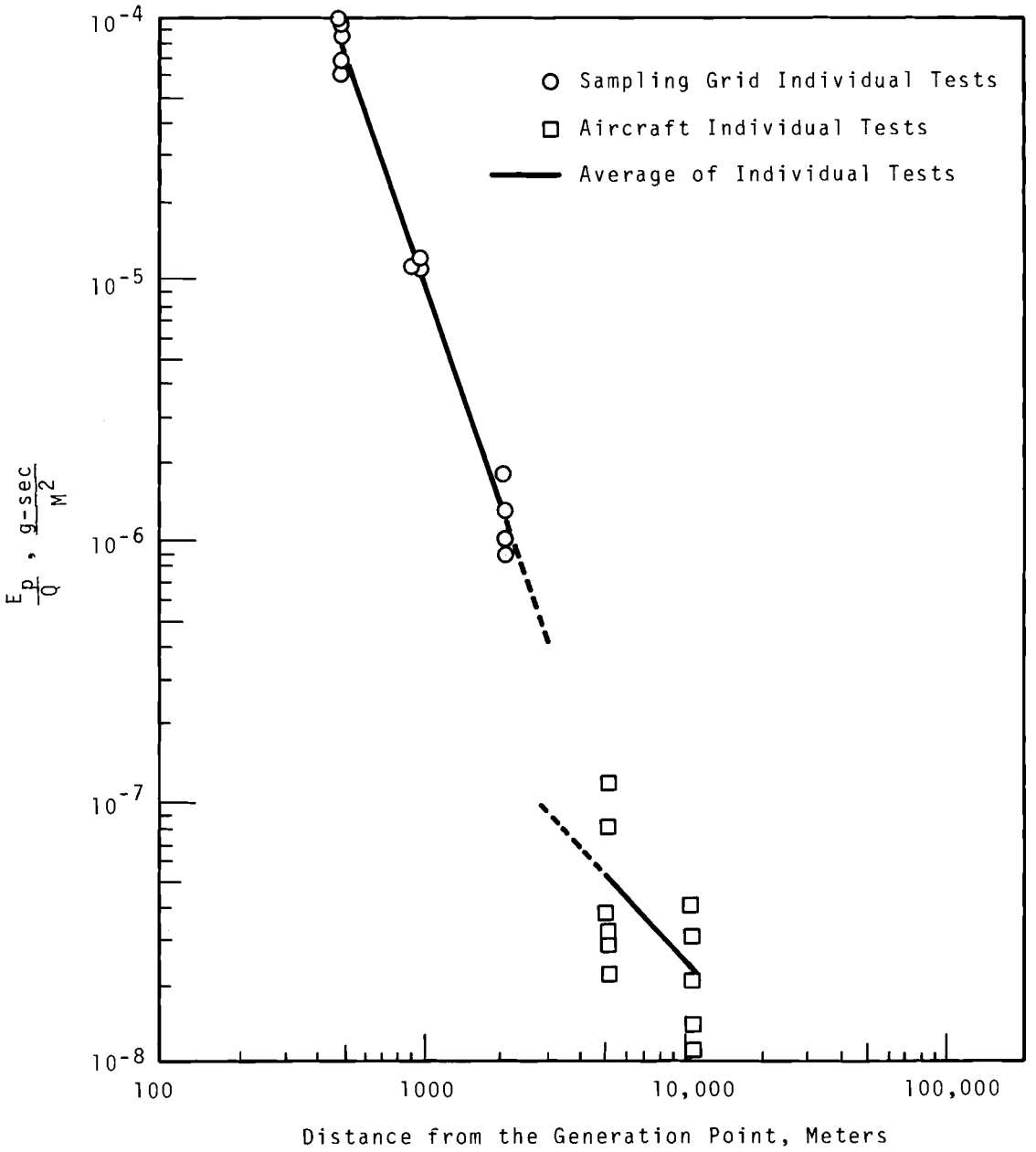

FIGURE 3. Decrease in Maximum Exposure Normalized to Source Strength of a Mean Plume with Distance

cliff at the coastline.[7] Turbulence measurements made at low levels (250-1250 ft) indicate an area of relatively strong turbulence at the coastline.[8] This region of turbulence would be necessary for the rapid diffusion observed to exist.

CONCLUSIONS

Analysis of 12 diffusion experiments has been conducted at Hanford and in an Air Force study to examine the relationship between the mean and instantaneous properties of a diffusing

plume. The analysis of the Hanford tests has verified Gifford's "Fluctuating Plume" dispersion model, and analysis of the Air Force tests showed that a combination of mean plume measurements and mean plume approximations describes diffusion in a realistic manner consistent with theory. It is possible, with the approximation techniques used in these analyses, to extend diffusion studies to difficult places and situation.

Continued examination of the relationship between the mean and instantaneous properties of a plume is planned in further diffusion experimentation at Hanford. These tests will be used to refine the techniques of approximation of the mean plume.

REFERENCES

1. F. A. Gifford. "Statistical Properties of a Fluctuating Plume Dispersion Model", Advances in Geophysics. Academic Press, New York 1959. vol. 6, pp. 117-137.

2. P. W. Nickola, M. O. Rankin, M. F. Scoggins, and E. M. Sheen. A Device for Recording Air Concentrations of Zinc Sulfide Fluorescent Pigment on a Real Time Scale, HW-SA-3317. Available from Clearinghouse for Federal Scientific and Technical Information, Springfield, Virginia, January 10, 1964.

3. P. W. Nickola and C. E. Elderkin. "Instantaneous Plume Detection," Pacific Northwest Laboratory Annual Report for 1966 to the USAEC Division of Biology and Medicine, Vol. II: Physical Sciences, Part 1, Atmospheric Sciences, BNWL-481-1, pp. 33-43. Pacific Northwest Laboratory, Richland, Washington, October 1967.

4. W. L. Dotson, P. W. Nickola, and M. A. Wolf. "Real Time Sampling of Airborne Tracer with Aircraft," Pacific Northwest Laboratory Annual Report for 1966 to the USAEC Division of Biology and Medicine, Vol. II: Physical Sciences, Part 1, Atmospheric Sciences, BNWL-481-1, pp. 53-68. Pacific Northwest Laboratory, Richland, Washington, October 1967.

5. J. J. Fuquay, C. L. Simpson, and W. T. Hinds. "Prediction of Environmental Exposures from Sources Near the Ground Based on Hanford Experimental Data," J. Appl. Meteorol., vol. 3, no. 6, pp. 761-770. December 1964.

6. I. Van der Hoven. "Atmospheric Transport and Diffusion at Coastal Sites," Nucl. Safety, vol. 8, no. 5, pp. 490-499. Sept-Oct 1967.

7. E. W. Hewson and L. E. Olsson. "Lake Effects on Air Pollution Dispersion," J. Air Pollution Control Assoc., vol. 17, no. 11, pp. 757-761. November 1967.

8. T. B. Smith, E. K. Kauper, S. Berman, and F. Vukovich. Micrometeorological Investigation of Naval Missile Facility, Point Arguello, California, Vol. I. Meteorology Research, Inc., 2420 North Lake Avenue, Altadena, California, 1964.

DIFFUSION OVER COASTAL MOUNTAINS OF SOUTHERN CALIFORNIA

W. T. Hinds

INTRODUCTION

During the past decade, the United States Air Force has supported large scale diffusion programs over a variety of terrain. These programs began with Project Prairie Grass[1] over flat prairie, continued with Project Green Glow[2] over rolling steppe, and with the Ocean Breeze and Dry Gulch diffusion programs[3] over flat coastal regions on the Atlantic and Pacific shores, respectively. The most recent large scale program in this series of diffusion studies from continuous ground level releases of about 15 to 30 sec duration was Operation Mountain Iron, carried out over the mountainous southern portion of Vandenberg Air Force Base (the considerably flatter northern portion of Vandenberg AFB was the site of the Dry Gulch program). This paper is a summarization of the results of Phase I of Mountain Iron. Phase II, to follow, is a comparable study at a slightly different location where diffusion in off-shore winds will be discussed.

The topics in this paper deal with brief descriptions of the site, an outline of the experimental technique, a description of the data and their availability, the development of techniques for estimating plume width, the development of a diffusion equation, and a discussion of the influence of terrain on plume geometry and general levels of exposure as compared to flat terrain in the same climate.

The symbols used in this paper are:

- E_p centerline ("peak") exposure, g-sec/m^{-3}
- Q_T total mass of tracer released, g
- t travel time, sec
- X distance, m
- $\bar{u}$ mean wind speed, m-sec^{-1}
- σ_y standard deviation of crosswind plume distribution, m
- σ_θ standard deviation of crosswind velocity fluctuations, degree
- ΔT temperature difference, °F
- β ratio of Lagrangian and Eulerian time scales.

DESCRIPTION OF THE SITE

South Vandenberg Air Force Base is located on the Point Arguello section of the California coastline. It is bounded on the north by the flat Santa Ynez River Valley, on the west and south by the Pacific Ocean, and on the east by a north-south line some 10 km inland from Point Arguello. A topographical map of the area is shown in Figure 1. Generally speaking, the northwest portion of the area is a rolling grassland and the balance of the area is a complex of ridge and canyon formations.

The major ridges of South Vandenberg are mostly covered with a dense stand of low growing chapparal and related shrubs, whereas the lowlands are generally grassland as exemplified by the floor of Honda Canyon, the Sudden Ranch area, and the Lompoc Terrace. Trees, except those east of the head of Honda Canyon

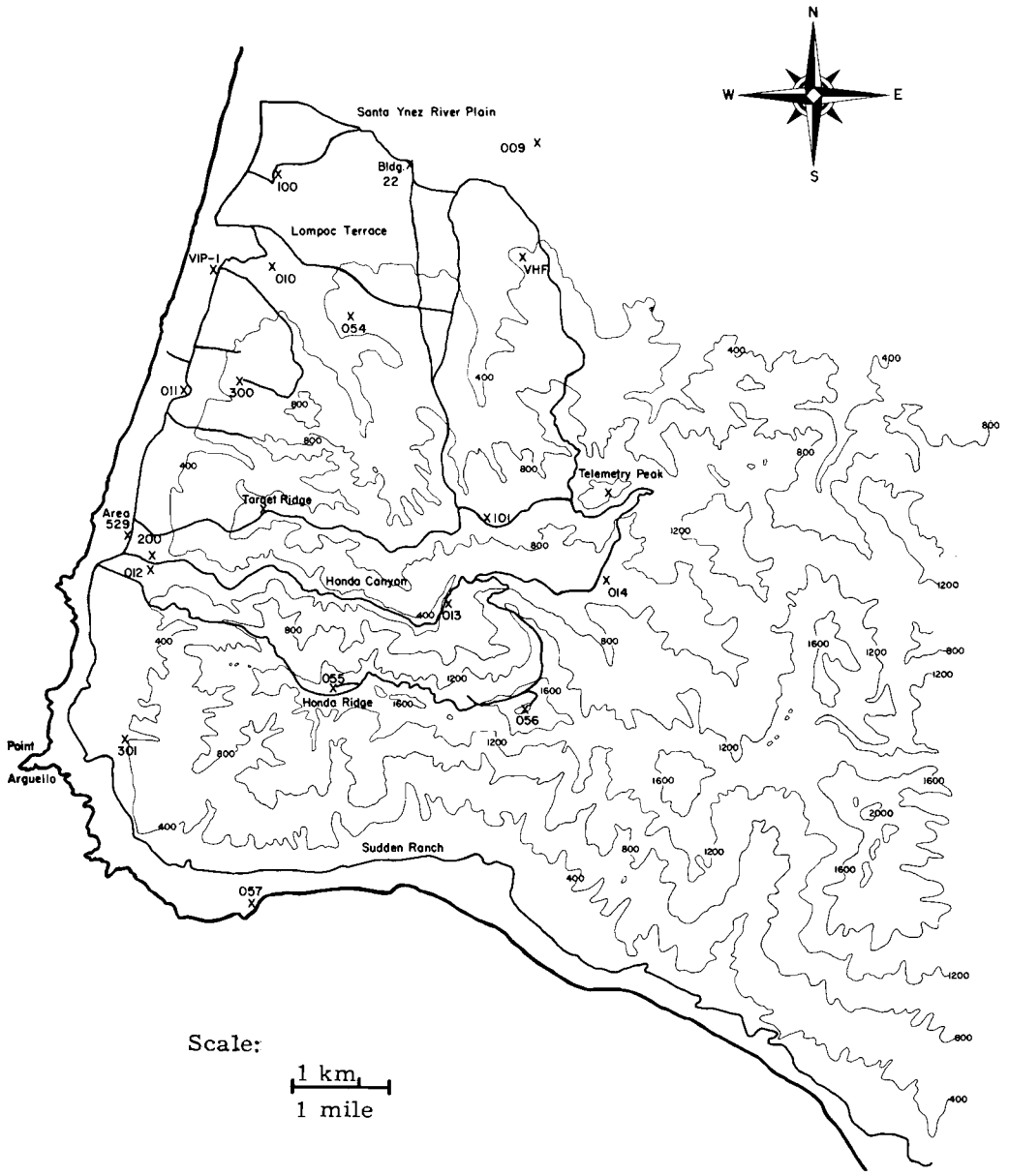

Neg. 0672792

FIGURE 1. Topographical Map of South Vandenberg

and along creek beds, are found in scattered clumps only. The vegetation changes rather rapidly with increasing distance from the ocean. Trees in increasing number follow the generally increasing average precipitation inland in this area.(4)

EXPERIMENTAL DESIGN

The steep slopes over much of South Vandenberg served to effectively prohibit the construction of a traditional diffusion grid, that is, a grid with samplers located on arcs

concentric about the source point. Existing roads and trails were used for sampler location, with the final configuration of the grid as shown in Figure 2. The first (two-digit) number indicates the sampling route number. The second (three digit) number* indicates the particular sampler number on the route. The air samplers were aspirated membrane filters used in many previous studies.[2]

Two source points were used, as indicated on Figure 2. Source A was the primary source point--80% of the 113 field tests were run from this point. Most of the samplers in the field were oriented toward Source A and, because of the separation between Source A and Source B, were consequently somewhat misoriented with respect to Source B. Attempts were made to account for the error so introduced during analysis of the Source B data. Samplers located along the floor of Honda Canyon were oriented into the prevailing up-canyon flow,[5] rather than toward Source A.

The tracer used was zinc sulfide, released through insecticidal foggers as in earlier series.[2] The nozzles of the foggers were aimed at a common point to provide essentially a point source with an effective source height of about 2 to 6 meters.

Sample assay techniques were identical to those of earlier test series, that is, scintillation counting of alpha particle bombardment of the zinc sulfide particles. The standard error of counting with this method is less than 0.048 for scintillation counts greater than 1000 per minute.[2] In general, data analysis was restricted to samples with count rates greater than this.

Meteorological data were gathered by three systems:

- Source point wind vector and temperature soundings,
- Outlying wind vector measurements at several points over South Vandenberg,
- Radiosonde releases at hourly intervals at four sites on South Vandenberg.

Portable cup-and-vane anemometry (at standard anemometer height) was used for the wind measurements at the source point and the outlying points. A wiresonde was used for the source point temperature measurements.

DESCRIPTION OF THE DATA

The 160,000 data bits collected during the Mountain Iron program defy publication, except in summary form,* in the format of this paper. Therefore, the types of data available will be described here. The data themselves will be available from the National Weather Records Center, Asheville, North Carolina. To prevent ambiguity, requests should specify data from the Mountain Iron diffusion program at Vandenberg Air Force Base during the years 1965 and 1966.

* *A decimal is understood before the final zero.*

* *Data summaries are included in Appendices to this report*

The data available are:

- Source point wind speed and direction, smoothed over 10-sec intervals and averaged over the length of release
- Source point temperature stratification, with hourly soundings from the surface to 300 ft above ground level
- Wind speed and direction averaged over 7 1/2 or 10-min intervals for each of the outlying sites located on Figure 2, and for 2 to 3 hr per test period
- Wind speed and direction, temperature, and relative humidity at 200-m intervals from hourly radiosonde releases at each of the radiosonde release sites located on Figure 2. Soundings routinely were followed to 5000 ft, with one sounding from each site followed to 10,000 ft for each test period
- Diffusion data consisting of exposure (normalized to source strength) at each of the sampling sites for each test (distance from source to samplers is included in the tabulation).

ANALYSIS

Primary emphasis during the analysis was placed on developing an equation for calculating centerline exposures at any arbitrary distance from a source, using standard meteorological measurements. In the process of developing the equation, two approaches, (1) to insure that the final equation was indeed the best possible, and (2) to investigate the application of techniques developed for use over flat terrain to mountainous terrain were followed. The two approaches were:

- The standard distance-dependent diffusion analysis
- A time-dependent diffusion analysis using the Hay-Pasquill[6] hypothesis for calculating plume width at downwind points.

The analysis thus required estimates of travel time and crosswind standard deviations of exposure, as well as the observed exposure distribution and known distances to samplers.

TRAVEL TIME

Estimation of travel time from a simple $x/\bar{u}$ calculation is appropriate only so long as the wind speed does not change. On South Vandenberg, wind speed usually increases radically from the level grassland to the crests of the ridges. Furthermore, the coastline in the Sudden Ranch region has often experienced higher wind speeds than the upwind ridge crests.[5] To account for the wide variation in wind speed, a series of regions surrounding each of the outlying wind sensors was laid out, and the wind field in each region was assumed to be characterized by the wind measured at the sensor. The pattern of wind regions laid out for tests from Source A is shown in Figure 3. Travel times were calculated by an iterative procedure beginning at the source, and with the transport speed changed as the center of the

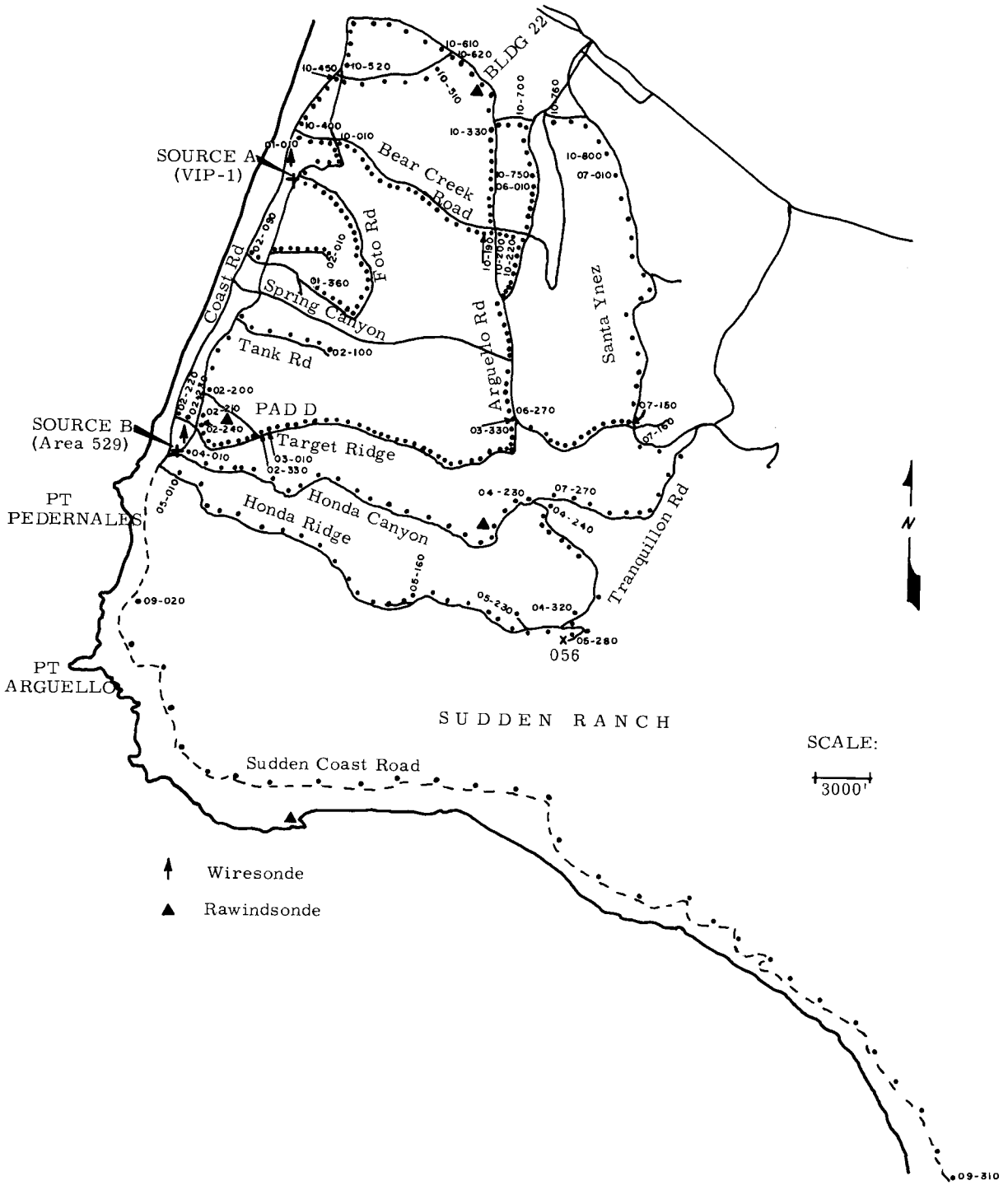

FIGURE 2. Sampling Grid for Mountain Iron Diffusion Tests

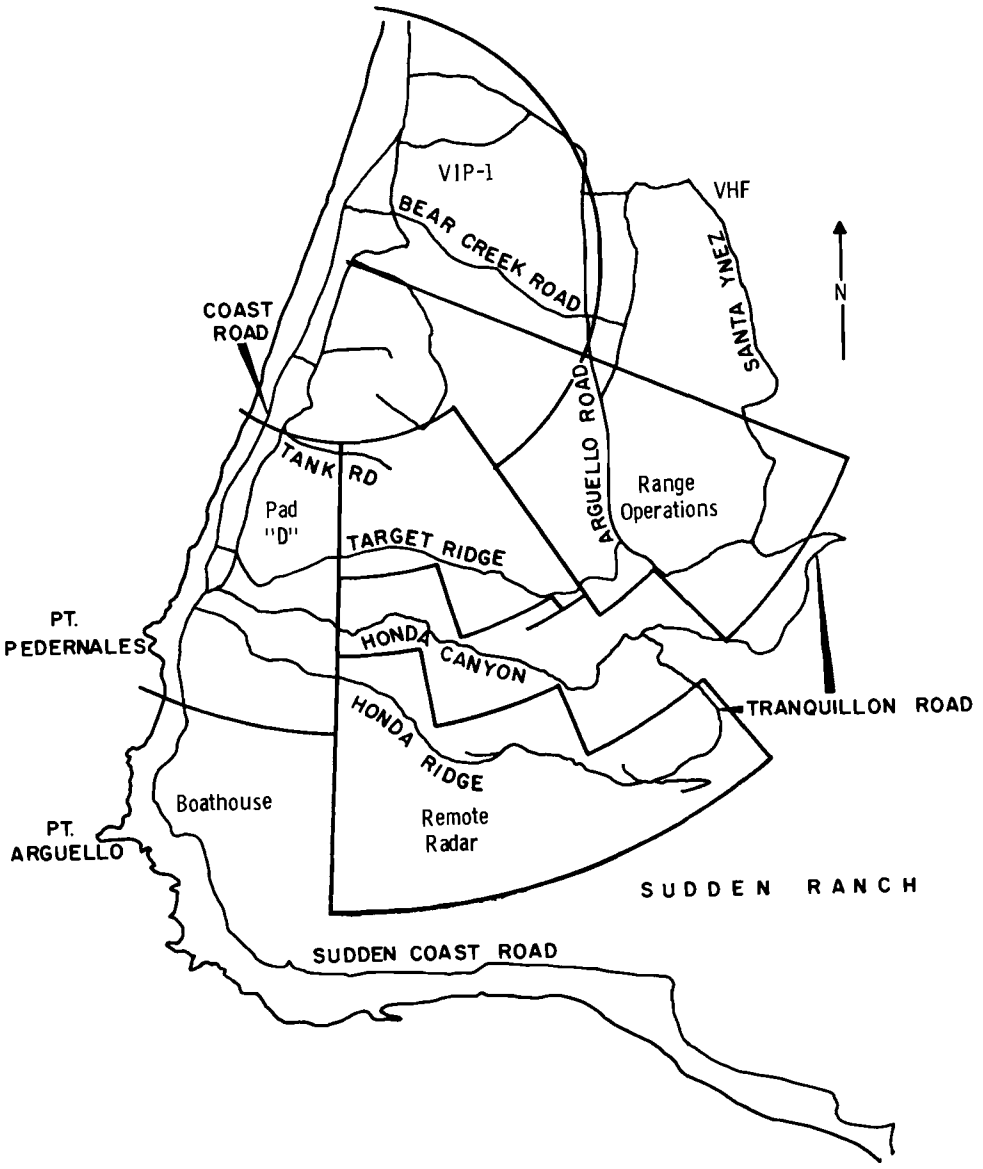

Neg. 0672563-1

FIGURE 3. Wind Regions for Tests from Source A

plume crossed each boundary. Times to succeeding ridge crests were calculated from the upwind ridge crest without regard for the lighter winds usually characteristic of the canyon floor. This method sometimes led to shorter travel times to crests downwind of a canyon than to the nearer canyon floor. This result is physically reasonable since canyon floor flow is usually decoupled from the flow over the crests, a point to be discussed later.

PLUME WIDTH ESTIMATION

Direct calculation of σ_y was usually impossible, since the sampling stations were not on concentric arcs or lines normal to the plume axis. Adjustment of the observed exposure values to place them on virtual concentric arcs would be misleading, since the correction would necessarily assume an arbitrary rate of diffusion. This, of course, is precisely the question to be answered in the first place. Therefore, plume width standard deviations for each test and distance from the source were estimated from exposure isopleths.

On a few occasions, the plumes did cross sampling routes at right angles where the routes were straight. Using these tests, standard deviations were calculated and compared with the estimated values leading to the results shown in Figure 4. The comparison was encouraging because the

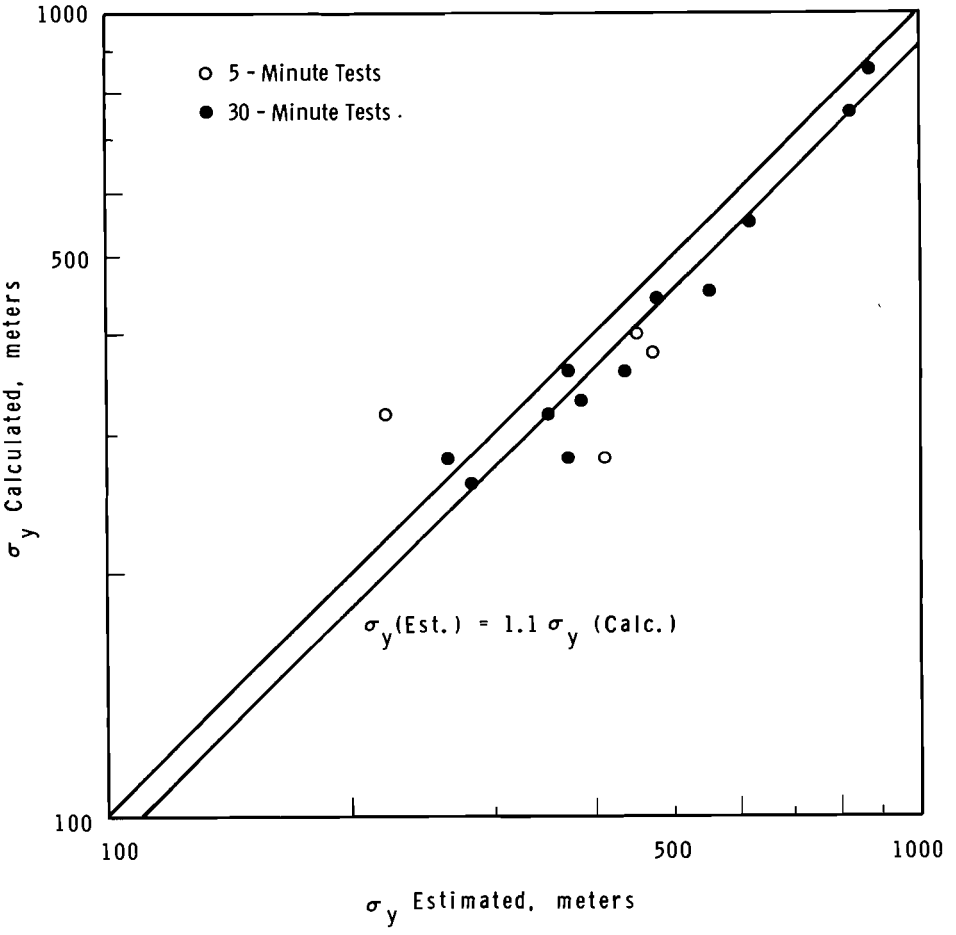

Neg. 0672563-2

FIGURE 4. Calculated and Estimated Values of σ_y for Tests with Appropriate Sampling

error indicated was only about 10%; so, wherever appropriate, the standard deviations were estimated.

The 10% error indicated in Figure 4 seems to be primarily caused by asymmetry. The average kurtosis of the distributions of the plumes used in the comparison was 3.1, compared to the Gaussian value of 3.0, whereas the average skewness of the plumes was 0.65, compared to the Gaussian value of zero. However, the systematic 10% overestimation could not be demonstrated to be a characteristic of all tests. Thus, no correction of estimated standard deviations were made to account for 10% error and the estimations were assumed to be accurate.

PLUME GROWTH OVER SOUTH VANDENBERG

The accumulated results of what are now a vast number of diffusion tests in the last 40 years by many workers have shown that σ_y increases as a power function of distance, with the exponent typically near 0.8. The South Vandenberg region was no exception, as shown in Figure 5. On the average, $\sigma_y = 0.65\ X^{0.75}$, with a substantial scatter that could be reduced by normalizing to σ_y. A better normalization uses σ_θ smoothed over intervals dependent on the travel time and β, the ratio of Langrangian and Eulerian time scales.[6] β is inversely related to the intensity of turbulence,[7] taken here to be measured by σ_θ. The best relationship between β and σ_θ for the South Vandenberg region was $\beta = 200/\sigma_\theta$, which led to the results shown in Figure 6. About 75% of the data lie within 40% of the mean, an encouragingly good fit. It must be noted that while $\beta = 50/\sigma_\theta$ gave σ_y predictions significantly poorer than $\beta = 200/\sigma_\theta$, using $\beta = 100/\sigma_\theta$ gave σ_y predictions little different than $\beta = 200/\sigma_\theta$. Thus, the Mountain Iron plume width data are not particularly sensitive to the value of β chosen, in common with results from many other diffusion tests.[8]

The magnitude of β calculated from $200/\sigma_\theta$ is larger than that ordinarily reported from other diffusion tests. While σ_θ varied from about 3 to 25°, β varied from about 60 to 8. However, the entire concept implied by β is not clearly appropriate at South Vandenberg because conditions obviously were not homogeneous, a basic assumption of the Hay-Pasquill hypothesis. Although the concept of smoothing the wind direction fluctuations over increasing intervals as travel time increased led to good estimates of σ_y, the strict interpretation of β (calculated from the $200/\sigma_\theta$ relation) as the ratio of Lagrangian and Eulerian time scales is incorrect at South Vandenberg.

DEVELOPMENT OF A DIFFUSION EQUATION

The development of a prediction equation is in some aspects an art, and sometimes requires a substantial investment of time for successful completion. To minimize the time

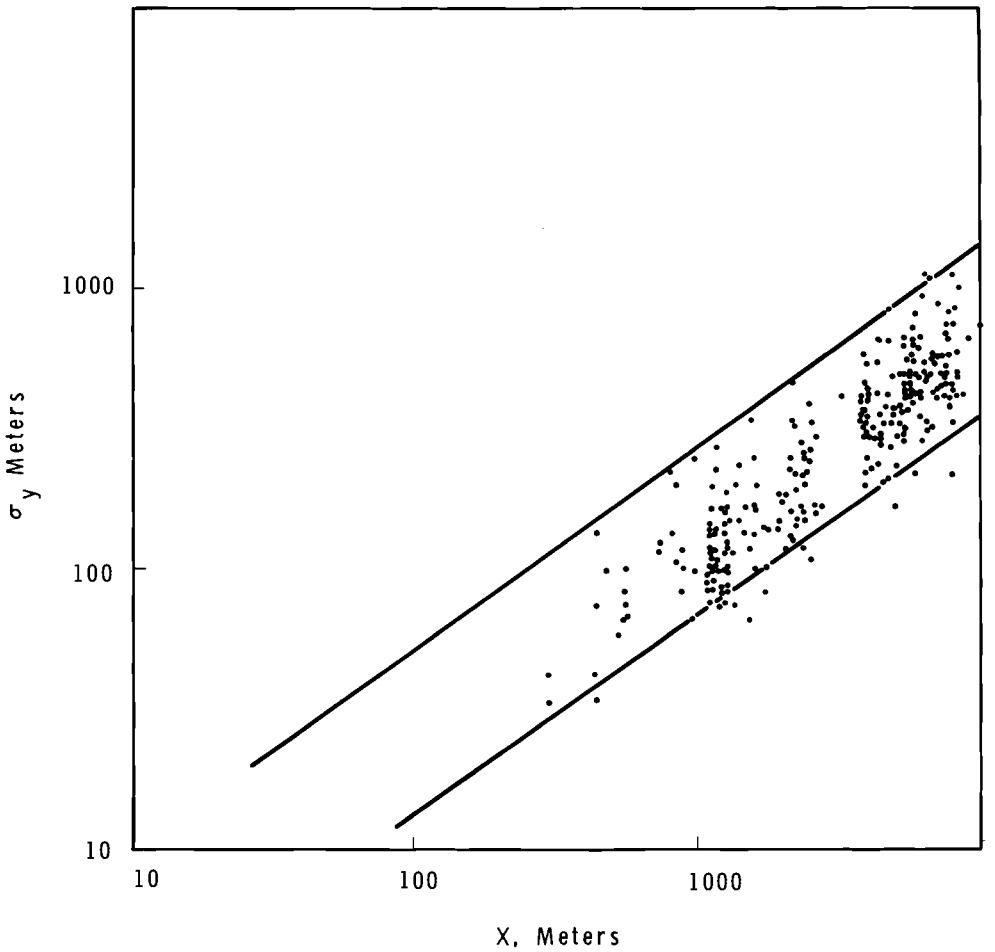

Neg. 0672578-3

FIGURE 5. σ_y Versus Distance for Mountain Iron, All Tests from Source A

required, a multi-variate regression technique was chosen to relate parameters that were chosen on physical or empirical grounds. A criterion by which success could be judged was taken as the degree of improvement obtained from the final equation when compared to a simple prediction of exposure as a function of distance alone. This relation was $E_p/Q_T = 0.390\ X^{-1.66}$. Of the observed data 92% were within a factor of four of this equation. The relative success of this simple equation was a surprise because the previous analysis of data from North Vandenberg[9] showed that a similar simple distance relation had only 72% within a factor of four of the equation. It was immediately clear that the South Vandenberg data had a smaller total scatter and were less dependent on extant atmospheric conditions. To a considerable degree, the development of the diffusion equation for South Vandenberg was a refinement of the simplest relation possible.

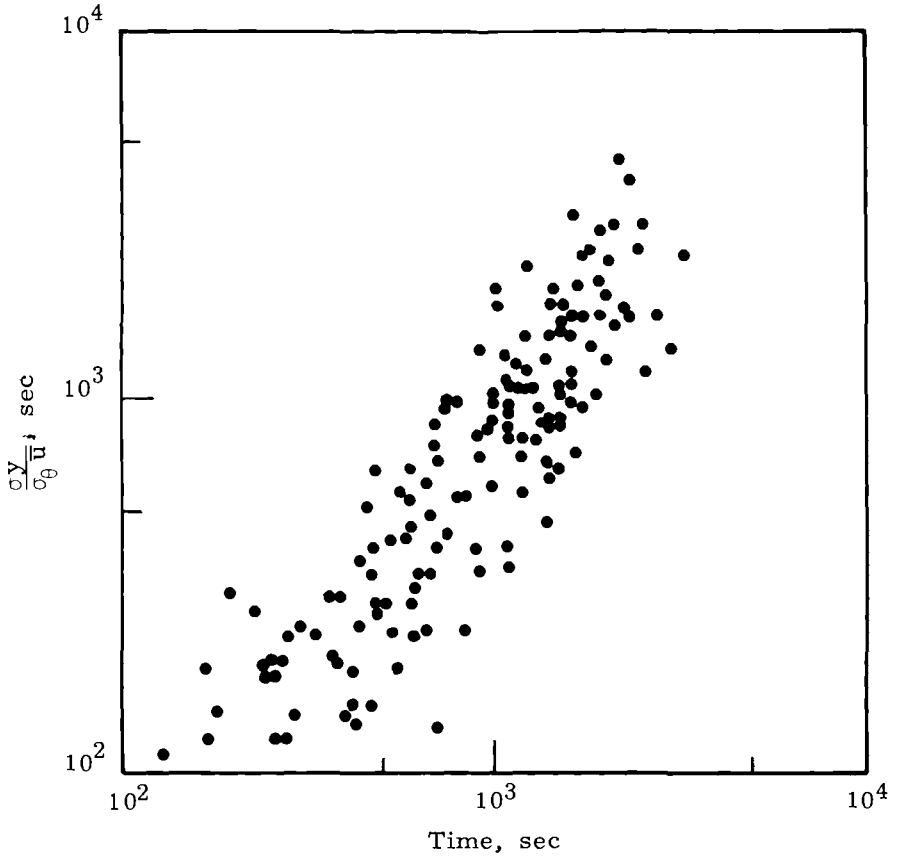

FIGURE 6. $\sigma_y/\sigma_\theta \bar{u}$ Travel Time for Tests from Source A, Using All Data Points from Figure 5 That Had σ_θ Available

The parameters chosen as physically necessary were some measure of downwind travel, crosswind diffusion, and atmospheric stability. Following the Hay-Pasquill method for estimating σ_y, the parameters selected were travel time, σ_θ smoothed over intervals t/β in length, wind speed, and temperature difference between 6 and 54 feet. The multi-variate regression analysis of this set of parameters yielded

$$E_p/Q_T = X\ 0.634\ t^{-1.88}(\sigma_\theta)_{t/\beta}^{-0.067} \bar{u}^{-2.20} (\Delta T+5)^{-1.21} \quad (1)$$

Of the observed exposures 93% were within a factor of four of values predicted from Equation (1). Of most importance in this exercise was the surprising and extremely small exponent on $(\sigma_\theta)_{t/\beta}$. The observed exposures were very nearly independent of crosswind fluctuations handled in the same manner that led to good predictions of σ_y. Furthermore, the very minor improvement in predictive ability, even with a selection of physically pertinent parameters, led to the abandonment of the concept of time and increasingly

smoothed σ_θ in attempts to improve the simple distance relation.

The alternate approach, that of divorcing the analysis from calculated travel time and avoiding completely the search for an explicit relation between σ_y and σ_θ, led to the equation

$$E_p/Q_T = 0.248\ X^{-1.82}\ \sigma_\theta^{-0.417}\ \bar{u}^{-1.03}(\Delta T + 5)^{1.55} \qquad (2)$$

The relation between exposure and the various parameters in Equation (2) is physically reasonable, and a significant dependence on each parameter exists. For Equation (2), 97% of the calculated values were within a factor of four of the observed values, a small but meaningful increase in accuracy over the simple distance relationship.

COMPARISON OF THE EQUATION WITH INDEPENDENT DATA

A measure of the merit of any equation may be made by applying it to independent data to which the equation should be applicable. Releases from the secondary source point, Source B, provided data suitable for such a check. The results of using Equation (2) against Source B data are shown in Figure 7. There was a clear tendency for the equation to overestimate, particularly at higher exposure values, that is, short distances. However, the singular position of Source B with respect to the sampling routes induced many problems near Source B. The sampling routes were essentially radial near Source B and the spacing was relatively coarse, so that the highest exposure during a given test may well have missed a sampler. Also, the air flow near the mouth of Honda Canyon was influenced by the canyon walls. Observations of wind flow over steep ravines in the area indicate that marked upward flow was often generated on the downwind side of the ravine with the result that tracer released on the upwind side of the ravine sometimes could not contact the downwind side.[5] Releases from Source B on a large scale were expected, in a similar manner, to produce seemingly incongruous diffusion results. Considering the complexity of the low level wind flow conditions, the check with independent data was satisfactory and in accord with expectations.

DISCUSSION OF GENERAL ASPECTS OF DIFFUSION OVER SOUTH VANDENBERG

During the analysis of the data, some insight into the character of diffusion over this mountainous region was inevitable. The most striking characteristic of these tests was the appearance of disjointed plumes due to the intervention of deep and steep canyons between the ridges. After discussion of this phenomenon, the data from the Mountain Iron test series will be compared to those from the Dry Gulch series over North Vandenberg to point out general aspects of rough terrain influence on a diffusing plume.

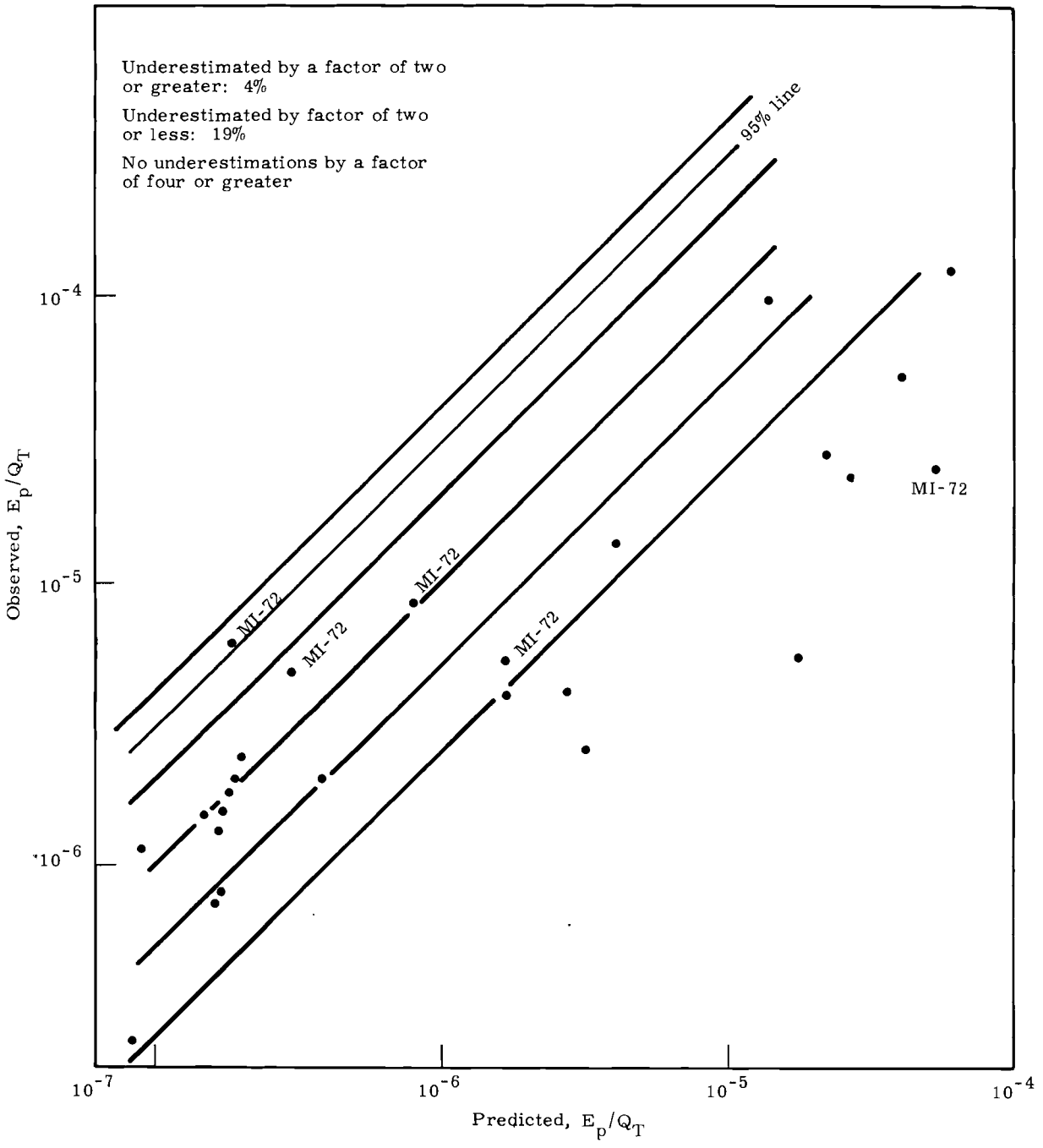

FIGURE 7. Observed and Predicted Values of Centerline Exposure, Using Data from Source B as Independent Data

DIFFUSION OVER AND IN CANYONS

A description of plume geometries observed during the test series includes three types which may be called the Modified Cigar, the Canyon Low, and the Multiple Maximum, or MC, CL, and MM, respectively. The MC is an ordinary monotonically-declining exposure pattern that may be bent or curved. The CL is a plume with anomalously low exposures interspersed between ordinary exposure levels. The low exposures are coincident with the canyon floor. The MM is an elaborate Canyon Low caused by flow over more than one ridge-canyon system. Some idea of the relative frequency of the different types is given, for tests from Source A, in the following tabulation.

Type	Frequency
MC	27% (21 tests)
CL	67% (52 tests)
MM	6% (5 tests)

The CL, plainly the predominant type, was observed at any time of day and during any season. The clearcut character of the canyon low is shown in Figure 8 as a night test, but the day tests provided equally clear examples. Examples of the other types are shown in Figure 9, the Modified Cigar, and in Figure 10, the Multiple Maximum.

The plumes during the night tests were almost exclusively CL or MM, while the day tests could be any type. Similar conditions could lead to either MC or CL during day tests depending partly upon the slope of the canyon walls at the point where the plume crossed the canyon. Steep walls enhanced the tendency toward CL types, although even shallow portions of canyons could exhibit CL types on occasion.

The average value of the ratio (canyon exposure/downwind ridge exposure), about 0.5 during the day tests and about 0.4 during the night tests, ranged from 0.1 to 0.8 due to the scatter in the ratios observed. The difference was not significant and day and night tests are considered most likely to produce the same reduction--about 50%--for CL geometries.

The effect of canyons on plume geometry, although definite, was one sided in that exposures along the floor were never higher than the upwind ridge. The tracer did not collect in the relatively stagnant air of the canyon floor to produce high exposures. Tests made during the transition between sea and land-breeze conditions that may have been expected to produce "pooling" in canyon floors in fact were never observed to do any such thing. Unfortunately, the difficult problems involved in timing the tracer release to coincide with transient conditions prevented running a significant number of tests in such conditions. Hence, the conclusion that high exposures were not observed along canyon floors does not carry the same certainty as the conclusion that Canyon Low plume types are the most common plume configuration.

The interaction of terrain and meteorological phenomena to produce

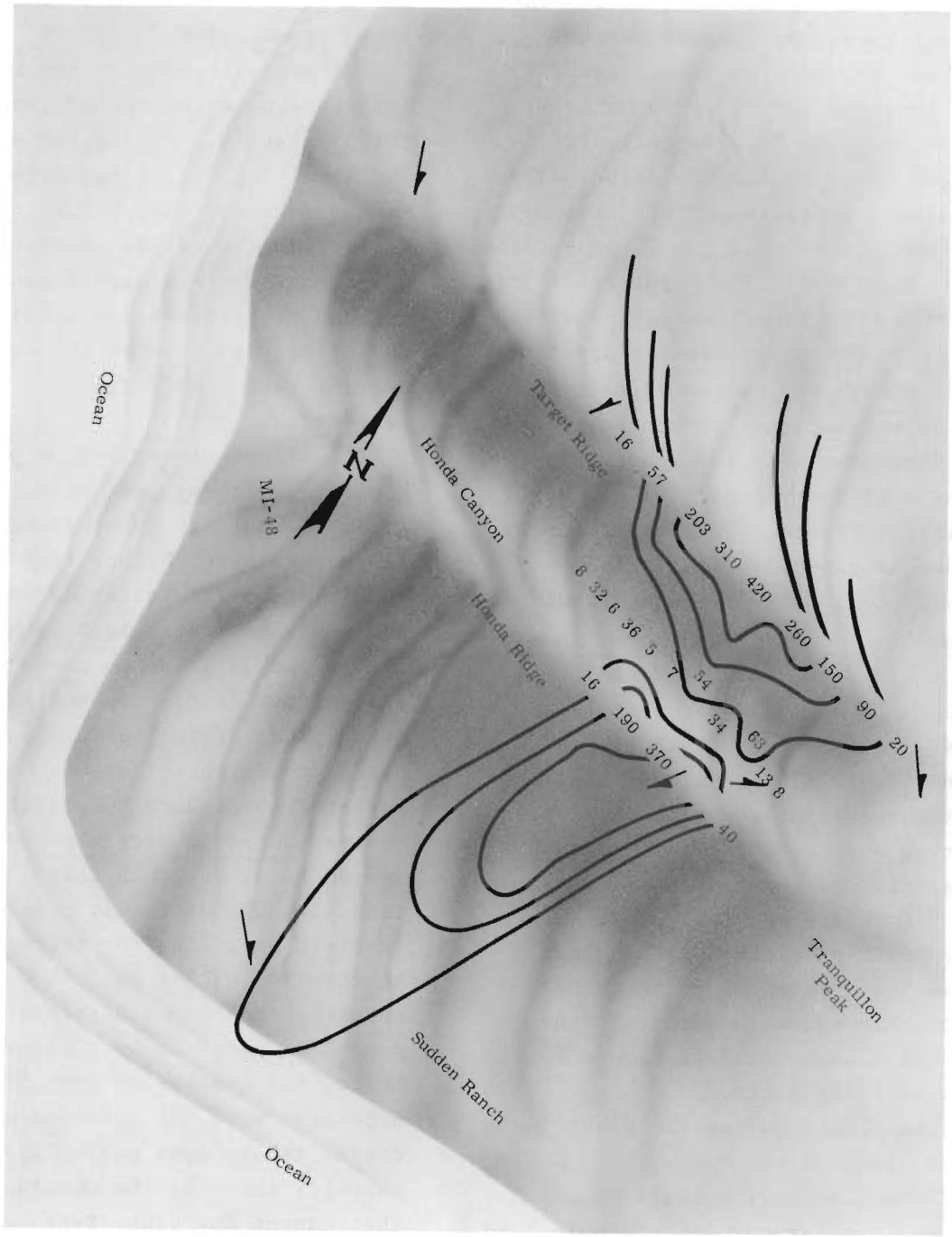

FIGURE 8. Canyon-Low Plume Geometry for a Night Test from Source A

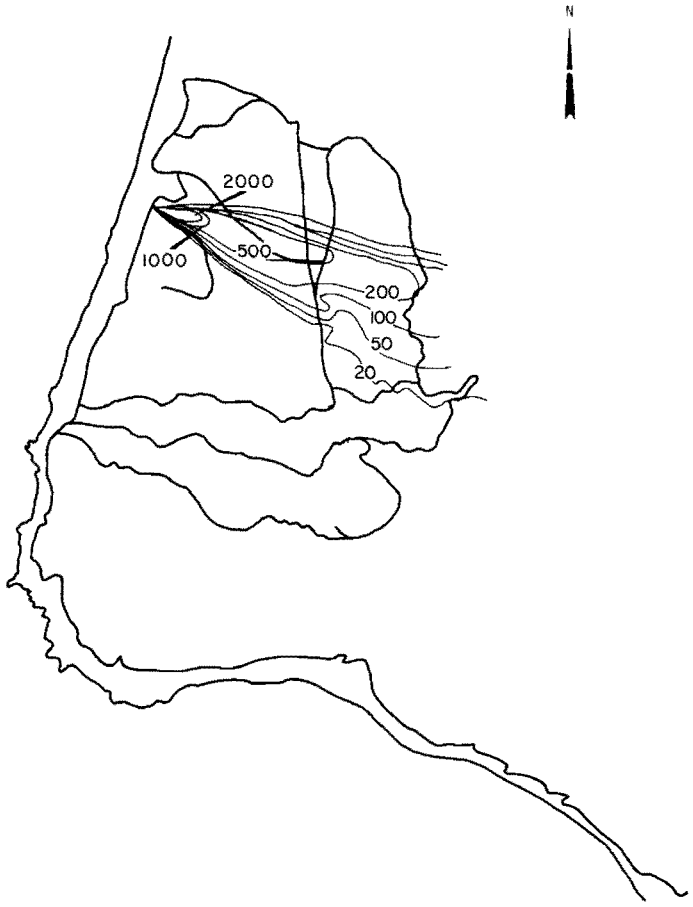

FIGURE 9. Modified Cigar Plume from a Source A Test

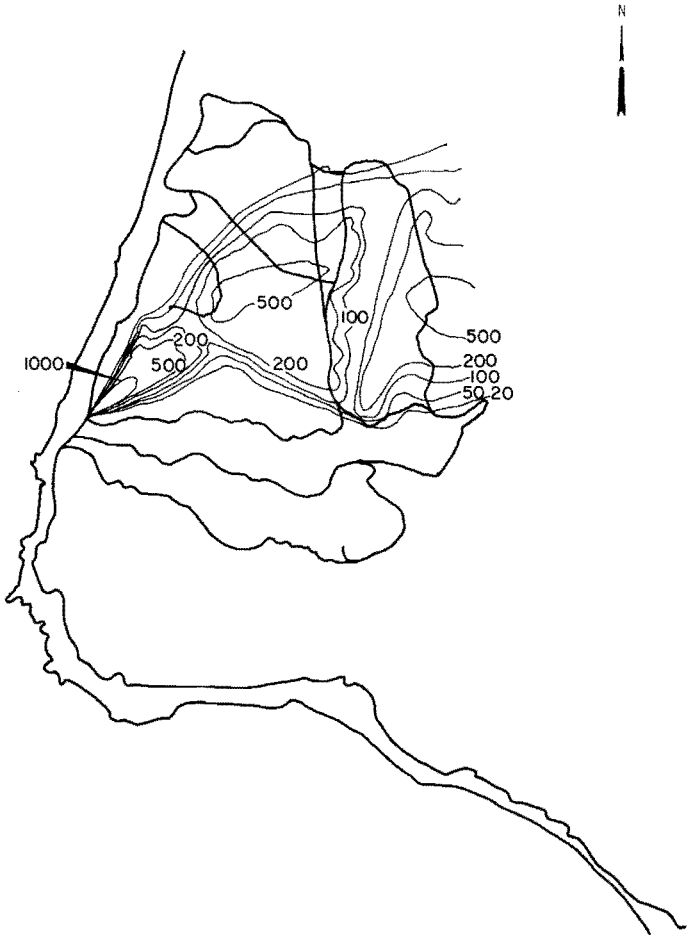

FIGURE 10. Multiple Maximum Plume from a Source B Test

Canyon Low plume geometries was not a simple relationship to unravel, and currently the prediction of CL plumes must be acknowledged to be an unsolved problem. There seems little doubt that wind speed and direction and temperature stratification were primary agents in determining whether significant amounts of the tracer penetrated into the canyon depths, but a superficial analysis was not expected to be successful, and a detailed analysis remains to be completed.

COMPARISON OF RESULTS FROM MOUNTAINOUS AND FLAT TERRAIN

A straightforward comparison of the Mountain Iron data with similar data from the Dry Gulch test series led to some interesting conclusions concerning the effects of rough terrain on diffusion from ground level sources. The Dry Gulch data were taken over the relatively flat terrain of North Vandenberg, only a few miles north of the Mountain Iron test area. To include the effects of climatic contrast in this comparison, some data from the Green Glow test series at Hanford will be included. The Hanford area is a semi-arid steppe region, considerably more continental in climatic character than the marine climate of the Vandenberg regions. A detailed comparison of data from Prairie Grass, Dry Gulch, Ocean Breeze, and Green Glow test series (as well as other continuous ground level release test series) is given by Fuquay and Simpson.[10]

The data averages for Dry Gulch, Mountain Iron, and Green Glow tests in night conditions are shown in Figure 11. The general term "night tests" is used here, rather than "stable", because the marine climate of the Vandenberg region is not usually subject to strong inversions at the surface. In fact, many nights in the area tend toward isothermal or very slightly inverted temperature stratifications that in more continental climates could be lumped into a "near-neutral" category. The Dry Gulch data indicate a higher level of exposure during winter nights than during summer nights, whereas the Mountain Iron data indicate just the opposite. The Hanford data were restricted to summer-like conditions and show the highest general level of exposure of the three areas.

The consequences of climate-terrain interactions can be seen from Figure 11. During the winter in the Vandenberg region, onshore wind flow at night is generally due to synoptic scale pressure gradients. Clear winter nights with pressure gradient winds allow the maximum effect of radiation surface cooling to be coupled with light onshore flow, leading to the rather rare and relatively high exposures on North Vandenberg. The South Vandenberg region, on the other hand, has sufficient topographical relief to induce drainage flow during radiation-cooling conditions that counter onshore pressure gradients. Thus, onshore night winds on South Vandenberg, associated usually with

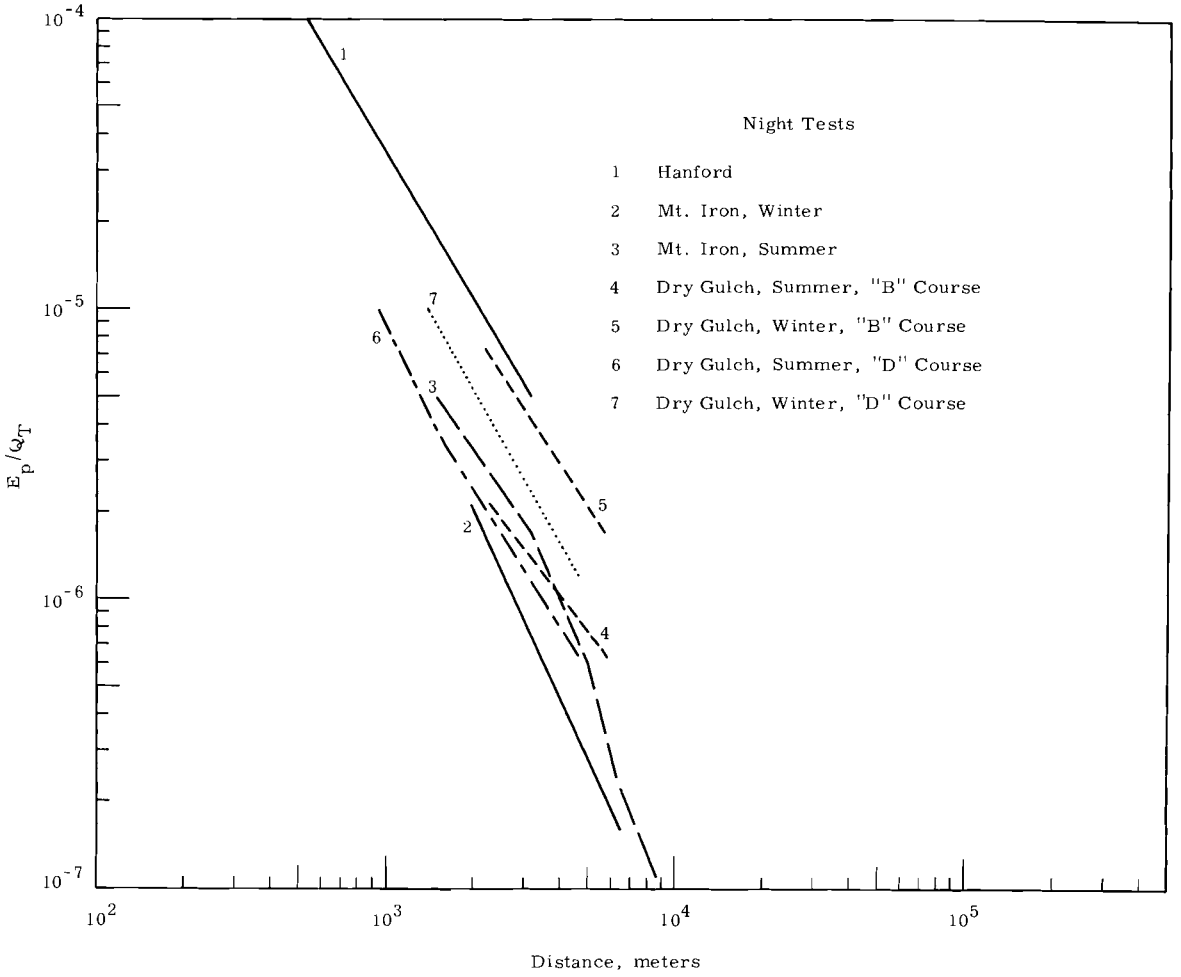

FIGURE 11. Exposure Data Averages from Mountain Iron, Dry Gulch and Green Glow Diffusion Test Series, Night Conditions

strong pressure gradients and neutral atmospheric conditions, result in relatively low exposures.

Summer night conditions in the Vandenberg region are markedly different in character from those of the winter nights. The prevailing onshore winds during the day often carry over into the evening and night to bring in extensive fog banks and stratus that remain until large scale drainage reverses the wind flow. Thus, onshore winds associated with neutral stability on North Vandenberg produce general exposure levels lower than those during winter nights. On South Vandenberg, pronounced elevational gradients facilitate marked drainage flows tending to counter the onshore night winds. The conditions required for onshore flow on South Vandenberg during the summer nights are thus similar to those for winter nights--onshore wind speeds high enough to counter drainage flow--with consequent exposure levels

similar to winter nights. The Hanford data, taken during summer nights in a dry cloud-free climate, reflect the strong low level stability (induced by radiative cooling of the surface) in high exposure levels.

The daytime tests indicated a very different situation, as shown in Figure 12. There was very little difference between seasons at a site, or between sites in general. A slight and probably insignificant tendency for lower data at Mountain Iron than at the other sites can be seen. A slightly to moderately unstable atmospheric condition (characteristic of conditions during day tests at all sites) led to very similar exposure levels. This condition can probably be attributed

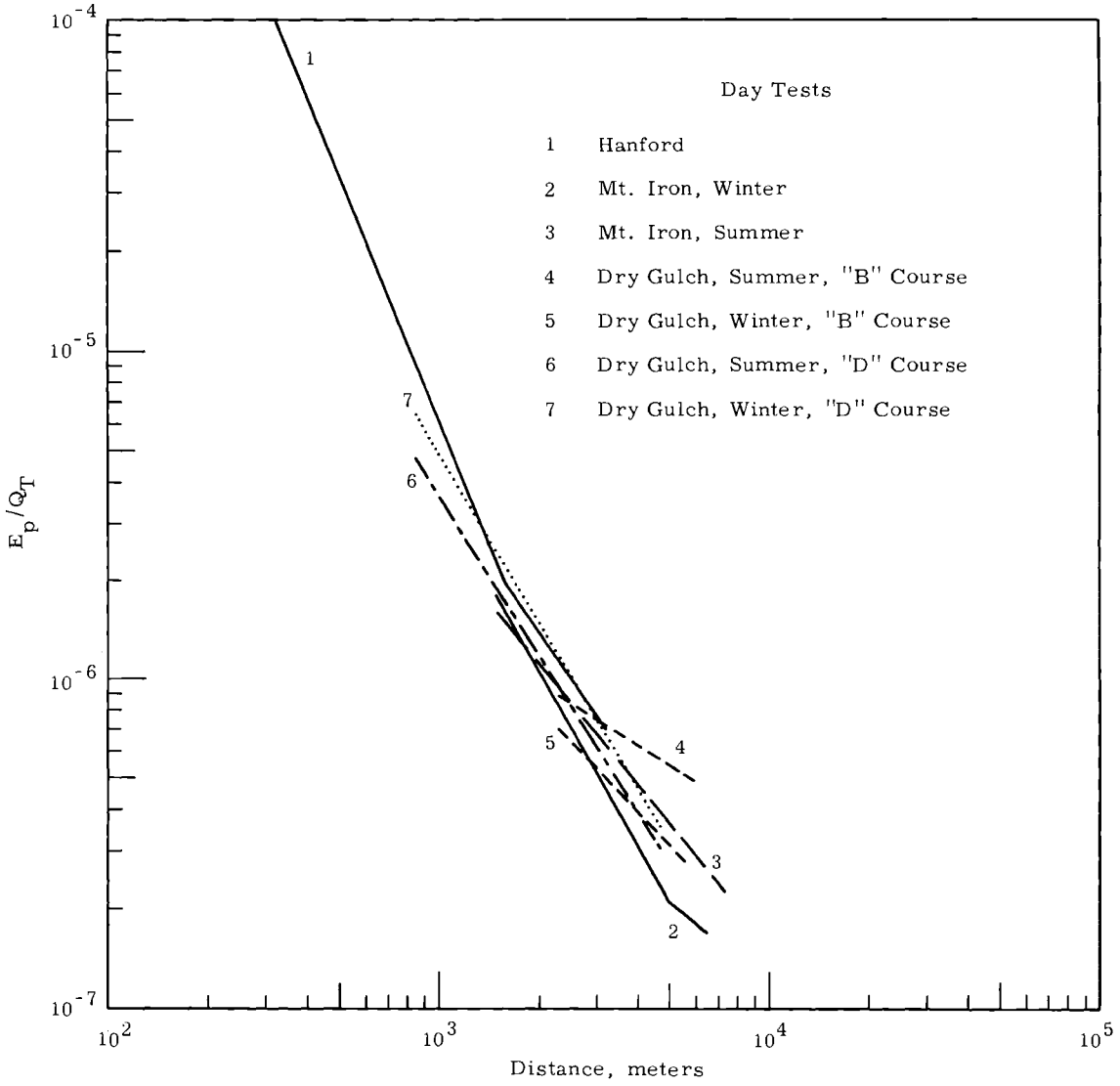

FIGURE 12. Exposure Data Averages from Mountain Iron, Dry Gulch and Green Glow Diffusion Test Series, Day Conditions

to atmospheric mixing sufficient to outweigh local terrain differences, and to the universal similarity of turbulence in moderately unstable conditions. Although there were differences in the depth of the mixing layer (from surface to the base of the inversion) between Vandenberg and Hanford, the atmospheric diffusion was essentially independent of local climatology. The importance of terrain during day conditions, pronounced in highly localized conditions such as exist on canyon floors, is not generally noted elsewhere.

This comparison serves to emphasize the fact that stable atmospheres are not so subject to generalization as unstable conditions. Local aspects of terrain and climatology can be expected to yield significant differences between regions in night time diffusion. In contrast, the local climate is considerably less important in determining diffusive conditions during day time conditions.

CONCLUSIONS

Many aspects of diffusion over and within mountainous regions remain to be considered. However, as a result of the Mountain Iron test series, the following conclusions seem appropriate:

- Techniques developed for estimating plume width over flat terrain can be suitably modified, at least for ground level sources, for use in the complex conditions prevailing in mountainous terrain.
- The advantages of using time as the downwind variable for predicting diffusion are minimized in rough terrain.
- Diffusion over a system of ridges and canyons usually results in lower exposures on the canyon floor than would occur at the same distance over flat terrain, with the average reduction being about 50%.
- Diffusion from a ground source over coastal mountains in the same climate, excluding sources within a ridge-canyon system for which no data are taken,[5] generally lead to somewhat lower exposures than are found over flat terrain.
- Unstable atmospheric conditions decrease the importance of local climate and terrain, while stable atmospheric conditions tend to emphasize differences in climate and terrain.

DATA SUMMARIES

The following appendices present a summarization of the data gathered during the tests. Appendix A includes the basic diffusion data:

- Centerline exposure (normalized to source strength)
- Distance to the exposure
- Estimated travel time to that distance
- Estimated σ_y wherever possible
- Source point crosswind fluctuation standard deviation, σ_θ
- Source point mean wind speed, $\bar{u}$
- Temperature difference from 6 to 54 and 6 to 300 feet

Appendix B presents a detailed description of the relative success of each of the 113 tests. Each of the possible types of data is explicitly listed as available (x) or not available (NA). Also listed is an indication of test conditions: length of release time, and source point. The macroscale conditions of the tests are indicated in Appendix C: source point wind speed and direction, and relative humidity; and an approximation to the geostrophic wind at the beginning and end of the test periods. This approximation, being the observed winds at 1600 meters MSL, serves to indicate whether the geostrophic conditions were stationary during the tests.

REFERENCES

1. *"Project Prairie Grass," Geophysical Research Paper No. 59, vol. I and II, edited by M. L. Barad. Geophysics Research Directorate, Air Force Cambridge Research Laboratories, Bedford, Massachusetts, 1958.*

2. *M. L. Barad and J. J. Fuquay. The Green Glow Diffusion Program, Vol I., AFCRL-62-251(I). Geophysics Research Directorate, Air Force Cambridge Research Laboratories, Bedford, Massachusetts, 1962.*

3. *The Ocean Breeze and Dry Gulch Diffusion Programs, Vol I, edited by D. A. Haugen and J. J. Fuquay, AFCRL-63-791(I). Air Force Cambridge Research Laboratories, Bedford, Massachusetts, 1963.*

4. *G. A. Demarrais, G. C. Holzworth, and C. R. Hosler. Meteorological Summaries Pertinent to Atmospheric Transport and Dispersion Over Southern California, Tech. Paper 54, Weather Bureau (ESSA), Dept. of Commerce, Washington, D.C., 1965.*

5. *T. B. Smith, E. K. Kauper, S. Berman, and F. Vukovich. Micrometeorological Investigation of Naval Missile Facility, Point Arguello, California, Vol. I. Meteorology Research, Inc., 2420 North Lake Avenue, Altadena, California, 1964.*

6. *F. Pasquill. Atmospheric Diffusion, D. Van Nostrand, London, 1962*

7. *F. B. Smith. "The Eulerian Lagrangian Time Scale Relationship in One-Dimensional Turbulence," U. S. Atomic Energy Commission Micrometeorological Information Symposium, Chalk River, Ontario. Published at Chalk River, 1968.*

8. *F. Gifford. "Variation of the Lagrangian-Eulerian Time Scale Ratio With Stability," U. S. Atomic Energy Commission Micrometeorological Information Symposium, Chalk River, Ontario. Published at Chalk River, 1968.*

9. *The Ocean Breeze and Dry Gulch Diffusion Programs, Vol. II, edited by D. A. Haugen and J. H. Taylor, AFCRL-63-791(II). Air Force Cambridge Research Laboratories, Bedford, Massachusetts, 1963.*

10. *J. J. Fuquay and C. L. Simpson. "Atmospheric Diffusion Experiments and Prediction Models," Nucl. Safety, vol. 5, no. 4, pp. 403-407. 1964.*

APPENDIX A

BASIC DATA FROM MOUNTAIN IRON PHASE I

TEST	E_p/Q_T Sec/m^3	X Meters	t Seconds	σ_y Meters	σ_θ Degrees	$\bar{u}$ Meters/sec	ΔT_6^{54} °C	ΔT_6^{300} °C
3	1.75^{-6}	1420	540	142	9.5	2.7	--	--
	9.40^{-7}	2540	940	251	9.5	2.7	--	--
	3.30^{-7}	5130	1250	368	9.5	2.7	--	--
	1.10^{-7}	7820	1600	535	9.5	2.7	--	--
4	3.60^{-7}	2540	590	251	6.0	4.3	--	--
	1.35^{-7}	5640	1200	--	6.0	4.3	--	--
	6.40^{-8}	7210	1500	--	6.0	4.3	--	--
5	1.20^{-6}	1420	270	135	5.5	5.3	--	--
	5.60^{-7}	2480	470	285	5.5	5.3	--	--
	9.70^{-8}	5500	930	--	5.5	5.3	--	--
	4.20^{-8}	6480	1120	--	5.5	5.3	--	--
	4.40^{-8}	8070	1170	--	5.5	5.3	--	--
6	2.80^{-6}	1290	180	109	6.5	7.1	--	--
	1.40^{-6}	1940	270	142	6.5	7.1	--	--
	2.05^{-7}	4080	550	335	6.5	7.1	--	--
7	5.70^{-7}	2300	1350	470	31.3	1.7	--	--
	1.60^{-7}	5300	2590	--	31.3	1.7	--	--
	6.00^{-8}	8700	3810	--	31.3	1.7	--	--
9	1.48^{-6}	2300	790	251	11.0	2.9	--	--
	9.14^{-7}	5560	1940	--	11.0	2.9	--	--
	9.01^{-7}	6130	2150	--	11.0	2.9	--	--
	5.66^{-7}	6800	2410	--	11.0	2.9		
	4.05^{-7}	7400	2640	--	11.0	2.9	--	--
11	7.55^{-7}	2400	--	--	--	--	--	--
	2.32^{-7}	5500	--	--	--	--	--	--
	1.63^{-7}	7820	--	--	--	--	--	--
12	6.20^{-7}	1290	540	201	18.5	2.4	--	--
	4.00^{-7}	2300	960	332	18.5	2.4	--	--
	2.24^{-7}	4600	1660	--	18.5	2.4	--	--
	1.40^{-7}	8700	2680	--	18.5	2.4	--	--
13	1.32^{-6}	1420	680	167	13.6	2.1	--	--
	6.57^{-7}	2300	1090	135	13.6	2.1	--	--
	1.74^{-7}	5640	1810	--	13.6	2.1	--	--
14	2.13^{-6}	1240	210	167	15.1	5.8	--	--
	4.00^{-7}	2630	450	--	15.1	5.8	--	--
	8.60^{-8}	4280	670	--	15.1	5.8	--	--
	4.70^{-8}	5580	840	--	15.1	5.8	--	--
15	1.15^{-5}	1240	200	142	10.2	--	--	--
	1.46^{-6}	2770	430	--	10.2	--	--	--
	4.59^{-7}	4120	580	--	10.2	--	--	--
	1.24^{-7}	4970	720	--	10.2	--	--	--

Note: The notation used for all exposure data in Appendix A is such that $2.00^{-6} = 2.00 \times 10^{-6}$

BASIC DATA FROM MOUNTAIN IRON PHASE I

TEST	E_p/Q_T Sec/m^3	X Meters	t Seconds	σ_y Meters	σ_θ Degrees	$\bar{u}$ Meters/sec	ΔT_6^{54} °C	ΔT_6^{300} °C
16	6.30^{-6}	1240	200	92	8.6	2.1	--	--
	9.08^{-7}	2670	430	109	8.6	2.1	--	--
	2.74^{-7}	4220	660	367	8.6	2.1	--	--
	4.90^{-8}	4950	810	--	8.6	2.1	--	--
	1.10^{-7}	5810	900	--	8.6	2.1	--	--
17	6.30^{-7}	1240	380	142	--	--	--	--
	5.30^{-8}	2630	790	267	--	--	--	--
	3.10^{-8}	4280	1200	318	--	--	--	--
	3.30^{-8}	5260	1450	--	--	--	--	--
18	2.39^{-6}	1340	520	142	15.8	2.6	-0.9	-0.8
	1.60^{-6}	2300	880	226	15.8	2.6	-0.9	-0.8
	3.21^{-7}	4600	1580	546	15.8	2.6	-0.9	-0.8
	2.01^{-7}	6150	2690	670	15.8	2.6	-0.9	-0.8
	2.19^{-7}	7420	3240	879	15.8	2.6	-0.9	-0.8
19	8.71^{-7}	1340	--	--	--	--	-1.3	-1.7
	2.62^{-7}	2540	--	--	--	--	-1.3	-1.7
	1.66^{-7}	4700	--	--	--	--	-1.3	-1.7
	1.58^{-7}	7130	--	--	--	--	-1.3	-1.7
21	1.52^{-6}	1390	510	167	12.9	2.7	-1.1	-1.4
	1.85^{-7}	5110	1660	836	12.9	2.7	-1.1	-1.4
	1.93^{-7}	6420	1960	930	12.9	2.7	-1.1	-1.4
	5.50^{-8}	7700	2570	--	12.9	2.7	-1.1	-1.4
23	1.18^{-6}	1660	540	134	6.5	3.1	-0.5	-0.9
	3.43^{-7}	5110	1410	268	6.5	3.1	-0.5	-0.9
	2.37^{-7}	6420	1630	286	6.5	3.1	-0.5	-0.9
	9.20^{-8}	7760	1860	--	6.5	3.1	-0.5	-0.9
25	2.28^{-6}	1270	290	92	9.2	4.4	-1.2	-1.6
	6.79^{-7}	2770	600	168	9.2	4.4	-1.2	-1.6
	3.55^{-7}	4080	760	300	9.2	4.4	-1.2	-1.6
	5.30^{-8}	7130	1130	570	9.2	4.4	-1.2	-1.6
26	3.39^{-6}	1420	250	100	5.5	5.7	-1.5	-0.8
	6.21^{-7}	2540	440	201	5.5	5.7	-1.5	-0.8
	5.40^{-8}	5010	700	335	5.5	5.7	-1.5	-0.8
27	9.24^{-7}	1420	280	117	5.8	5.0	-0.9	-1.4
	2.49^{-7}	2430	490	--	5.8	5.0	-0.9	-1.4
	7.80^{-8}	5300	900	--	5.8	5.0	-0.9	-1.4
	3.50^{-8}	7420	1130	450	5.8	5.0	-0.9	-1.4
28	5.75^{-6}	1080	400	100	16.9	2.7	-0.6	+0.8
	7.04^{-7}	4030	1420	351	16.9	2.7	-0.6	+0.8
	4.10^{-8}	6050	1900	838	16.9	2.7	-0.6	+0.8
29	6.16^{-7}	1870	--	--	--	--	-0.9	-1.2
	1.04^{-7}	4970	--	--	--	--	-0.9	-1.2
	6.10^{-8}	6660	--	--	--	--	-0.9	-1.2
30	7.46^{-6}	1340	480	92	5.6	2.8	0.0	+0.2
	5.18^{-6}	2300	820	126	5.6	2.8	0.0	+0.2
	7.97^{-7}	4600	1370	277	5.6	2.8	0.0	+0.2
	1.68^{-7}	7130	1940	--	5.6	2.8	0.0	+0.2

BASIC DATA FROM MOUNTAIN IRON PHASE I

TEST	E_p/Q_T Sec/m^3	X Meters	t Seconds	σ_y Meters	σ_θ Degrees	$\bar{u}$ Meters/sec	ΔT_6^{54} °C	ΔT_6^{300} °C
31	1.24^{-6}	2300	350	192	4.7	6.6	-0.1	+0.2
	2.52^{-7}	5600	810	--	4.7	6.6	-0.1	+0.2
	1.09^{-7}	6480	1110	418	4.7	6.6	-0.1	+0.2
	7.70^{-8}	8700	1150	--	4.7	6.6	-0.1	+0.2
32	4.41^{-6}	1420	260	76	4.5	5.4	-0.1	+0.3
	9.70^{-7}	2480	460	218	4.5	5.4	-0.1	+0.3
	1.65^{-7}	5600	920	293	4.5	5.4	-0.1	+0.3
	9.80^{-8}	7210	1460	--	4.5	5.4	-0.1	+0.3
33	1.60^{-6}	1530	260	76	3.7	5.9	-0.4	-0.5
	2.36^{-7}	4970	960	--	3.7	5.9	-0.4	-0.5
	2.33^{-7}	5850	1180	226	3.7	5.9	-0.4	-0.5
	3.60^{-8}	8110	1790	--	3.7	5.9	-0.4	-0.5
34	3.14^{-6}	1390	240	75	3.8	5.9	-0.2	-0.2
	2.29^{-7}	4750	770	335	3.8	5.9	-0.2	-0.2
	1.92^{-7}	6420	1000	351	3.8	5.9	-0.2	-0.2
35	3.52^{-6}	1080	200	67	3.5	5.5	-0.4	-0.4
	3.78^{-7}	4060	710	218	3.5	5.5	-0.4	-0.4
	1.37^{-7}	6700	1060	335	3.5	5.5	-0.4	0.4
36	2.87^{-6}	1390	170	84	3.2	8.1	--	--
	3.99^{-7}	4060	490	--	3.2	8.1	--	--
	1.37^{-7}	7500	880	--	3.2	8.1	--	--
38	2.01^{-6}	1660	620	118	10.9	2.7	-1.6	-1.4
	4.89^{-7}	5110	1540	335	10.9	2.7	-1.6	-1.4
	1.94^{-7}	6800	1940	--	10.9	2.7	-1.6	-1.4
39	2.00^{-6}	720	--	--	--	--	-1.4	-1.5
	7.76^{-7}	1080	--	--	--	--	-1.4	-1.5
	3.47^{-7}	4620	--	--	--	--	-1.4	-1.5
	2.21^{-7}	7500	--	--	--	--	-1.4	-1.5
40	4.47^{-6}	1270	260	84	7.0	4.9	-1.7	-0.9
	6.83^{-7}	4080	700	349	7.0	4.9	-1.7	-0.9
	3.07^{-7}	5060	900	488	7.0	4.9	-1.7	-0.9
	8.30^{-8}	7110	1060	--	7.0	4.9	-1.7	-0.9
41	1.17^{-6}	2000	430	84	4.3	4.7	-1.6	-2.0
	2.24^{-7}	5620	1050	502	4.3	4.7	-1.6	-2.0
	2.33^{-7}	6640	1250	316	4.3	4.7	-1.6	-2.0
42	2.98^{-6}	1240	240	60	31.2	5.2	-0.9	-1.3
	1.52^{-7}	2770	510	--	31.2	5.2	-0.9	-1.3
	1.08^{-7}	4320	690	200	31.2	5.2	-0.9	-1.3
	3.40^{-8}	5810	950	435	31.2	5.2	-0.9	-1.3
	2.30^{-8}	9820	1540	--	31.2	5.2	-0.9	-1.3
43	4.26^{-6}	1290	270	84	6.9	4.7	-0.3	-1.4
	2.51^{-6}	2050	440	151	6.9	4.7	-0.3	-1.4
	9.49^{-7}	2730	560	--	6.9	4.7	-0.3	-1.4
	3.47^{-7}	4080	730	465	6.9	4.7	-0.3	-1.4
	1.82^{-7}	5060	930	--	6.9	4.7	-0.3	-1.4
	6.00^{-8}	5810	960	--	6.9	4.7	-0.3	-1.4
	3.00^{-8}	9600	1470	--	6.9	4.7	-0.3	-1.4

BASIC DATA FROM MOUNTAIN IRON PHASE I

TEST	E_p/Q_T Sec/m^3	X Meters	t Seconds	σ_y Meters	σ_θ Degrees	$\bar{u}$ Meters/sec	ΔT_6^{54} °C	ΔT_6^{300} °C
44	3.99^{-6}	1760	340	67	2.9	5.2	-0.7	-1.6
	1.68^{-7}	4750	820	207	2.9	5.2	-0.7	-1.6
	3.50^{-8}	8110	1360	218	2.9	5.2	-0.7	-1.6
45	5.06^{-6}	360	70	42	9.9	3.7	--	--
	1.53^{-7}	4060	1030	335	9.9	3.7	--	--
	1.37^{-7}	5740	1290	502	9.9	3.7	--	--
46	2.54^{-6}	1290	430	100	11.0	3.6	-0.2	+0.1
	1.84^{-6}	2730	880	159	11.0	3.6	-0.2	+0.1
	3.52^{-7}	4080	1120	302	11.0	3.6	-0.2	+0.1
	9.40^{-8}	4950	1350	419	11.0	3.6	-0.2	+0.1
	1.91^{-7}	5810	1490	419	11.0	3.6	-0.2	+0.1
	9.00^{-8}	9820	2830	--	11.0	3.6	-0.2	+0.1
47	2.25^{-6}	1470	--	--	--	--	--	--
	4.99^{-7}	2850	--	--	--	--	--	--
	3.32^{-7}	4060	--	--	--	--	--	--
	1.52^{-7}	4420	--	--	--	--	--	--
	1.09^{-7}	5220	--	--	--	--	--	--
	7.20^{-8}	8130	--	--	--	--	--	--
48	2.72^{-6}	1340	--	--	--	--	-0.2	+0.2
	1.31^{-6}	2560	--	--	--	--	-0.2	+0.2
	4.27^{-7}	4830	--	--	--	--	-0.2	+0.2
	3.73^{-7}	7110	--	--	--	--	-0.2	+0.2
	6.00^{-8}	9820	--	--	--	--	-0.2	+0.2
49	2.76^{-6}	390	--	--	--	--	-1.4	-1.8
	7.50^{-8}	5620	--	--	--	--	-1.4	-1.8
50	1.00^{-6}	1870	400	100	4.4	4.7	-1.3	-1.3
	2.00^{-7}	5460	1190	302	4.4	4.7	-1.3	-1.3
51	1.81^{-6}	670	--	107	--	--	0.0	+0.4
	2.62^{-7}	1320	--	--	--	--	0.0	+0.4
	1.04^{-7}	7090	--	581	--	--	0.0	+0.4
52	8.04^{-6}	390	--	--	--	--	-1.8	-2.2
	6.60^{-7}	1200	--	235	--	--	-1.8	-2.2
	1.52^{-7}	6090	--	553	--	--	-1.8	-2.2
53	2.20^{-6}	720	690	117	23.9	3.2	-0.6	-1.8
	3.17^{-7}	4080	1190	419	23.9	3.2	-0.6	-1.8
54	1.58^{-7}	7740	2120	158	10.7	3.7	-1.5	-0.5
55	9.59^{-6}	390	--	--	--	--	-5.3	-5.5
	4.02^{-7}	1200	--	--	--	--	-5.3	-5.5
	2.40^{-8}	6090	--	--	--	--	-5.3	-5.5
56	5.37^{-7}	570	200	--	18.7	--	-0.6	0.0
57	1.23^{-6}	670	--	--	--	--	-2.1	-2.7
	7.60^{-7}	1320	--	--	--	--	-2.1	-2.7
	8.40^{-8}	5620	--	--	--	--	-2.1	-2.7
	8.90^{-8}	7050	--	--	--	--	-2.1	-2.7

BASIC DATA FROM MOUNTAIN IRON PHASE I

TEST	E_p/Q_T Sec/m^3	X Meters	t Seconds	σ_y Meters	σ_θ Degrees	$\bar{u}$ Meters/sec	ΔT_6^{54} °C	ΔT_6^{300} °C
58	2.30^{-6}	390	--	--	--	--	-2.1	-2.5
	4.07^{-7}	1230	--	--	--	--	-2.1	-2.5
	1.83^{-7}	5790	--	--	--	--	-2.1	-2.5
59	4.57^{-7}	1870	480	201	12.4	3.9	-1.7	-2.5
	1.42^{-7}	4400	1110	--	12.4	3.9	-1.7	-2.5
	1.70^{-7}	5110	1280	--	12.4	3.9	-1.7	-2.5
	1.30^{-7}	6910	1710	--	12.4	3.9	-1.7	-2.5
60	1.36^{-6}	900	230	84	9.8	3.9	-0.6	-1.5
	1.97^{-7}	4060	1010	402	9.8	3.9	-0.6	-1.5
	1.62^{-7}	6050	1430	637	9.8	3.9	-0.6	-1.5
61	4.27^{-7}	1120	400	--	15.8	--	-0.2	-1.6
	1.03^{-7}	5340	3190	--	15.8	--	-0.2	-1.6
	4.80^{-8}	7660	3860	--	15.8	--	-0.2	-1.6
62	3.52^{-6}	390	100	67	15.8	3.9	-2.2	-2.5
	6.04^{-7}	1320	340	335	15.8	3.9	-2.2	-2.5
63	1.36^{-6}	1120	390	116	8.0	2.9	-2.5	-3.0
	7.80^{-8}	6300	2350	--	8.0	2.9	-2.5	-3.0
64	5.12^{-6}	280	90	--	--	--	-1.2	-1.8
	1.82^{-7}	5380	--	--	--	--	-1.2	-1.8
	1.15^{-7}	7480	--	--	--	--	-1.2	-1.8
65	4.75^{-7}	3910	--	--	27.3	--	--	--
66	2.87^{-6}	390	--	--	--	--	-2.0	-2.2
	9.77^{-7}	670	--	--	--	--	-2.0	-2.2
	1.07^{-7}	5180	--	--	--	--	-2.0	-2.2
67	2.62^{-7}	5320	2080	--	16.3	--	-1.2	-1.5
	2.00^{-7}	5580	1890	386	16.3	--	-1.2	-1.5
	2.44^{-7}	7660	2610	--	16.3	--	-1.2	-1.5
	2.04^{-7}	7480	2690	--	16.3	--	-1.2	-1.5
68	7.00^{-6}	390	100	67	12.0	4.0	-0.8	-1.3
	2.16^{-6}	670	170	134	12.0	4.0	-0.8	-1.3
	8.56^{-7}	1200	300	201	12.0	4.0	-0.8	-1.3
	1.45^{-7}	5790	1450	502	12.0	4.0	-0.8	-1.3
69	6.91^{-7}	1080	280	--	13.2	3.8	-0.9	-1.3
	5.21^{-7}	1390	370	167	13.2	3.8	-0.9	-1.3
	1.36^{-7}	6050	1590	670	13.2	3.8	-0.9	-1.3
70	6.26^{-7}	1870	550	167	16.4	3.4	-1.1	-0.7
	6.05^{-7}	4620	1430	670	16.4	3.4	-1.1	-0.7
	3.94^{-7}	6800	2210	--	16.4	3.4	-1.1	-0.7
71	5.07^{-6}	260	59	42	47.0	4.4	-0.8	-1.4
	1.30^{-7}	5540	1360	--	47.0	4.4	-0.8	-1.4
	1.14^{-7}	7900	1650	837	47.0	4.4	-0.8	-1.4

BASIC DATA FROM MOUNTAIN IRON PHASE I

TEST	E_p/Q_T Sec/m^3	X Meters	t Seconds	σ_y Meters	σ_θ Degrees	$\bar{u}$ Meters/sec	ΔT_6^{54} °C	ΔT_6^{300} °C
72	2.50^{-6}	370	130	100	14.0	2.8	--	--
	5.25^{-7}	2420	860	386	14.0	2.8	--	--
	8.40^{-7}	3600	1290	--	14.0	2.8	--	--
	4.75^{-7}	6130	2140	1120	14.0	2.8	--	--
	5.95^{-7}	7950	2740	1120	14.0	2.8	--	--
73	6.60^{-6}	260	60	33	9.2	4.7	-1.1	-2.7
	3.35^{-7}	1400	300	151	9.2	4.7	-1.1	-2.7
	2.55^{-7}	4090	850	351	9.2	4.7	-1.1	-2.7
	1.99^{-7}	5420	1080	502	9.2	4.7	-1.1	-2.7
74	1.17^{-6}	1660	503	167	14.6	3.3	-0.1	-0.6
	2.77^{-7}	4030	1260	553	14.6	3.3	-0.1	-0.6
	2.36^{-7}	6700	2290	1105	14.6	3.3	-0.1	-0.6
75	1.97^{-6}	720	360	118	--	--	-0.2	0.0
76	2.25^{-6}	720	270	--	--	--	-0.3	-0.2
	5.02^{-7}	4030	1470	--	--	--	-0.3	-0.2
	2.00^{-7}	6050	2120	--	--	--	-0.3	-0.2
77	3.65^{-6}	1420	260	116	9.4	5.5	-0.4	-0.2
	1.57^{-6}	2300	420	134	9.4	5.5	-0.4	-0.2
	2.90^{-7}	5300	1120	235	9.4	5.5	-0.4	-0.2
	1.30^{-7}	8070	1700	384	9.4	5.5	-0.4	-0.2
	3.30^{-8}	11400	1990	670	9.4	5.5	-0.4	-0.2
78	5.40^{-6}	1270	260	118	13.4	4.9	--	--
	3.20^{-6}	2050	420	140	13.4	4.9	--	--
	5.70^{-7}	4700	930	302	13.4	4.9	--	--
	8.80^{-8}	6400	1540	467	13.4	4.9	--	--
	1.06^{-7}	7420	1350	502	13.4	4.9	--	--
	9.60^{-8}	10200	1560	418	13.4	4.9	--	--
79	8.20^{-6}	1420	570	84	5.2	2.5	+0.2	-0.1
	3.00^{-6}	2540	1010	117	5.2	2.5	+0.2	-0.1
	7.54^{-7}	5130	1470	167	5.2	2.5	+0.2	-0.1
	1.27^{-7}	8010	1930	418	5.2	2.5	+0.2	-0.1
	2.20^{-8}	10500	2100	604	5.2	2.5	+0.2	-0.1
80	8.05^{-6}	1420	590	100	5.1	2.4	--	+0.6
	3.00^{-6}	2540	1050	151	5.1	2.4	--	+0.6
	5.95^{-7}	4830	1400	209	5.1	2.4	--	+0.6
	5.40^{-8}	6620	2090	460	5.1	2.4	--	+0.6
	1.10^{-7}	7420	1730	418	5.1	2.4	--	+0.6
	8.10^{-8}	10200	1920	335	5.1	2.4	--	+0.6
81	9.20^{-6}	1420	300	84	4.9	4.8	0.0	+0.4
	2.97^{-6}	2480	520	163	4.9	4.8	0.0	+0.4
	5.52^{-7}	5500	1060	302	4.9	4.8	0.0	+0.4
	9.60^{-8}	6710	2110	--	4.9	4.8	0.0	+0.4
	2.33^{-7}	8700	1650	511	4.9	4.8	0.0	+0.4
	4.30^{-8}	10800	1690	418	4.9	4.8	0.0	+0.4
82	1.20^{-5}	260	60	34	11.5	4.1	-2.1	+0.4
	1.56^{-7}	6130	1870	502	11.5	4.1	-2.1	+0.4
	1.03^{-7}	7900	2260	753	11.5	4.1	-2.1	+0.4

BASIC DATA FROM MOUNTAIN IRON PHASE I

TEST	E_p/Q_T Sec/m^3	X Meters	t Seconds	σ_y Meters	σ_θ Degrees	$\bar{u}$ Meters/sec	ΔT_6^{54} °C	ΔT_6^{300} °C
83	1.49^{-7}	5970	1840	--	24.0	--	-1.2	-2.0
84	1.60^{-6}	1870	640	167	24.6	2.9	--	--
	3.56^{-7}	5720	1540	435	24.6	2.9	--	--
	2.33^{-7}	7000	1890	486	24.6	2.9	--	--
85	2.01^{-6}	1390	500	184	24.6	2.8	--	--
86	7.59^{-6}	1390	460	84	12.7	3.0	--	--
	6.23^{-7}	4060	1540	334	12.7	3.0	--	--
	2.36^{-7}	5640	3970	--	12.7	3.0	--	--
	1.72^{-7}	6300	3030	418	12.7	3.0	--	--
	7.10^{-8}	7970	3950	--	12.7	3.0	--	--
87	3.97^{-6}	720	140	48	5.7	5.2	--	--
	1.08^{-6}	1260	--	100	5.7	5.2	--	--
	5.39^{-6}	3310	--	418	5.7	5.2	--	--
	3.27^{-7}	4400	--	--	5.7	5.2	--	--
88	6.17^{-6}	1420	360	126	6.3	3.9	+0.1	+0.1
	2.54^{-6}	2560	650	217	6.3	3.9	+0.1	+0.1
	1.21^{-6}	4600	1110	293	6.3	3.9	+0.1	+0.1
	1.43^{-7}	6150	1810	418	6.3	3.9	+0.1	+0.1
89	4.19^{-6}	2270	520	116	5.4	4.4	+0.1	+0.1
	9.78^{-7}	5620	1140	318	5.4	4.4	+0.1	+0.1
	2.66^{-7}	6860	2640	326	5.4	4.4	+0.1	+0.1
	1.96^{-7}	7700	2040	675	5.4	4.4	+0.1	+0.1
	1.41^{-7}	8800	2150	502	5.4	4.4	+0.1	+0.1
	4.70^{-8}	13200	2400	745	5.4	4.4	+0.1	+0.1
90	5.08^{-6}	1870	480	134	7.9	3.9	-0.3	-0.3
	4.90^{-7}	5620	1630	435	7.9	3.9	-0.3	-0.3
91	4.09^{-6}	1270	380	117	8.5	3.3	0.0	+0.4
	1.54^{-6}	2670	780	335	8.5	3.3	0.0	+0.4
	9.11^{-7}	4220	1010	581	8.5	3.3	0.0	+0.4
	2.42^{-7}	4950	1180	670	8.5	3.3	0.0	+0.4
	2.02^{-7}	7130	1400	558	8.5	3.3	0.0	+0.4
	5.70^{-8}	10000	1640	836	8.5	3.3	0.0	+0.4
92	8.58^{-6}	390	90	174	5.7	4.5	-0.1	+0.2
	1.98^{-6}	670	150	232	5.7	4.5	-0.1	+0.2
	6.11^{-7}	940	210	465	5.7	4.5	-0.1	+0.2
	3.27^{-7}	5260	820	--	5.7	4.5	-0.1	+0.2
93	7.07^{-6}	390	70	--	10.7	5.5	-0.5	0.0
	2.80^{-6}	670	120	226	10.7	5.5	-0.5	0.0
	1.18^{-6}	940	170	268	10.7	5.5	-0.5	0.0
	1.07^{-7}	5260	660	670	10.7	5.5	-0.5	0.0
94	4.98^{-6}	1290	330	100	6.5	3.9	--	--
	2.76^{-6}	2300	590	159	6.5	3.9	--	--
	9.15^{-7}	4600	1040	227	6.5	3.9	--	--
	1.31^{-7}	6400	1510	--	6.5	3.9	--	--
	2.03^{-7}	7130	1530	--	6.5	3.9	--	--
	6.90^{-8}	10200	1950	--	6.5	3.9	--	--

BASIC DATA FROM MOUNTAIN IRON PHASE I

TEST	E_p/Q_T Sec/m^3	X Meters	t Seconds	σ_y Meters	σ_θ Degrees	$\bar{u}$ Meters/sec	ΔT_6^{54} °C	ΔT_6^{300} °C
95	5.98^{-7}	5320	3920	627	18.1	2.2	-1.3	-1.0
	2.35^{-7}	7480	5120	--	18.1	2.2	-1.3	-1.0
96	6.99^{-6}	390	140	--	16.2	2.8	-1.6	-1.4
	2.55^{-6}	860	310	--	16.2	2.8	-1.6	-1.4
	5.35^{-7}	1200	430	--	16.2	2.8	-1.6	-1.4
	3.60^{-8}	5790	1380	418	16.2	2.8	-1.6	-1.4
	5.50	15100	2420	--	16.2	2.8	-1.6	-1.4
97	2.10^{-7}	7480	3320	--	11.0	--	-3.0	-4.2
98	5.96^{-6}	1270	400	93	7.8	3.2	-0.4	-0.1
	7.49^{-7}	4320	1220	402	7.8	3.2	-0.4	-0.1
	1.32^{-7}	5810	1460	465	7.8	3.2	-0.4	-0.1
	6.30^{-8}	9600	2080	--	7.8	3.2	-0.4	-0.1
99	8.67^{-6}	1270	470	76	6.0	2.7	-0.2	-0.1
	4.55^{-6}	2730	980	169	6.0	2.7	-0.2	-0.1
	2.13^{-6}	4088	1510	297	6.0	2.7	-0.2	-0.1
	3.76^{-7}	7110	1880	--	6.0	2.7	-0.2	-0.1
100	5.40^{-6}	1290	--	136	--	--	-0.4	-0.3
	3.08^{-6}	2050	--	187	--	--	-0.4	-0.3
	7.05^{-7}	4080	--	678	--	--	-0.4	-0.3
	1.54^{-7}	9840	--	--	--	--	-0.4	-0.3
101	2.76^{-6}	2300	1920	--	18.8	--	-0.4	0.0
102	5.61^{-6}	1290	640	109	11.4	2.0	-0.3	0.0
	3.25^{-6}	2170	1080	184	11.4	2.0	-0.3	0.0
	1.69^{-6}	4600	1580	293	11.4	2.0	-0.3	0.0
	2.48^{-7}	7130	1880	--	11.4	2.0	-0.3	0.0
	5.70^{-8}	10000	2320	419	11.4	2.0	-0.3	0.0
103	4.04^{-6}	1240	680	134	14.9	2.0	--	-0.1
	1.25^{-6}	2730	1290	302	14.9	2.0	--	-0.1
	9.15^{-7}	4080	1510	441	14.9	2.0	--	-0.1
	1.82^{-7}	5060	1800	710	14.9	2.0	--	-0.1
	2.80^{-7}	7110	2090	418	14.9	2.0	--	-0.1
	6.80^{-8}	9920	2510	754	14.9	2.0	--	-0.1
104	498^{-6}	2000	1000	142	8.4	2.0	-0.5	+0.1
	3.81^{-6}	2270	1140	177	8.4	2.0	-0.5	+0.1
	6.16^{-7}	5620	2270	419	8.4	2.0	-0.5	+0.1
	1.53^{-7}	6680	2980	--	8.4	2.0	-0.5	+0.1
	2.93^{-7}	8330	2630	--	8.4	2.0	-0.5	+0.1
106	2.89^{-6}	1270	510	136	14.3	2.5	-0.4	-0.2
	1.30^{-6}	2730	1070	--	14.3	2.5	-0.4	-0.2
	1.67^{-7}	5700	1860	560	14.3	2.5	-0.4	-0.2
	1.33^{-7}	9620	2540	--	14.3	2.5	-0.4	-0.2
107	1.56^{-6}	2000	620	102	9.4	3.2	-0.7	0.0
	5.02^{-7}	5480	1580	--	9.4	3.2	-0.7	0.0
109	5.00^{-7}	4030	1460	--	8.8	2.8	-1.9	-1.9
	3.24^{-7}	6260	2350	627	8.8	2.8	-1.9	-1.9

BASIC DATA FROM MOUNTAIN IRON PHASE I

TEST	E_p/Q_T Sec/m^3	X Meters	t Seconds	σ_y Meters	σ_θ Degrees	$\bar{u}$ Meters/sec	ΔT_6^{54} °C	ΔT_6^{300} °C
110	1.53^{-6}	2230	830	144	15.4	2.7	-0.6	-0.7
	7.37^{-7}	4060	1400	254	15.4	2.7	-0.6	-0.7
	3.75^{-7}	5740	1700	507	15.4	2.7	-0.6	-0.7
111	1.99^{-6}	900	280	101	11.5	3.2	-2.1	-2.8
	6.65^{-7}	4030	1180	--	11.5	3.2	-2.1	-2.8
	3.75^{-7}	6260	1550	--	11.5	3.2	-2.1	-2.8
112	2.16^{-6}	1200	380	102	10.3	3.2	-0.9	-0.9
	6.06^{-7}	4060	1210	336	10.3	3.2	-0.9	-0.9
113	8.73^{-7}	2400	560	152	4.6	4.3	-0.4	-0.8

APPENDIX B

SOURCE POINT, LENGTH OF RELEASE, AND AVAILABILITY OF DATA

Test	Source Point	Date	Time On	Length of Release	Source Wind	Point Temp.	Out-lying Winds	WIND	Upper Air Source Radiosonde Sites
3	A	1 Dec. 65	1145	30	x	NA	x	NA	1
4	A	10	1201	30	x	NA	x	NA	2
5	A	13	1200	30	x	NA	x	NA	2
6	A	14	1202	30	x	NA	x	NA	2
7	A	15	1210	30	x	NA	x	NA	2
8	A	16	-	-	x	NA	NA	NA	1
9	A	17	1435	30	x	NA	x	NA	1
10	A	20	1200	30	NA	NA	x	NA	1
11	A	3 Jan. 66	1218	34	NA	NA	NA	NA	2
12	A	4	1242	30	x	NA	x	3	3
13	A	5	1145	30	x	NA	x	NA	3
14	A	11	1104	30	x	NA	x	3	3
15	A	11	1345	30	NA	NA	x	3	3
16	A	14	1047	30	x	NA	x	3	3
17	A	17	1055	30	NA	NA	x	3	3
18	A	18	1045	30	x	x	x	NA	3
19	A	24	1040	30	NA	x	NA	4	3
20	A	25	1156	30	NA	NA	x	NA	3
21	A	27	1155	30	x	x	x	4	2
22	A	28	1147	15	NA	NA	NA	4	3
23	A	31	1145	15	x	x	x	4	3
24	A	3 Feb. 66	1130	15	NA	NA	NA	4	3
25	A	7	1045	15	x	x	x	4	3
26	A	7	1255	15	x	x	x	4	3
27	A	8	1159	15	x	x	x	NA	3
28	A	16	1200	15	x	x	x	3	3
29	A	17	1109	15	NA	x	x	3	4
30	A	23	1845	15	x	x	x	NA	4
31	A	24	1845	15	x	x	x	NA	4
32	A	24	2056	15	x	x	x	NA	4
33	A	25	1845	15	x	x	x	3	4
34	A	25	2110	15	x	x	x	3	4
35	A	26	0000	15	x	x	x	3	3
36	A	1 Mar. 66	1900	15	x	NA	x	3	4
37	A	3	0110	15	NA	NA	x	2	4
38	A	7	1146	5	x	x	x	NA	4
39	A	8	1145	15	NA	x	x	3	4
40	A	14	1102	5	x	x	x	3	4
41	A	15	1056	5	x	x	x	3	4
42	A	17	1102	5	x	x	x	3	4
43	A	17	1407	5	x	x	x	4	4
44	A	21	1108	5	x	x	x	4	4
45	A	25	1106	5	x	NA	x	3	4
46	A	28	2310	5	x	x	x	3	4
47	A	29	0253	15	NA	NA	x	3	4

SOURCE POINT, LENGTH OF RELEASE, AND AVAILABILITY OF DATA

Test	Source Point	Date	Time On	Length of Release	Source Wind	Point Temp.	Out-lying Winds	WIND	Upper Air Source Radiosonde Sites
48	A	29	2315	5	NA	x	x	3	4
49	B	6 Apr. 66	1306	15	NA	x	x	2	4
50	A	8	1210	15	x	x	x	NA	4
51	B	11	1302	15	NA	x	x	3	4
52	B	12	1051	30	NA	x	x	3	4
53	A	13	1205	44	x	x	x	3	4
54	B	20	1245	30	x	x	x	5	4
55	B	21	1109	30	NA	x	x	3	4
56	B	22	1115	30	NA	x	x	NA	4
57	B	25	1055	30	NA	x	x	7	4
58	B	25	1407	30	NA	x	x	8	4
59	A	26	1213	48	x	x	x	7	3
60	A	27	1255	29	x	x	x	8	4
61	B	28	1107	30	NA	x	x	NA	4
62	B	2 May 66	1315	30	x	x	x	6	4
63	B	4	1302	20	x	x	x	8	4
64	B	5	1328	30	NA	x	NA	NA	4
65	B	5	1645	30	NA	NA	NA	NA	4
66	B	6	1323	30	NA	x	x	NA	4
67	B	10	1014	30	NA	x	x	7	4
68	B	11	1007	30	x	x	x	NA	4
69	A	12	1005	30	x	x	x	8	4
70	A	19	1505	30	x	x	x	10	5
71	B	20	1535	30	x	x	x	10	4
72	B	20	1830	30	x	NA	x	10	4
73	A	23	1032	30	x	x	x	8	4
74	A	24	1000	30	x	x	x	11	4
75	A	25	0957	28	NA	x	x	9	4
76	A	26	1100	30	NA	x	x	10	4
77	A	31	1838	30	x	x	x	9	4
78	A	31	2125	30	x	NA	x	9	4
79	A	1 June 66	1834	30	x	x	x	9	4
80	A	1	2145	30	x	NA	x	9	4
81	A	2	2040	30	x	x	x	NA	4
82	B	6	1000	30	x	x	x	9	4
83	B	7	1012	30	NA	x	x	9	4
84	A	10	0942	30	x	NA	x	10	4
85	A	10	1245	30	x	NA	x	10	4
86	A	13	1000	30	x	NA	x	10	4
87	A	13	1310	30	x	NA	x	10	4
88	A	20	2215	30	x	x	x	NA	4
89	A	21	0107	30	x	x	x	NA	4
90	A	21	2300	30	x	x	x	NA	4
91	A	22	0203	30	x	x	x	NA	4
92	B	22	2305	30	x	x	x	NA	4

SOURCE POINT, LENGTH OF RELEASE, AND AVAILABILITY OF DATA

Test	Source Point	Date	Time On	Length of Release	Source Wind	Point Temp.	Out-lying Winds	WIND	Upper Air Source Radiosonde Sites
93	B	23	2215	30	x	x	x	NA	4
94	A	24	0105	30	x	NA	x	NA	4
95	B	28	1112	30	x	x	x	NA	4
96	B	29	1112	30	x	x	x	NA	4
97	B	30	1106	30	NA	x	x	NA	4
98	A	6 Jul 66	1906	30	x	x	x	NA	4
99	A	6	2208	30	x	x	x	NA	4
100	A	7	1900	30	NA	x	x	NA	4
101	A	11	1903	30	NA	x	x	NA	4
102	A	12	1900	30	x	x	x	NA	4
103	A	12	2202	30	x	NA	x	NA	4
104	A	13	1905	25	x	x	x	NA	4
105	A	14	1933	30	NA	NA	x	NA	4
106	A	15	1915	30	x	x	x	NA	3
107	A	18	1102	30	x	x	x	NA	4
108	A	20	1110	30	NA	NA	x	NA	4
109	A	21	1157	30	x	x	x	NA	4
110	A	22	1055	30	x	x	x	NA	4
111	A	25	1400	30	x	x	x	NA	4
112	A	26	1400	30	x	x	x	NA	4
113	A	27	1345	30	x	x	x	NA	4

APPENDIX C

SUMMARY OF ATMOSPHERIC CONDITIONS DURING MI TESTS

Test	Source Point			Geostrophic Condition			
				Beginning		End	
	Speed mps	Direction degrees	Relative Humidity %	Speed mps	Direction degrees	Speed mps	Direction degrees
3	2.7	315	54	5.7	358	5.1	002
4	4.3	325	69	4.6	337	4.6	016
5	5.3	320	57	6.7	337	5.7	348
6	7.1	360	77	9.8	338	8.7	347
7	1.7	035	50	3.6	329	3.6	329
9	2.9	330	40	01.5	041	1.5	002
11	-	350	63	11.3	326	6.7	024
12	2.4	335	67	05.1	310	3.6	309
13	2.1	325	69	04.1	350	7.7	315
14	5.8	355	52	11.0	350	11.6	353
15	-	355	54	8.1	194	11.3	351
16	2.1	360	52	16.1	358	13.1	355
17	-	005	39	16.7	80	10.2	081
18	2.6	340	41	5.9	281	4.3	259
19	-	-	61	6.6	010	11.2	010
20	-	-	62	15.0	136	12.1	145
21	2.7	305	66	-	-	-	-
22	-	-	56	5.4	141	2.3	191
23	3.1	300	72	8.2	324	9.4	325
24	-	-	67	14.5	159	17.6	148
25	4.4	355	56	12.0	335	13.0	331
26	5.7	335	54	13.0	331	11.5	347
27	5.0	335	56	9.2	010	11.0	360
28	2.7	285	67	4.8	217	9.5	190
29	-	340	77	0.8	256	2.9	237
30	2.8	355	90	1.0	223	1.0	238
31	6.6	330		9.0	327	8.1	357
32	5.4	335		8.2	358	7.0	360
33	5.9	310	88	10.3	308	7.6	310
34	5.9	300	81	11.7	325	15.5	310
35	5.5	290	76	13.5	310	6.0	325
36	8.1	315	69	14.0	321	19.1	310
37	-	-	65	15.4	336	14.9	344
38	2.7	295	68	8.0	337	9.5	330
39	-	-	78	9.0	263	7.5	275
40	4.9	345	76	19.0	337	16.3	350
41	4.7	325	72	7.8	339	7.5	318
42	5.2	005	25	14.2	357	15.0	351
43	4.7	340	44	10.3	015	11.0	007
44	5.2	320	64	19.8	350	19.5	355
45	3.7	265	81	5.7	035	4.2	016
46	3.6	345	-	9.5	013	8.7	005
47	-	-	-	9.0	353	8.5	351
48	-	-	95	7.6	015	5.9	030
49	-	-	-	9.0	142	7.5	147

SUMMARY OF ATMOSPHERIC CONDITIONS DURING MI TESTS

	Source Point			Geostrophic Condition			
				Beginning		End	
Test	Speed mps	Direction degrees	Relative Humidity %	Speed mps	Direction degrees	Speed mps	Direction degrees
50	4.7	320	98	15.0	320	2.7	360
51	-	-	-	11.7	310	7.2	003
52	-	-	78	8.2	325	6.1	347
53	3.2	290	72	5.5	121	6.2	124
54	3.7	280	71	9.9	120	9.7	130
55	-	-	68	4.7	343	7.3	355
56	-	270	78	4.5	035	3.2	055
57	-	315	75	0.6	135	1.2	192
58	-	-	75	2.3	245	1.8	216
59	3.9	320	80	19.4	355	14.6	356
60	3.9	300	80	7.8	160	11.5	139
61	-	275	79	5.6	093	5.0	099
62	3.9	320	78	6.1	136	4.9	135
63	2.9	280	63	8.8	159	9.1	151
64	-	-	59	9.0	175	9.6	187
65	-	290	80	8.5	217	5.2	205
66	-	-	65	0.2	005	1.7	254
67	-	265	72	1.6	100	1.9	050
68	4.0	335	72	4.2	287	6.6	310
69	3.8	300	76	3.8	192	3.7	187
70	3.4	315	82	3.7	125	1.7	103
71	4.4	240	78	7.1	153	6.4	152
72	2.8	220	78	5.5	175	5.5	180
73	4.7	265	77	6.2	027	6.5	022
74	3.3	305	89	4.2	100	5.7	113
75	-	295	92	4.3	119	3.8	134
76	-	310	89	6.1	046	8.2	036
77	5.5	305	84	4.0	023	4.0	067
78	4.9	310	87	5.0	054	5.2	019
79	2.5	335	76	1.5	271	1.1	055
80	2.4	340	85	Calm	Calm	2.5	131
81	4.8	335	77	6.0	046	6.3	037
82	4.1	225	70	7.0	220	7.0	210
83	-	255	65	3.0	115	3.0	110
84	2.9	330	84	14.0	010	7.9	009
85	2.8	295	94	-	-	-	-
86	3.0	320	82	2.0	094	1.0	135
87	5.2	250	84	0.5	270	2.0	055
88	3.9	335	90	6.0	340	3.0	325
89	4.4	330	92	4.0	318	13.0	320
90	3.9	325	89	12.0	325	15.0	330
91	3.3	360	94	16.0	339	24.0	345
92	4.5	360	99	11.0	359	8.0	360
93	5.5	005	91	5.0	018	10.0	342
94	3.9	340	96	6.0	314	6.0	328

SUMMARY OF ATMOSPHERIC CONDITIONS DURING MI TESTS

Test	Source Point			Geostrophic Condition			
				Beginning		End	
	Speed mps	Direction degrees	Relative Humidity %	Speed mps	Direction degrees	Speed mps	Direction degrees
95	2.2	260	80	3.0	094	2.0	087
96	2.8	320	80	2.0	215	3.0	204
97	-	275	76	4.0	270	2.0	304
98	3.2	355	91	3.0	255	3.0	240
99	2.7	350	94	3.0	349	3.0	238
100	-	335	87	4.0	196	6.0	216
101	-	340	89	1.0	227	1.0	292
102	2.0	335	87	7.0	359	5.0	357
103	2.0	360	12	4.0	015	6.0	002
104	2.0	325	86	3.0	024	4.0	065
105	-	-	89	7.0	070	2.0	014
106	2.5	350	92	5.0	162	3.0	158
107	3.2	330	81	10.0	009	3.0	027
108	-	-	80	12.0	308	5.0	330
109	2.8	300	80	4.0	117	14.0	151
110	2.7	270	-	6.0	128	7.0	123
111	3.2	305	83	4.0	315	3.0	006
112	3.2	305	90	1.0	012	1.0	164
113	4.3	330	84	2.0	020	3.0	359

ELECTRONIC DESIGN AND CONSTRUCTION OF A NOBLE GAS ATMOSPHERIC TRACER SYSTEM

J. J. Lashock

An electronic system combining much available commercial equipment along with transistor and integrated circuit components specially designed to continuously collect and store data from at least 63 field located radiation detectors has been developed and built. Atmospheric beta activity introduced by means of a radioactive noble gas tracer, ^{85}Kr, is monitored by 63 Geiger counters. The resultant signals enter preamplifiers specially designed to facilitate, through a long cable of up to 1600 meters, transmission to a central data sorting and accumulation and readout center.

An atmospheric tracer program requiring the emission of continuous and puff releases of radioactive gases for investigating various parameters of wind transport and diffusion is underway at Battelle-Northwest.

To implement the tracer program and allow the variety of desired uses, a major effort was extended in the design and construction of complementary electronic equipment. Measurement of the tracer material was anticipated to be performed by field located radiation detectors. Several problems relating to information transmission from field locations to the central accumulation site required solution. Since measurement of short term wind fluctuations was desirable, particularly in the case of puff-type tracer releases, an automatic real-time electronic data collection system was necessary. In order to properly define the down-wind behavior of a tracer with time, a large number of data points necessitating a rather large computer type memory storage system along with its associated programming was required. A more general description of the system, including its application in a field study, is being published.[1] The communication covers a brief description of the design and construction of the critical electronic components. A description including all of the essential circuit designs and logic is also being prepared.

The overall tracer detection system consists of 63 field located detectors from which counting information is relayed to a central data collection center. This central data center is housed within a specially instrumented trailer. A block diagram of the system is shown in Figure 1. A photograph of the centrally located electronics components located in a trailer on the Meteorology Grid is shown in Figure 2.

The field package consists of a radiation detector and preamplifier sealed inside a weatherproof lead shield. The detectors are large-window, halogen-quenched counters with a high sensitivity for beta particles. A special preamplifier was designed and assembled

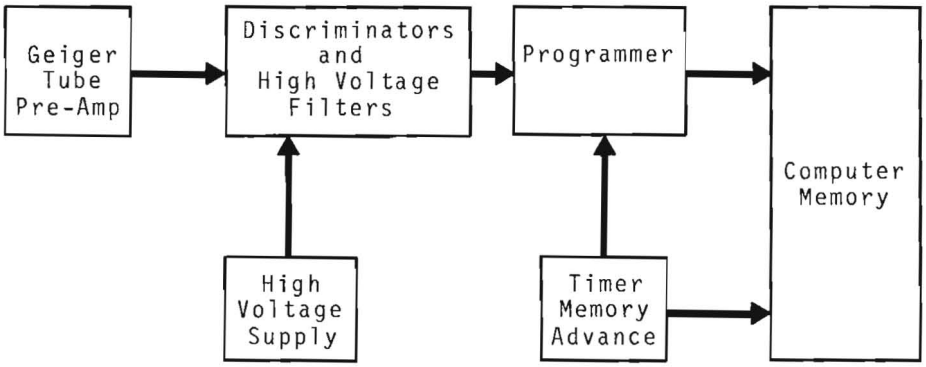

FIGURE 1. Block Diagram of the Complete Data Accumulation and Storage System

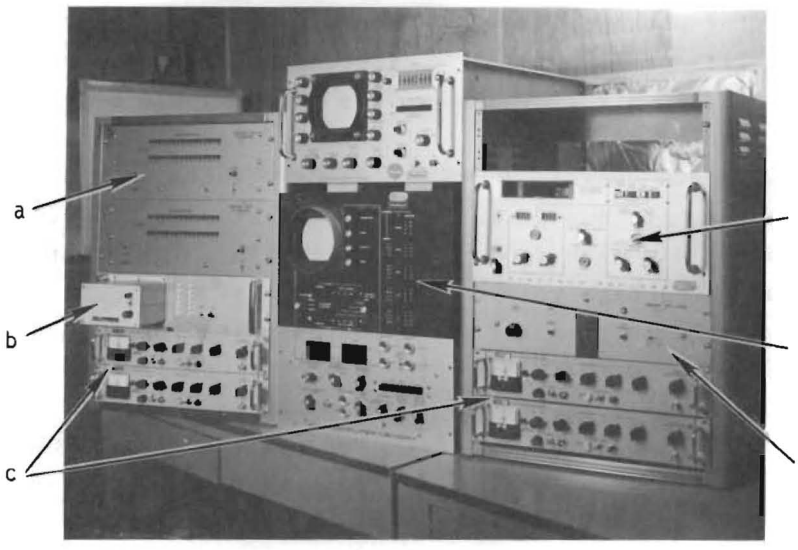

FIGURE 2. Complete Sorting and Storage System

a. Discriminators and High Voltage Filters
b. Programmer
c. High Voltage Supply
d. Magnetic Tape Transport
e. Computer Memory
f. Timer Memory Advance

in a solid state electronics system to facilitate transmission of the Geiger signals over long cable distances to the central electronics. Incorporated in its design were field reliability, low current consumption, and the ability to utilize power from the high voltage supply for operation.

Information relayed from the field packages is received at the central data collection center. Here the signals first enter a post type discriminator designed to reject the small line-type noise pulses. The discriminator output pulses are normalized as to amplitude and duration before transmission to the encoding gates of the programmer. The two discriminator chassis are constructed to accomodate the input signals from a total of 64 field detector packages. Each chassis consists of 16 printed circuit boards with two discriminators per board. A total of 32 detectors is handled by each chassis and each chassis contains its own power supply. Integrated into each discriminator circuit is a high voltage filter network which decouples incoming signals from the high voltage supply. This function is necessary since each high voltage supply operates several detectors.

Special modified high voltage power supplies are utilized for the Geiger counters (John Fluke model 412 A/B). These were provided with a monitor to measure the overall current drain created by the field detectors. In order to supply sufficient power for the 64 field packages, four such high voltage supplies were necessary.

The discriminator output signals enter the programmer whose function is manifold. This critical instrument, with integrated circuit design, serves as the heart of the electronic transformation. The programmer serves fundamentally as the interface between the 64 separate discriminators and as the timer memory advance for the computer memory. The 64 discriminator positions are uniquely encoded by the programmer so that their respective positions (field locations) are identified in the computer memory by a 6 bit binary code. The command from the timer memory advance unit is also transformed into a 6 bit code which serially shifts the position of storage in the computer memory in groups of 64. The count rate information from the 64 field detectors is thus encoded by the programmer and fed into specific memory groups of 64 channels where these groups are shifted at predetermined time intervals. The programmer will start a storage cycle in the memory after selecting a channel. This unit was constructed on one chassis and may be seen in Figure 2 with its own power unit protruding from the left side.

Two purposes are served by the timer memory advance. This solid state unit, utilizing printed circuit boards, serves first as an electronic switch for the computer memory commanding the operations of accumulation and stopping. Subsequently, it directs automatic magnetic tape

readout. The second function is to direct time interval programming through the programmer as previously described. The time interval selector which essentially determines the data integration time of the computer in each step is operated from a crystal controlled oscillator. This unit, comprising an 18 stage binary scaler from which specific rigid time intervals are selected, contains its own power supply.

The computer memory (Packard Instrument Co. Model 45 LaGrange, Ill.) is a 4096 address which accepts a 12 bit binary code consisting of two 6 bit identifications from the programmer. A scope display incorporated in this instrument allows one to visually observe data accumulation entering from all of the field packages. When the 4096 address system has been filled, the accumulated data are automatically dumped to the magnetic tape deck.

REFERENCES

1. *J. D. Ludwick, J. J. Lashock, R. E. Connally and P. W. Nickola. "Automatic Real-Time Air Sampling of ^{85}Kr Utilizing the 4096 Memory of a Multiparameter Analyzer." Accepted for publication by Review of Scientific Instruments, 1968, and also published in this report.*

AUTOMATIC REAL-TIME AIR MONITORING OF ^{85}Kr UTILIZING THE 4096 MEMORY OF A MULTIPARAMETER ANALYZER*

J. D. Ludwick, J. J. Lashock, R. E. Connally and P. W. Nickola

A noble gas atmospheric monitoring field grid system in which ^{85}Kr is used as a tracer has been designed, assembled and used for studying atmospheric transport and diffusion. This system has demonstrated its usefulness in the quantitative measurement of the transport and diffusion of both continuous and true puff-type radioactive gas releases on a real-time basis. Small fluctuations in the air concentrations of the tracer are determined by using electronic instrumental data collection times as short as one second. The system consists of a large group of field detectors which relay their information to a 4096 address memory. The memory is programmed to accept information from 64 detectors. Information is accumulated in groups of 64 time channels and these groups are automatically stepped by the programmer. A time interval selector can be set to automatically regulate the stepping process at a slow or fast rate in effecting the desired differential data accumulation. The memory is read out on magnetic tape and the equipment is ready for the next field test 35 sec after completion of the first.

INTRODUCTION AND DISCUSSION

Experimental atmospheric diffusion research over considerable distances generally involved a major effort in manpower and equipment over a considerable time period in order to produce definitive results. Factors relating to uncertain meteorological conditions compound the problems associated with conducting a successful field test, and increase the expense of holding large crews until the onset of acceptable meteorological conditions. As a consequence of this situation and other factors to be described, an automatic field monitoring system has been developed for use in studying atmospheric diffusion processes.

Atmospheric diffusion research is concerned with fundamental processes which, when understood, enable practical models to predict air concentrations of pollutants at various distances from a point of release. Such information is essential for estimating the downwind air concentrations resulting from accidental or controlled releases of radioactive or other physiologically harmful materials. Because of technical and financial limitations, certain critical diffusion experiments which could improve the models upon which predictions are based have never been satisfactorily accomplished or, in many cases, even attempted. The system described in this paper is an improvement in several areas in which these difficulties have precluded extensive experimentation. These areas include (1) The use of an inert gas tracer to precisely

* *BNWL-SA-1555, Accepted for Publication, Review of Scientific Instruments, 1968.*

follow atmospheric motions, (2) the generation of an instantaneous puff of an atmospheric tracer, and (3) the simultaneous measurement in real time of downwind atmospheric tracer concentrations at many locations.

Our investigation over a period of several years with various particulate and gaseous air tracers[1,2,3] has led to the conclusion that use of a rare gas radioisotope as a tracer would enable these essential experiments to be rather easily conducted. Studies were conducted to select the radionuclide and detector combination most favorable to reliable functioning under normal field conditions. Consideration was given to the wide temperature and other environmental variation anticipated in the field. It was found that ^{85}Kr would provide the most acceptable atmospheric tracer for the desired studies. Detection of this isotope was satisfactorily accomplished by measurement of its moderate air range beta particle (0.69 MeV) with Geiger counters. Its long half-life (10.76 yr) would allow storage until meteorological conditions were proper for its release. This noble gas tracer is easily handled, is chemically inert, and would be expected to follow exactly the atmospheric transport and diffusion processes. Adequate specific activity sources of this isotope are available and sources of small physical size could be readily prepared for release as true instantaneous puffs. Simple dilution techniques could be easily performed to provide sources more satisfactory for continuous emission when desired.

Experimentation with various gaseous and scintillation detectors indicated that a large-face, thin window, halogen-quenched Geiger-Muller counter would be most satisfactory for the simple rugged field detector package desired.[4] A preamplifier, designed and built into the field packages to drive a coaxial cable at its characteristic impedance of 50 ohms, allows signals to traverse at least two miles of cable to the central data collection station. Here the signals are decoupled, shaped, and encoded for storage in the memory of a 4096 channel analyzer. The data, after collection in the memory and transfer to magnetic tape, are then available for subsequent processing and readout. Some very important features of the final instrumental design include real-time tracer detection, rather long distance data relay, real-time information discrimination, accumulative field data display, and rapid instrumental recovery for consecutive atmospheric diffusion tests. In addition to these important features, a marked savings in time and crew size to conduct a successful field test was achieved.

In practice, a typical experimental field test was started by first releasing the ^{85}Kr tracer material either as a continuous source or as a puff. In the case of a continuous release, the analyzer memory was started prior to the

tracer release at a 38.4 sec data accumulation interval. The variable time interval, selected to suit the experiment, allowed 41 min of counting, since there were 64 available intervals. For puff releases, a visual watch was made of the 4096 memory scope display. At the first indication of increasing activity, the 64 time interval cycle was initiated. The process of initiating the cycle when activity is first observed, conserves the memory of the computer for the pertinent differential data. At high wind speeds, better differential data can be obtained by selecting the 1.2 or 2.4 sec time intervals, since the tracer activity quickly traverses the 800 m arc. The memory, even at slow speeds and using the 4.8 sec interval, is often filled before the tracer has completely negotiated the downwind detector system. The data in these cases are immediately dumped to the magnetic tape, the memory cleared, and the programmer restarted. Although time losses of 35-40 sec result during this process, the more valuable features of short-time interval and real-time differential data collection are maintained.

There are, of course, methods of relieving the technical problems associated with the finite size of the computer memory. As a compromise between the number of detectors and time intervals available, the 4096 channels were originally divided into a 64 by 64 network to provide the minimum of desired detectors while leaving a reasonable number of time intervals for differential data collection. It is apparent from the observed tracer sensitivities that a field network of detectors extending to a 3200 m arc and having a capacity of over 200 would be very useful during favorable meteorological conditions. To accomodate such a large system with a similar or even reduced size memory, a much faster tape dump would be needed. Computer compatible tape decks capable of dumping 1600 channels in considerably less than 1 sec are presently available. The network can be divided in this way to accommodate more detectors, and the memory can be filled and then dumped in a much shorter time. An even more desirable arrangement, also quite feasible, would be one in which two smaller memories alternately store and dump to the tape deck, thus allowing continuous data collection.

The entire field operation, including meteorological information collection, tracer release, and analytical data collection is only a two-man operation. This personnel requirement is in marked contrast to the crew of 10 or more men often required for atmospheric diffusion tests in which a single sample is collected at each monitoring location for subsequent analysis. In addition, this process requires a very short preparation time to become operational (on the order of 10 min). This aspect is very important since it allows advantage to be taken of meteorological situations not otherwise available because of the longer preparation times involved.

After completion of a field test, the data contained on the magnetic tapes are transferred back into the 4096 memory. The memory is then read out by an Optikon unit (Nuclear Data Inc. Palatine, Ill., OPTIKON model ND 307) which provides a photographic reproduction of the counts accumulated in each channel. The entire 4096 channels are reproduced by a four-quadrant readout each with data from 16 of the 64 time intervals. The vertical position on the photographs identifies the field detector location with the exception of a live time count appearing in the first channel of each column. Field detectors are identified by 63 of the total of 64 channels. The first 31 detector channels represent a sampling network located 200 m downwind, while the last 32 represent the 800 m sampling arc. As one reads down the display he is proceeding across the pertinent arc with respect to the ground level samplers. After 20 positions, the tower samplers of that arc are introduced. The same is true for both detector arcs. Figure 1 is a typical display of such data utilizing the 4.8 sec counting interval during a puff release. Those channels containing significant information above the normal background levels are evident. This display includes only 30 of the 64 time intervals, and the rapid buildup and decline in count rate is a result of the rather high wind speed during this field test. One can readily distinguish the puff of activity abruptly approaching some of the 200 m detectors both on the ground and on towers. Then, after passing in this vicinity for 20 to 30 sec, the activity continues downwind to the 800 m ground and tower locations. The very clear delineation of the tracer activity from the normal background activity of about 1 count/sec makes this technique very valuable in wind transport diffusion studies.

ACKNOWLEDGEMENT

The authors wish to express their gratitude for the continuous support and encouragement given them on this project by Mr. C. L. Simpson, Manager, Atmospheric Sciences Section.

REFERENCES

1. *J. D. Ludwick and R. W. Perkins. "Liquid Scintillation Techniques Applied to Counting Phosphorescence Emission, Measurement of Trace Quantities of Zinc Sulfide," Anal. Chem., vol. 33, p. 1230. August, 1961.*

2. *J. D. Ludwick. "Atmospheric Diffusion Studies with Fluorescein and Zinc Sulfide Particles as Dual Tracers," J. Geophys. Res., vol. 71, pp. 1553-1558. March 15, 1966.*

3. *J. D. Ludwick, "Xenon-133 as an Atmospheric Tracer," J. Geophys. Res., vol. 71, pp. 4743-4748. October 15, 1966.*

4. *J. D. Ludwick. "Krypton-85 as an Atmospheric Tracer," Pacific Northwest Laboratory Annual Report for 1966 to the U.S.A.E.C. Division of Biology and Medicine, Volume II: Physical Sciences, Part 2. Radiological Sciences, BNWL-481-2, pp. 18-20. Pacific Northwest Laboratory, Richland, Washington, 1967.*

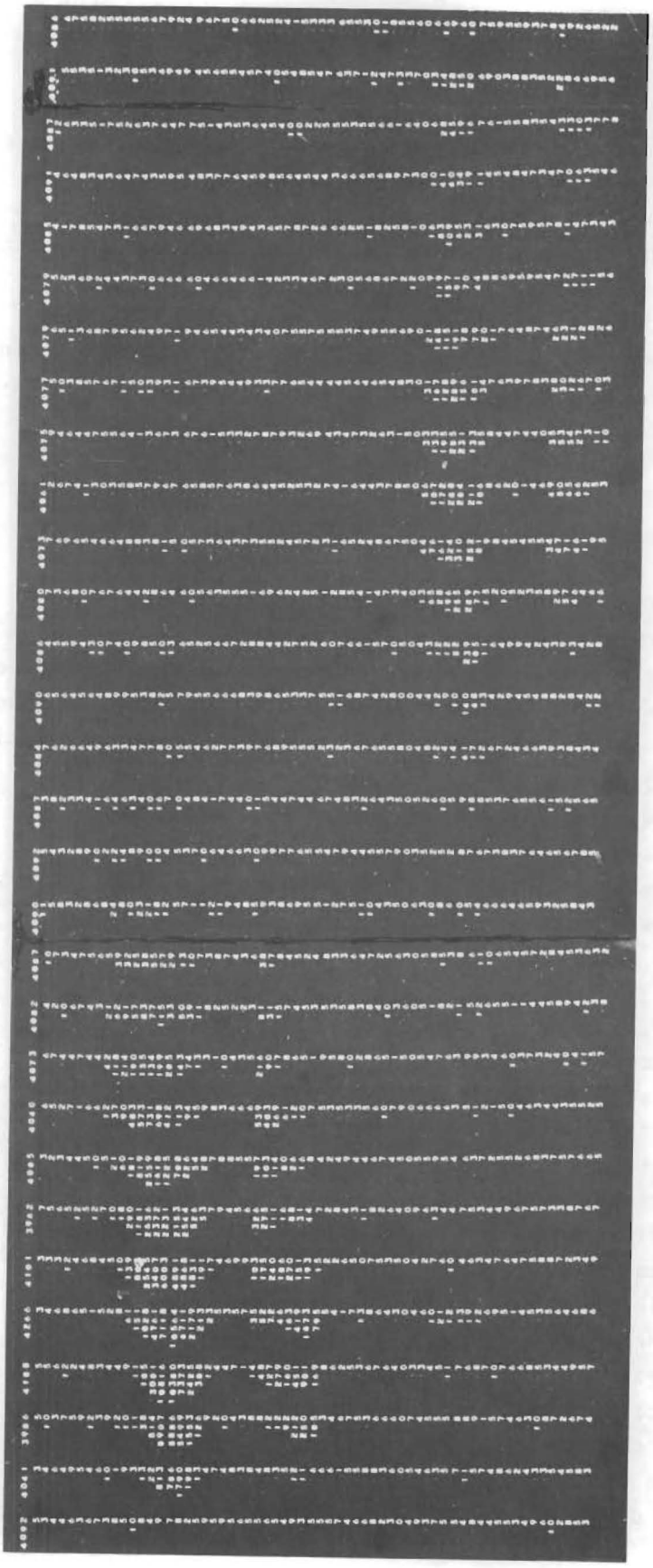

FIGURE 1. Data Display from ^{85}Kr Puff-Release

Neg. 0674166

POLAROGRAPHIC TECHNIQUES APPLIED TO PROSPECTIVE ATMOSPHERIC PARTICULATE TRACERS

J. D. Ludwick

INTRODUCTION

Many problems associated with cloud nucleation, ice crystal formation, and washout studies can be fruitfully investigated by using particulate materials as tracers. The size distribution of these materials in most cases affects their response to the atmospheric processes. Consequently, one would desire to conduct this type experiment with multiple tracers, each of which would represent a known particle size range.

The measuring of a minimum of one single tracer particle in a rain drop or snow crystal requires special low level analysis techniques. The tedious chemical and physical processing often involved in this operation emphasizes the need for simple analytical methods applicable to potential tracer materials. Polarographic methods, including pulse polarography and anodic stripping analysis, provide a high degree of sensitivity for the determination of certain chemicals. In addition, these methods are highly specific and permit measurement of selected materials in the presence of large concentrations of other ions such as sodium, potassium, and calcium. Among those elements easily measured by polarography are cadmium, zinc, and antimony, all of which have insoluble compounds suitable for use as tracers. Natural background concentrations of 0.1, 30, and <1 ppb for Sb, Zn, and Cd, respectively, measured in rain samples collected on the Washington coast, were sufficiently low to permit measurement of these materials at the concentrations to be expected in tracer studies.

EXPERIMENTAL

The most sensitive polarographic method is the anodic stripping technique, in which the material to be analyzed is first cathodically reduced and concentrated as an amalgam in a mercury surface or drop. This process quantitatively removes the element from solution, provided the reduction is conducted for a sufficient time interval. In order to achieve the highest sensitivity, the cathodic concentration step requires at least 30 minutes. The material is then quickly (5 to 30 sec) stripped from the mercury by reversing the potential, and the amount of material present is determined from the current produced.

Samples suspected of containing greater than 1.6×10^{-7}g of cadmium may be successfully analyzed by the much more rapid pulse polarographic method. The following tabulation indicates the time required for the anodic stripping process and the concentration at which pulse polarography is applicable to the

determination of cadmium. These measurements were made using rain water and standard amounts of trace material.

Cadmium Content, g	Molarity	Analytical Method
1.6×10^{-9}	5×10^{-9}	Anodic Stripping, 30 min
1.6×10^{-8}	5×10^{-8}	Anodic Stripping, 5 min
1.6×10^{-7} (or greater)	5×10^{-7} (or greater)	Direct Pulse Polarograph

The sensitivity of this method allows measurement of one CdS particle containing about 1.6×10^{-9} g Cd and averaging 10 μ in diameter. However, as noted, a period of more than 30 min is required for analysis of each sample.

In order for the tracer material to be useful in the field, an insoluble form necessitating dissolution before analysis must be utilized. Sensitivity in the case of zinc is thus reduced because its oxidation-reduction potential in an acid medium lies in a region where interference from a competing water reaction can result. In the case of antimony, the tracer compound must be carefully selected since its amphoteric nature does not lend itself to simple dissolution techniques.

The potential for dual tracer analysis is illustrated in Figure 1. This polarogram was obtained from a solution 5×10^{-7} M in both Cd and Sb. The wide divergence in their respective oxidation potentials makes resolution of these elements relatively easy.

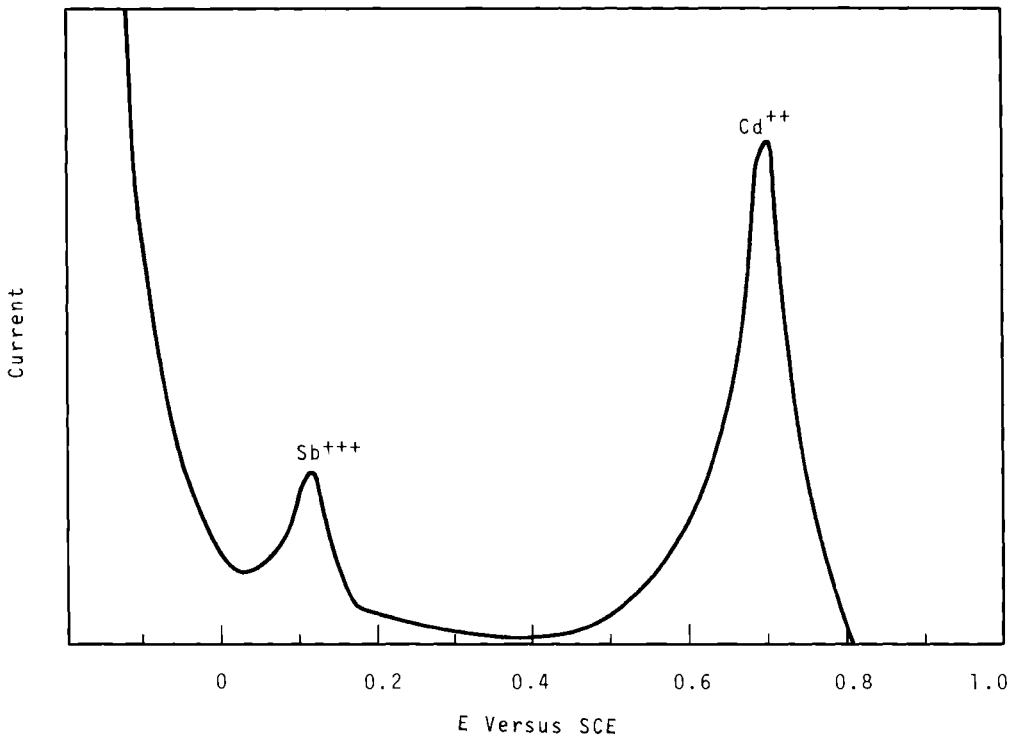

FIGURE 1. Stripping Analysis

THE MEASUREMENT OF PARTICULATE PLUME DEPLETION IN THE ATMOSPHERE BY COMPARISON WITH AN INERT GASEOUS TRACER

P. W. Nickola and J. D. Ludwick

The depletion of a plume of fluorescent particles (FP 2210) was computed by comparing it to a plume of a nondepleting noble gas (^{85}Kr). Both plumes were released simultaneously from a common source at an elevation of 1.5 meters. Exposure measurements were made on a grid of samplers at distances of 200 m and 800 m from the source. The sampling array included samplers on 10 towers. It was found that, during traversal of the distance from 200 m to 800 m from the source, 16% of the particulates in the plume was depleted. Depletion was highest near the surface. At breathing level (1.5 m) at 800 m, the crosswind integrated exposure of the particulate plume was found to be only half that of the inert gas plume.

INTRODUCTION

The release of tracers to the atmosphere to study atmospheric diffusion and transport is relatively commonplace.[1 to 11] Generally, a gaseous or small particulate tracer material is released to the atmosphere and its dosage or concentration is measured at downwind locations. Concurrent measurement of meteorological parameters in the zone of plume transport permits the development or testing of diffusion models relating transport and diffusion to existing meteorology.

Few atmospheric tracers or contaminants follow precisely the motions of the atmosphere. These contaminants, be they man-injected wastes, aerosols generated by nature or, in most instances, purposely generated atmospheric tracers, are depleted from the atmosphere by such processes as deposition, adsorption, or chemical reaction with other atmospheric constituents, with vegetation, with the earth's surface, or with man-made structures. Tagging of air "molecules" and measurement of their subsequent spatial distribution would provide an ideal standard with which to compare the behavior of all other atmospheric tracers or pollutants. The development of a field diffusion technique employing the inert gas krypton comes very close to this ideal standard. This ^{85}Kr system, developed by Ludwick, et al. is described elsewhere in this report.* As stated, a considerable number of diffusion and transport studies have incorporated field releases of less than ideal atmospheric tracers. It would be of interest to compare the plume depleting characteristics of these tracers with the nondepleting ^{85}Kr plume.

Several different fluorescent particulates (FP) have been employed

* *J. D. Ludwick, J. J. Lashock, R. E. Connally, and P. W. Nickola. "Automatic Real-Time Air Monitoring of ^{85}Kr Utilizing the 4096 Memory of a Multiparameter Analyzer," pp. 58 of this report.*

as atmospheric tracers by different investigators.[5 to 9] A mass mean diameter of 2.5 μ and a specific gravity of 4 are typical of these. Measurements or estimates of plume depletion by fallout loss have varied[7,9,12] but have generally been based on considerable assumption or meager measurement. Loss of fluorescence under certain conditions has been shown to be a problem[7,9] although proper choice of FP appears to be a solution here.

The primary atmospheric tracer used at Hanford has been FP 2210, manufactured by U. S. Radium Corporation. This tracer has been used at Hanford since 1953. The resulting Hanford FP 2210 technique and subsequent improvement has been cited frequently in these annual reports commencing in 1960. Hundreds of field experiments employing this technique have been carried out at Hanford, and several hundred more were completed at Air Force installations.*[13] This paper deals primarily with the comparison of a plume of FP 2210 with a plume of ^{85}Kr, with the latter considered as a standard.

EXPERIMENTAL PROCEDURES

The field grid employed in this experiment consisted of two sampling arcs concentric about a common tracer source point. The distances of these arcs from the source were 200 m and 800 m. On the 200 m arc, five towers of 27 m height permitted vertical tracer sampling. At 800 m, five towers extended to heights of 42 m. On both arcs, the towers were spaced at 8° increments. The arcs and towers were heavily instrumented for sampling of FP 2210 but, since the field ^{85}Kr layout was primarily intended for use as a prototype system, the extent of ^{85}Kr samplers was limited. The distribution of samplers is shown schematically (but not to scale) in Figure 1. Both arcs were instrumented at the 1.5 m elevation for sampling of FP and ^{85}Kr at 2° angular increments. FP samplers extended from 70° to 160°, while ^{85}Kr samplers were limited to the range 94° to 132°. Vertically, sampling of FP extended to 27.0 m on the 200 m arc, and to 42.0 m on 800 m arc. Corresponding extents of sampling at 200 and 800 m for ^{85}Kr were 42.0 m and 21.4 m, respectively. For FP, vertical sampling took place on towers at 98°, 106°, 114°, 122°, and 130° on both arcs; for ^{85}Kr, only towers at 98°, 114°, and 130° were instrumented. Furthermore, only five ^{85}Kr samplers were on each of the 6 towers, while 16 FP samplers were distributed on each of the 10 towers.

The experiment took place on November 8, 1967 during a period when the wind speed at the 1.5 m elevation averaged 2.6 mps. The atmosphere was slightly thermally stable. The temperature at an elevation of 24 m was about 0.8F° warmer than at 1.5 m. The period

---

* *W. T. Hinds. "Diffusion over Coastal Mountains of Southern California," in this report.*

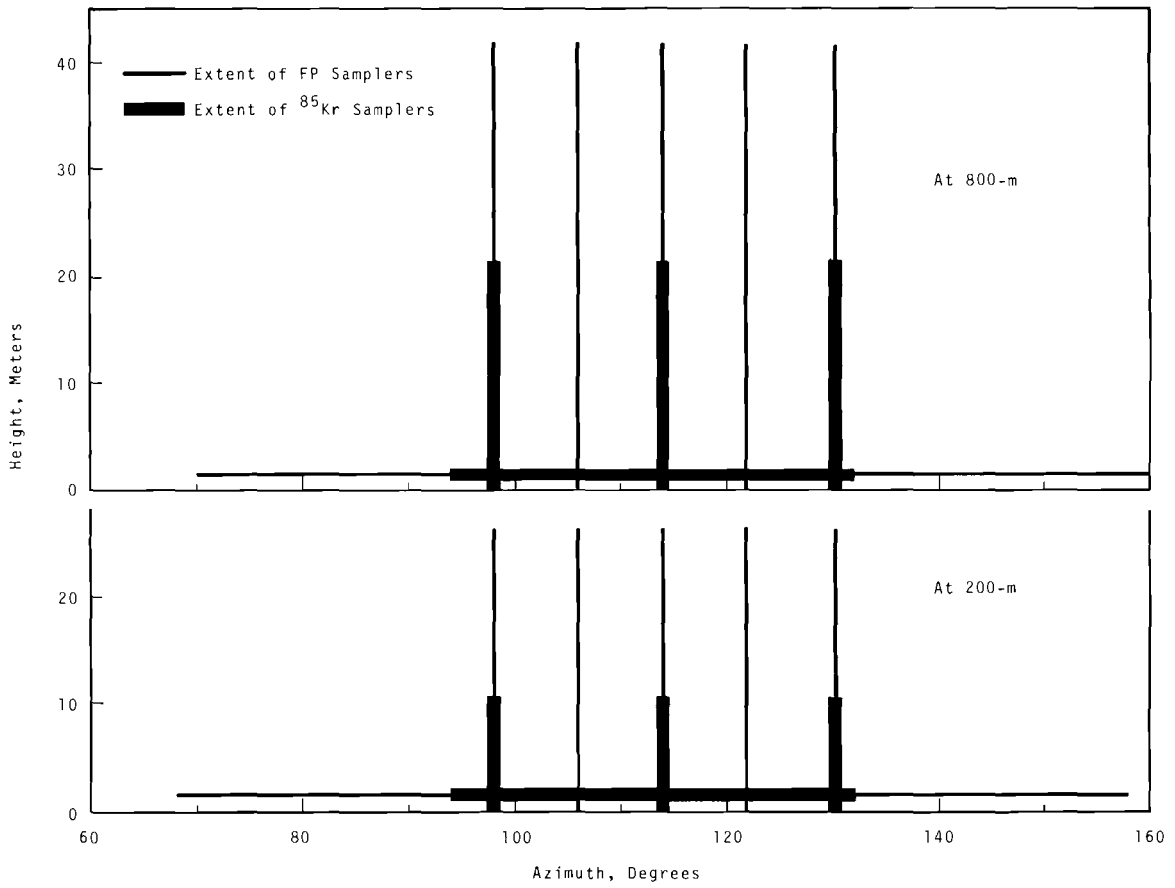

FIGURE 1. Extent of Field Sampling Grid

of tracer release was from 0512:22 PST to 0532:13 PST. Generation of both FP and ^{85}Kr began and ended within 3 sec of each other. The source heights were about 2 m. Fortunately the distribution of tracer plumes remained almost entirely within the horizontal extent of the field grid. However, the vertical extent of the tracers exceeded the heights of the uppermost samplers on both sampling arcs. Extrapolation of measured tracer values suggests about 8% of both tracers passed above the 800 m arc towers.

ANALYSIS AND RESULTS

In the Rankin counting technique for analysis of FP 2210 on filter samples, the count obtained per unit time is directly proportional to the mass of FP on the sample and hence to the exposure (mass/flow rate) for each field location. In the ^{85}Kr system, the exposure accumulated at a specific field location is directly proportional to the integral of all counts on the Geiger counter at that location. Since the analysis technique required only relative exposure units rather than

absolute, the data were manipulated as "counts" rather than exposures for both FP and ^{85}Kr samples.

First analysis was concerned with the 1.5 m level samples. For ^{85}Kr samples on the 200 m arc, the sum of counts for each sampler was compiled. The sum of all the 1.5 m counts gave an estimate of the crosswind integrated counts for the ^{85}Kr ($CWIC_{Kr}$). The relative contribution of each individual sampler count was related to the $CWIC_{Kr}$ in terms of a percentage of this whole. The ^{85}Kr crosswind distribution is the solid line on Figure 2.

For FP samples a similar procedure was followed. "Rankin" counts for filters along the arc were summed and the individual filter counts were specified as a percentage of the $CWIC_{FP}$. The resulting FP crosswind distribution is the dotted line on Figure 2.

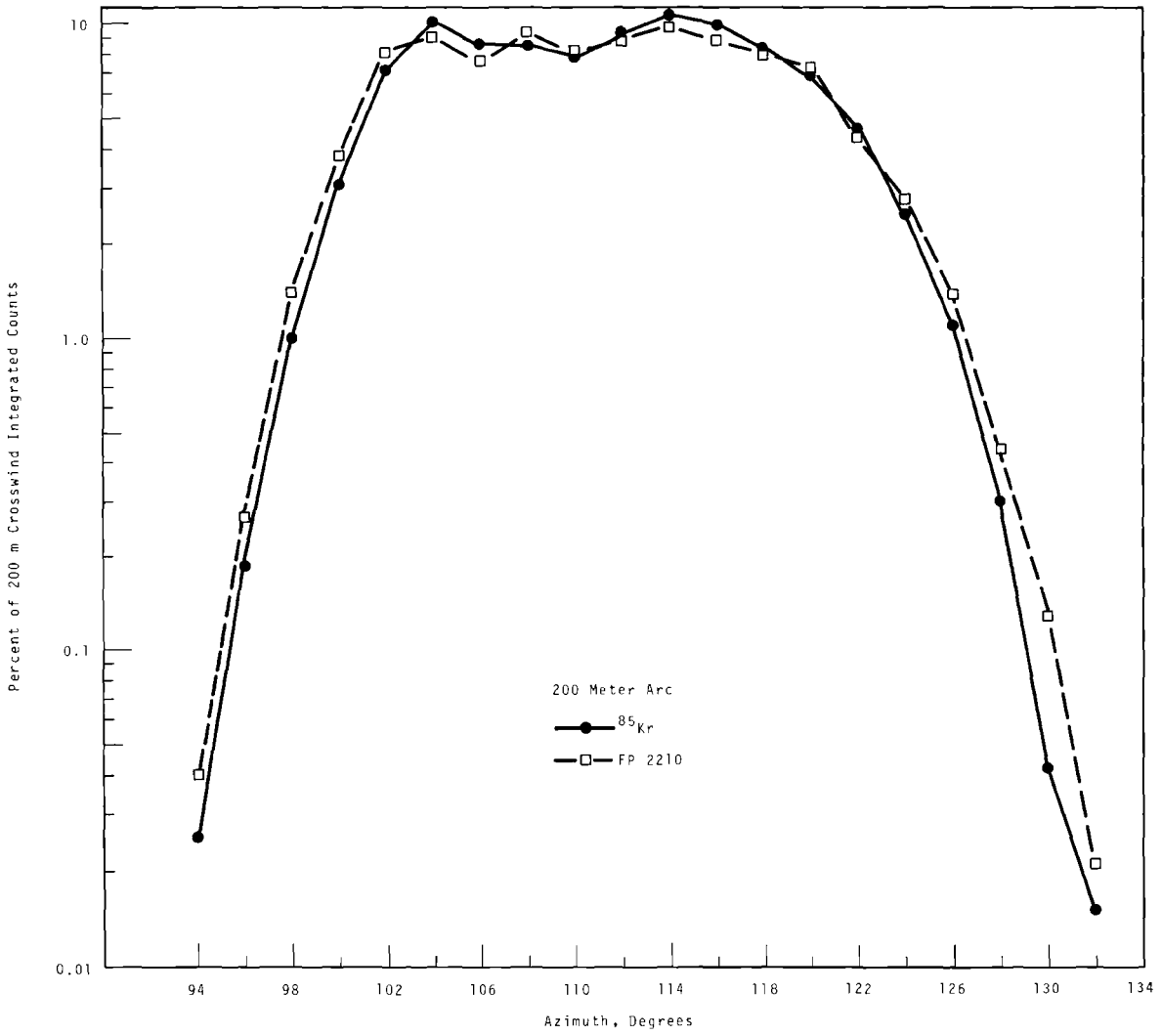

FIGURE 2. Crosswind Distribution of Count on 200 m Arc

That the areas under the two curves on Figure 2 are similar is not surprising. Near identical areas were forced on them. The similarity in shapes of the distributions lends some confidence to the validity of the independent sampling and assay techniques and suggests that, at this 1.5 m elevation, no great distortion of the FP plume from the ideal ^{85}Kr has taken place in the first 200 m of transport.

It was assumed that the ^{85}Kr truly follows the motion of the atmosphere. With this assumption in mind, the accumulated counts for each ^{85}Kr sampling position at 800 m and the $CWIC_{Kr}$ for the 800 m arc were computed as percentages of the $CWIC_{Kr}$ observed at the 200 m arc. If the same procedures were followed for FP, and if the FP were in fact being depleted as it traversed from the 200 to the 800 m arc, then the percentage of FP at 800 m with respect to the $CWIC_{FP}$ at 200 m would be less than the similar values for ^{85}Kr. As can be seen in Figure 3, this was the case at all locations except 104°, 106°, and 108°. The area under the FP curve is only 50.5% of that under the ^{85}Kr curve. It should be noted that the percentages here are plotted on a logarithmic scale only for better definition of point separation. The value of 50.5% can be interpreted as the crosswind integrated percent of FP remaining at the 1.5 m level with respect to the use of the ^{85}Kr values at that level as standards.

The reason for the displacement of the 800 m FP distribution to the left of the ^{85}Kr standard is not obvious. Suffice it to say that although this change in crosswind tracer distribution may be a clue to the depletion mechanism, vertical data points were too sparse in the present test to pursue the clue in detail.

Assuming the passage of equal crosswind integrated exposures at the 1.5 m level on the 200 m arc, the data imply that an individual standing on the ground at the 800 m arc would breathe, on the average, only half the amount of FP as he would ^{85}Kr. Identical fluxes of both tracers passing the vertical cylindrical surface of the 200 m arc would not, however, necessarily be in the 2 to 1 ratio at the 800 m surface.

However, computations based on the sampling data generated from towers and 1.5-m level samplers permit the mentioned flux calculations. The accuracy of these calculations is undoubtedly degraded by the fact that a maximum of only three counts is available for a given level at each arc except, of course, at the 1.5 m level.

In the manner outlined for the 1.5 m samples, CWIC values for both ^{85}Kr and FP were computed and the fractions of FP remaining at 800 m were computed for 14 elevations. In the zone below the uppermost samplers, interpolation permitted the confident selection of counts for input to the calculations. The count values above the elevation of

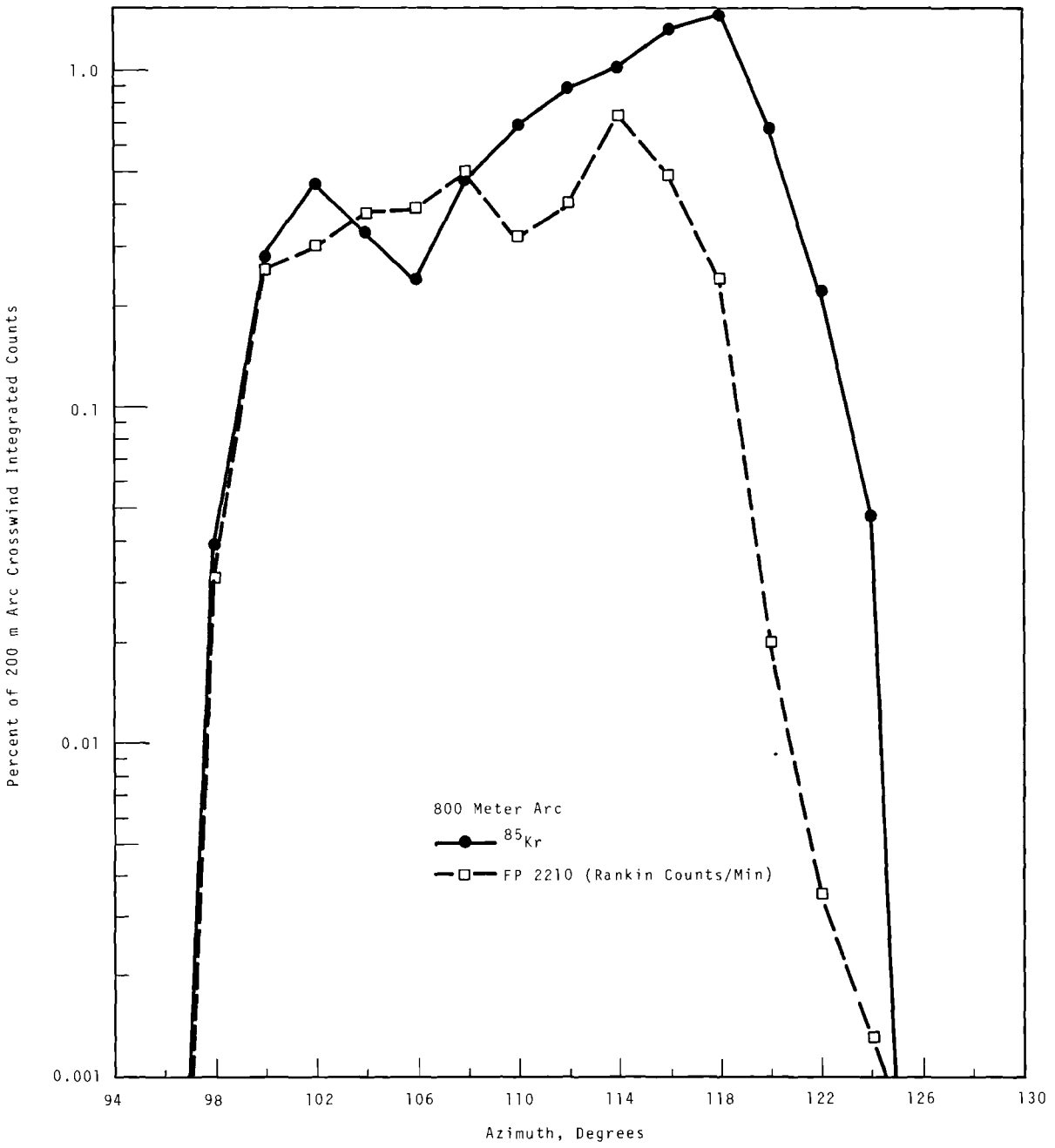

FIGURE 3. Crosswind Distributions of Count on 800 m Arc

the uppermost samples were derived from extrapolated counts. The primary tools used in the extrapolation were (1) the shape of the individual and integrated count versus height curves for both tracers, and (2) the shape of the distribution with height of the ratio of CWIC values between the two tracers.

Obviously the extrapolation procedure entailed some subjectivity, but objectivity was attempted in

the extrapolations. In the instance where these tools did seem to offer the most latitude, the extrapolations were first made to what were felt to be the most reasonable values. Extrapolations were then made to the extremes. Figure 4 shows the resulting distributions of the crosswind integrated fraction of FP remaining versus height. Curves are given for the "best" estimate and for the "extremes."

Multiplication of the standard counts (i.e., the $CWIC_{Kr}$) at the 800 m arc by the wind speed at the elevation of a layer, and multiplication of this result by a factor proportional to the thickness of the layer for which the count was considered to be representative resulted in a number proportional to the ^{85}Kr flux through that layer. Smaller layer thicknesses were chosen near the surface where a steeper count gradient was found. A summation of the fluxes through all layers resulted in the total ^{85}Kr flux passing the 800 m arc. Multiplication of the ^{85}Kr fluxes for each layer by the appropriate fraction of FP remaining for that layer resulted in fluxes of FP for each layer. Again, summing yielded the total FP flux passing the 800 m arc. The resulting 800 m arc distributions of flux with height are shown in Figure 5. Only the "best" estimates are given.

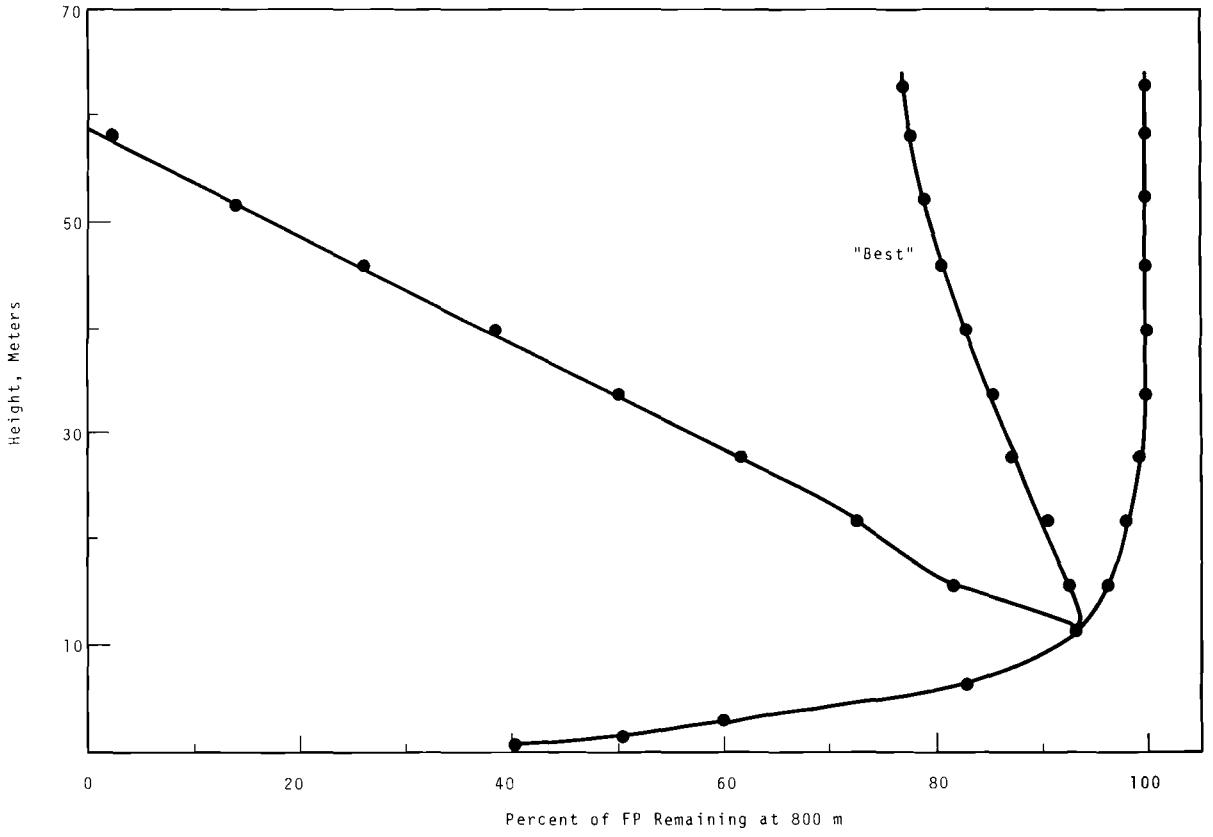

FIGURE 4. Crosswind Fraction of FP Remaining at 800 m Versus Height

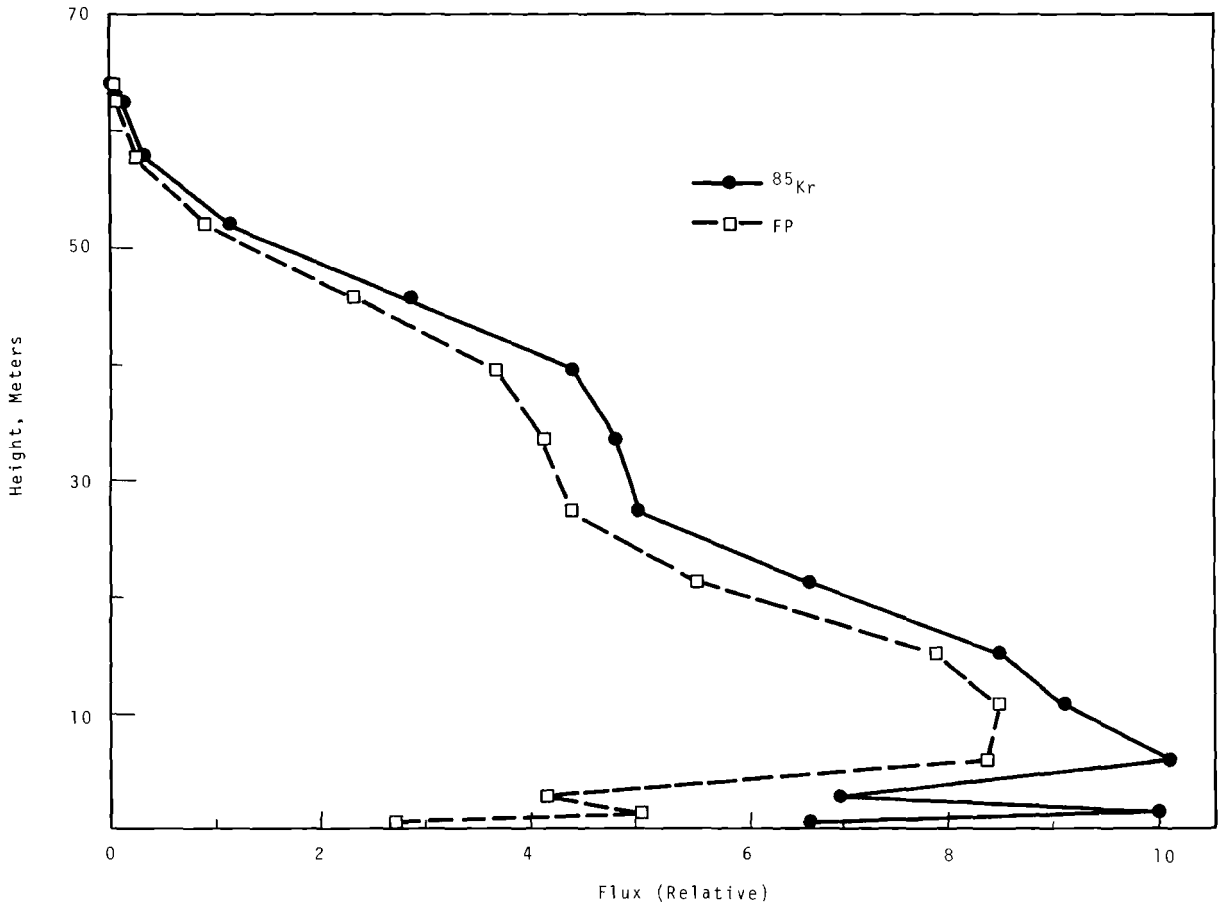

FIGURE 5. Relative Flux at the 800 m Arc Versus Height

The ratio of FP flux to ^{85}Kr flux for the 800 m arc discloses the "best" estimate of the fraction of FP remaining at 800 m to be 84%. The "extreme" estimates result in FP-remaining fractions of 65% and 87%.

Simpson,[12] in 1961, made a similar investigation based on a mass balance technique. He worked with FP 2210 data also. His technique involved measurement of the FP passing through vertical planes at successively greater distances from the source. Plotting of the cross-wind distributions and subsequent planimetering along isopleths of exposure for each distance, plus a knowledge of wind speed distribution with height, permitted the computation of total mass passing at each distance. The difference in mass between successive planes was considered to have been deposited. In the four tests examined by Simpson, the ratios of mass passing the 800 m arc to that passing at 200 m were 0.81, 0.74, and 0.27. The tests which Simpson analyzed were carried out in very stable

atmospheres. The present test, carried out in a slightly stable atmosphere, showed (with a ratio of 0.84) somewhat less plume depletion between the 200 and 800 m distances.

In Figure 4, the shape of the "best" curve might be explained by two depletion processes working on the FP plume. The modest depletion above 12 m could be explained by the gravitational settling of (primarily) the larger FP particles. Thus the higher fractions remaining at successively lower levels resulted from the feeding of these levels by particles from higher levels. The strong depletion near the surface was quite likely, primarily because of heavy deposition on the surface of the earth and on vegetation. Sagebrush in the area is moderately dense and averages roughly 1 m in height. Lower vegetation includes cheat grass and tumbleweeds.

REFERENCES

1. M. E. Smith, I. A. Singer, F. E. Bartlett, and L. Marcus. "The Variations of Effluent Concentrations During Temperature Inversions," J. Air Pollution Control Assoc., vol. 7, p. 194. 1958.

2. M. L. Barad and B. Shorr. "Field Studies in Diffusion of Aerosols," Am. Ind. Hyg. Assoc. Quart., vol. 15, p. 316. 1954.

3. H. E. Cramer. "Diffusion Measurement During Project Prairie Grass," Geophys. Res. Paper No. 59, edited by M. L. Barad, AFCRL-TR-58-235 (I). Air Force Cambridge Research Laboratories, Bedford, Massachusetts, 1958.

4. J. S. Hay and F. Pasquill. "Diffusion Experiments from a Fixed Source at a Height of a Few Hundred Feet in the Atmosphere," J. Fluid Mech., vol. 2, p. 299. 1957.

5. R. R. Braham, B. K. Seely, and W. D. Crozier. "A Technique for Tagging and Tracing Air Parcels," Trans. Am. Geophys. Union, vol 33, p. 825. 1952.

6. Green Glow Diffusion Program, Volume I, edited by M. L. Barad and J. J. Fuquay, HW-71400 VOL I. Available from Clearinghouse for Federal Scientific and Technical Information, Springfield, Virginia, 1962.

7. P. A. Leighton, W. A. Perkins, S. W. Grinnell, and F. X. Webster. "The Fluorescent Particle Atmospheric Tracer," J. Appl. Meteor., vol. 4, p. 334. 1965.

8. E. W. Bierly and G. C. Gill. "A Technique for Measuring Atmospheric Diffusion," J. Appl. Meteor., vol. 2, p. 145. 1963.

9. A. E. J. Eggleton and N. Thompson. "Loss of Fluorescent Particles in Atmospheric Diffusion Experiments by Comparison with Radioxenon Tracer," Nature, vol. 192, p. 935. 1961.

10. E. Robinson, J. A. McLeod, and C. A. Lapple. "A Meteorological Technique Using Uranine Dye," J. Appl. Meteor., vol. 16, p. 63. 1959.

11. R. K. Dumbauld. "Meteorological Tracer Technique for Atmospheric Diffusion Studies," J. Appl. Meteor., vol. 1, p. 437. 1962.

12. C. L. Simpson. Some Measurements of the Deposition of Matter and Its Relation to Diffusion from a Continuous Point Source in a Stable Atmosphere, HW-69292 REV. Available from Clearinghouse for Federal Scientific and Technical Information, Springfield, Virginia, April 1961.

13. D. A. Haugen and J. J. Fuquay. The Ocean Breeze and Dry Gulch Diffusion Programs, Volume I, HW-78435. Available from Clearinghouse for Federal Scientific and Technical Information, Springfield, Virginia, 1963.

ADDITIONAL METEOROLOGICAL ANALYSES OF SHOT SMOKY, PLUMBBOB TEST SERIES

W. E. Davis, C. A. Oster, B. C. Scott,
and J. M. Thorp

INTRODUCTION

An in-depth meteorological analysis of Shot Smoky (August 31, 1957) was started during 1966 in the Plumbbob Test series. Results of the work completed prior to March, 1967 were reported in the last annual report.[1] In summary, it was shown that meteorological data provided as a special support for Shot Smoky contained errors. When included in the stream function analysis, these errors resulted in a trajectory pattern not consistent with other measured parameters. Deletion of these data resulted in a realistic stream function analysis, and the derived trajectory analysis provided a cloud travel path in spatial and temporal agreement with an aircraft observation to within a time period of 20 min at a distance of 770 km.

Research on Shot Smoky this year was directed toward the following objectives:

- To attempt further isentropic trajectory verification
- To correlate meteorological observations of precipitation with cloud passage
- To compare the results of the DELFIC program[2] representation of close-in fallout on Shot Smoky with manual calculations and the observed fallout pattern.

DISCUSSION

The 1966 annual report[1] showed that isentropic trajectory calculations were confirmed at 770 km to within a time of 20 min by correlation with an aircraft observation. Further confirmation of this technique to depict the temporal displacement of a debris cloud is now available. Cedar City, Utah is approximately 310 km from ground zero along the cloud path. The portion of the cloud following the 330° θ surface was computed to have arrived at this location at 3.5 hr after shot time. A U.S. Weather Bureau observer reported the nuclear debris cloud overhead on the 1558 Z August 31 meteorological surface observation. At the same time, an observer at Delta, Utah reported a nuclear cloud to the south coinciding with the computed arrival time of the 340° θ trajectory shown in Figure 1.

Measurements of the radioactive fallout material in the vicinity of Rock Springs, Wyoming[3] were higher than those of the surrounding area by a factor of five, i.e., a hot spot in the pattern. This finding can be attributed to depletion of the nuclear cloud material and subsequent ground deposition by scavenging mechanisms associated with precipitation. It has

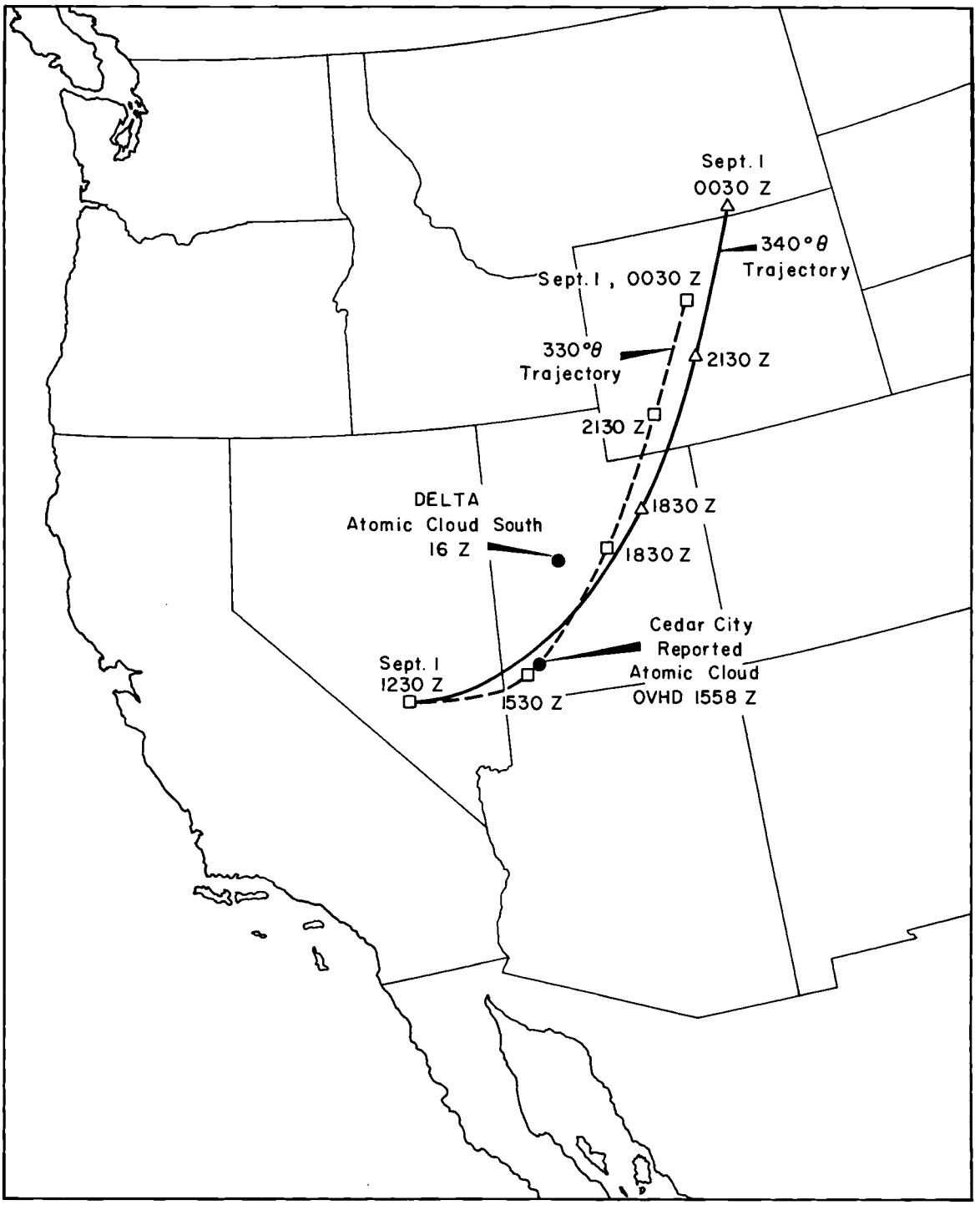

FIGURE 1. Isentropic Trajectories for Shot Smoky. Aug. 31, 1230Z to Sept. 1, 0030Z, 1957 $\theta = 330°$ *dashed line* $\theta = 340°$ *solid line*
Time of arrival is noted along the paths.

long been hypothesized and supported by experimental programs,[4,5,6,7,8] that when a particulate cloud coincides in space and time with a precipitating cloud then the particulates will be depleted from the atmosphere and deposited on the ground. Isentropic trajectory analyses for Shot Smoky showed that the debris cloud, travelling along the 320° θ surface, would arrive at Rock Springs, Wyoming at 13 to 14 hr after shot time, as shown by Figure 2. Meteorological observations from the U.S. Weather Bureau station at Rock Springs, Wyoming, as officially recorded, indicated precipitation at that time. Although specific in-cloud and below-cloud observations of radioactivity are not available, the coincidence of events provides an explanation for the "hot spot." However, the possibility that this high radiation measurement could have been deposited by previous shots cannot be entirely discounted.[4]

One other area where the computed cloud path coincided with a precipitation area was in North Central Wyoming. The upper air sounding at Lander, Wyoming during nuclear cloud passage indicated that the unstable conditions could have permitted precipitation scavenging up to about the 330° θ surface as shown by Figure 3. However, the lack of radioactivity measurements in this area precludes corroborative evidence of the washout mechanism.

A time consuming manual computation of the surface deposition pattern was performed for this study. A typical procedure fully defining a fallout pattern and the size separation was developed to include the required computations of mean vector winds for many layers in the atmosphere. These data were then averaged with respect to time and applied successively to the various particle size fractions, assumed to fall at constant velocities as a function of particle size until intersection with the ground. The Defense Land Fallout Interpretive Code (DELFIC) computational model[2] was developed to perform these functions. This DELFIC program was modified for use in the Univac 1108 and employed to define fallout pattern out to 170 km (manual methods were used for greater distances). The one condition necessary for use of the DELFIC model, i.e., intersection of the ground surface by the fireball, was satisfied by Shot Smoky.[4]

Meteorological input data as measured at Yucca Flat approximately 26 km south of ground zero were used as initial conditions (Figure 4). These vertical profiles of temperature and wind defined an initially stabilized cloud adjusted for wind deformation. The model computed the cloud top to be 12,290 m above sea level, whereas the one available observation placed the top at 11,500 m as shown in the following tabulation.

	Cloud Top	Cloud Bottom	Cloud Radius
Smoky[3]	11,500 m	∿6,100 m	Not observed
DASA	12,290 m	7,983 m	4,000 m

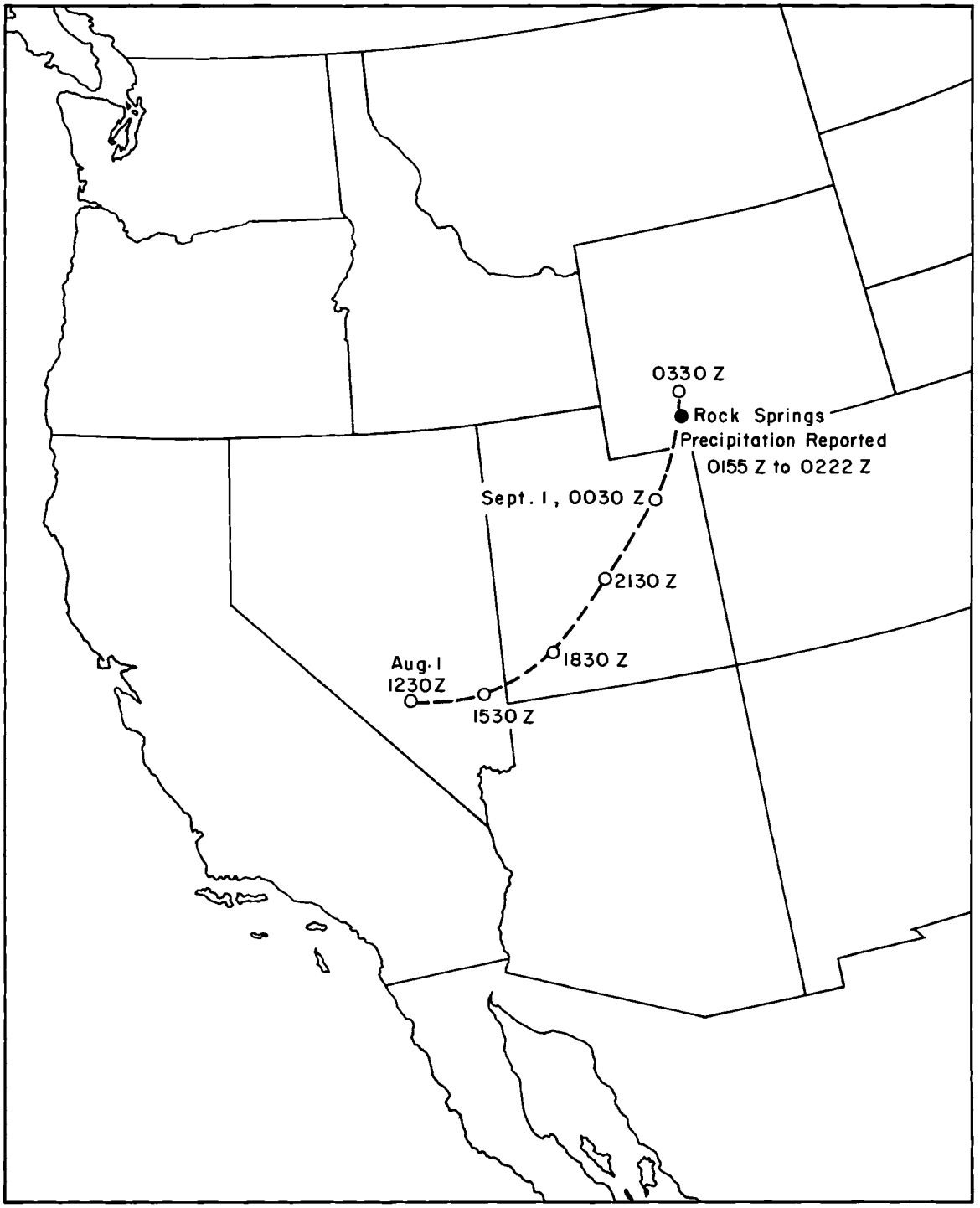

FIGURE 2. Isentropic Trajectory for Shot Smoky. Aug. 31, 1230Z to Sept. 1, 0030Z, 1957 θ = 320°

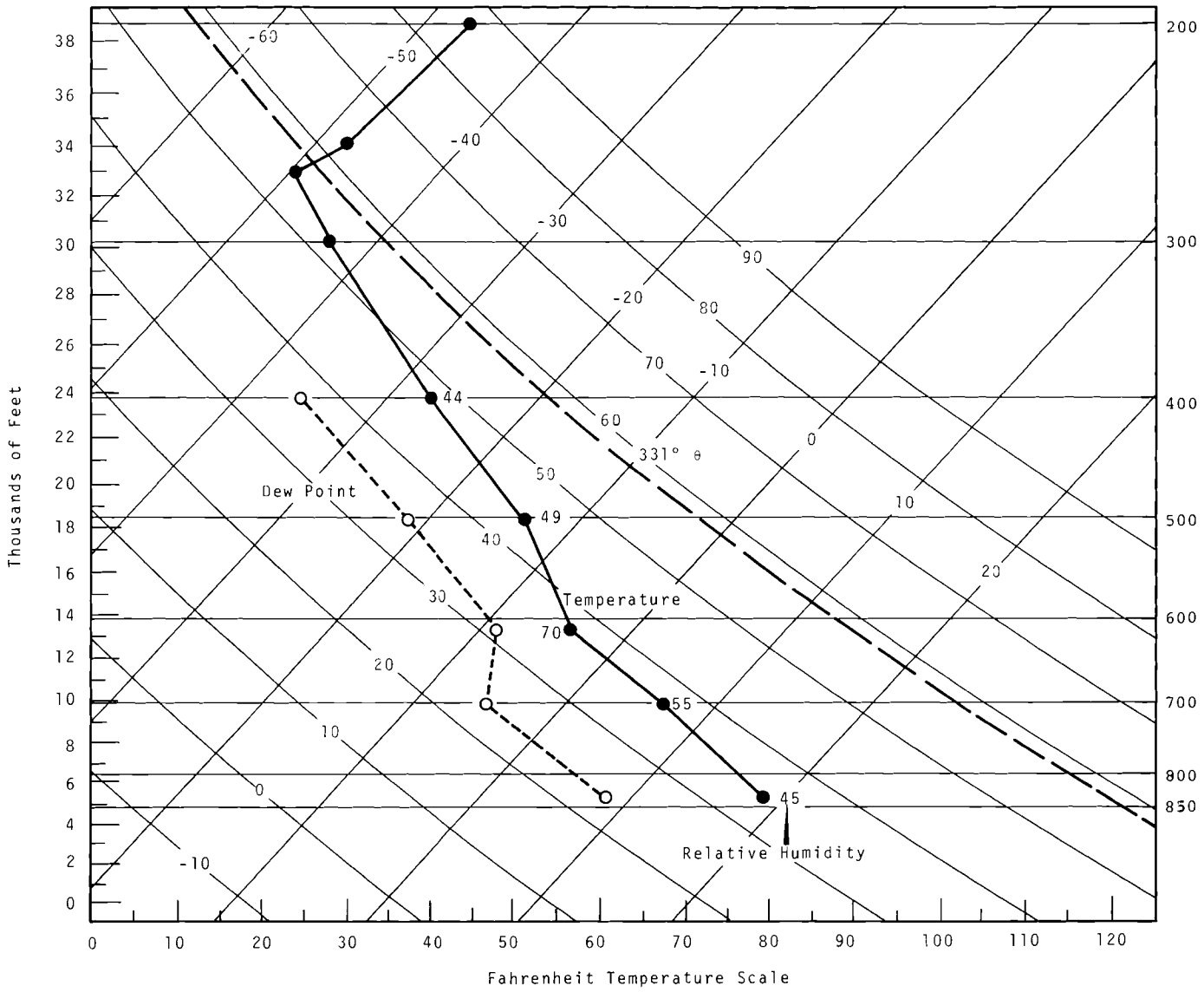

FIGURE 3. Plot of Radiosonde Report of Pressure, Temperature, Dew Point and Relative Humidity for Lander, Wyoming, Sept. 1, 00Z, 1957

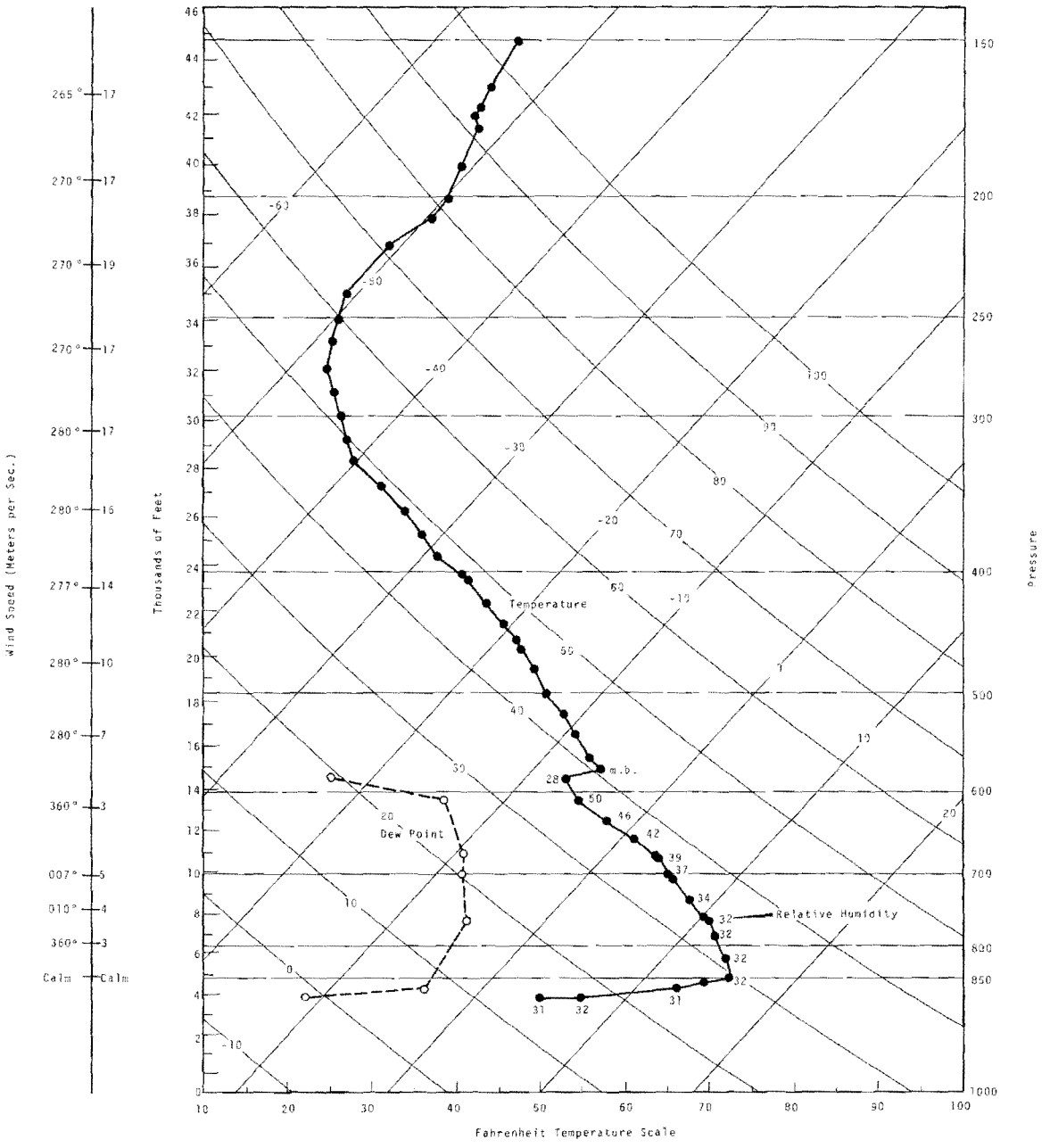

FIGURE 4. Plot of Radiosonde Report of Pressure, Temperature, Dew Point and Relative Humidity plus Upper Air Wind Report for Yucca, Nevada, Aug. 31, 1230Z, 1957

In practice, the DELFIC computations considered the wind field defined by the 10 data points nearest the cloud. These were processed and combined as inputs to the transport module, with the particle population as defined by the model. The cloud was moved in accordance to these data until new wind data were entered. This process was continued until the particles were calculated to have intersected the ground or the particles had passed through the boundary of the model.

The transport model also has a capability to consider local circulation cells. In the Shot Smoky analysis this option caused the program to cycle and resulted in an excessive use of computer time without producing usable results. The option was then removed and a deposition pattern was produced. The deposition patterns produced by the DELFIC[2] computations were compared with the measured values.[3] The following results were obtained:

- An anomalous low value near Sheep Mountain coincided with the measured value reported by K. H. Larson, et al.[3] As yet, which factors in the DELFIC model calculation are responsible for this result is not known.
- The computed mid-line coincided with the measured mid-line out to 90 km. Beyond 90 km, the computed mid-line was defined as being <5 km south of the measured mid-line.
- Computed and measured arrival times are in good agreement out to H + 3 hours. However, beyond that point and away from the centerline, disagreements of as much as 2 hr are noted.

Consideration of the vertical wind profile (Figure 4) indicated need for a north-south separation of particle sizes in the pattern as a result of the shear in the wind direction profile at 5 km above mean sea level. This is evident in the skewed distribution of the observed time of arrival to the south of the measured mid-line shown in Figure 5.[3]

Previously unpublished patterns[5] of observed particle sizes <44 μ, 44-88 μ, 88-105 μ, and 105-125 μ in diameter (Figures 6, 7, 8, and 9) were compared to the DELFIC prediction.

The computed and measured mid-lines were in good agreement for the 88-105 μ and 105-125 μ-size fractions out to 50 km from ground zero. From 50 km to 90 km, the computed mid-line diverged to a position about 5 km to the north of the observed mid-line at 90 km from ground zero.

Manual and DELFIC model calculations indicate that the <44 μ and 44-88 μ-size fractions should have been deposited along the southern part of the pattern (Figure 10). In fact, however, the measurements[3] indicate that the mid-line deposition for these particle sizes occurred along the mid-line prediction for the 100 μ to 350 μ-size particles as shown in Figures 6, 7, and 10. One possible explanation for this disagreement between predicted and observed deposition patterns for the

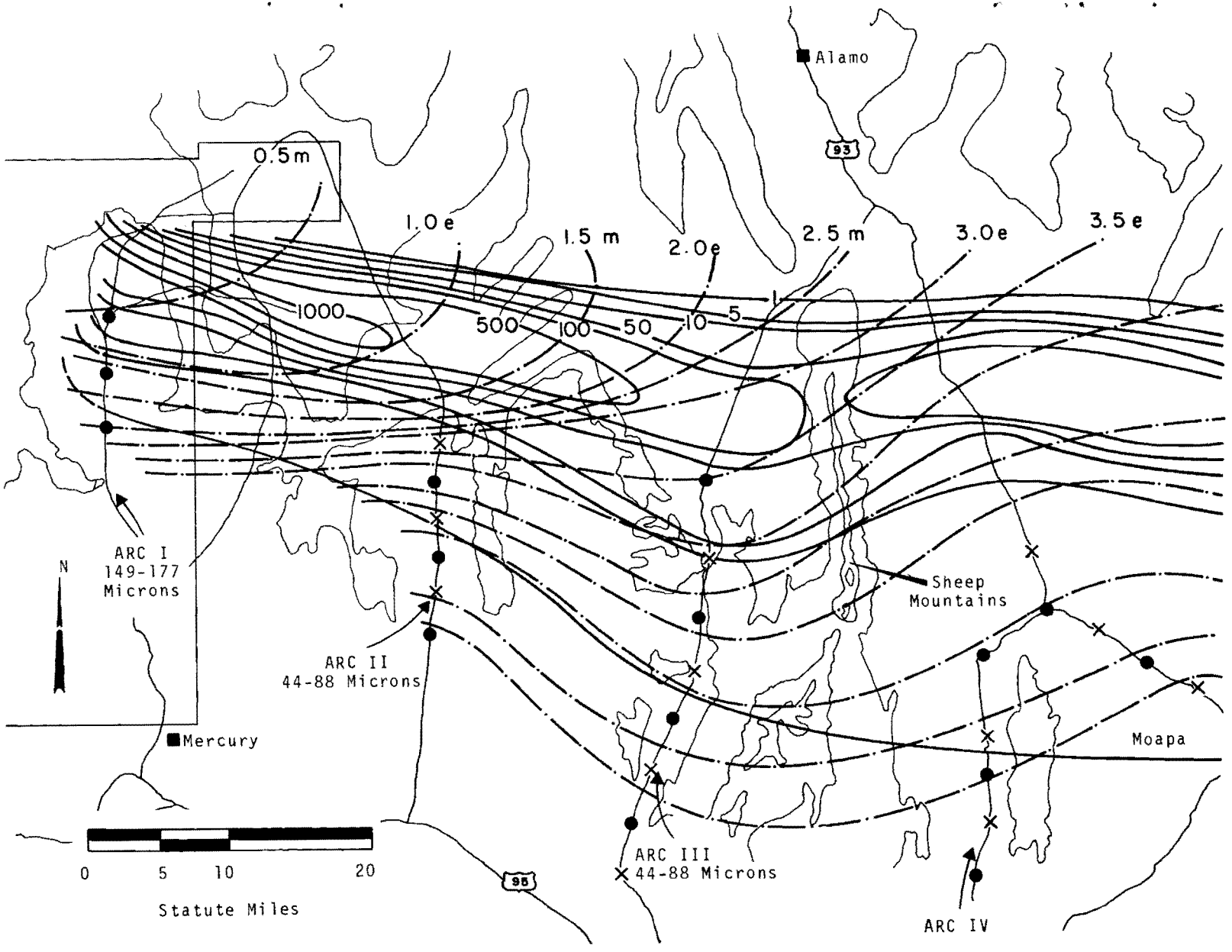

FIGURE 5. Smoky Fallout Pattern. Dose Rate Contours (solid line) MR/hr at H + 12 hr. Time of Arrival (H + hours) Shown by Dashed-Dot Lines

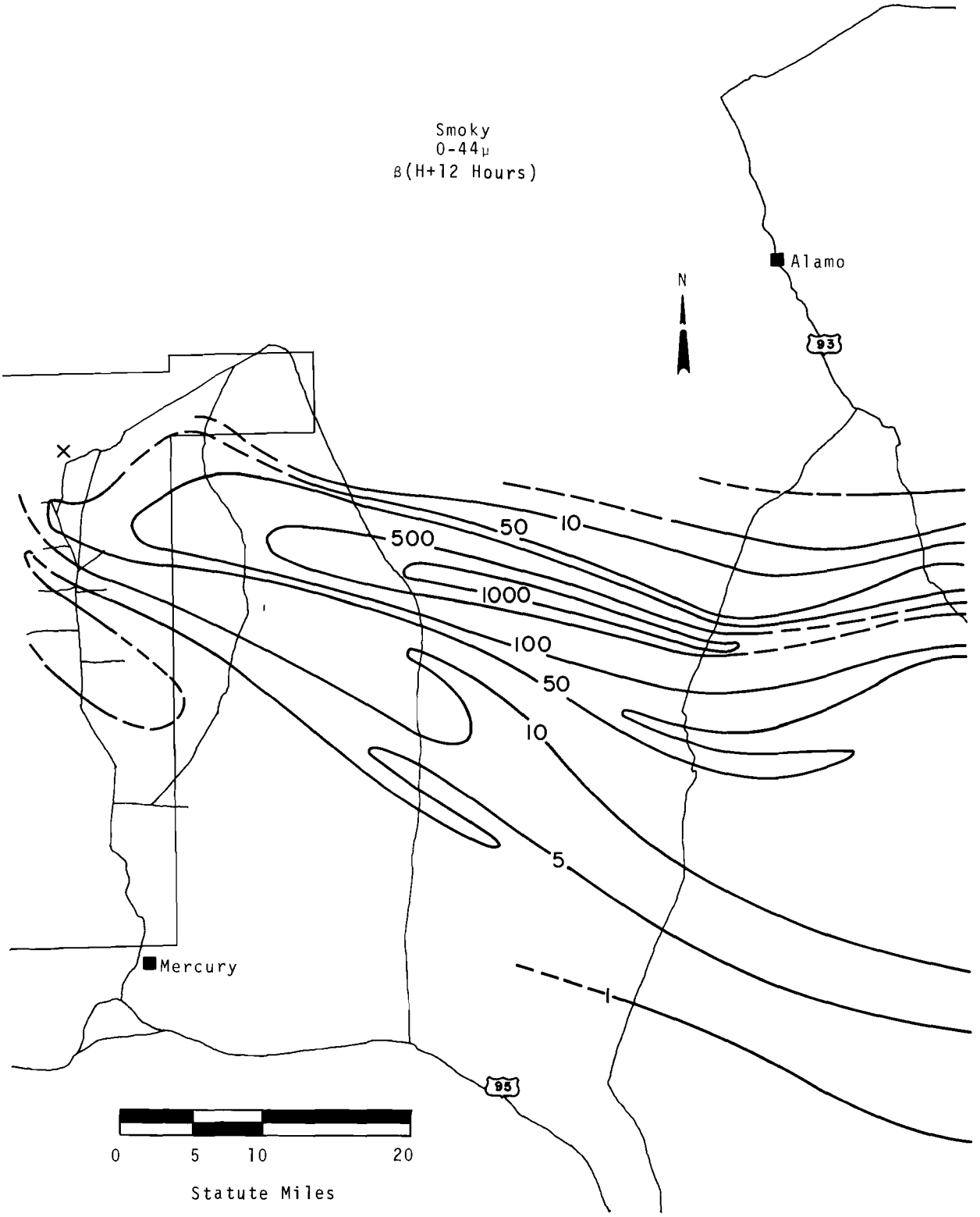

FIGURE 6. Smoky Fallout Pattern for <44 μ Diameter Particle. β(μc/ft²) at H + 12 hr

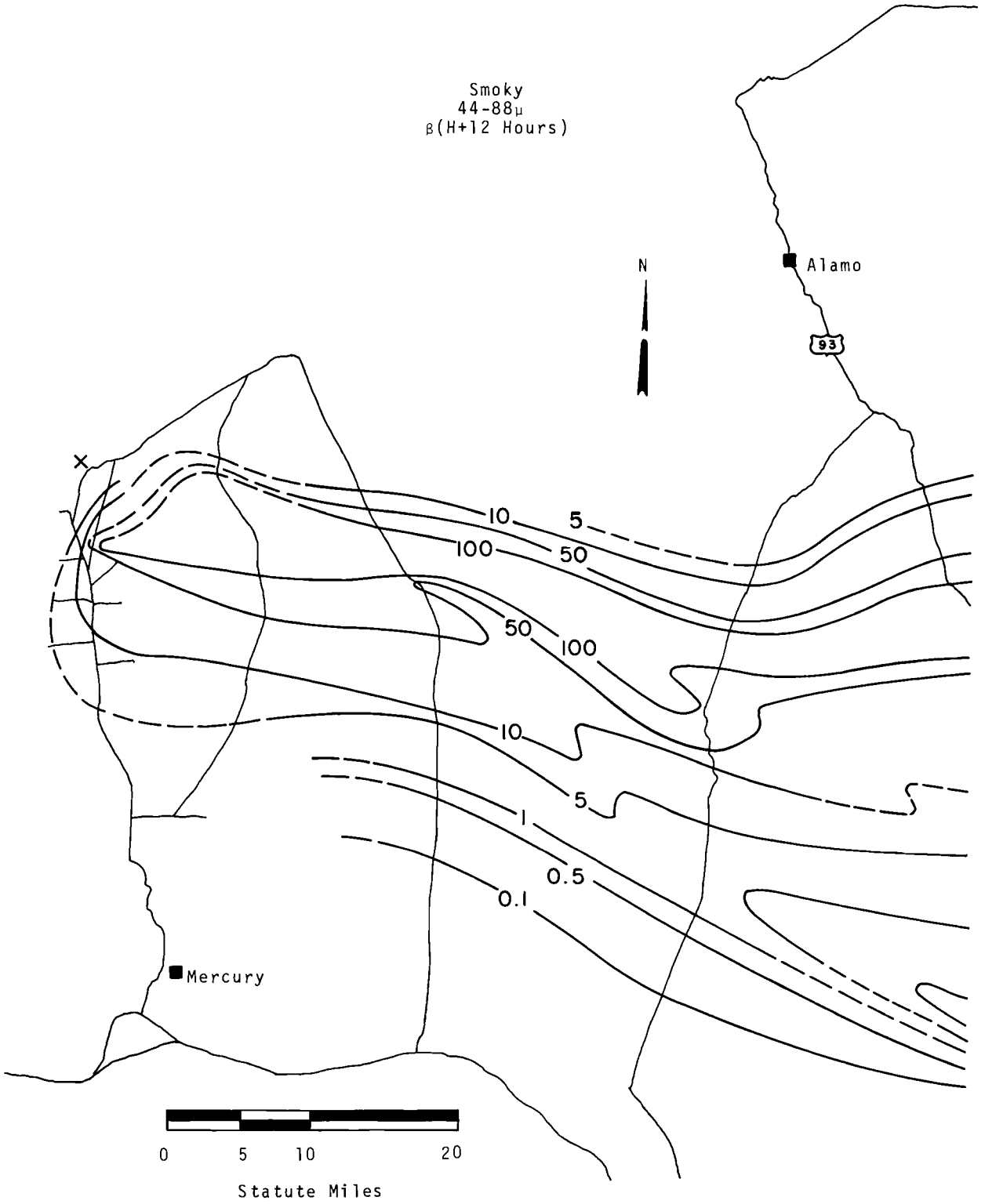

FIGURE 7. Smoky Fallout Pattern for 44 μ to 88 μ Diameter Particle. β(μc/ft²) at H + 12 hr

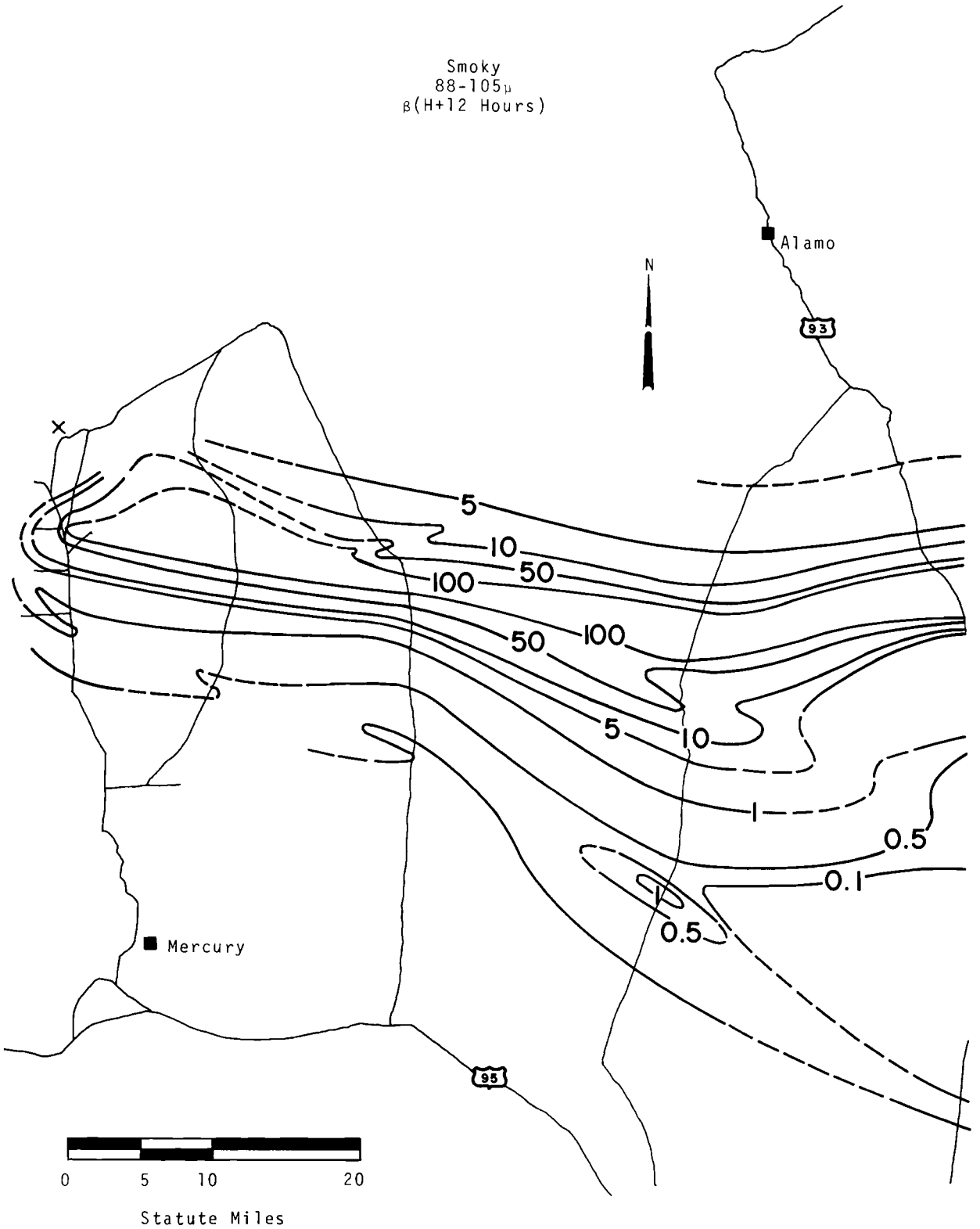

FIGURE 8. Smoky Fallout Pattern for 88 μ to 105 μ Diameter Particle. β(μc/ft²) at H + 12 hr

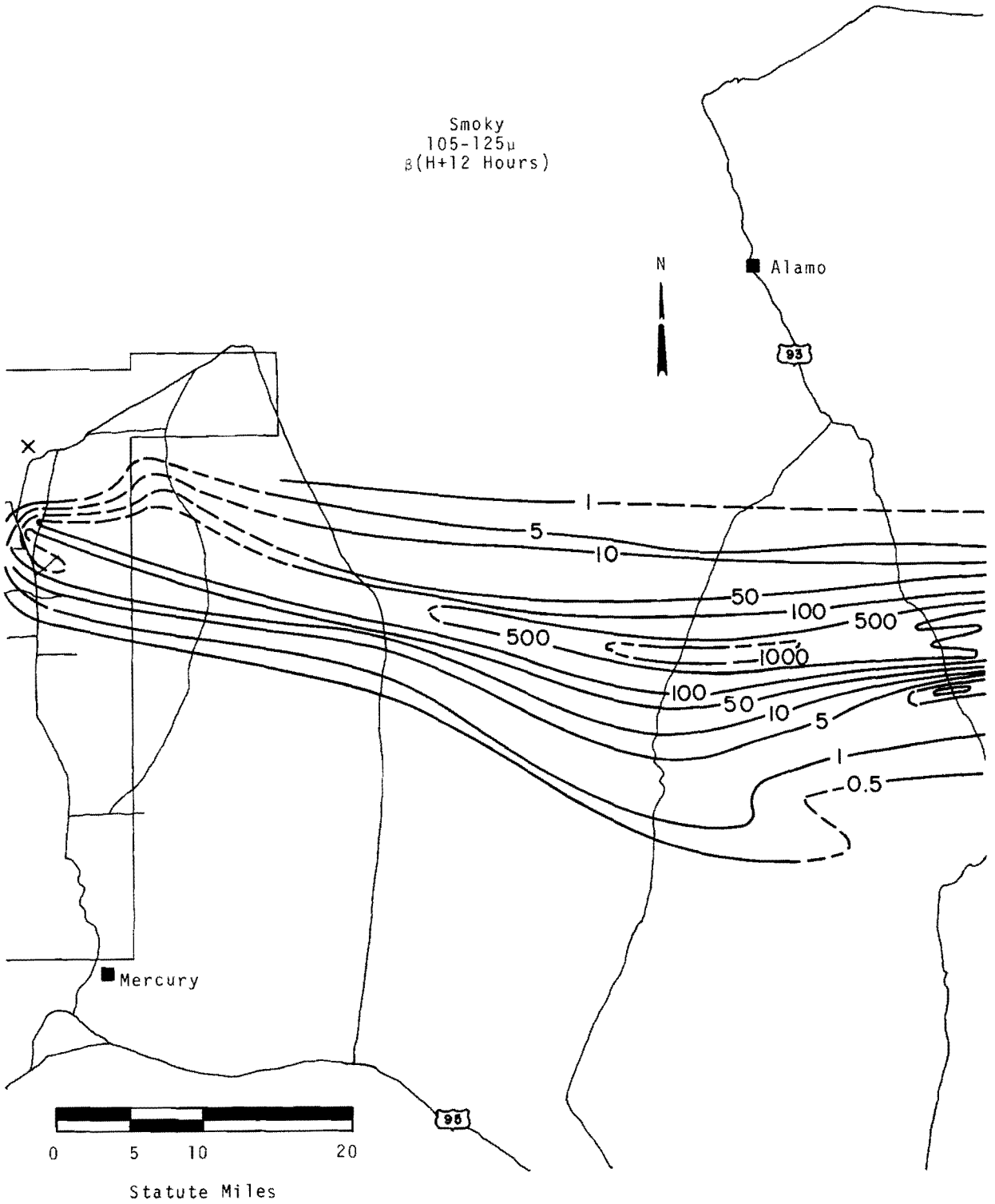

FIGURE 9. Smoky Fallout Pattern for 105 μ to 125 μ Diameter Particle. β(μc/ft²) at H + 12 hr

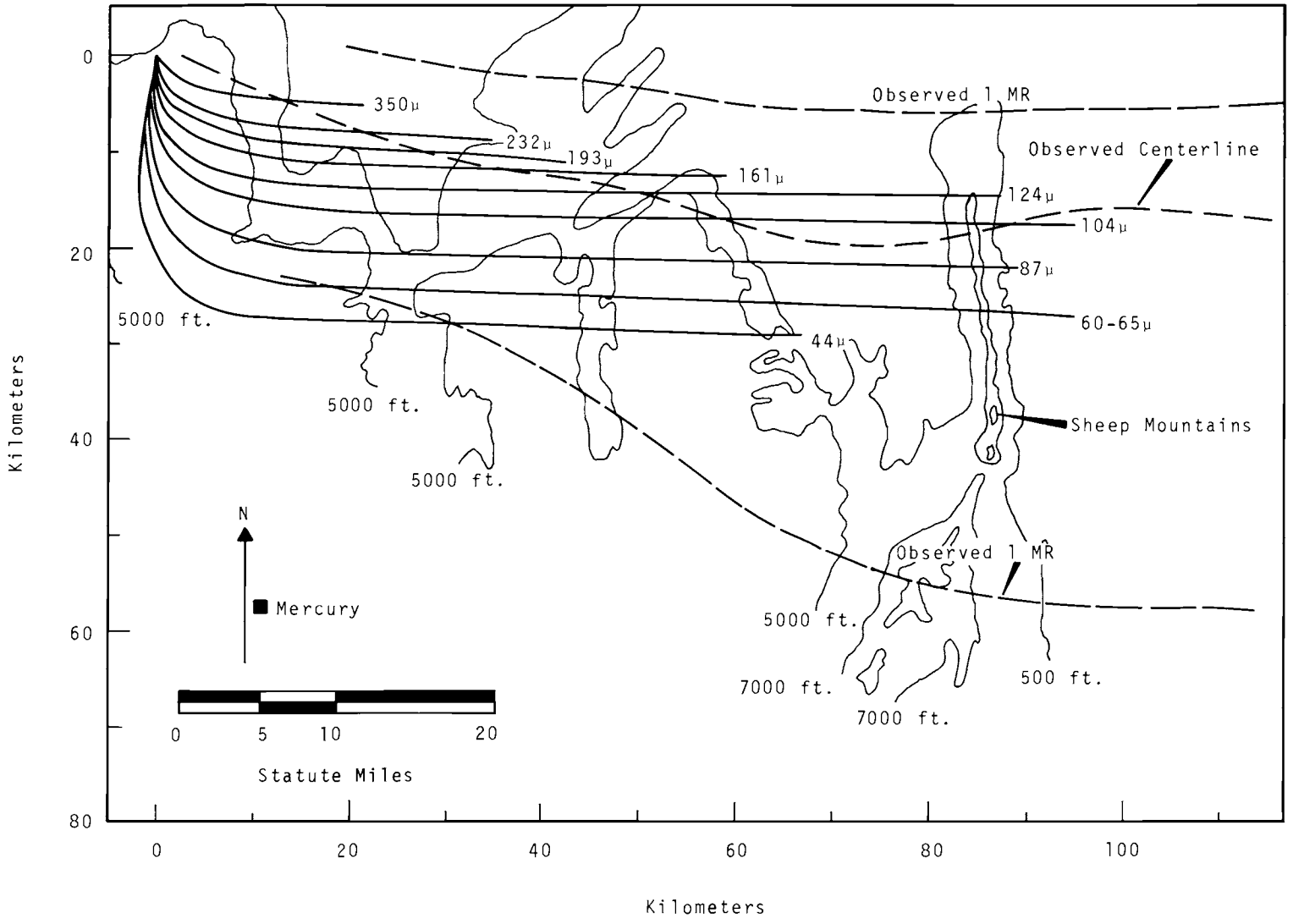

FIGURE 10. Deposition Centerlines for Shot Smoky for 44 μ to 350 μ Diameter Particles as Predicted by Manual and DELFIC Calculations

<44 μ and 44-88 μ particle fractions is that the smaller particles were induced to fall faster than the predicted rate by a scavenging mechanism associated in some manner with the larger (100 μ to 350 μ) inert particles. Proof of this hypothesis will require more theoretical or experimental work.

CONCLUSIONS

The Shot Smoky research accomplished this year produced the following results:

- Demonstration that a correlation of isentropic trajectories of the nuclear debris cloud with meteorological observations of precipitation could explain measured high values in the surface deposition patterns near Rock Springs, Wyoming.[3]
- Further demonstrations that the isentropic trajectory technique can predict cloud travel in space and time. Examples of verification of the cloud trajectory as derived from observations made by meteorological data gathering stations were presented.
- The DELFIC fallout computational model[2] was used to compute the close in (<200 km) deposition patterns for Shot Smoky. The centerline of deposition agreed to within 5 km out to a distance of 170 km. Time of arrival agreed out to H + 3 hr and the model predicted a low deposition value where a low was observed over Sheep Mountain, Nevada.

REFERENCES

1. *W. E. Davis and R. J. Engelmann. "Selected Meteorological Analysis of Plumbbob Nuclear Tests," Pacific Northwest Laboratory Annual Report for 1966 to the USAEC, Division of Biology and Medicine, Volume II: Physical Sciences, BNWL 481-1, pp. 68-73. Pacific Northwest Laboratory, Richland, Washington, 1967.*

2. *Department of Defense Land Fallout Prediction System, AD-483897; DASA-1800, vol. 1-7. Defense Atomic Support Agency, Washington, D.C., June, 1966.*

3. *K. H. Larson, J. W. Neel, H. A. Hawthorne, H. M. Mark, R. H. Rowland, L. Baurmash, R. G. Lindberg, J. H. Olafson, and D. W. Kowalewsky. Distribution, Characteristics, and Biotic Availability of Fallout, Operation Plumbbob, WT-1488. University of California, Los Angeles, California, 1966.*

4. *K. H. Larson. Unpublished Data. May 1968. (Personal Communication)*

5. *K. H. Larson. Unpublished Data. Laboratory of Nuclear Medicine and Radiation Biology, The University of California at Los Angeles.*

PARTICLE DEPOSITION WITHIN A CURVED SAMPLING PROBE

G. A. Sehmel and L. C. Schwendiman

Particle deposition was measured in 4.7 to 5.8-in. lengths of 0.135 to 0.40 in. ID tubing formed on a 4.4 in. radius of curvature. For a constant sampling velocity, the deposition increased with an increase in particle size and a decrease in tubing ID. For a constant tube ID, deposition increased with both flow rate and particle size until re-entrainment became important. For transition flow between laminar and turbulent, the deposition was minimum for an intermediate Reynolds number for any constant particle size for which re-entrainment was not important. The deposition was significant for all flow rates and must be considered in interpreting the data for any sample passed through a curved tube in either laminar or turbulent flow.

Airborne particle samples must often be collected under conditions in which the filter collector medium cannot be placed directly in the air stream. Hence, the sampled air must reach the collection medium through a passageway which may include divergent nozzles used for obtaining isokinetic flow, long straight conduits used for remote sampling, and also curved conduits. These various passageways provide surfaces affording particle deposition opportunities. Deposition data for a curved conduit have been obtained for the case in which the curved conduit is a short probe through which sample air is withdrawn from a duct. Neglect of the deposition within a curved probe can compromise the accuracy of any collected sample.

The importance of deposition in a curved sampling probe was established during experiments concerning isokinetic and anisokinetic sampling. In that study, monodispersed aerosol particles from the spinning disc aerosol generator were passed upwards through a 2.81-in. ID vertical tube serving as a wind tunnel. The air was sampled from the tube center through curved lengths of cylindrical probes. The probe inlets were tapered to knife edges at the inside surfaces to obtain a low air turbulence at the inlet. The probes, from 4.7 to 5.8 in. long and bent on a 4.4 in. radius of curvature, resulted in an elbow with an arc of about 62 degrees. Filter holders were connected to the probe outlets.

The deposition data are reported in Figures 1 through 3, as the fraction of material entering the probe inlet and deposited in the 4.7 to 5.8-in. long probes. The deposition is shown as a function of particle diameter with Reynolds number as a parameter. The Reynolds numbers were calculated on the basis of the average flow rate in the probe. Although only average velocities are considered, the complex flows in curved tubes must be considered in any attempt to correlate these deposition data.

In Figure 1 is shown the deposition in a 0.402 in. ID probe for laminar and turbulent flow conditions. The deposition for a Reynolds

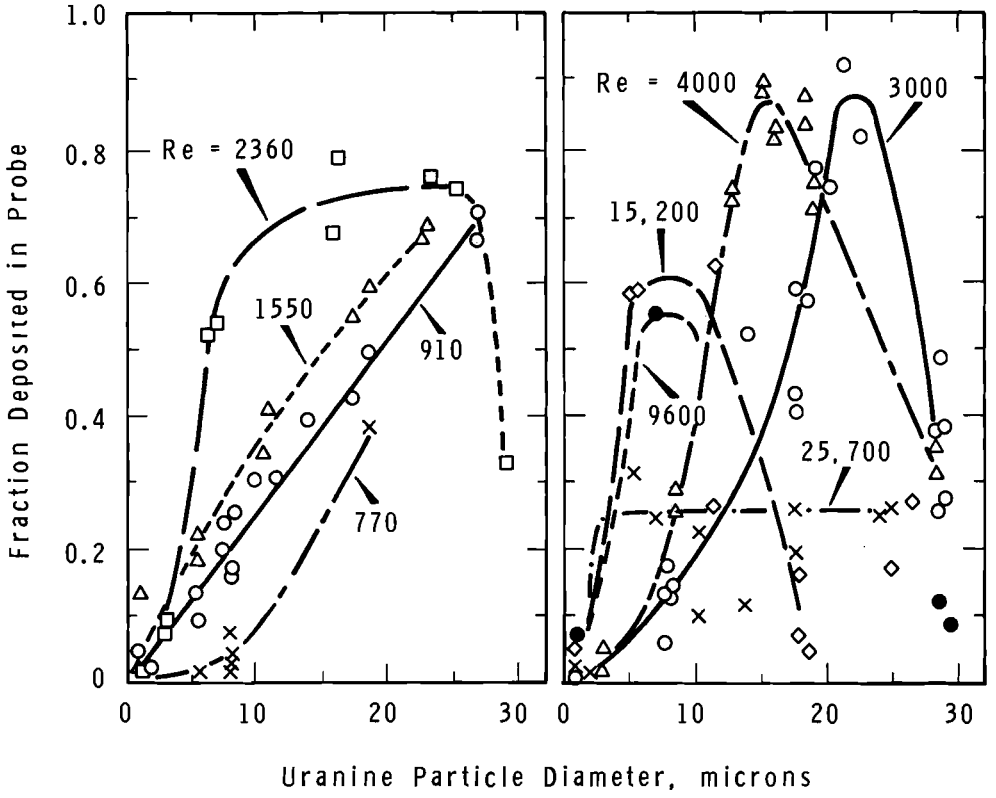

Neg. 0674029-1

FIGURE 1. Deposition Within a 4.7 in. Long Curved Sampling Probe

number of 4000 has not been previously reported and is seen to be consistent with the other data.

The deposition for laminar flow is shown on the left side of Figure 1. The simplifying assumption is made that laminar flow can be described by Reynolds number criteria based on average flow. The deposition is seen to be a complex function of flow rate and particle size. Nevertheless, the generalization is made that deposition is significant and increases rapidly with particle size. The maximum observed deposition is about 75% for a Reynolds number of 2360. For this Reynolds number, re-entrainment becomes significant above about 25 μ and, hence, the deposition decreases for larger sized particles.

On the right side of Figure 1, the deposition for turbulent flow based on average flow rates is shown. As for laminar flow, the data show that deposition increases with flow rate and particle size up to a particle size of about 3 to 4 μ. Above this particle size range, particle re-entrainment for a Reynolds number of 25,700 causes the deposition to remain constant

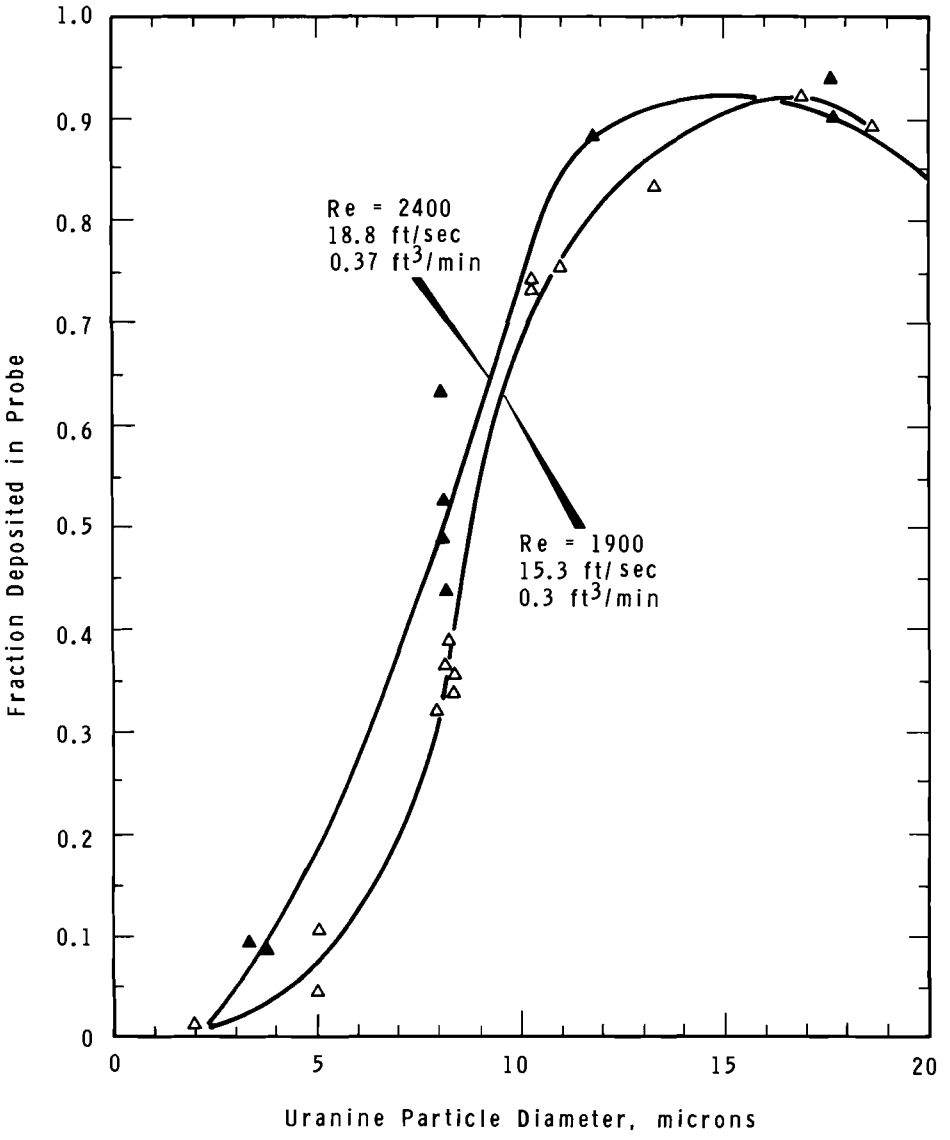

Neg. 0681315-1

FIGURE 2. Deposition Within a 5.8 in. Long Curved Sampling Probe

or to decrease. The deposition continues to increase with particle size and as lower Reynolds numbers are increased until re-entrainment occurs for each Reynolds number. The particle sizes for which re-entrainment is important are indicated by the maxima in the curves. Beyond the maxima, the nonreproducibility of the data is interpreted to mean that the particle accommodation to the probe surface appears to be important.

Deposition has also been measured in smaller diameter tubes. The radius of curvature has been

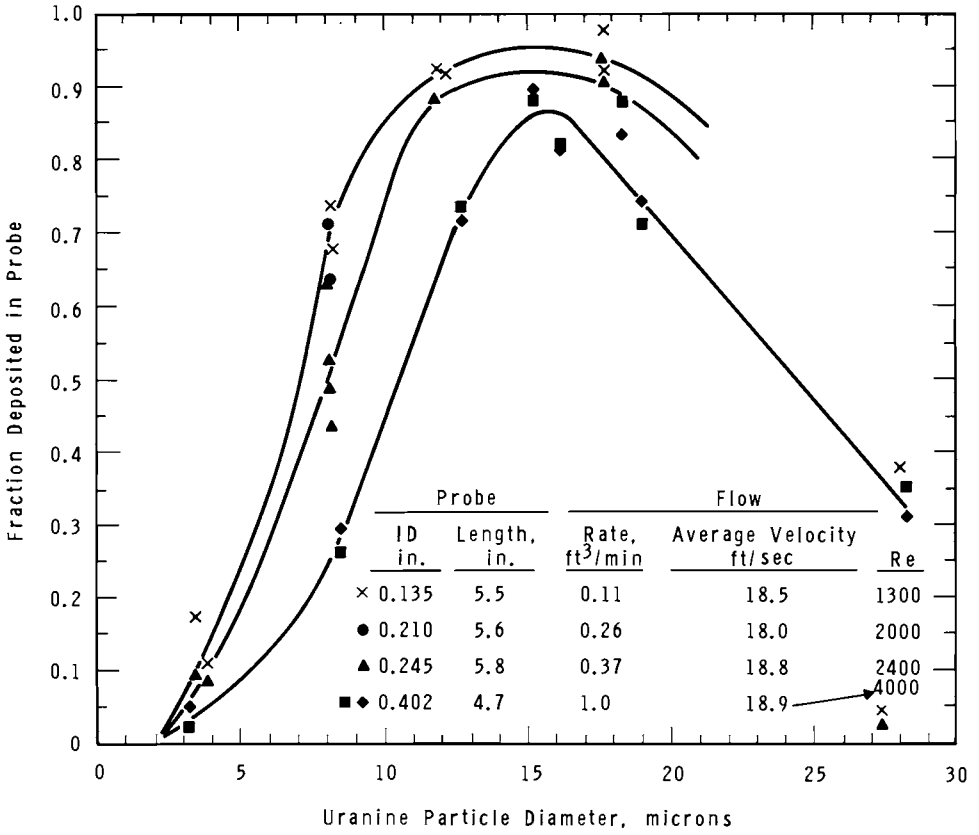

Neg. 0681315-2

FIGURE 3. Deposition Within Curved Sampling Probes at a Constant Velocity of 18 ft/sec

held constant, but the total tube lengths show some variation.

In Figure 2, the deposition is shown for a 0.245 in. ID probe for two flow rates. The deposition is seen to increase for an increase in Reynolds numbers from 1900 to 2400.

In Figure 3, the deposition is shown for a constant velocity as a function of probe diameter. The deposition increases with a decrease in probe diameter or Reynolds number.

From these figures the following conclusions are drawn:

- Deposition may be significant in tube bends for either laminar or turbulent flow.
- For a constant tube diameter, deposition increases with Reynolds number in either laminar flow or turbulent flow.
- For transition between laminar and turbulent, the mechanisms of deposition must change since deposition can be higher for a lower Reynolds number.
- For a constant flow velocity, deposition increases with a decrease in probe diameter.

Since these data have not been correlated, the direct application to comparable Reynolds numbers for other probe sizes or elbows is probably unwarranted. However, the neglect of deposition in any curved probe or elbow can be the source of significant errors in the interpretation of any collected sample. The data show that in contrast to deposition in a straight tube, the deposition in a curved probe is significant for both laminar and turbulent flow.

THE EFFECT OF SAMPLING PROBE DIAMETER ON SAMPLING ACCURACY

G. A. Sehmel and L. C. Schwendiman

Isokinetic sampling of particles from an air stream is regarded as essential for greatest accuracy. Errors can, nevertheless, result from several sources even when the isokinetic condition is maintained. One such source is the size and shape of the sampling probe. A study was carried out in which uranine particles of a single size (1 to 28 μ diam) were isokinetically sampled through 0.135, 0.210, 0.245, and 0.402 in. ID probes whose inlets were located on the axis of a 2.81 in. ID vertical tube. Sampling velocities from 18.0 to 19.6 ft/sec were equal to the maximum centerline velocities of the sampled tube. The measured concentrations from the sampled air ranged from about 0.8 to 1.2 times the average concentrations in the sampled tube. The measured concentrations are a function of the probe diameter and also are affected by the preferentially enhanced concentration of large particles in the region next to the sampled tube wall.

THE EFFECT OF SAMPLING PROBE DIAMETER ON SAMPLING ACCURACY

Particles may be sampled from an air stream to determine the airborne particle concentration, the size distribution, or the composition. Isokinetic sampling, accepted as an important sampling requirement, is obtained only when the sample is withdrawn without disturbing the initial air motion or streamlines in the moving air. Isokinetic sampling requires the sampling entry probe or collector to face into the air flow, the sampling rate to equal the rate of air approaching into the projected area of the sampler, and the sample inlet probe to be streamlined to minimize entry effects. For turbulent flow in the conduit, the tacit assumption is made that isokinetic conditions prevail when the probe entry velocity is the same as the average air velocity, since an average constant sampling velocity cannot match the instantaneous random velocity impulses due to turbulence. The

significance of this simplifying assumption has not been investigated. Other simplifying assumptions generally made are that particle electrical charge effects and sample probe diameter effects are negligible.

The purpose of this study is to determine isokinetic sampling errors as a function of sampling probe diameter for a particular conduit and probe geometry.

The sampling probes were axially located within a 2.81 in. ID vertical tube. The probes were aluminum tubes with ID of 0.135, 0.210, 0.245, and 0.402 inch. The walls of the probe inlet were tapered for about 1/8 in. to sharp-edged inlets. The probes were formed on a 4.4 in. radius of curvature and were passed through and welded to 2 x 2 1/2 in. saddles conforming to the outside diameter of the larger tube to be sampled. Dimensions were such that clamping of the saddles to the larger tube centered the probe reproducibly on the tube axis.

Isokinetic sampling errors were determined using single-sized uranine particles produced with a spinning disc aerosol generator. The particles passed from the generator into a 7 ft^3 aerosol holding chamber and thence into the entrance of a 2.81 in. ID vertical tube, from which the sample was withdrawn. One sample probe was inserted at 15 ft and a second at 28 ft from the tube entrance--distances adequate for avoiding entrance effects. Aligned butt joints in the 2.81 in. ID tubing occurred at both levels of the sample probe inlets. The joints, however, were smooth and inconsequential for the purpose of this study.

Particle mass balances were made to determine the sample concentration and the average concentration to be sampled. The average concentration was determined from the total material entering the sample probes, the particles depositing on the tube walls, and the particles collecting on a glass fiber filter 5 ft downstream from the second sample probe. After the air was sampled for a period, a mass balance of uranine was made starting at the inlet level of each probe. This mass balance was obtained by dissolving the uranine on the tube surfaces and filter in water and measuring the fluorescence of the solutions with a calibrated fluorimeter. For each probe used, the masses determined were the total N_B by-passing the probe and N_S entering the probe. Thus the total mass approaching a probe was $N_T = N_B + N_S$.

The true average air concentration, C_O, of particles passing through the tube and the air concentration, C, of the sample collected by the probe can be determined from these masses of uranine and the flow rates. The average tube concentration is

$$C_O = \frac{N_T}{U_T t}, \qquad (1)$$

where U_T is the total flow rate through the tube and probe, and t is the time for the duration of the experiment. Similarly, the calculated concentration, C, from the sample is

$$C = \frac{N_S}{U_S t}, \qquad (2)$$

where U_S is the flow rate through the sample probe. From the above two equations, the concentration ratio is

$$\frac{C}{C_0} = \frac{N_S}{N_T} \frac{U_T}{U_S} \quad . \qquad (3)$$

In turbulent flow, the average velocity increases from about 0.8 to 0.9[1] of the maximum flow velocity for the Reynolds numbers of interest. Consideration of these velocity profiles indicates that a true isokinetic flow rate for turbulent flow when the sample is taken near the tube axis would be 1.1 to 1.3 times that indicated by the average flow in the tube.

Isokinetic sample rates, U_0, based upon the maximum tube velocity, were studied for an average velocity of 18.0-19.6 ft/sec. In Figure 1 are shown concentration ratios as a function of particle size for each probe diameter studied. The concentration ratios are near unity and range from about 0.8 to 1.2. In general, for particle diameters less than 15 μ, concentration ratios are higher for the smaller diameter probe.

The concentration ratios range from 0.78 to 0.85 for 28 μ particles. This decrease in concentration ratio below unity can be attributed to the effects of particle concentration profiles[2] across the sampled tube. For 28 μ particles at these flow conditions, the particle concentration is greater near the sampled tube wall than at the tube axis. As a result of this concentration difference, fewer particles are collected in the sample probe than in a uniform concentration. In the definition of C_0, the concentration was assumed to be uniform. Consequently, when C is divided by C_0, the ratio is less than unity.

The apparent anomaly of isokinetic samples as much as 20% higher than the average concentration has not been satisfactorily explained. The effect is greater than could be attributed to experimental errors in setting flow rates and in determining particle mass balances. The effect may be caused by changes in air flow velocities and air turbulence resulting from the presence of the sample probe in the 2.81 in. ID tube. The effect is more pronounced for smaller diameter probes and yet is also apparent for the 0.402 in. diameter probe.

REFERENCES

1. *R. H. Perry, C. H. Chilton, and S. D. Kirkpatrick. "Fluid and Particle Mechanics," Chemical Engineer's Handbook, Fourth Edition, pp. 5-8. McGraw-Hill Book Company, New York, N.Y., 1963.*

2. *G. A. Sehmel. Particle Sampling Bias Introduced by Anisokinetic Sampling and Deposition Within the Sampling Line, BNWL-SA-1795. Pacific Northwest Laboratory, Richland, Washington. April 1968.*

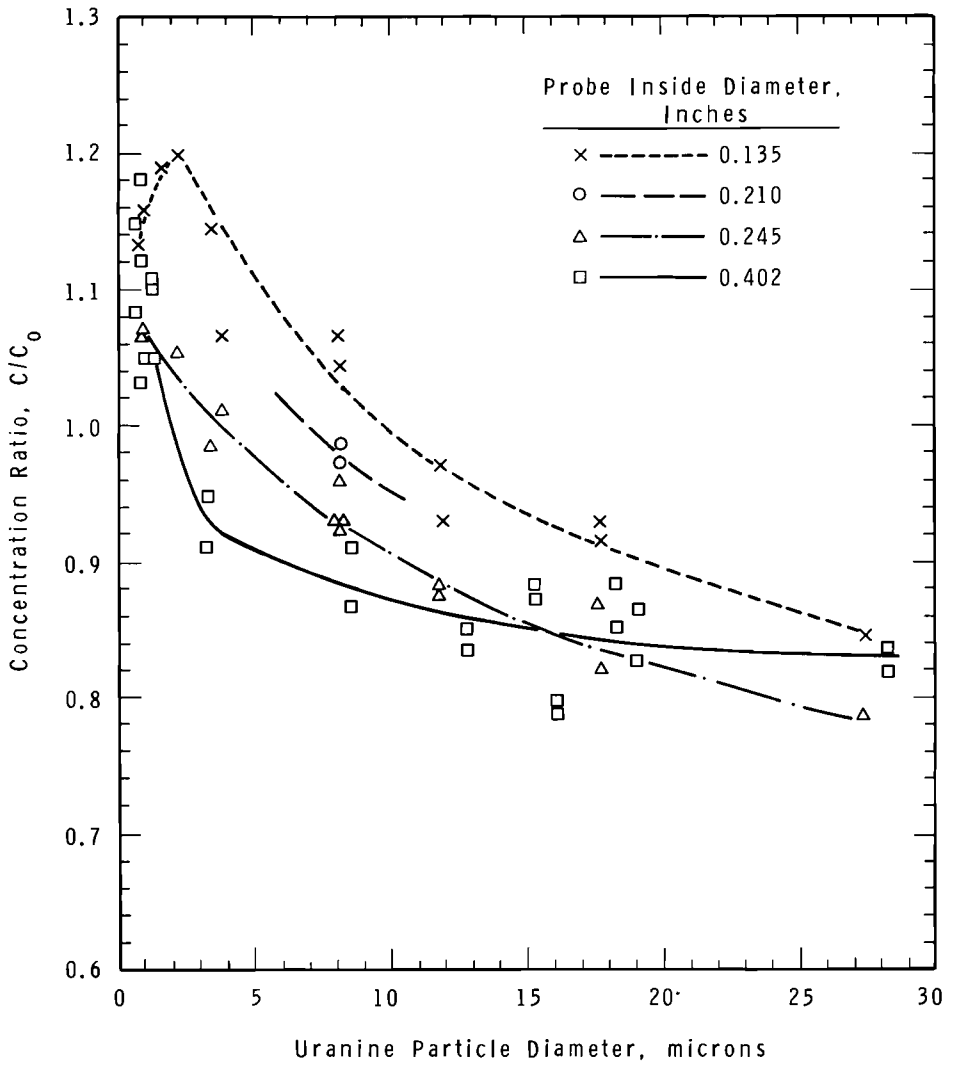

Neg. 0674029-5

FIGURE 1. Effect of Probe Diameter on Concentration Ratios for Isokinetic Flow Based on Maximum Flow Velocity

PARTICLE COLLECTION EFFICIENCIES ON WIRES

G. A. Sehmel and L. C. Schwendiman

Collection efficiencies of monodispersed 4 to 27 μ uranine particles were determined for 0.020 in. diam wires for an air velocity of 18.6 ft/sec. The wires were covered with a thin layer of petroleum jelly. Collection efficiencies decreased as the projected wire area covered by particles increased above about 1%. This decrease has not been previously reported and may explain some of the scatter in literature values of impaction efficiencies.

PARTICLE COLLECTION EFFICIENCIES ON WIRES

Several investigators have studied theoretically[1-4] and experimentally[5-16] the impaction efficiency of particles on cylindrical wires. While general agreement is shown in these studies, the experimental data show a significant scatter between investigations.

Conceivably, fine wires could serve as particle samplers near surfaces or in other situations demanding small disturbances of the sampled air. Good sensitivity, adequate reproducibility, and accuracy would have to be shown before impaction on wires could be qualified as an acceptable sampling method.

The purposes of the present study were to determine experimentally the precision obtainable for collection efficiencies and to determine the best correlation for these efficiencies.

Impaction efficiencies were experimentally determined by spacing three 0.020 in. diam wires at 0.5 in. intervals within a joint between two sections of 2.81 in. ID vertical tubing. One inch downstream from the wires was placed a filter within a slip joint in the tubing. Monodispersed uranine particles were passed vertically upward through the tube. The particles were carried in a turbulent air flow of 38.4 cfm (Re = 21,000) corresponding to a maximum air velocity of 18.6 ft/sec. Some particles impact on the wires, and the remaining particles were collected on the filter. After particle collection, the filter was cut into concentric annuli and washed with water to dissolve the uranine. Also, the central 1 in. length of each wire was cut off and washed to dissolve the impacted uranine particles. The wash solutions were analyzed fluorimetrically for uranine and the results used to calculate a particle mass balance.

The flux (mass/area) of particles approaching the central 1 in. length of each wire was calculated from the mass balance. The flux was determined from the sum of the uranine on the filter annulus above the wire and the uranine on the wire.

The impaction efficiency was defined as the ratio of the average amount of uranine collected on the wire per unit projected wire area

divided by the particle flux. The impaction efficiency was found to be affected by the type of wire surface.

The wires were coated with melted petroleum jelly to form a smooth tacky surface. The average diameter of the wire with the tacky surface is used since particles as small as 4 μ diameter (smallest used) are not as effectively collected on untreated wires. For an untreated wire, the collection efficiency, ε, for 6 μ particles was 21.8%, while ε for the tacky wire was 33.2 - 33.5%.

The length of an experimental run has been found to affect the observed collection efficiencies on the tacky surfaced wires. However, the effect is not associated with either thinning of the tacky surface or re-entrainment of previously deposited particles. This independency was established by putting one wire in the particle free air stream for 20 min before introducing particles, and by leaving one wire in a particle-free air stream for 20 min following the impaction experiment. The comparisons are:

Particle Diameter, μ	Collection Efficiency, % 20 min Treatment	Standard Procedure
14	80.0 (post)	80.5 - 82.5
26	90.5 (pre)	92.0 - 93.0

No significant difference exists.

The collection efficiency is related to the fraction of collector surface area covered by particles. Fractional coverage was calculated as the ratio of the projected area of all the particles on the wire to the projected area of the wire.

Collection efficiencies are shown in Figure 1 as a function of the fraction of the projected wire area covered by particles. The impaction efficiencies are seen to decrease as the coverages increase above about one percent. For very high coverages, collection efficiencies might be expected to decrease due to the change in air flow caused by the presence of the impacted particles. However, the observed dependency of impaction efficiency has not been previously suggested for such observed low coverages.

Impaction efficiencies are usually correlated as a function of the Stokes number,

$$Stk = S/D$$

where D is the wire diameter and S is the stopping distance. The stopping distance is calculated from the expression

$$S = \frac{\rho\, d^2\, v}{18\mu}$$

where

ρ = particle density
d = particle diameter
v = air velocity at tube axis
μ = air viscosity.

The smoothed curves representing the impaction data in Figure 1 are shown in Figure 2 as a function of the Stokes number. For any Stokes number, the impaction efficiencies are seen to increase as the coverage decreases.

The present data are compared to literature[11] values of impaction efficiencies shown in the following

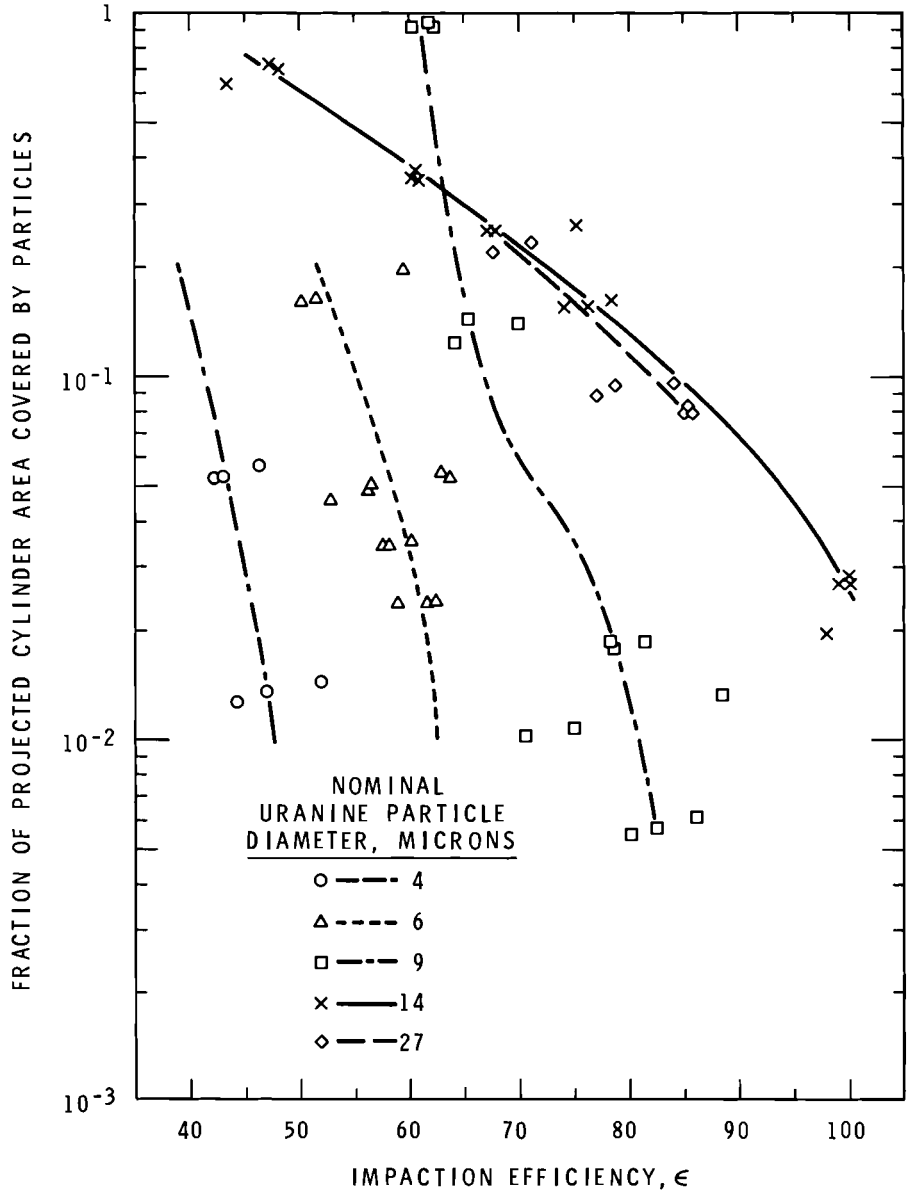

Neg. 0680346-1

FIGURE 1. Impaction Efficiencies for Cylinders as a Function of the Fractional Cylinder Area Covered by Particles at an Air Velocity of 18.6 ft/sec (Diameter Range of Petroleum Jelly Covered Cylinders is 0.020-0.021 in.)

tabulation. The ranges of data tend to overlap which suggests that the data are consistent and that the effect of coverage has been neglected in previously reported data.

The conclusions to date for this continuing study are that:

- Impaction efficiencies decrease as the wire coverage increases;

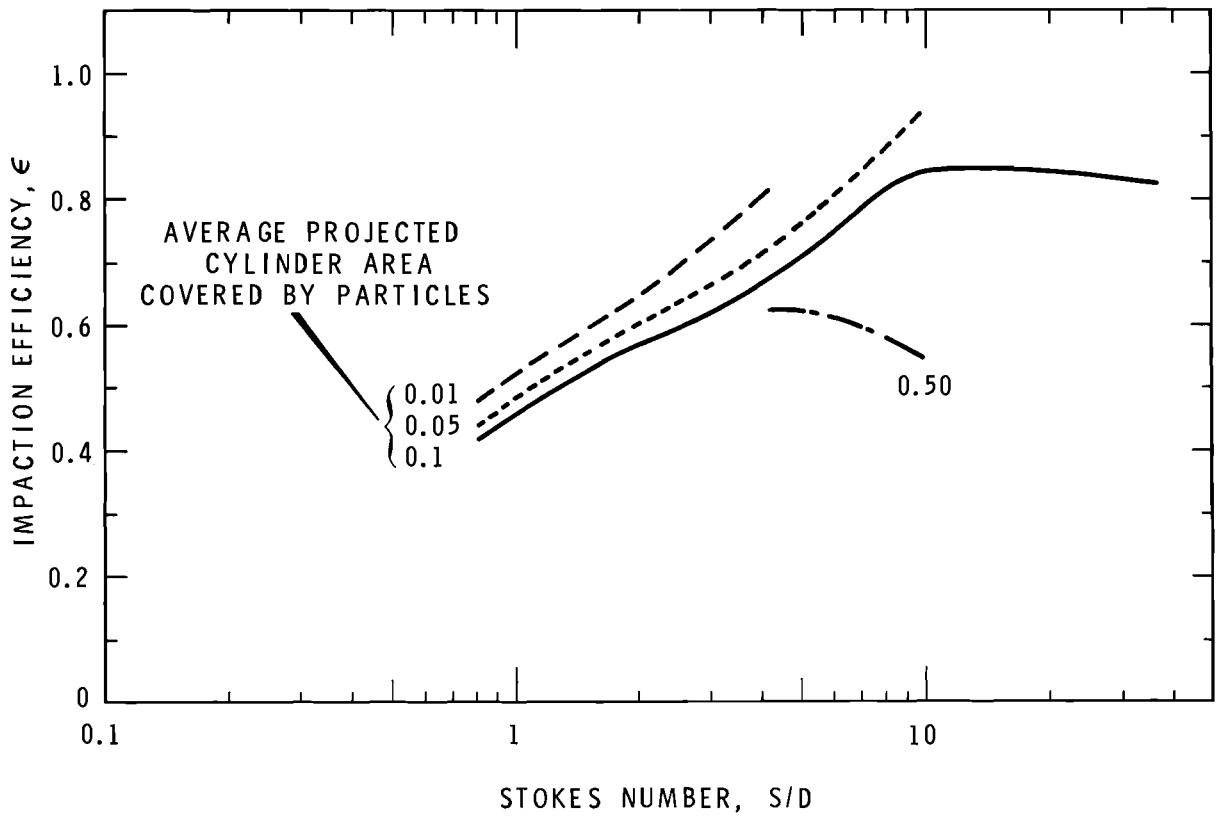

Neg. 0680346-3

FIGURE 2. Impaction Efficiencies for Cylinders as a Function of the Stokes Number and Fractional Cylinder Area Covered by Particles (Average Cylinder Diameter of Petroleum Jelly Covered Wires is 0.0205 in.)

- The impaction efficiencies are not simply correlated by the Stokes number;
- The literature values show a wide range of values which partially bracket the present experimental results; and
- The dependency of impaction efficiencies on wire coverage is a source of the scatter in literature correlations of impaction efficiencies.

A comparison of the impaction efficiencies follows:

Stokes Number S/D	Impaction Efficiency, % Range of Present Data	Literature Range of Data
1	47 - 54	40 - 57
3	62 - 73	63 - 81
6	61 - 80+	73 - 89

REFERENCES

1. *R. J. Brun, W. Lewis, P. J. Perkins, and J. S. Serafini. Impingement of Cloud Droplets on a Cylinder and Procedure for Measuring Liquid-Water Content and Droplet Sizes in Supercooled Clouds by Rotating Multicylinder Method, NACA 1215. Lewis Flight Propulsion Laboratory, Cleveland, Ohio. 1955.*

2. C. N. Davies and C. V. Peetz. "Impaction of Particles on a Traverse Cylinder," Proc. Roy. Soc., Ser. A., vol. 234, pp. 269-295. 1956.

3. I. Langmuir and K. B. Blodgett. A Mathematical Investigation of Water Droplet Trajectories, RL 225. General Electric Co., Research Laboratory, Schenectady, New York, July 1945.

4. G. Zebel. "Deposition of Aerosol Flowing Past a Cylindrical Fiber in a Uniform Electric Field," J. Colloid. Sci., vol. 20, pp. 552-543. 1965.

5. A. G. Amelin, M. I. Belyakov. "To the Problem of Particle Deposition from a Stream," Doklady Akad. Nauk. USSR, vol. 108, no. 1, pp. 31-33. 1956.

6. G. Asset and T. G. Hutchins. "Leeward Deposition of Particles on Cylinders from Moving Aerosols," Amer. Ind. Hyg. Assoc. J., vol. 28, pp. 348-353. July-August 1967.

7. A. C. Chamberlain. "Deposition of Particles to Natural Surfaces," Symposia of the Society for Microbiology, Number XVII, Airborne Microbes, pp. 138-164. 1967.

8. M. N. Golovin and A. A. Putnam. "Inertial Impaction on Single Elements," Ind. Eng. Chem. Fundamentals, vol. 1, no. 4, pp. 264-273. 1962.

9. P. H. Gregory. "Deposition of Airborne Lycopodium Spores on Cylinders," Ann. Appl. Biol., vol. 38, pp. 357-377. 1951.

10. H. D. Landahl and R. G. Herrmann. "Sampling of Liquid Aerosols by Wires, Cylinders, and Slides, and the Efficiency of Impaction of the Droplets," J. Colloid. Sci., vol. 4, pp. 103-136. 1949.

11. K. R. May and R. Clifford. "The Impaction of Aerosol Particles on Cylinders, Sphere, Ribbons, and Discs," Ann. Occup. Hyg., vol. 10, pp. 83-95. 1967.

12. W. E. Ranz and J. B. Wong. "Impaction of Dust and Smoke Particles," Ind. Eng. Chem., vol. 44, no. 6, pp. 1371-1381. 1952.

13. J. Rosinski and C. Nagamoto. "Particle Trajectories and Adherence to Cylindrical Sticky Surfaces," Kolloid-Zeitschrift, vol. 175, no. 1, pp. 29-33. 1961.

14. J. R. Starr. "Inertial Impaction of Particulates Upon Bodies of Simple Geometry," Ann. Occup. Hyg. vol. 10, pp. 349-361. 1967.

15. W. L. Torgeson. Investigation of Impaction Mechanisms of Particles on Collectors in Turbulent Flow, QPR-7 3057. Applied Science Division, Litton Systems, Inc., Minneapolis, Minnesota, 1967.

16. J. B. Wong, W. E. Ranz, and H. F. Johnston. "Inertial Impaction of Aerosol Particles on Cylinders," J. Appl. Phys., vol. 26, no. 2, pp. 244-294. 1955.

WIND TUNNEL FOR PARTICLE DEPOSITION MEASUREMENTS

G. A. Sehmel, L. C. Schwendiman and T. W. Horst

A wind tunnel was designed and installed for measuring particle deposition onto surfaces. The tunnel has a 2 x 2 ft cross section, with a test section 30 ft long.

The transport of airborne particles from the bulk carrying stream across boundary layers to a solid surface is a process of considerable theoretical and practical significance. A full understanding of the parameters controlling the deposition of fine particulate material on surfaces would permit calculation of particle depletion from an atmosphere moving over terrain, would allow estimates of particle losses to the wall of ducts and sampling lines, and would clarify the significance of rebounding and reentrainment of particles in a variety of situations.

Particle deposition has been characterized by a deposition velocity K, defined as the number of particles deposited per unit area per second per unit average concentration in the gas over the surface.

Models to predict deposition velocities have been based upon the assumption that particle concentration always decreases as a deposition surface is approached. This assumption would be expected to apply if particles were to diffuse down a concentration gradient. However, recent experimental data[1] show that concentration profiles in tubes are not always those predicted from diffusion theory. For deposition to dry surfaced tubes, the maximum concentration may be adjacent to the tube wall instead of at the tube center.

The purpose of this study is to determine the deposition behavior of particles on simulated larger scale surfaces in controlled laboratory experiments. The experimental relationships between deposition, particle concentration, profiles in the air, and turbulence of the carrying airstream will be investigated. A wind tunnel for these studies was designed and installed.

The wind tunnel is shown in Figure 1 with the significant features labeled. The tunnel is a single pass system, with both the entering and exiting air directed through filters. The tunnel shell is constructed of 1/8 in. steel. The air enters the wind tunnel through a 6 x 6 ft bank of high efficiency filters. Immediately downstream is a section for inserting screens and baffles for controlling air turbulence. The test aerosol is injected downstream of the screens. The tunnel is next contracted to a 2 x 2 ft cross section through a nozzle designed to reduce turbulence.

The test section is a 30 ft length of 2 x 2 ft cross section.

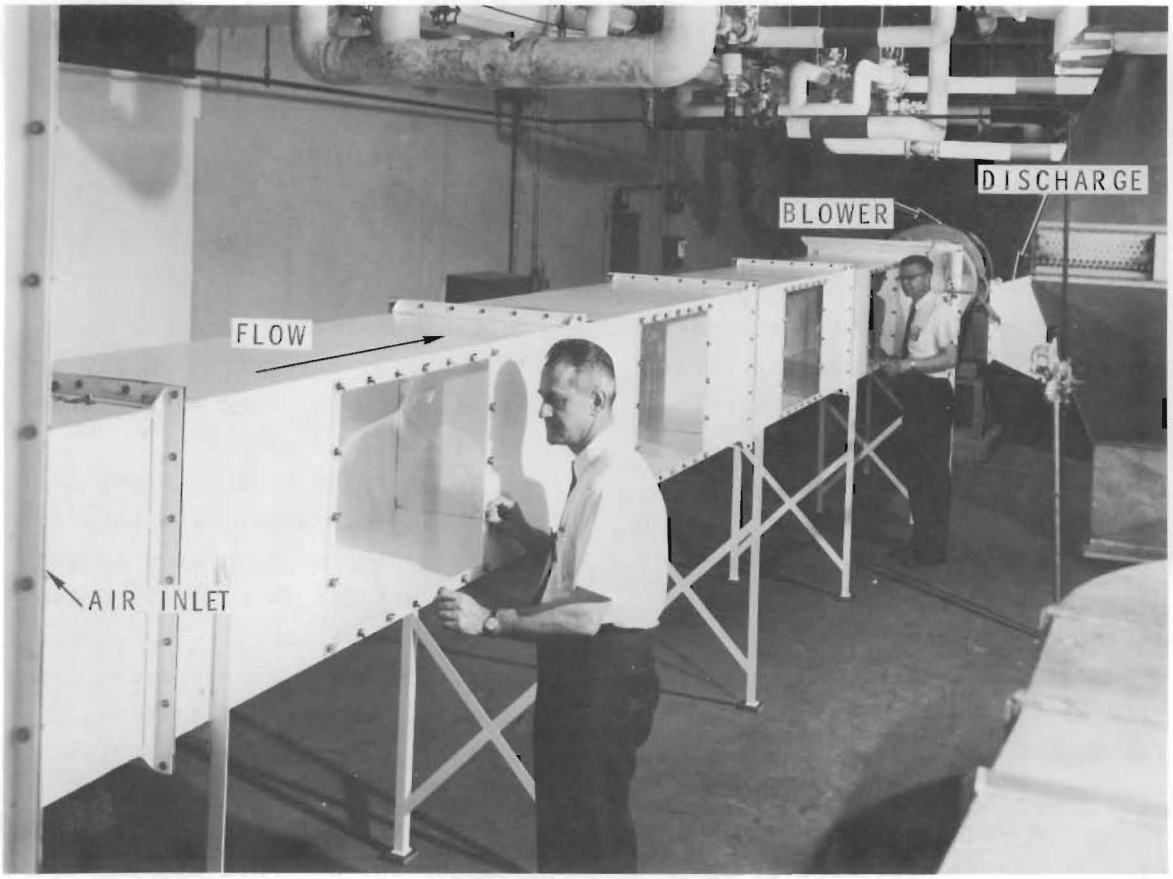

Neg. 0682228-10

FIGURE 1. Photograph of Wind Tunnel

Windows are provided (2 ft, 4 in. x 1 ft, 9 in.) to introduce the test specimens with various geometries.

Downstream is the blower which will pull air through the test section at a calculated maximum flow rate of 27 mph. The air leaving the blower is passed through high efficiency filters.

Particle deposition will be studied for various test surfaces, including flat surfaces at various orientations, rough surfaces typical of soil, water surfaces, and various types of vegetation. Concurrent with deposition, air turbulence will be measured using an X-array constant temperature anemometer system. The relating of deposition to turbulence is expected to permit better prediction of deposition over open terrain.

Deposition models are to be derived from the experimental data. To develop these models and to

check their accuracy, particle concentration profiles above the deposition surfaces will also be measured. These concentration gradients should be the greatest near the deposition surface. To measure these concentrations accurately, a particle sampler of small dimensions is required.[2]

Impaction on wires is one possible method under investigation to determine the concentrations.[3]

REFERENCES

1. G. A. Sehmel. "Particle Deposition Velocities and Particle Concentration Profiles above Deposition Surfaces," this report, p. 103.

2. G. A. Sehmel and L. C. Schwendiman. "The Effect of Sampling Probe Diameter on Sampling Accuracy," this report, p. 92.

3. G. A. Sehmel and L. C. Schwendiman. "Particle Collection Efficiencies on Wires," this report, p. 96.

PARTICLE DEPOSITION VELOCITIES AND PARTICLE CONCENTRATION PROFILES ABOVE THE DEPOSITION SURFACES

G. A. Sehmel and L. C. Schwendiman

Particle deposition was measured for turbulent flow in 1.152 in. ID aluminum tubes. Simultaneously, particle concentration was measured as a function of distance from the deposition surfaces. Since the concentration may be maximum near the tube surface, the deposition is a more complex function of the observed concentration profiles than could be ascribed to simple diffusion models. Measurements of concentration profiles with observed deposition are needed to understand more fully the mechanisms of particle deposition.

The transport of airborne particles from the bulk carrying stream across boundary layers to a solid surface is a process of considerable theoretical and practical significance. A full understanding of the parameters controlling the deposition of fine particulate material on surfaces would permit calculation of particle losses to the wall of ducts and sampling lines, and would clarify the significance of rebounding and re-entrainment of particles in a variety of situations. Since the particle under many circumstances becomes a tracer for the movement of the carrying air, a confirmation of concepts and theories regarding air turbulence and eddy diffusivity may accrue from studies of particle deposition.

Particle deposition[1] has been characterized by a deposition velocity, K, defined as the number of particles deposited per unit area per second per unit average concentration in the gas over the surface. Particles carried in an air stream through a conduit are deposited on the walls to a degree

depending upon the deposition velocity, tube length, diameter, the average velocity in the stream, the tube surface conditions, and perhaps other variables. The deposition velocity may be calculated from a simplified particle mass balance around a tube from the model,

$$\ln \frac{C}{C_o} = - 4 \frac{K}{V_{av}} \frac{L}{D}, \qquad (1)$$

in which C is the average concentration of particles in the air at a distance, L, downstream of the initial entering concentration, C_o; V_{av} is the average air velocity; and D is the tube inside diameter.

Models have been used to predict the deposition velocities for cases in which a tube surface is a perfect particle sink. In these models, the assumption has always been made that the concentration of particles is maximum in the turbulent core and that the concentration decreases as the tube wall is approached. The transport of particles to the tube wall has been explained in terms of the concentration gradient--particles go from a high concentration to a low concentration at a rate proportional to the particle diffusivity.

It is the purpose of this study to determine the quantitative relationships among the variables governing particle deposition during turbulent flow of air in conduits, and to establish deposition models supported by the data. The present experimental results are to show the observed deposition velocities as a function of particle concentration profiles above dry-walled tube surfaces.

Experimental data were obtained for deposition of monodispersed uranine particles in vertical tubes of 1.152 in. ID. Data were simultaneously obtained for deposition velocities and radial concentration profiles of particles within the tubes. The experimental technique was as follows.

Monodispersed uranine particles were generated with the spinning disc aerosol generator and passed upwards through the 1.152 in. ID aluminum tubes. A filter was located at a slip-fit joint in the tubing. A tight fitting wire screen within the joint served as a backing for the filter. The screen was cemented with silicone rubber to the tube wall. Care was taken to minimize protrusion of the silicone rubber inward from the tube wall. The filter was placed against the screen and then the tubes were pressed firmly together. The inner shoulder of the slip joint pressed against the filter which, in turn, pressed against the silicone rubber. The slip joint was sealed with tape to prevent inleakage. The seal was positive since the seal region was devoid of particles after an experiment.

Mass balances were made on the deposited uranine. The tubes and filter were washed to dissolve the deposited uranine. These solutions were subsequently analyzed fluorimetrically for uranine. After particle collection, each filter was simultaneously cut into concentric annuli for fluorimetric analysis to determine the filter loading of uranine. The filter loadings on

each annular section were normalized to the filter loading per unit area on the filter center section of 0.5 in. diameter.

Examples of the normalized filter loadings are shown plotted in Figure 1 for the 0.103-in. wide annulus next to the tube wall. The filter loadings are a function of both flow rate and particle size. To be emphasized is that this normalized loading can be greater than the loading at the filter center.

A normalized filter loading greater than unity is the result of a greater air-borne concentration of particles in the region adjacent

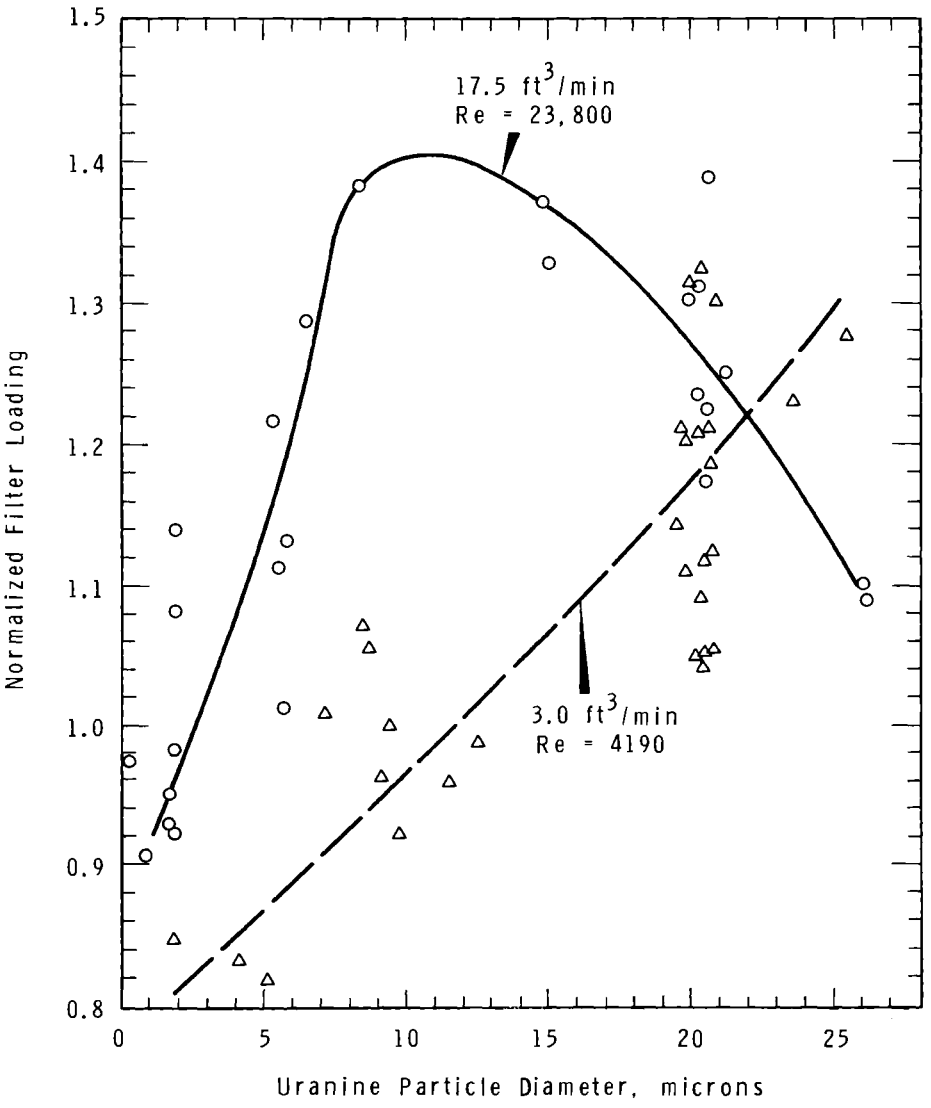

Neg. 0674029-2

FIGURE 1. Normalized Filter Loadings in a 0.103-in. Wide Annulus Adjacent to a 1.152-in. ID Tube Wall

to the tube wall. This high concentration has also been confirmed by isokinetic sampling studies. The high concentration is attributed to those particles re-entrained from the tube wall.

After re-entrainment, these particles may remain near the tube surface due to electrical space charge effects. The charges are acquired during re-entrainment. If the particles are all similarly charged, the charges will cause the particles to be forced toward the tube walls. The combined flux toward the wall, caused by both electrical effects and turbulent diffusion, is opposed by the flux caused by re-entrainment.

The deposition velocities shown in Figure 2 were calculated from the total observed deposition in

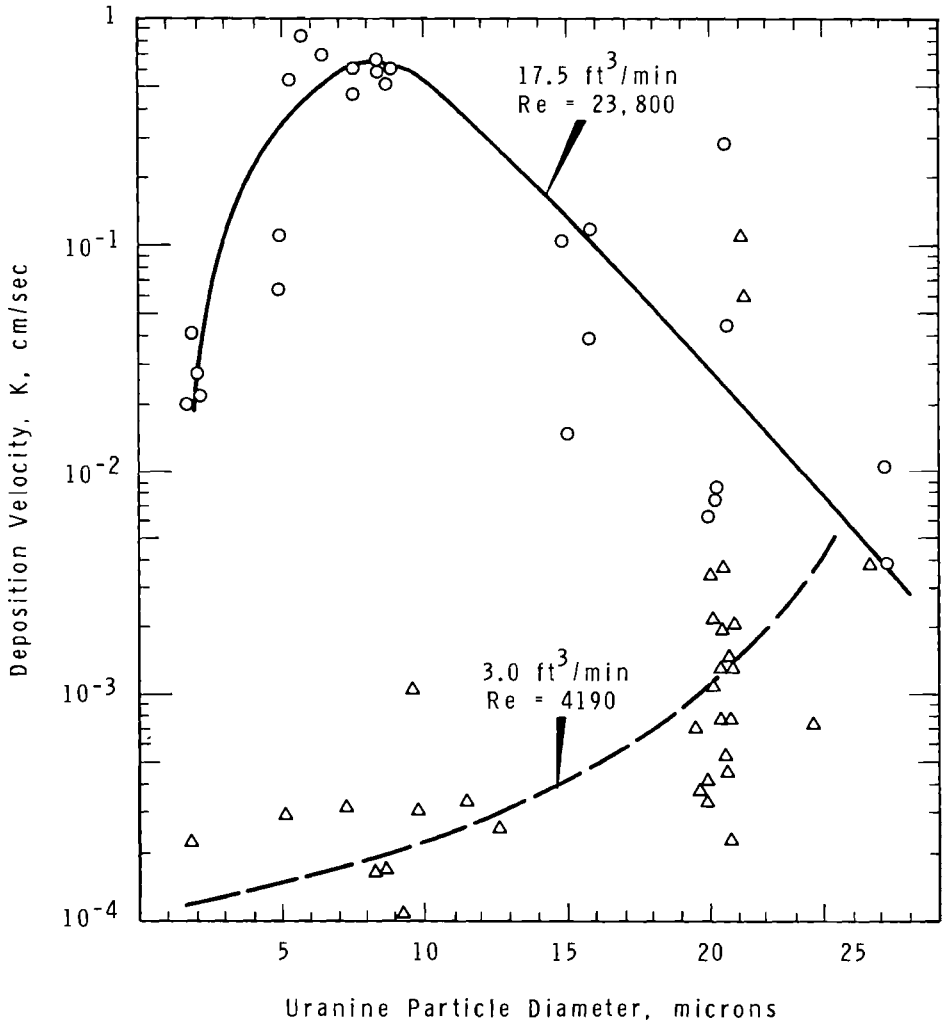

Neg. 0674029-3

FIGURE 2. Deposition as a Function of Particle Size for Particles in 1.152-in. ID Tubes

12-ft lengths of tubing and from the quantity of particles not depositing on the tube surfaces. Equation (1) was used for the calculation. For a Reynolds number of 4190, the deposition velocity for a Reynolds number of 23,800 shows a maximum at a particle size of 8 μ. The decrease in deposition velocities for larger sized particles is attributed to effective particle re-entrainment, defined as a decrease in deposition velocity caused by either an increase in particle size or an increase in turbulent flow rate.

The curves through the data shown in Figures 1 and 2 have been cross plotted in Figure 3 to show the dependency of the deposition velocity on the normalized filter loading in the annulus adjacent to the tube surface. In Figure 3, the particle size is shown as a parameter along each curve.

For a Reynolds number of 4190, the deposition velocity increases continuously with both particle

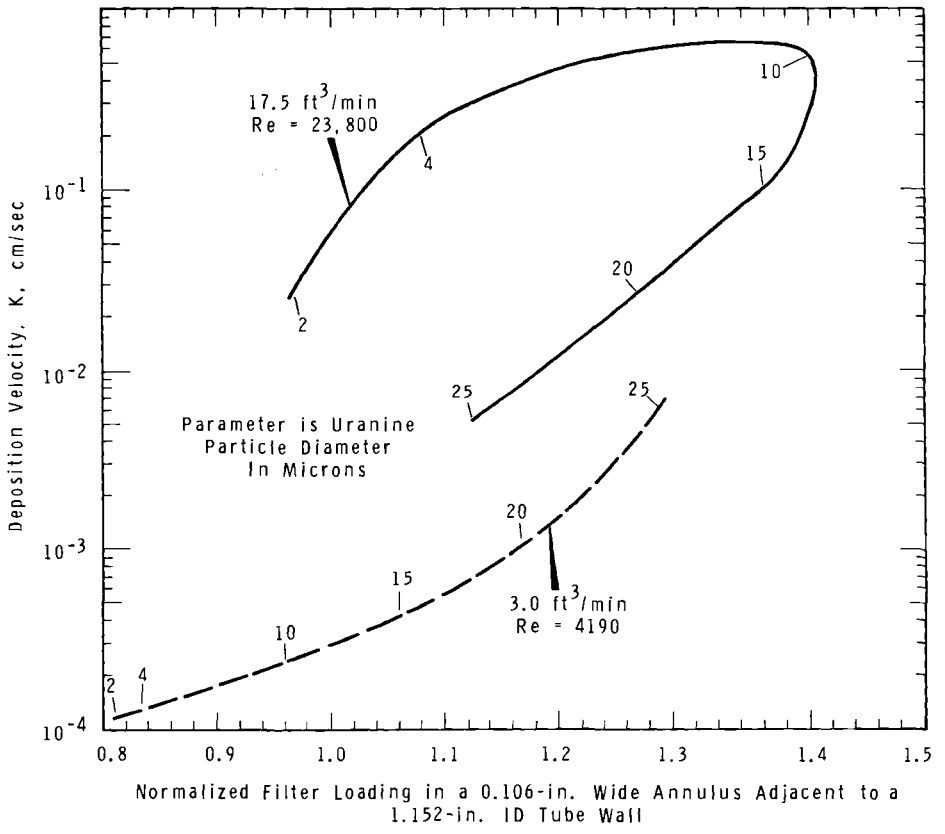

Neg. 0674029-14

FIGURE 3. Deposition Velocity as a Function of the Average Particle Flux in an Annulus Adjacent to a 1.152 in. ID Tube Wall

size and filter loading. The normalized filter loading is 1.4 for a 25 μ particle size. Filter loadings greater than unity are attributed to particle re-entrainment. However, effective re-entrainment is not observed as measured by a decrease in deposition velocity with an increase in particle size.

The relationship between deposition velocities and filter loading is double-valued for a Reynolds number of 23,800. Either one filter loading or one deposition velocity can be attributed to two particle sizes. The normalized filter loading is greater than unity for particles above about 3 μ. The filter loading increases with particle size until a maximum deposition velocity range is reached. This maximum is a characteristic of effective re-entrainment as measured by a decrease in deposition velocity as particle size is incresed. For particles larger than about 10 μ, both deposition velocities and filter loading decrease from their maxima. This decrease may be caused by particles being re-entrained by more energetic air eddies as the particle size increases. The greater energy is expanded in causing the particles to be thrown increasingly closer to the tube axis.

The data have shown that deposition in tubes is a function, not of the average particle concentration, but of the concentration profile above the deposition surface. Maximal concentrations are observed near the surface. This type of profile could not be predicted from the simple diffusion theories of deposition. To obtain data from which more adequate theories can be based, a conclusion of the present study is that concentration profiles above deposition surfaces should be simultaneously measured with particle deposition.

REFERENCES

1. *G. A. Sehmel. Aerosol Deposition from Turbulent Airstreams in Vertical Conduits, BNWL-578. Pacific Northwest Laboratory, Richland, Washington, March 1968.*

ATMOSPHERIC TURBULENCE STUDIES

C. E. Elderkin

Turbulence studies have been directed toward continued measurement of turbulence in the atmospheric boundary layer, and toward extended study of previously measured and analyzed data. Turbulence instrumentation has been modified to provide temperature fluctuation data simultaneously with measurements of three-wind component fluctuations in the on-going turbulence field tests.

Continued study of previously reported results deals with diabatic effects on spectral shapes and shifts. Measured spectra are compared with the magnitude of spectral shapes and shifts. Measured spectra are compared with the magnitude of spectral estimates in the inertial subrange, anticipated from Kolmogorov's expression, with the dissipation rate obtained from the turbulent energy budget equation where diabatic effects are estimated from wind and temperature profiles. A number of assumptions are made which will be evaluated in the continuing experimental effort.

The turbulent energy budget equation for steady state, horizontally homogeneous, two-dimensional flow normalized with mechanical energy production for neutral conditions, u_*^3/kz, is

$$\phi - Z/L - \phi_\varepsilon - \phi_D = 0 \qquad (1)$$

where

$$\phi = u_*^2 \frac{\partial \bar{U}}{\partial z} \Big/ \frac{u_*^3}{kz} = \frac{kz}{u_*} \frac{\partial \bar{U}}{\partial z}$$

is the normalized mechanical energy production

$$Z/L = -\frac{g}{T} \frac{H}{\rho c_p} \frac{kz}{u_*^3}$$

the normalized convective energy production

$$\phi_\varepsilon = \frac{\varepsilon u_*^3}{kz}$$

the normalized dissipation, and

$$\phi_D = \frac{kz}{u_*^3} \frac{\partial}{\partial z} \overline{(w'E')}$$

the normalized flux divergence.

The importance of the last term, the turbulent energy flux divergence, has been open to question for some time. Evaluation of measurements from the Brookhaven National Laboratory meteorological tower[1] has led to estimates of the flux divergence which cannot be ignored in comparison to other terms in the energy budget equation. However, recent analysis of Round Hill turbulence data applied to Equation (1) by Busch and Panofsky[2] indicates the flux divergence must be near zero for both unstable and stable cases. The differences could occur

because the simplified version of the energy budget equation given in Equation (1) does not completely account for all the factors involved. It is suggested by Frenzen[3] that the Brookhaven result contains also the effect of inhomogeneities producing the observed energy flux divergence. Equation (1) can be used with Kolmogorov's similarity theory expression for the energy spectrum in the inertial subrange, and with Taylor's hypothesis, to write

$$\frac{n[S_w(n)]_{in}}{u^2} = [\phi - Z/L - \phi_D]^{2/3} \cdot \frac{a}{k^{2/3}} \left(\frac{nZ}{\bar{U}}\right)^{-2/3} \qquad (2)$$

Here, the spectral energy for the vertical component, $n\,S_w(n)$, is normalized with the square of the friction velocity, u_*, and expressed for the inertial subrange (as indicated by the subscript, in). If the divergence of the turbulent energy flux is zero, on the average, the normalized diabatic inertial subrange spectrum becomes

$$\frac{n[S_w(n)]_{in}}{u_*^2} = \frac{a}{k^{2/3}} \left[\left(\frac{1}{\phi - Z/L}\right) \cdot \left(\frac{nZ}{\bar{U}}\right)\right]^{-2/3} \qquad (3)$$

The entire spectrum for the vertical component is plotted in Figure 1 with the diabatic spectral shift, indicated in Equation (3) for the inertial subrange, imposed over the entire wave number range. This treatment is consistent with Monin-Obukhov similarity theory expectations that, in the energy producing region, the spectral energy normalized to the square of the friction velocity (the only external parameter with velocity dimensions) is a function of normalized wave number, $\frac{nz}{\bar{U}}$, and stability, Z/L. For the diabatic factor, ϕ, in Equation (3), a function of Z/L was calculated with the friction velocity determined directly from the turbulence data and with the measured mean wind profile. The stability, Z/L, was estimated for unstable conditions by equating it to the gradient Richardson's number as suggested by Pandolfo.[4] For the stable case, the relation given by McVehil,[5] $Z/L = \frac{Ri}{1 - 7\,Ri}$, was used. Figure 1 compares the average spectrum for neutral cases at 3 and 6 m (Curve I), with the average unstable spectrum at 3 and 6 m (Curve II), and individual spectra from 12.2 m height in unstable (Curve III), and in stable (Curve IV) conditions. Near coincidence of the spectra at high wave numbers normalized to height and stability is observed as expected while, at the low wave number energy producing end, the curves separate for different stabilities. With a large sample of data covering a wide range of stabilities, this manner of normalizing and of organizing the spectra is expected to offer the best basis for modeling diabatic spectra for all stabilities.

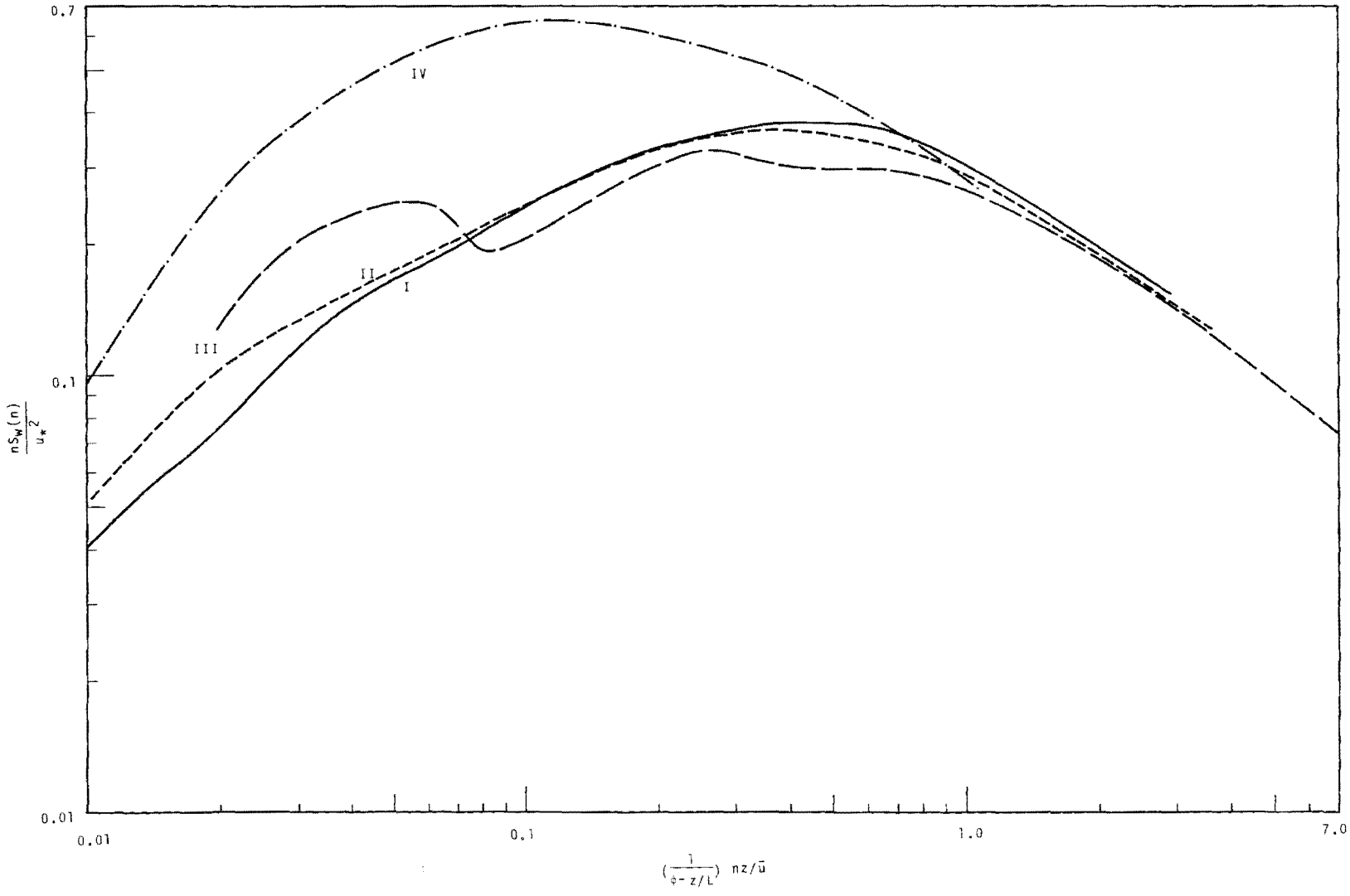

FIGURE 1. Vertical Component Spectra Normalized for Diabatic Effect

The calculated dimensionless wind shear (normalized mechanical energy contribution), ϕ; the estimated Monin-Obukhov stability parameter (normalized convective energy contribution), Z/L; and the difference between the two providing the factor to normalize the wave number axis of Figure 1 for diabatic effects in accordance with Equation (3) are tabulated as follows:

Curve in Figure 1		ϕ	Z/L	ϕ-Z/L
II	Average Unstable Tests at 3 and 6 m	0.94	-0.064	1.00
III	Unstable Test at 12.2 m	0.76	-0.18	0.94
IV	Stable Test at 12.2 m	6.70	0.02	6.68

It should be noted that all data used in this comparison were from measurements reasonably close to the ground where the mechanically generated energy was larger than the bouyant energy. The preceeding tabulation shows, even for the unstable case of 12.2 m where the differences between the magnitudes of ϕ and Z/L was least, mechanical energy about four times that of the convective contribution. Flux divergence effects comparable in magnitude to the convective energy might go undetected in this comparison. This effect, at any rate, may be stated as small in comparison to the mechanical energy term.

It is interesting to notice that, as the stability parameter becomes increasingly negative for unstable conditions, the dimensionless wind shear is correspondingly reduced below 1.0, thus maintaining the difference ϕ - Z/L, close to unity. This result is consistent with the findings of Busch and Panofsky for the Round Hill data. As long as this is true, no shift occurs in the spectrum, normalized as in Figure 1. On the other hand, the large shift in the spectrum for the stable case occurs almost solely through the large wind shear.

A more extensive data collection effort was initiated to provide a basis for modeling the turbulence spectra over conditions of large stability and instability. Seventeen additional turbulence tests were conducted in 1967 in both daytime and nighttime conditions. To accurately describe the stability and to investigate the characteristics of the convective energy input to the turbulence, the wind component meter turbulence sensor was altered to enable the measurement of temperature fluctuations. A micro-bead thermistor circuit developed and tested by A. G. Dunbar is responsive to temperature fluctuations up to about 10 cps and has a relative accuracy of ±0.05 °C and ±0.01 °C on the fluctuation range settings of ±5 °C and ±1 °C, respectively. The fluctuation range can be set arbitrarily about any selected temperature between -15 °C and +45 °C. Unbalanced bridge current, compensating for nonlinearity in the thermistor calibration curve, yields a continuous signal directly proportional to temperature with a constant calibration factor. The signal is compatible with the

three-wind component signals simultaneously measured at the same point and recorded on magnetic tape. The modified turbulence instrument was put into use in January, 1968 with temperature and wind fluctuation data gathered in five tests in unstable and stable conditions at 1.5, 3.0, and 6.1 meters.

Continued testing, to include measurement at greater heights where convective energy will be comparable to, or greater than, the mechanical energy is planned. Significant turbulent energy flux divergence can be detected with multiple level rapid response sampling of the turbulence, also planned, and can be studied relative to the other terms in the turbulent energy budget equation.

REFERENCES

1. *H. A. Panofsky. "The Budget of Turbulent Energy in the Lowest 100 Meters," J. Geophys. Res., vol. 67, p. 3161. 1962.*

2. *N. E. Busch and H. A. Panofsky. "Recent Spectra of Atmospheric Turbulence," Preprint of Paper Presented at the Unguided Rocket Ballistics Meteorology Conference, University Park, New Mexico, November 1967.*

3. *P. Frenzen. "On Measuring Vertical Fluxes of Momentum and Heat with Cup Anemometers," Symposium on Theory and Measurement of Atmospheric Turbulence and Diffusion in the Planetary Boundary Layer, Albuquerque, New Mexico, Preprint, pp. 39-40. December 1967.*

4. *J. P. Pandolfo. "Wind and Temperature Profiles for Constant-Flux Boundary Layers in Lapse Conditions with a Variable Eddy Conductivity to Eddy Viscosity Ratio," J. Atmospheric Sci., vol. 23, p. 495. 1966.*

5. *G. E. McVehil. "Wind and Temperature Profiles Near the Ground in Stable Stratification," Quart. J. Roy. Meteorol. Soc., vol. 90, pp. 136-146. 1964.*

COMPARISON OF TURBULENCE SPECTRA FROM HANFORD, WASHINGTON, AND LIBERAL, KANSAS

C. E. Elderkin

INTRODUCTION

Turbulence data have been collected at Hanford, Washington for some years in connection with the diffusion research. In August of 1965, turbulence measurements were made jointly with AFCRL at their micrometeorological site at Liberal, Kansas. The purpose of this paper is to describe the turbulence spectra for each of the three-wind components measured under a variety of wind speed and stability conditions at Hanford, and to compare them with the spectra for the single

test at Liberal in slightly unstable conditions. The roughness characteristics of the two areas are different. Hanford is located in a relatively flat basin bordered by bluffs on one side and a mountain ridge on the other. There are additional elevation changes of a few hundred feet within a 10-mile range over the basin. The region is primarily sage-brush covered and the roughness length is about 3 cm. The Kansas site is extremely flat and at the time of measurement the ground was bare or covered with short stubble for several miles around. The roughness length was about 1 cm.

INSTRUMENTATION

The turbulence data presented here were collected at both sites with a fast response sensor, termed the wind component meter. The sensor signals were recorded on a magnetic tape recorder and later analyzed on an analog computer.

The wind component meter, originally designed by J. J. Fuquay of Battelle-Northwest Laboratories at Hanford, is similar in some respects to earlier sensors described by G. C. Gill[1] and H. E. Cramer,[2] utilizing heated thermocouple wires.

M. Miyake[3] has developed an improved version of the wind component meter with heated thermocouple sensors similar to the Fuquay model but incorporating more complex electronic circuitry.

The instrument senses the three components of the wind at a given single point and produces continuous voltage signals related to the three spherical wind components. A more detailed description has previously been given in the Annual Report for 1964.[4]

MEASUREMENTS

In the summer of 1964, a series of turbulence measurements was conducted with the wind component meter mounted on the Hanford portable micrometeorological mast at the 3.0 and 6.1-m levels. Measurements made in neutral, unstable, and stable conditions were accompanied by winds of from 2 to 9 mps.

Since data collected at greater heights were desired, the wind component meter was mounted later in the summer of 1964 at 12.2 m where a single test in stable conditions was conducted. In the following spring, two additional tests were conducted at 12.2 m and two more at 6.1 m in neutral and unstable conditions. The final test, also under unstable conditions, was made with the wind component meter mounted at 87 m on the Hanford 400-ft meteorological tower. A total of 18 tests was conducted at Hanford.

The turbulence data were recorded on an Ampex FR-1100 tape recorder at 3 3/4 ips tape transport speed for all tests. Calibration signals of zero and one volt were recorded with the data to assure accurate reproduction of the data during the analysis period. The data were stored on the tapes

until the analysis could be carried out a few months after the tests with analog computer programs.

Turbulence measurements were made with the same sensor at the invitation of the Air Force Cambridge Research Laboratories at their Liberal, Kansas micrometeorological measurement site during their instrumentation checkout test phase in August, 1967. One good measurement period was recorded on magnetic tape during unstable conditions with the wind component meter mounted at a height of 5.6 m on the site's micrometeorological tower. Again, the data were stored in analog form on magnetic tape for later analysis on the analog computer, with the same programs and techniques used on the Hanford data.

RESULTS

Following coordinate transformation into a cartesian coordinate system with the X-axis oriented along the mean wind and with removal of all mean components, signals proportional to the u', v', and w' turbulent wind components were re-recorded.

These signals were replayed into other analog computer programs including a filtering program producing power spectral estimates. Another program provided total variances, σ_u^2, σ_v^2, and σ_w^2 with which the spectra were normalized. The wave length, estimated by $\overline{U}/n$ where n is frequency and $\overline{U}$ is mean wind speed, was normalized by the height, z. When the eddy sizes were normalized in this manner and the normalized spectral energy, $nS(n)/\sigma^2$, was plotted against the normalized wave number, $nz/\overline{U}$, similarity of the spectral distributions was observed most consistently with the vertical component, reasonably well with the longitudinal component--particularly at high wave numbers, and least clearly with the lateral component. These results have been discussed thoroughly in previous annual reports.[5,6]

The shape of the spectra and the location of the spectral peaks for the vertical component in the Hanford investigation do not differ greatly from prior reports of such features. The comparison by Panofsky and McCormick[7] of data from various sites shows peaks in $nS_w(n)$ ranging from $nz/\overline{U} = 0.2$ to 0.6, agreeing quite well with the occurrence of the w spectra peaks for Hanford at about $nz/\overline{U} = 0.4$. Similarly, the present work agrees with the sharp drop-off previously found for turbulent energy in the vertical component at low wave numbers, well before $nz/\overline{U} = 0.01$. Normalized vertical velocity spectra reported by Gurvich[8] also show spectral peaks in the same general $nz/\overline{U}$ region.

The occurrence of the peaks and the shape of the Hanford longitudinal spectra agree in general with longitudinal spectra summarized by Berman[9] for a number of sites. However, additional dependence on height beyond the $nz/\overline{U}$ scaling was found by Berman for the occurrence of the spectral peak. The additional

height dependence was not detected at Hanford, although the variability in the longitudinal component spectral estimates at low wave numbers where the peaks occurred may have hidden such a dependence.

The Kansas data, collected in unstable conditions, are compared with the Hanford unstable cases at 3.0 and 6.1 m for the vertical component spectra in Figure 1. The individual spectral estimates were plotted for the Kansas Test WAM-4, while curves were drawn through the data for each of the Hanford tests. The shapes of the normalized spectra are observed to compare favorably. The peaks occur at the same value of $nz/\overline{U}$ and the minus five-thirds law is approached reasonably well over the same range of $nz/\overline{U}$. At low wave numbers, the shapes of the spectra again compare well with a convective energy input indicated in the Kansas data although, as with the low level Hanford data, a convective peak statistically significant at the 80% confidence level could not be identified as it could for the Hanford cases above 12 meters.

The longitudinal component spectra for the two sites are compared in Figure 2. The shapes of the spectra again compare favorably. The values of $nz/\overline{U}$ for the peak in the spectra and the $nz/\overline{U}$ range fitting the minus five-thirds law agree quite well. However, the Kansas spectrum demonstrates a slight drop in energy at about $nz/\overline{U} = 0.1$, which was not found in the Hanford unstable data.

The lateral component spectra, compared in Figure 3, demonstrate some agreement in shape between the Kansas spectrum and one of the Hanford spectra. However, even here significant differences are found with a larger fraction of the turbulent energy, including the peak in the spectrum, occurring at lower wave numbers for the Kansas case.

The difference in surface roughness between the two sites is found to have no noticeable effect on the scale of turbulent eddy sizes generated, or on the resulting power spectral distributions for the unstable cases compared here where difference in instrumentation and analysis methods have been eliminated. It is expected that only the total variances with which the spectral densities are normalized should vary with surface roughness. Differences due to mesoscale effects, detected in the comparison of the horizontal component spectra between sites suggested in these data, might be much more noticeable for stable conditions. Indeed, comparisons of Hanford spectra with a summary of lateral component spectra presented by Panofsky and Deland[10] show considerably less turbulent energy at low wave numbers in stable spectra for O'Neill, Nebraska, and Brookhaven, New York, than for Hanford. Further comparison between Hanford, Washington, and Liberal, Kansas, spectra is desirable, particularly for stable conditions.

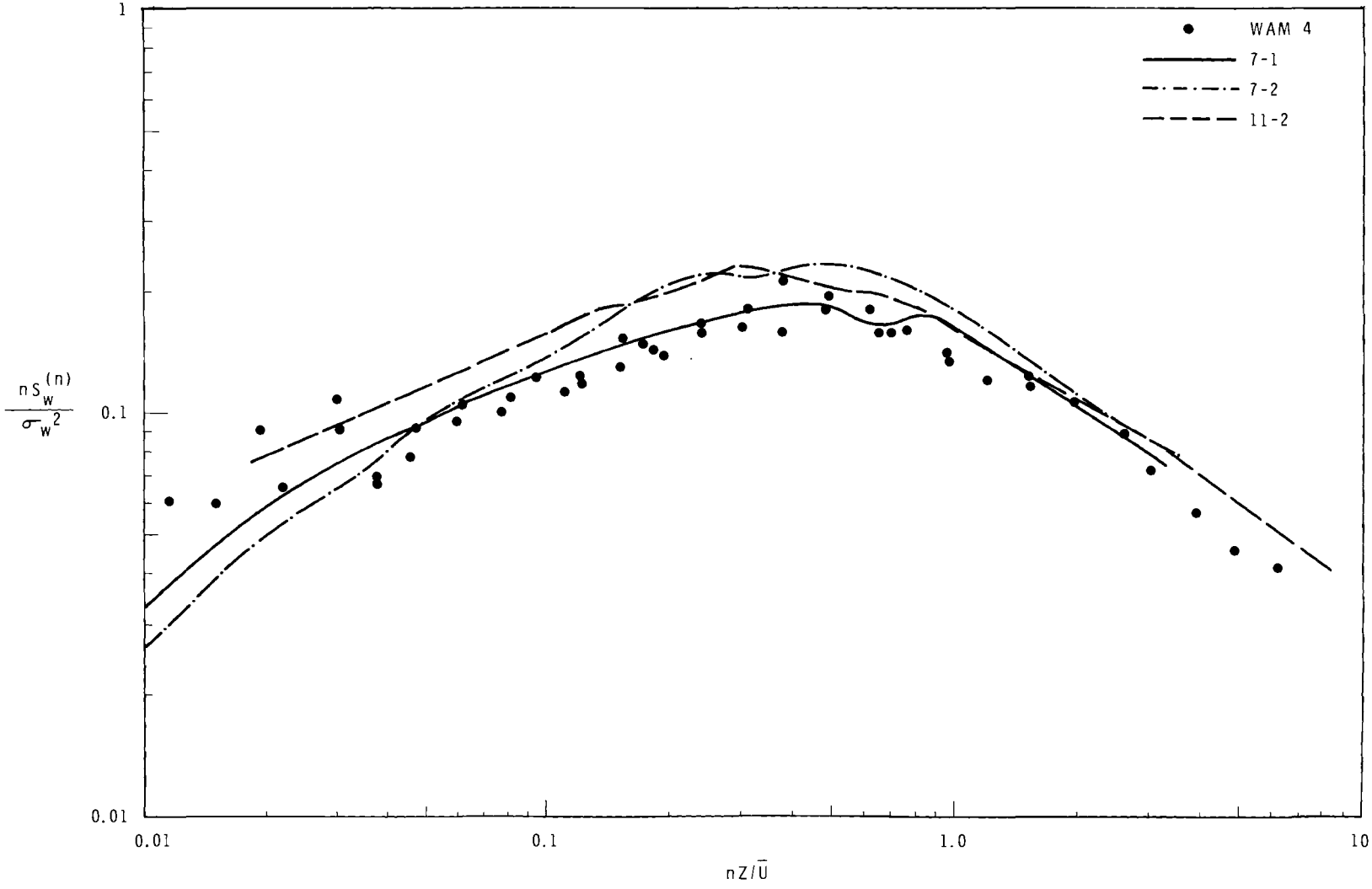

Neg. 0672982-2

FIGURE 1. Vertical Wind Component Spectra

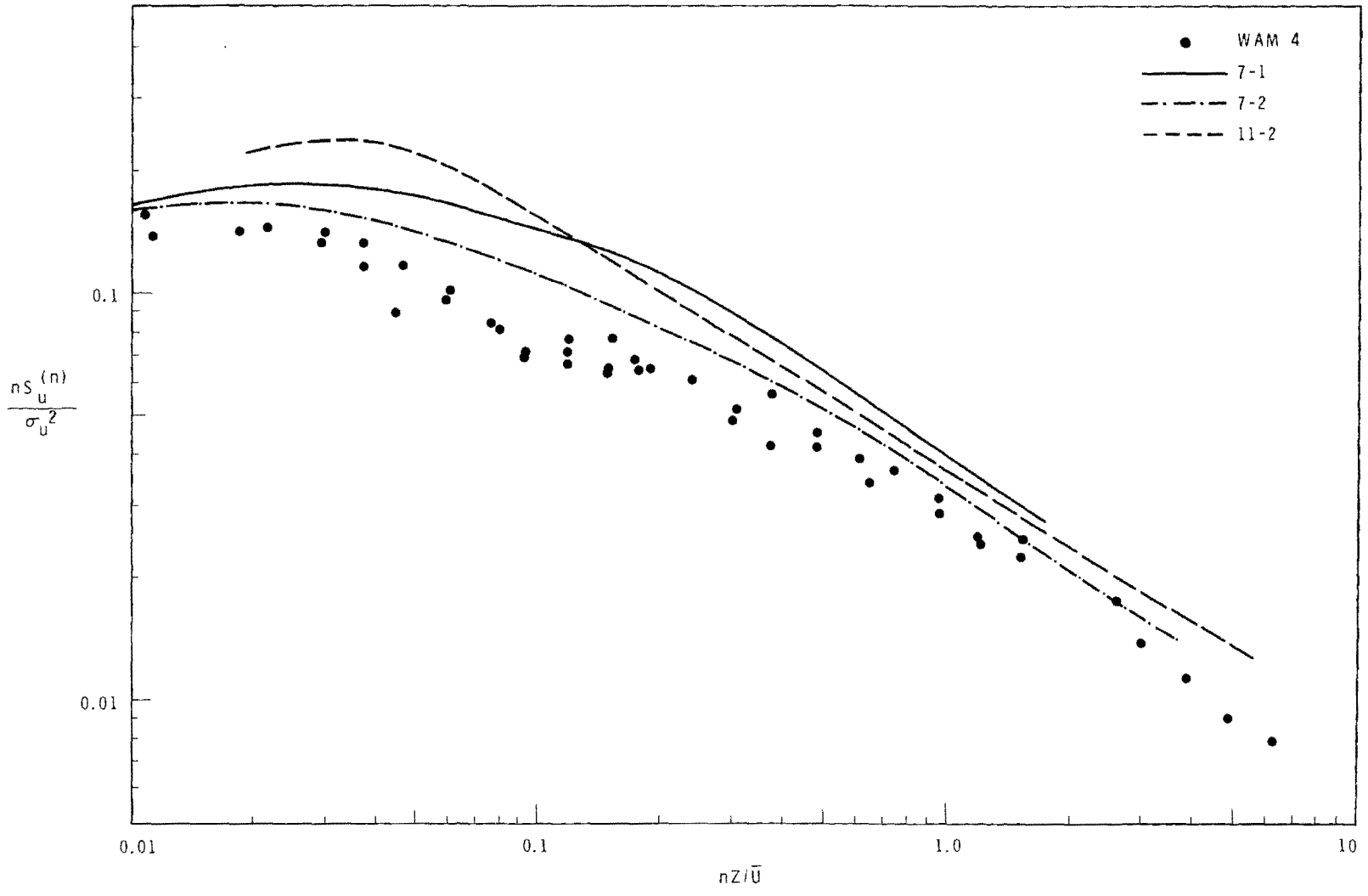

Neg. 0672982-1

FIGURE 2. Longitudinal Wind Component Spectra

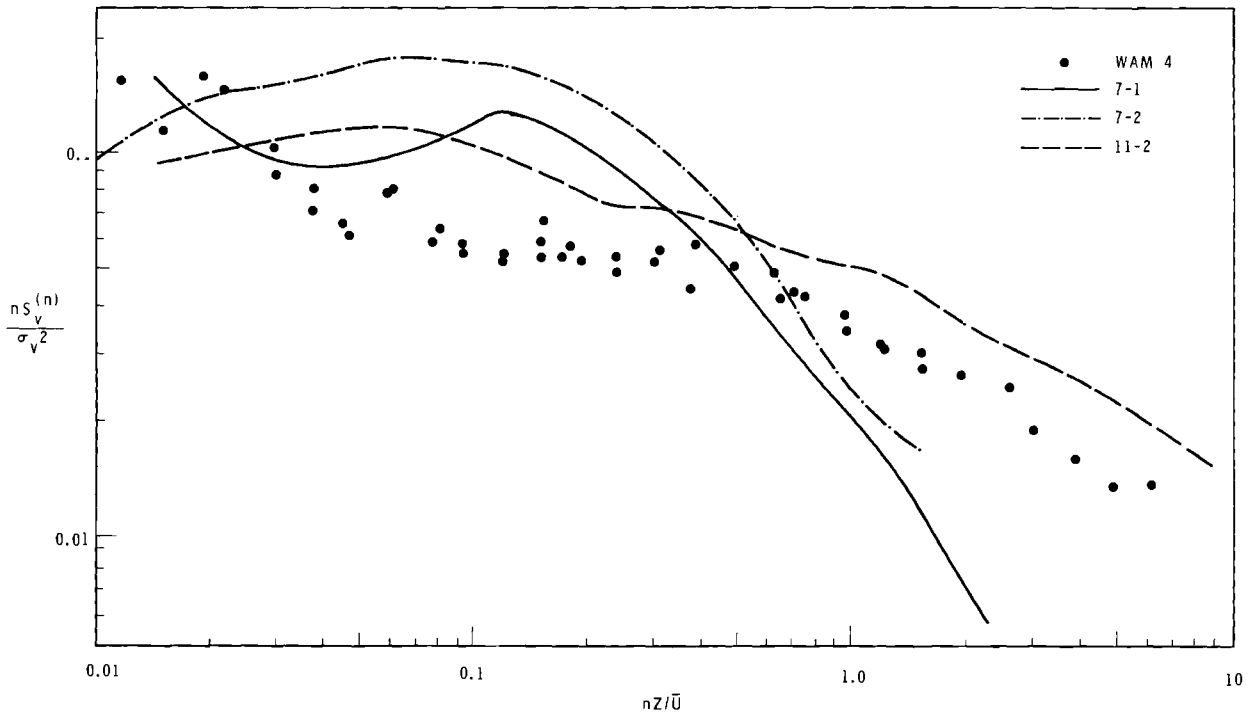

Neg. 0672982-3

FIGURE 3. Lateral Wind Component Spectra

REFERENCES

1. *G. C. Gill. "A Fast Response Anemometer for Micrometeorological Investigation," Bull. Am. Meteorol. Soc., vol. 35, 1954.*

2. *H. E. Cramer. "Measurements of Turbulence Structure near the Ground Within the Frequency Range from 0.5 to 0.01 Cycles Sec^{-1}," Advan. Geophys. vol. 6, p. 75. 1959.*

3. *M. Miyake. A Constant Temperature Wind Component Meter Development and Application, Final Report, Contract No. AT(45-1)-1545, Department of Atmospheric Sciences, University of Washington, Seattle, Washington. 1965.*

4. *C. E. Elderkin. "Atmospheric Turbulence Measurements," Hanford Radiological Sciences Research and Development Annual Report for 1964, BNWL-36-1. Pacific Northwest Laboratory, Richland, Washington, January 1965.*

5. *C. E. Elderkin. "Spectral Distribution of Atmospheric Turbulence," Pacific Northwest Laboratory Annual Report for 1965 in the Physical Sciences to the USAEC Division of Biology and Medicine, Volume 1: Atmospheric Sciences, BNWL 235 1. Pacific Northwest Laboratory, Richland, Washington, May 1966.*

6. *C. E. Elderkin. "Turbulence Investigations," Pacific Northwest Laboratory Annual Report for 1966 to the USAEC Division of Biology and Medicine, Volume II: Physical Sciences, Part I. Atmospheric Sciences, BNWL 481 1. Pacific Northwest Laboratory, Richland, Washington, October 1967.*

7. *H. A. Panofsky and R. A. McCormick. "The Spectrum of Vertical Velocity near the Surface," Quart. J. Roy. Meteorol. Soc., vol. 86, p. 495. 1960.*

8. *A. S. Gurvich. "Frequency Spectra and Distribution Functions of Vertical Wind Components," Izvestya, ANSSR, Geophy. Ser., no. 7, p. 1042. 1960.*

9. *S. Berman. "Estimating the Longitudinal Wind Spectrum near the Ground," Quart. Meteorol. Soc., vol. 91, p. 302. 1965.*

10. *H. A. Panofsky and R. J. Deland. "One-Dimensional Spectra of Atmospheric Turbulence in the Lowest 100 Metres," Advan. Geophys., vol. 6, p. 41. 1959.*

ON A GENERAL RELATION BETWEEN AUTOCORRELOGRAMS AND VARIANCE

W. T. Hinds

INTRODUCTION

The statistics of randomly fluctuating variables have for many years been an abundant source of insights into atmospheric motions and behavior. One facet of these statistics is the behavior of the statistical parameters when the random variable is subjected to smoothing before the statistics are calculated. Smoothing such as that due to the sluggishness of instruments used to measure turbulent parameters may be inadvertent. Alternatively, the smoothing may be imposed in a purposeful manner with low-pass filters, so that the distribution of energy in the turbulent fluctuations may be studied in a systematic manner. An extended discussion of this relation between the variance of smoothed and unsmoothed variables, including the existence of general relations between smoothed variance and the autocorrelogram can be found in Pasquill.[1] Kahn,[2] taking into account the effect of finite averaging of the signal before the autocorrelogram is calculated, derived a very general expression for the autocorrelogram. One particular result of his argument can be expressed in terms of the variances of the smoothed and unsmoothed signal (σ_s^2 and σ_o^2, respectively) and the autocorrelogram, R(s):

$$\frac{1}{2}\frac{d^2}{ds^2}\left(s^2\,\frac{\sigma_s^2}{\sigma_o^2}\right) = R(s) \qquad (1)$$

This relation has the advantage of yielding the autocorrelogram by calculation of variances rather than by the more awkward autocovariances usually required. However, second derivatives are notoriously difficult to handle except when an analytical function is available, a condition not often met in turbulent studies.

Kahn developed the expressions leading to Equation (1) by consideration of the spectrum of the fluctuations. A somewhat different and simpler expression follows if the initial approach is from the definition of the variance of a smoothed variable.

Let X be a single valued, continuous stationary random variable

- τ be time, the independent variable
- t be the relatively short smoothing interval
- T be the relatively long length of record
- X_s be the smoothed value of X, over the interval t
- $\overline{X}$ be the average value of X, over the interval T
- σ_o^2 be the variance of X over the interval T
- σ_s^2 be the variance of X_s over the interval T

The smoothed variable is defined by

$$X_s = \frac{1}{t}\int_{\tau-t/2}^{\tau+t/2} X(\lambda)\, d\lambda \qquad (2)$$

where a dummy variable λ has been introduced as the variable of integration. The definition of variance in terms of X_s is then

$$\sigma_s^2 = \frac{1}{T}\int_{-T/2}^{T/2} (X_s - \overline{X})^2\, d\lambda \qquad (3)$$

It may be noted that the operation of smoothing X over periods of length, t, yields a continuous variable if overlapping means are considered, and a discrete variable if end-to-end means are considered. Here, overlapping means will be assumed.

Expanding $(X_s - \overline{X})^2$ and differentiating with respect to t yields

$$\frac{d\sigma_s^2}{dt} = \frac{1}{T}\int_{-T/2}^{T/2} \left(2X_s \frac{dX_s}{dt} - 2\overline{X}\frac{dX_s}{dt}\right) d\lambda \qquad (4)$$

The derivative of X_s is a function of the limits on the integral (2) (when the integral is differentiated) and X_s,

$$\frac{dX_s}{dt} = -\frac{1}{t}X_s + \frac{1}{t}\left[X(\tau+t/2)\frac{d(\tau+t/2)}{dt} - X(\tau-t/2)\frac{d(\tau-t/2)}{dt}\right]$$

$$= -\frac{1}{t}X_s + \frac{1}{t}\left[\frac{1}{2}X(\tau+t/2) + \frac{1}{2}X(\tau-t/2)\right]$$

For simplicity, let $\frac{1}{2}\left[X(\tau+t/2) + X(\tau-t/2)\right]$ be defined as X_L. Then

$$\frac{dX_s}{dt} = \frac{1}{t}(X_L - X_s) \qquad (5)$$

Inserting this expression for dX_s/dt in Equation (4) yields

$$\frac{d\sigma_s^2}{dt} = \frac{2}{t}\left[\underbrace{\frac{1}{T}\int_{-T/2}^{T/2} X_s X_L d\lambda}_{(I)} - \underbrace{\frac{1}{T}\int_{-T/2}^{T/2} X_s^2\, d\lambda}_{(II)} - \underbrace{\frac{1}{T}\int_{-T/2}^{T/2} \overline{X}X_L d\lambda}_{(III)} + \underbrace{\frac{1}{T}\int_{-T/2}^{T/2} \overline{X}X_s d\lambda}_{(IV)}\right] \qquad (6)$$

Each of the numbered integrals will now be examined.

First, consider Integral IV in Equation (6). It can be written as

$$\bar{X}\left[\frac{1}{T}\int_{-T/2}^{T/2} X_s\,d\lambda\right] \tag{7}$$

This is just the average of X_s over the interval -T/2 to T/2, which is equal to $\bar{X}$. Thus

$$\frac{1}{T}\int_{-T/2}^{T/2} \bar{X}X_s\,d\lambda = \bar{X}^2 \tag{8}$$

Consider now Integral III. This can be written

$$\frac{1}{T}\int_{-T/2}^{T/2} \bar{X}X_L\,d\lambda = \frac{\bar{X}}{2T}\int_{-T/2}^{T/2} X(\tau+t/2)\,d\lambda + \frac{\bar{X}}{2T}\int_{-T/2}^{T/2} X(\lambda-t/2)\,d\lambda \tag{9}$$

These are integrals of X over a slightly different record than originally used to define $\bar{X}$ and σ_s^2, with a shift in record of t/2 at each end of the interval -T/2 to T/2, as shown in Figure 1. The first integral in Equation (9) involves a loss of t/2 length at -T/2, and a gain of t/2 length beyond T/2. Conversely, the second integral involves a gain of t/2 length at -T/2 (i.e., integration over a portion of X preceding -T/2) and a loss of t/2 length of the original record at T/2. Thus, the first integral in Equation (9), ignoring $\bar{X}$ for the moment, is

$$\frac{1}{2}\left[\frac{1}{T}\int_{-T/2}^{T/2} X\,(\lambda+t/2)\,d\lambda\right] = \frac{1}{2}\left[\frac{1}{T}\int_{-T/2}^{T/2} X(\lambda)\,d\lambda - \frac{1}{T}\int_{-T/2}^{-T/2+t/2} X(\lambda)\,d\lambda + \frac{1}{T}\int_{T/2}^{T/2+t/2} X(\lambda)\,d\lambda\right] \tag{10}$$

while the second integral is

$$\frac{1}{2}\left[\frac{1}{T}\int_{-T/2}^{T/2} X(\lambda-t/2)\,d\lambda\right] = \frac{1}{2}\left[\frac{1}{T}\int_{-T/2}^{T/2} X(\lambda)\,d\lambda + \frac{1}{T}\int_{-T/2-t/2}^{-T/2} X(\lambda)\,d\lambda - \frac{1}{T}\int_{T/2-t/2}^{T/2} X(\lambda)\,d\lambda\right] \tag{11}$$

After summing Equations (10) and (11), it can be seen that the Integral III in Equation (6) is very nearly $\bar{X}^2$. The difference between Integral III and $\bar{X}^2$ is only that, due to interchange of -t/2 -T/2 with -T/2 +t/2 and T/2 -t/2 with T/2 +t/2, the record within t/2 outside the bounds of the original record is added and the record within t/2 inside the bounds of the original record is deleted. This odd manipulation results from the differentiation of the limits on X_s. Nevertheless, if X is stationary, an assumption implicit in this entire argument, the sum of Equation (10) and (11) is very nearly $\bar{X}^2$.

At this point, both Integral III and IV in Equation (6) have been shown to be very nearly $\bar{X}^2$, but with opposite sign.

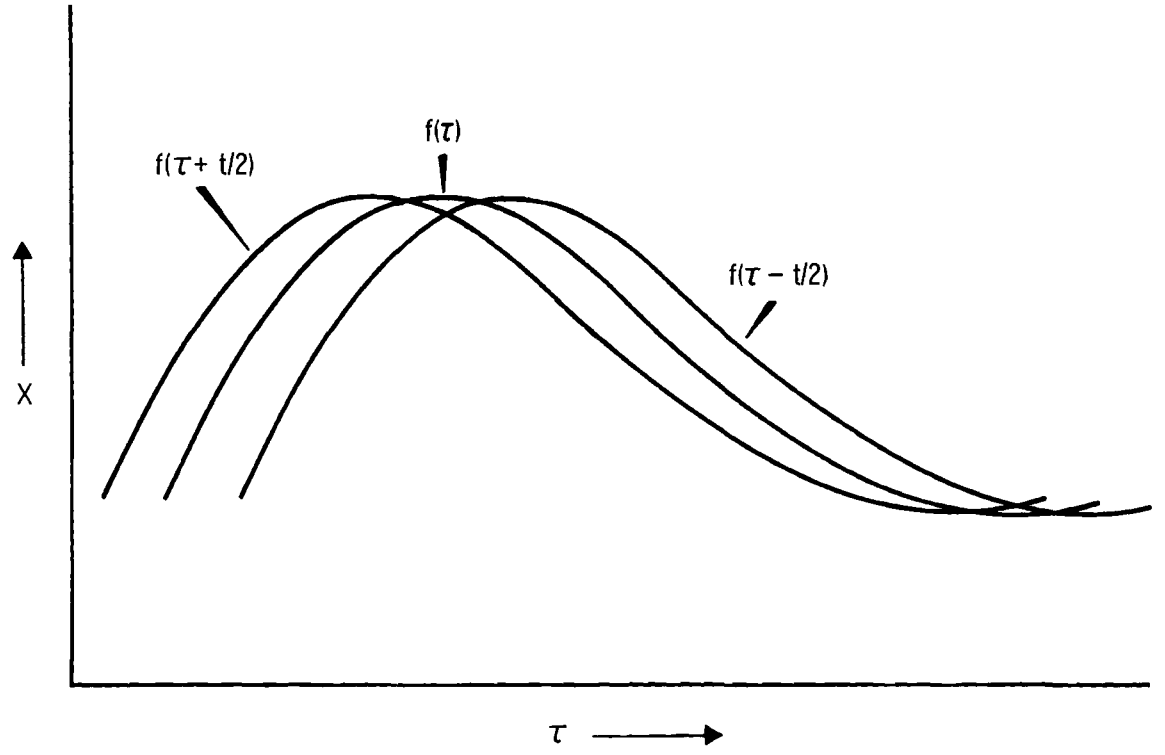

Neg. 0672184-2

FIGURE 1. Shift of Record when f(τ) is Changed to f(τ±t/2)

Consider now Integral I in Equation (6). The integrand can be written as a product of mean and fluctuating values:

$$X_s X_L = (\bar{X}_s + X_s')(\bar{X}_L + X_L')$$
$$= (\bar{X} + X_s')(\bar{X} + X_L')$$
$$= \bar{X}^2 + \bar{X}X_L' + \bar{X}X_s' + X_s'X_L'$$

since $\bar{X}_s = \bar{X}_L = \bar{X}$ as shown above. When each term is averaged over the interval -T/2 to T/2,

$$\overline{X_s X_L} = \bar{X}^2 + \overline{X_s'X_L'} \qquad (12)$$

A similar procedure applied to Integral II in Equation (6) yields

$$\overline{X_s^2} = \overline{(\bar{X} + X_s')^2} = \bar{X}^2 + \overline{2\bar{X}X_s'} + \overline{X_s'^2}$$
$$= \bar{X}^2 + \overline{X_s'^2} \qquad (13)$$

Thus Equation (5) can be written as

$$\frac{d\sigma_s^2}{dt} = \frac{2}{t}\left[\bar{X}^2 + \overline{X_s'X_L'} - \bar{X}^2 - \sigma_s^2\right]$$
$$= \frac{2}{t}\left[\overline{X_s'X_L'} - \sigma_s^2\right] \qquad (14)$$

An insight into the character of $X_s'X_L'$ is possible by defining $X_s'(\tau)$ in terms of $X'(\tau)$, the primitive deviation of the function from the mean. At any time τ (the midpoint of the interval over which X_s is defined) we may write

$$X'(\tau) = X_s'(\tau) + X_s''(\tau) \qquad (15)$$

Then, using the expanded form of X_L,

$$\overline{X_s'X_L'} = \overline{[X'(\tau) + X''(\tau)]}$$

$$\overline{\left[\frac{1}{2} X'(\tau+t/2) + \frac{1}{2} X'(\tau-t/2)\right]}$$

or, if $X(\tau)$ is stationary, so that

$$\overline{X'(\tau)\, X'(\tau+t/2)} = \overline{X'(\tau)\, X'(\tau-t/2)},$$

$$\overline{X_s'X_L'} = \overline{X'(\tau)\, X'(\tau+t/2)}$$

$$+ \overline{X_s''(\tau)\, X'(\tau+t/2)} \qquad (16)$$

Equation (16) indicates that $\overline{X_s'X_L'}$ is closely related to the autocovariance of X at lag t/2. The term $\overline{X_s''(\tau)\, X'(\tau+t/2)}$ approaches zero by definition as $t \to 0$, and must finally approach zero at large t, since it is a correlation. A maximum value may be attained at some lag time, but the magnitude cannot be large and seems likely to be zero, since 1) X_s'' is itself small compared to X', and 2) X_s'' may be either positive or negative for a given sign on X'. Thus, to a good approximation,

$$\overline{X_s'X_L'} = \overline{X'(\tau)\, X'(\tau+t/2)} \qquad (17)$$

Let $P(t/2) = \overline{X'(\tau)\, X'(\tau+t/2)}$, so that Equation (14) may be written

$$\frac{d\sigma_s^2}{dt} + \frac{2}{t}\sigma_s^2 = \frac{2}{t} P(t/2) \qquad (18)$$

If Equation (18) is divided by σ_o^2,

$$\frac{d}{dt}\left(\frac{\sigma_s^2}{\sigma_o^2}\right) + \frac{2}{t}\frac{\sigma_s^2}{\sigma_o^2} = \frac{2}{t} R(t/2) \qquad (19)$$

where R(t/2) is the autocorrelation of X at lag t/2. Multiplying by t/2, then,

$$\frac{t}{2}\frac{d}{dt}\left(\frac{\sigma_s^2}{\sigma_o^2}\right) + \frac{\sigma_s^2}{\sigma_o^2} = R(t/2) \qquad (20)$$

or, letting $t/2 \equiv s$, so that $dt = 2ds$,

$$\frac{s}{2}\frac{d}{ds}\left(\frac{\sigma_s^2}{\sigma_o^2}\right) + \frac{\sigma_s^2}{\sigma_o^2} = R(s) \qquad (21)$$

Now, considering that

$$\frac{1}{2}\frac{d}{ds}\left(s\frac{\sigma_s^2}{\sigma_o^2}\right) = \frac{s}{2}\frac{d}{ds}\left(\frac{\sigma_s^2}{\sigma_o^2}\right) + \frac{1}{2}\frac{\sigma_s^2}{\sigma_o^2} \qquad (22)$$

it appears that Equation (21) can be written as

$$\frac{1}{2}\frac{d}{ds}\left(s\frac{\sigma_s^2}{\sigma_o^2}\right) + \frac{1}{2}\frac{\sigma_s^2}{\sigma_o^2} = R(s) \qquad (23)$$

which can be compared directly to Kahn's result

$$\frac{1}{2}\frac{d^2}{ds^2}\left(s^2\frac{\sigma_s^2}{\sigma_o^2}\right) = R(s) \qquad (24)$$

A substantial simplification has been made, since in Equation (23) only a single differentiation is required to calculate R(s).

However, all theoretical implications involved in the derivation of Equation (18) are not yet clear. In particular, the implications of assuming that

$$\overline{X''(\tau)\, X'(\tau+t/2)} = 0 \qquad (25)$$

are especially troublesome.

Some insight into the problem is perhaps possible by considering an alternate derivation* of Equation (18). Starting with G. I. Taylor's[3] result for variance in terms of the autocorrelation function, as written by Frenzen[4]

$$\frac{\sigma_s^2}{\sigma_o^2} = \frac{2}{T^2}\int_o^T \int_o^t R(\xi)d\xi\, dt \qquad (26)$$

or, using Kampi de Feriet's form (Pasquill)[1]

$$\frac{t^2}{2}\frac{\sigma_s^2}{\sigma_o^2} = \int_o^t (t - \xi)\, R(\xi)d\xi \qquad (27)$$

then, differentiating Equation (27) with respect to the smoothing interval t,

$$t\frac{\sigma_s^2}{\sigma_o^2} + \frac{t^2}{2}\frac{d}{dt}\left(\frac{\sigma_s^2}{\sigma_o^2}\right) = \int_o^t R(\xi)d\xi + tR(t) - tR(t) \qquad (28)$$

or, multiplying by $2\sigma^2/t^2$

$$\frac{d\sigma_s^2}{\sigma_o^2} + \frac{2}{t}\sigma_s^2 = \frac{2}{t^2}\int_o^t P(\xi)d\xi \qquad (29)$$

Hence, Equations (18) and (29) are the same if

$$\frac{2}{t^2}\int_o^t P(\xi)d\xi = \frac{2}{t}P(t/2) \qquad (30)$$

that is, if

$$\int_o^t P(\xi)d\xi = t\,P(t/2) \qquad (31)$$

Since Equation (31) must hold for all t, and since $P(\xi)$ is in general a monotonically declining function, Equation (31) implies that $P(\xi)$ must be linear. This is a surprising result, since no such approximation was overtly made in the derivation of Equation (18). Linearity, if somehow implied by the approximation of Equation (25), seems subtle indeed in its appearance.

Clearly, the theoretical work needs more thought, but the simplicity found in Equations (18) and (23) points to the hope that useful results will be possible. It has already been shown [for example Hinds[5]] that simple approximation in Equation (18) can yield quite satisfactory results. For example, if Equation (18) is rearranged to

$$\frac{d\sigma_s^2}{\sigma_s^2} = 2\left[\frac{P(t/2)}{\sigma_s^2} - 1\right]\frac{dt}{t}$$

then by assuming*

$$2\left[\frac{P(t/2)}{\sigma_s^2} - 1\right] = b + kt$$

the solution is

$$\frac{\sigma_s^2}{\sigma_{s,o}^2} = \left(\frac{t}{t_o}\right)^b e^{k(t - t_o)} \qquad (32)$$

Comparison of Equation (32) with observed data is shown in Figure 2.

---

* *Dr. Paul Frenzen suggested this approach.*

* *Note that if it is assumed that* $2\left[\frac{P(t/2)}{\sigma_s^2} - 1\right] = b$, *the hypothesis suggested by Singer, et al.*[6] *(i.e. a simple power law connects variance and smoothing interval) immediately follows.*

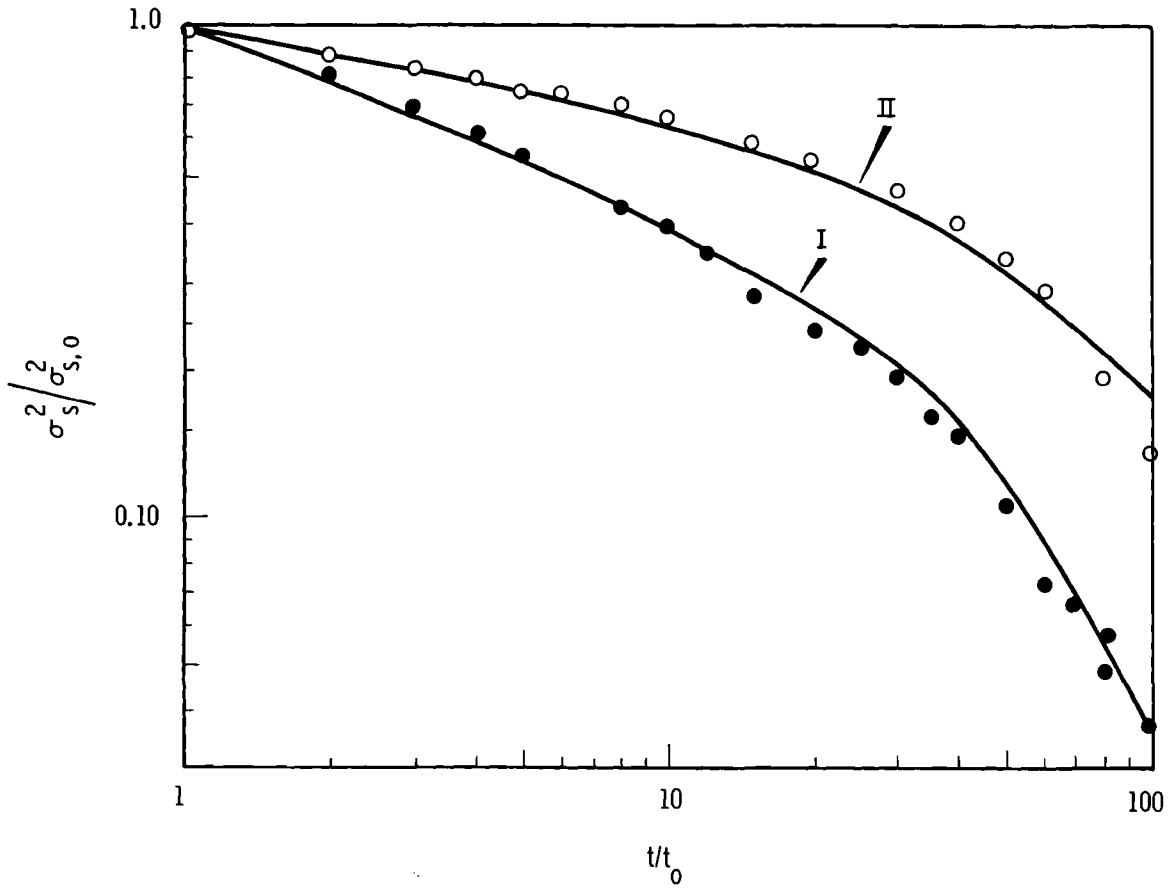

Neg. 0672184-1

FIGURE 2. Comparison of Observed Values of $\sigma_s^2/\sigma_{s,0}^2$ by o) and with Values Calculated from the Solution to Equation (32) (solid line).

The data for Curve I came from the observed fluctuations of concentration in the wake of a building during a diffusion trial. For Curve II, the data were observed as crosswind fluctuations at a height of 50 feet. The observed and calculated forms are satisfactorily close.

The assumption leading to Equation (32) implies a form for the autocovariance function, P(t/2):

$$P(t/2) = \frac{2 + b + kt}{2}\sigma_s^2 \qquad (33)$$

which may be compared with data, also as shown in Figure 3. Again, the fit is satisfactory. Although the detail of the observed autocovariance function is missing in the calculated function, the scale and general behavior are well represented.

The approach to calculating the variance of an increasingly smoothed variable presented here then leads to workable results with simple equations, and may provide a usable tool for working with rather complex functions and relations.

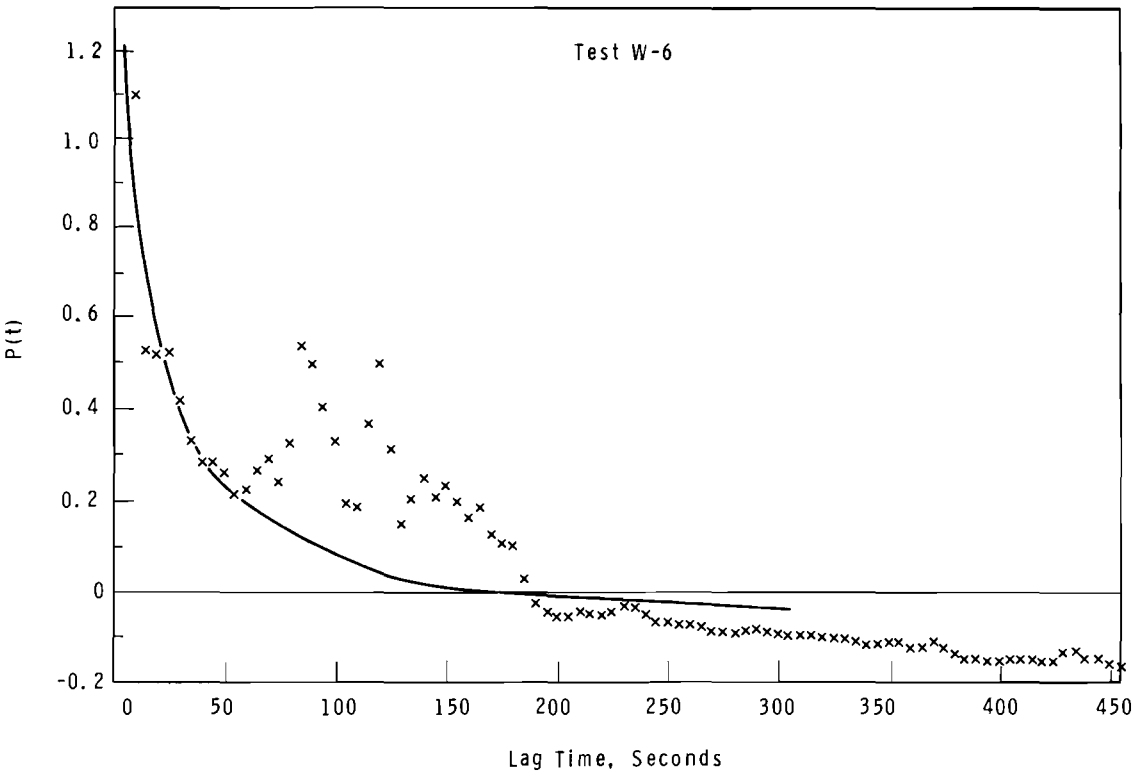

Neg. 0672563-6

FIGURE 3. Observed Values of Autocovariance Function (indicated by x) Compared with Values Calculated from Equation (33) (solid line).

REFERENCES

1. *F. Pasquill. Atmospheric Diffusion. D. Van Nostrand, Inc., Princeton, New Jersey, 1962.*

2. *A. B. Kahn. "A Generalization of Average-Correlation Methods of Spectrum Analysis." J. Meteorol. vol. 14, no. 9, 1957.*

3. *G. I. Taylor. "Diffusion by Continuous Movements," Proc. London Math. Soc., ser.2, vol.20, p. 196. 1921.*

4. *P. F. Frenzen. "Determination of Turbulence Dissipation by Eulerian Variance Analysis." Quart. J. Roy. Meteorol. Soc., vol. 91, p. 28. 1965.*

5. *W. T. Hinds. On the Variance of Concentration in Plumes and Wakes, BNWL-SA-1435. Pacific Northwest Laboratories, Richland, Washington, 1967.*

6. *I. A. Singer, K. Imai and R. G. DelCampo. "Peak-to-Mean Pollutant Concentration Ratios for Various Terrain and Vegetation Cover," J. Air Pollution Control Assoc., vol. 13, no. 1, p. 40-42. 1963.*

EXPERIMENTAL STUDIES IN PRECIPITATION SCAVENGING

M. T. Dana and M. A. Wolf

INTRODUCTION

The importance of submicron particles as carriers of fission products has resulted in the present research emphasis on the scavenging process. This present contribution discusses the extension of the earlier work of Engelmann, et al.[1] in establishing the washout coefficient and characteristics of the submicron silver iodide aerosol and investigating the role of dry deposition in the scavenging experiments. The development and utilization of new equipment is also discussed.

SILVER IODIDE STUDIES

Washout Coefficients

Results of silver iodide scavenging tests not included in a previous report by Engelmann and Hagen[2] are now available. The results of all 13 valid tests are shown in Figure 1. It is seen that the washout in rain and in mixed snow and rain apparently does not differ from the washout in snow. It is of particular interest that washout coefficients on the 100 ft and 200 ft arcs for Test 22 differ by a factor of greater than two. It is suggested that the increase on the outer arc is due to dry deposition enhanced at greater distances from an elevated source by increased concentration near the surface. Such deposition might likewise account for the observed scatter of data. It is seen that dry deposition can account for three times the removal by precipitation if the lower line in the figure represents washout only and the upper line is an approximation to the sum of washout and maximum dry deposition. Studies of dry deposition, described in the next section were initiated as a result of these observations.

Particle Size

Silver iodide particle size was required for the comparison of theory with field results.* An electron microscope grid previously exposed in the smoke plume resulting from combustion of an acetone solution of silver iodide was photographed in an electron microscope. The particle images appearing on a print of 45000X magnification were sized statistically. The resultant log-normal distribution of particle size had a median diameter of 0.012 μ.

There was some concern that the low inertia of the minute particles would result in their retention in the flow around the grid so that only the smallest particles, those responsive to diffusive forces, would be collected. Attempts were

* *See "Precipitation Scavenging of Submicron Particles: A Comparison of Theory with Field Results" by D. I. Hagen in this Report.*

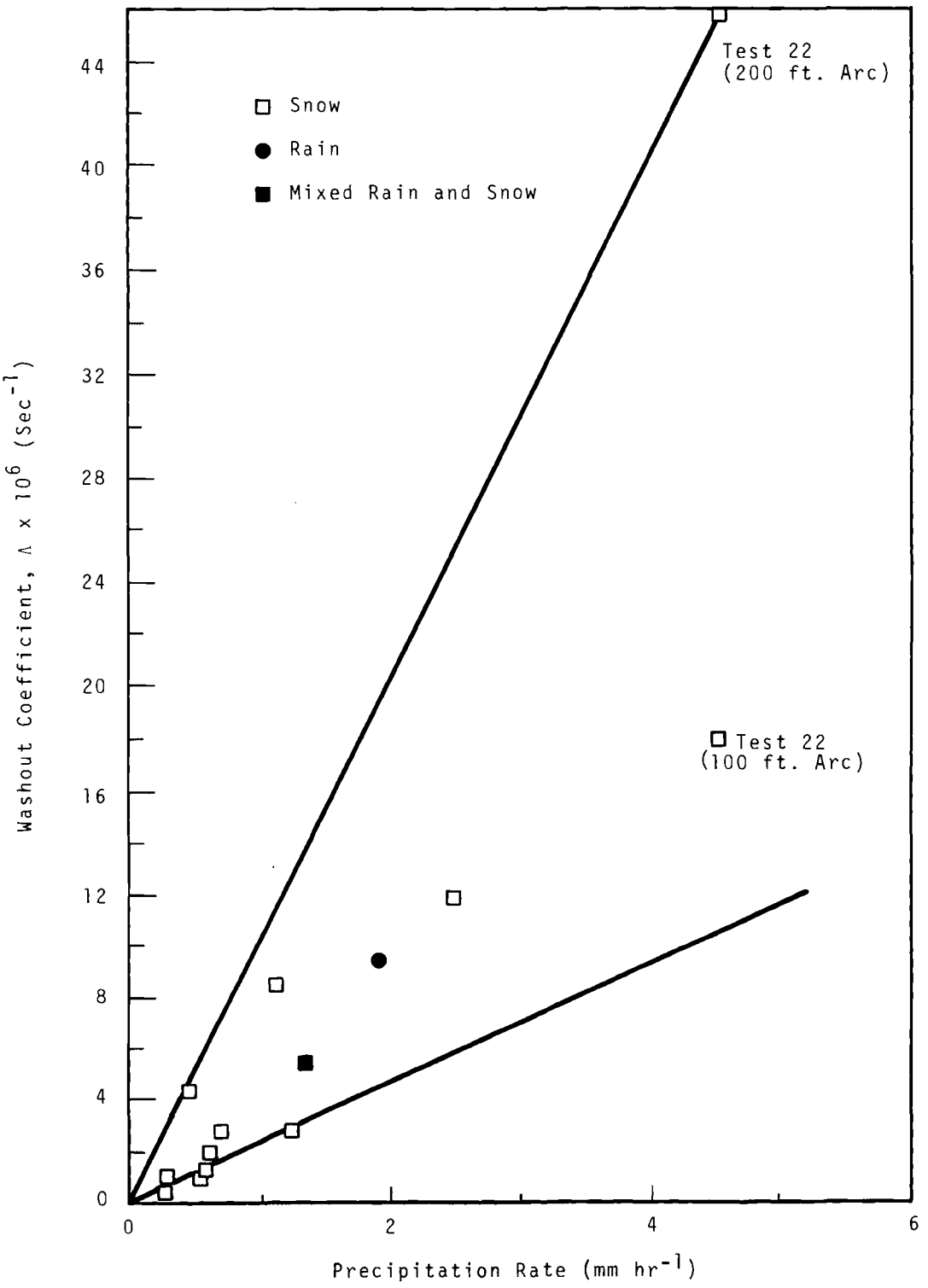

FIGURE 1. Silver Iodide Washout Coefficients

made to sample the smoke by thermal and electrostatic precipitators in order to avoid small particle bias. No successful size distributions were obtained with these precipitators due to irregular deposition on the microscope grid. Presumably, this irregular deposition was due to aerosol coagulation and to deposition and reentrainment of the aerosol in the transport tube.

Another consideration in establishing the particle size of silver iodide smoke is the nature of the generated aerosol. Sodium iodide, added with silver iodide to the acetone to permit solution of the silver iodide, is hygroscopic. Consequently, the size of the emitted aerosol particles may be increased through combination with water. An analysis of the vapor pressure equations for solution droplets, along with the assumption that the smoke acts as a solute, led to an estimate that the droplets could be three times the diameter of the initial particle. Recent experiments by dePena and Caimi[3] have shown that diameters of water droplets formed on similarly produced particles were up to 60 times the particle diameters. These authors expressed doubt as to the chemical composition of the resultant particles. Efforts will be continued in an attempt to resolve the question of particle size.

DRY DEPOSITION STUDIES

The probability that dry deposition contributed silver iodide to the precipitation samples used in the determination of washout coefficients led to an investigation of this mode of aerosol removal in conjunction with scavenging operations. The approach selected for obtaining this information with the least modification to the existing techniques for scavenging studies was to collect rain samples on several arcs in each test, observe differences in aerosol washout coefficient with distance, and measure aerosol exposure with air filter samples located at precipitation sampler height to verify aerosol presence near the ground.

Fluorescein Aerosol System

An additional system sufficiently sensitive to allow assay of an aerosol in individual precipitation samples and on individual filters for their comparison was required. This capability also would permit the documentation of plume containment. Moreover, it was desired that the system permit rapid and inexpensive assay in the field. Such a system could be provided by using fluorescein as the aerosol and a G. K. Turner Associates, Model 110 fluorometer for assay. The high humidities present during precipitation scavenging experiments ruled out the wet generation technique described by Nickola[4] and a dispenser, described in a later section, was developed.

Field Operation

It was desired that dry deposition of silver iodide be directly

observed, although the fluorescein system was anticipated to describe the extent of dry deposition more fully. It was decided, therefore, to release both aerosols concurrently and to observe the dry deposition of silver iodide only through enrichment at more distant arcs. Due to operational problems, only two tests in this series of six were dual releases. Another test involved silver iodide only and the remaining three tests utilized fluorescein alone.

Multiple arc sampling was provided for all tests with samples at 6° intervals on at least two of the arcs A, B, and C at 50, 100, and 150 ft, respectively. Insofar as has been determined from the fluorescein analysis, the plumes were contained. Because analysis of silver iodide samples has not been completed, no additional discussion of that phase will be presented here.

This test series was performed at Quillayute, Washington, near the coast on the Olympic Peninsula. Tests were conducted in a variety of precipitation conditions with winds between 2 and 6 m/sec and rainfall rates between 1.5 and 8 mm/hr. Rainfall rate was measured with a rapid response rain gage. The raindrop size spectra were determined with Ozalid paper in a manner similar to that previously reported by Engelmann.[5] Measurements of turbulence were attempted during each test with a three-component propeller and bidirectional vane sensor in an effort to observe the relationship of dry deposition and turbulence. Conventional surface and upper air meteorological parameters were available from the Weather Bureau station at Quillayute.

At least two, and generally four, air filters were exposed during each fluorescein test. Positions adjacent to precipitation samplers on the 100 ft arc were sampled in all but one fluorescein test. In the other test, filter samplers were located on the 50 and 150 ft arcs. The filters were faced downward on special mounts located about 15 in. above the ground. Plastic hoods protected the filter face from the rain. No wetting by direct rain or splash was observed on examination of the filter after exposure. Sampling rate was approximately 4 cfm but the effective sampling rates are unknown. Tests conducted at Hanford on the comparative effective sampling rates of upwind-facing and downward-facing filters, while inconclusive, have suggested that the efficiencies or effective sampling rates are dependent on wind speed.

It was planned to generate fluorescein for 30 min in each test. The first test was terminated after 15 min because release of an excessive amount was suspected. Subsequent tests were for periods of three and five minutes duration. Although no differences in the distributions relating to the duration of release were apparent, longer releases will be made in the future. Table I presents some pertinent information on the field operations.

TABLE I. Field Operation Data

Test No.	Duration of Aerosol Emission, min	Sampler Locations	
		Precipitation	Air
UIL-1	15 min	Arcs A and B	Arcs B and C
UIL-2	3	Arcs A and B	Arc B
UIL-3	3	Arcs A and B	Arcs B and C
UIL-4	5	Arcs A and B	Arc B
UIL-6	5	Arcs A, B and C	Arcs A and C

RESULTS

The calculated washout coefficients for all precipitation scavenging tests with fluorescein at Quillayute, contrary to scavenging theory but consistent with previous indications of dry deposition, showed significantly increased values with distance. The calculated washout coefficients are shown as a function of rainfall in Figure 2. These coefficients were calculated using the experimental data contained in Table II and the equation

$$\Lambda = \frac{\bar{u}\ \Delta Y \Sigma C}{QA}, \text{ where} \qquad (1)$$

- Λ is the washout coefficient, sec^{-1}
- u is the mean wind speed at source height, cm/sec
- ΔY is the precipitation sampler spacing along the arc, cm
- A is the precipitation sampler horizontal cross-sectional area, cm^2
- Q is the amount of fluorescein released, g
- ΣC is the total amount of fluorescein recovered on each arc, g.

It should be noted that ΣC is reduced for background, measured during the test but containing whatever contribution may result from dry deposition.

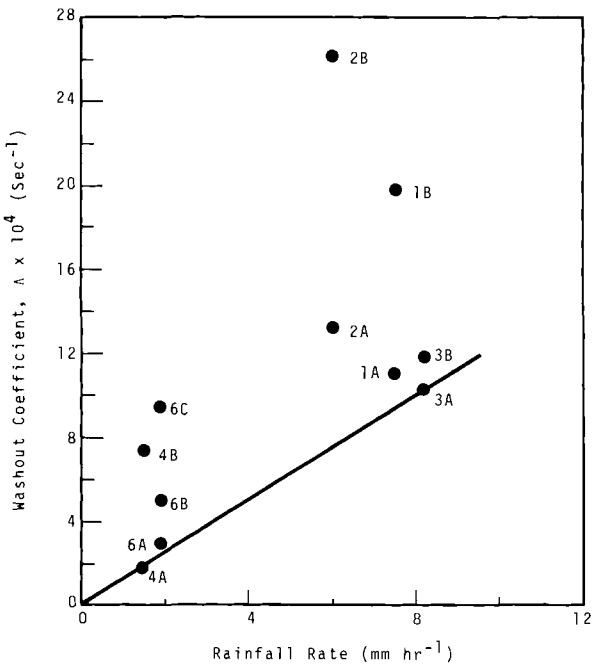

FIGURE 2. Fluorescein Washout Coefficients from Quillayute Tests

The distributions of fluorescein mass for each test are shown in Figures 3a through 3e. Areas under the curves are proportional to the total mass deposited along each arc per unit downwind distance. These curves clearly show the increased removal with distance which, presumably, is due to dry deposition. Each set of curves would, with only washout involved, be expected to resemble the set for UIL-3, that is, the peak lowered and width broadened with distance as the cloud diffuses laterally in its downwind travel. The more symmetrical curves, Arc A for Tests 3 and 4, are associated with the least dry deposition, as shown in Figure 2.

TABLE II. Experimental Data

a. Washout Data

Test No.	Mean Wind Speed, cm/sec	Rainfall Rate, R* mm/hr	Source, g	Total Mass Recovered, mg Arc A	Arc B	Arc C
UIL-1	492	7.5	298	3.75	3.40	....
UIL-2	581	6.0	25	0.324	0.320	....
UIL-3	380	8.2	44	0.676	0.391	....
UIL-4	380	1.5	83	0.215	0.447	....
UIL-6	179	1.9	106	1.01	0.813	1.02
			ΔY (cm)	160	320	480

The sampler cross-sectional area, A, was calculated to be 920 cm^2.

b. Deposition Data

Test No.	Arc A I	Arc A II	Arc B I	Arc B II	Arc C I	Arc C II
UIL-1	...	...	36.2	418	...	...
UIL-2	...	...	3.54	22	...	...
UIL-3	...	...	0.07	56	...	...
UIL-4	...	...	11	98	...	...
UIL-6	0.2	72	...	...	13	264

I - *Fluorescein mass in air sampler filters (μg)*

II- *Fluorescein mass in adjacent precipitation samplers (μg)*

The effect of dry deposition could be removed from the test data should the curve in Figure 2 (through the Arc A points of Tests 3 and 4) be assumed to represent the relationship of washout coefficient to rainfall rate in the absence of dry deposition. The apparent washout coefficients plotted in Figure 2, the corrected coefficients located on the curve at appropriate rainfall rates, and the ratio of the latter to the former are summarized in Table III. Using the corrected values of washout coefficient, the amount of aerosol removed by washout can be calculated from Equation (1) and the amount removed by dry deposition thereby determined from the measured total collection. All three values are tabulated in Table IV.

Pasquill[6] and others note that aerosol dry deposition is proportional to the aerosol exposure above

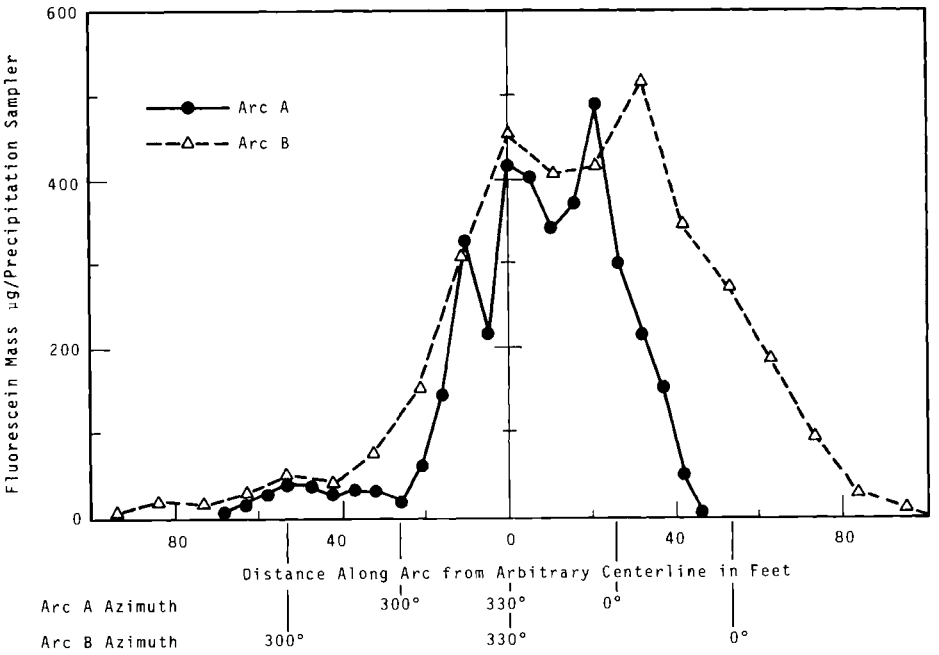

FIGURE 3a. Surface Distribution of Fluorescein for Test UIL-1

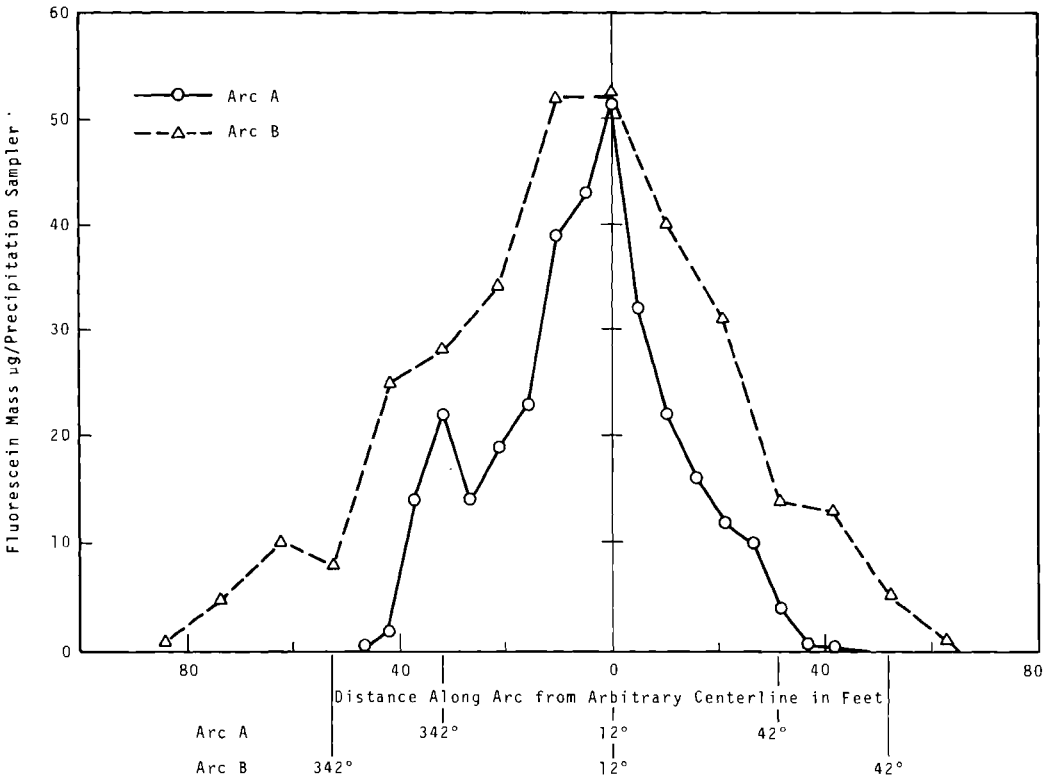

FIGURE 3b. Surface Distribution of Fluorescein for Test UIL-2

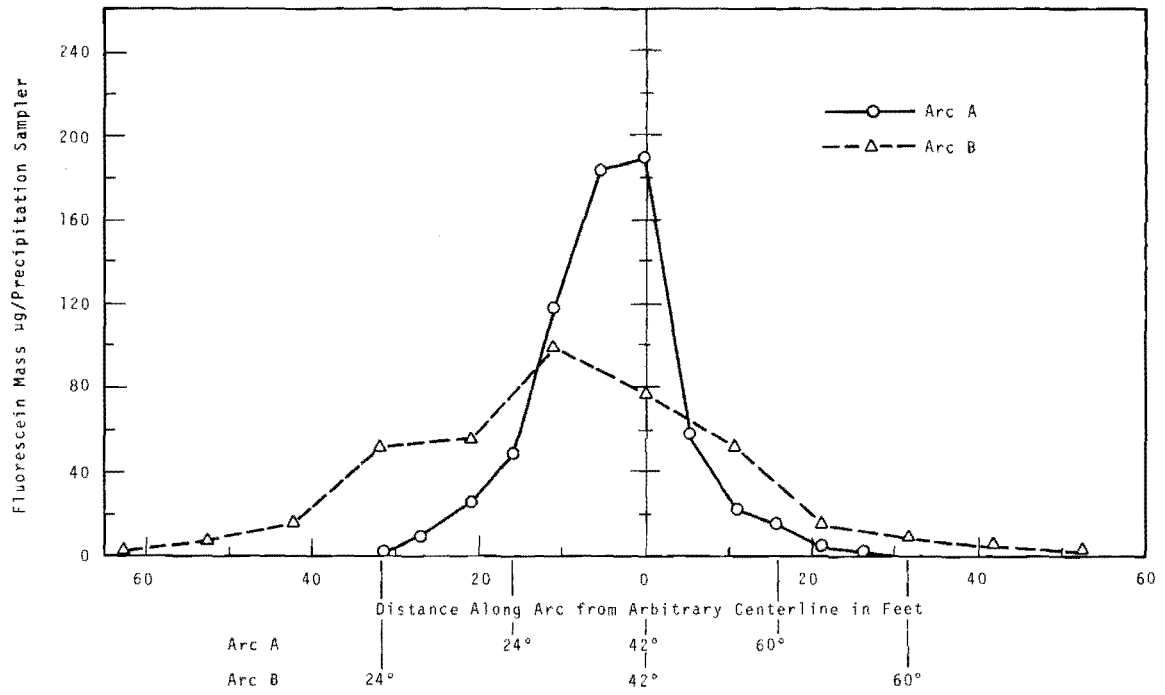

FIGURE 3c. Surface Distribution of Fluorescein for Test UIL-3

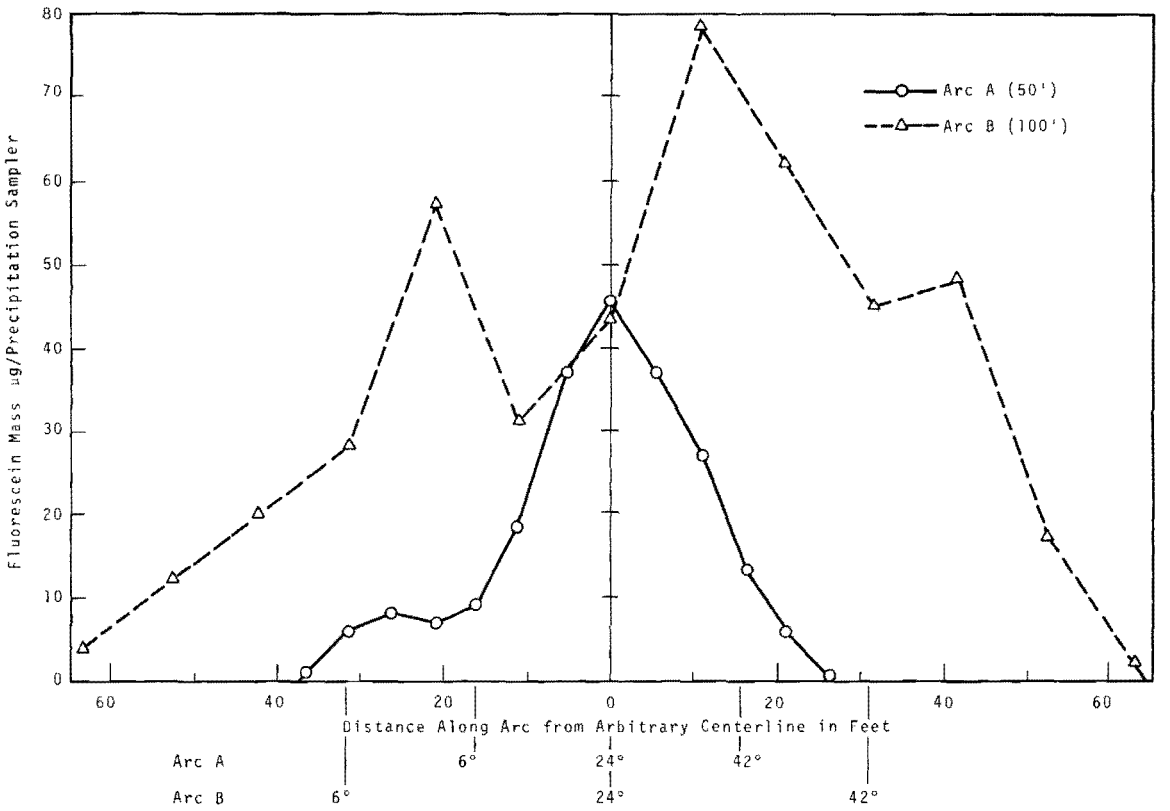

FIGURE 3d. Surface Distribution of Fluorescein for Test UIL-4

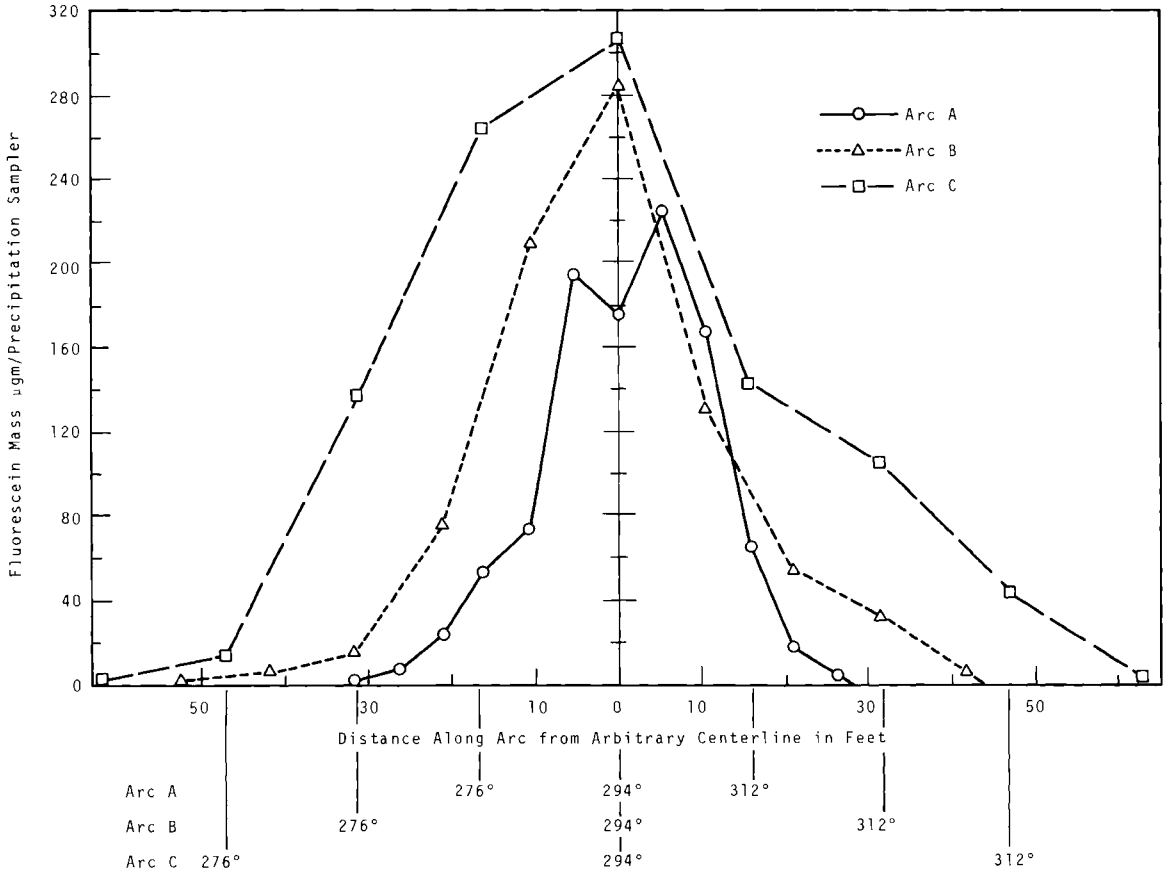

FIGURE 3e. Surface Distribution of Fluorescein for Test UIL-6

TABLE III. Washout Coefficients

Test No.	Arc A			Arc B			Arc C		
	I	II	III	I	II	III	I	II	III
UIL-1	11.0	9.4	0.86	19.8	9.4	0.48	...	...	....
UIL-2	13.2	7.5	0.57	26.2	7.5	0.29	...	...	....
UIL-3	10.3	10.3	1.0	11.9	10.3	0.87	...	...	....
UIL-4	1.8	1.8	1.0	7.4	1.8	0.24	...	...	....
UIL-6	3.1	2.3	0.74	5.0	2.3	0.46	9.5	2.3	0.24

I - *Apparent washout coefficient* $\Lambda_A \times 10^4$ sec^{-1}

II - *Corrected washout coefficient,* $\Lambda_C \times 10^4$ sec^{-1}

III - Λ_C/Λ_A

TABLE IV. Dry Deposition

Test No.	Arc A			Arc B			Arc C		
	I	II	III	I	II	III	I	II	III
UIL-1	3.75	3.28	0.47	3.40	1.64	1.76	...	...	...
UIL-2	0.324	0.186	0.138	0.320	0.093	0.227	...	...	...
UIL-3	0.676	0.685	0	0.391	0.342	0.049	...	...	...
UIL-4	0.215	0.226	0	0.447	0.113	0.334	...	...	...
UIL-6	1.01	0.78	0.23	0.813	0.391	0.422	1.02	0.26	0.76

I - *Total mass removed along the arc, mg*
II - *Mass removed by washout, mg*
III - *Mass removed by dry deposition, mg*

the surface. The ratio of dry deposition per unit area, D, to the exposure, E, has been termed the deposition velocity given by

$$V_d = \frac{D}{E} \qquad (2)$$

Two pathways are available for determining whether the values established for dry deposition infer reasonable deposition velocities. The first uses the exposure and deposition values measured at adjacent precipitation and filter samplers. The second compares the arc-integrated dry deposition mass with exposure theoretically determined from experimental meteorological data and diffusion theory.

Filter mass is taken directly from Table IIb and the exposure determined by dividing by the sampling rate of 6 cfm. The dry deposition mass is derived from the precipitation sampler mass reduced by the factors, the ratios of Column III to Column II in Table IV. The dry deposition mass divided by the cross-sectional area of the precipitation sampler is the deposition, D, required by Equation (2). Discussion of deposition velocities determined in this manner and appearing in Table V is deferred to explain the method of obtaining the theoretical values also shown in Table V.

The mean dry deposition for the arc-integrated, dry-deposited mass to be used in Equation (2) is simply the dry deposition value in Table IV, C_d, divided by the product of the precipitation sampler cross-sectional area and the number of samplers used to collect the total mass, $\frac{\Sigma C_d}{NA}$.

The cross-wind integrated exposure at the surface is obtained from the equation given by Pasquill[6] for a continuous point source by integrating cross-wind between plus and minus infinity as

$$CIE = \frac{Qe^{-1/2(\frac{z}{\sigma z})^2}}{(2\pi)^{1/2}\bar{u}\sigma_z} \qquad (3)$$

TABLE V. Deposition Velocities, $\overline{V_d}$, cm/sec^{-1}

Test No.	Arc	Experimental	Theoretical
UIL-1	A	....	1.21
UIL-2	A	....	2.12
UIL-6	A	246	6.10
UIL-1	B	17.8	3.34
UIL-2	B	13.2	6.69
UIL-3	B	300	0.69
UIL-4	B	19.9	3.94
UIL-6	B	....	1.08
UIL-6	C	31.6	2.21

where,

σ_z is the standard deviation of aerosol distribution in the vertical

$\bar{u}$ is the source height mean wind

z is the source height

Q is the amount of aerosol released

The mean exposure, then, is $\frac{CIE}{N\Delta Y}$, and the deposition velocity can be written as

$$V_d = \frac{(2\pi)^{1/2}\bar{u}\sigma_z\Delta Y\Sigma C_d\, e^{1/2(z/\sigma_z)^2}}{AQ} \quad (4)$$

An approximation of σ_z, using turbulence measurements, is given by Islitzer[7] as 0.81 σ_ϕX. Although σ_ϕ, the standard deviation of the bivane elevation angle, was measured at Quillayute, complete data are not available. However, σ_u, the standard deviation of the longitudinal wind component, was measured for all tests and, as shown by Elderkin and Hinds,[8] the standard deviation of the vertical wind component is related to σ_u by σ_w = 0.67 σ_u, where σ_u is determined with a 160 sec running mean. It is appropriate here since σ_u was determined for a 3 min sampling. Thus

$$\sigma_\phi = \frac{\sigma_w}{\bar{u}} = 0.67\,\frac{\sigma_u}{\bar{u}} \quad (5)$$

The resulting values for this theoretical calculation of deposition velocity are included in Table V with the deposition velocities calculated from measured exposures. The latter determination is observed to have larger values in all instances. In addition, the associated mean wind speeds shown in Table IIa are inversely related to these experimentally determined deposition velocities. If mass collected by a filter oriented normal to the mean wind is reduced, larger values of deposition velocity would be accounted for but the inverse relation with deposition velocity would not. Generally, increased wind speed also implies increased turbulence. Were an increase in the vertical component of turbulence to result in increased impaction on the filter, the inverse relationship of speed and deposition velocity would result. A factor to account for both wind speed and the vertical component of turbulence in the experimental equation for deposition velocity, therefore, appears necessary. This factor, of course is σ_ϕ, the ratio of σ_w and $\bar{u}$.

With this factor identified, another interpretation is available. Equation (2), rewritten with the added factor and substitution of

the experimental notation of the exposure term becomes

$$V_d = \frac{D\sigma_\phi}{m_f/R} = \frac{D}{m_f/(S\frac{\sigma_w}{\bar{u}})\,V} \qquad (6)$$

where,

m_f is the mass on the filter
R is the filter flow rate
S is the filter area
V is the sampling velocity

It is apparent immediately that $S\frac{\sigma_w}{\bar{u}}$ is exactly the effective filter area for small values of σ_ϕ and a good approximation for all reasonable values. In the absence of mean wind, turbulence also should be absent and the term undefined. Therefore, under calm situations, the term should be omitted.

The experimental values of Table V are listed again in Table VI with the previously calculated values of σ_ϕ and their product. The two extremely high values were omitted since, in both cases, the measured masses on the filters were too low to be significant. The corrected deposition velocities, independent of wind speed, have been reduced to the approximate magnitude of the deposition velocities calculated from exposures determined from diffusion theory. Furthermore, mean values of these two sets of deposition velocities are within a factor of two of the deposition velocity of 5 cm/sec cited by Pasquill[6] as appropriate for a surface acting as a "perfect sink." Retention of soluble fluorescein on a wet surface should provide such a condition.

CONCLUSIONS

Analysis of this precipitation scavenging series with fluorescein is continuing. Availability of the silver iodide assay will provide an opportunity to compare results for the two materials. Subsequent series will provide additional data from which more definite conclusions can be drawn. Thus far, this first series has conclusively shown the presence of dry deposition in washout experiments. In addition, this dry deposition can be accounted for quantitatively by using the concept of deposition velocity with exposures either measured in the field or calculated from diffusion theory with appropriate turbulence measurements.

TABLE VI. Corrected Experimental Deposition Velocities

Test No.	Arc	Experimental V_d, cm/sec	σ_ϕ	$\sigma_\phi V_d$, cm/sec	$\bar{u}$, cm/sec
UIL-1	B	17.8	0.306	5.48	492
UIL-2	B	13.2	0.463	6.10	581
UIL-4	B	19.9	0.162	3.24	380
UIL-6	C	31.6	0.206	6.51	179

Finally, the washout coefficient for fluorescein is closely estimated, apparently, by the curve of Figure 2.

REFERENCES

1. *R. J. Engelmann, D. I. Hagen, W. A. Haller, and R. W. Perkins. Washout Coefficients for Silver Iodide, BNWL-SA-798. Pacific Northwest Laboratory, Richland, Washington, 1966.*

2. *R. J. Engelmann and D. I. Hagen. "Precipitation Scavenging Studies," Pacific Northwest Laboratory Annual Report for 1966, Volume II: Physical Sciences, Part 1. Atmospheric Sciences, BNWL-481 1, pp. 43-52. Pacific Northwest Laboratory, Richland, Washington, 1967.*

3. *R. G. dePena and E. A. Caimi. "Hygroscopicity and Chemical Composition of Silver Iodide Smoke Used in Cloud Seeding Experiments," J. Atmospheric Sci., vol. 24, no. 4, pp. 383-386. 1967.*

4. *P. W. Nickola. "Field Testing of a Fluorescein Zinc Sulfide Dual Atmospheric Tracer Technique," Hanford Radiological Sciences Research and Development Annual Report for 1964, BNWL-36. Pacific Northwest Laboratory, Richland, Washington, 1965.*

5. *R. J. Engelmann, Rain Scavenging Particulates, HW-79382. Available from Clearinghouse for Federal Scientific and Technical Information, Springfield, Virginia, 1963.*

6. *F. Pasquill. Atmospheric Diffusion, D. Van Nostrand Co. Ltd., London, 1962. pp. 231-235.*

7. *N. F. Islitzer. "Short-Range Atmospheric Dispersion Measurements from an Elevated Source," J. Meteorol., vol. 18, no. 4, pp. 443-450. 1961.*

8. *C. E. Elderkin and W. T. Hinds. "Prediction of Exposures from an Elevated Source," Pacific Northwest Laboratory Annual Report for 1965 in the Physical Sciences to the USAEC Division of Biology and Medicine, Volume I: Atmospheric Sciences, BNWL-235 1. Pacific Northwest Laboratory, Richland, Washington, 1966.*

STUDIES OF PRECIPITATION ELECTRICAL CHARGE

M. T. Dana

INTRODUCTION

The raindrop charge spectrometer, developed and modified over several years by C. A. Ratcliffe,[1,2] was designed specifically for the measurement of weak electrical charges associated with non-thunderstorm precipitation. The present instrument, technical details of which appear in another contribution to this report,* provides valuable data in support of studies of the precipitation scavenging process and other aspects of precipitation and cloud physics.

---

* *See "Improvements in Raindrop Charge Measuring System" by C. A. Ratcliffe and N. C. Hoitink, p. 155.*

The instrument system consists of a transducer, power supply, external amplifier, and a Brush two-channel electric writing recorder. In field operation, the transducer is mounted on a camera tripod (Figure 1) to allow adjustment of the angle of the inducing ring axis and is located at sufficient distance from the recorder to limit the influence of extraneous electric fields, mainly 60 cps power lines.

Charge pulses from falling hydrometeors are displayed on the Brush tape either as a sharp spike--indicating passage through the inducing ring without contact--or as a sharp initial voltage rise followed by exponential decay. The latter shape indicates contact with the ring and subsequent direct drainage of the charge into the circuit. Laboratory calibration with water drops artificially charged to known values revealed a response of 1.61 picocoulombs per volt output for the former pulse type, and 1.45 picocoulombs per volt for the latter. Typical sensitivity in field operation allows a charge magnitude of about 3×10^{-15} coulomb (three millipicocoulombs) to be read with ease from the record, but observations of charges as low as two millipicocoulombs--near the assumed internal noise level of the instrument--have been noted.

FIGURE 1. The Raindrop Charge Spectrometer

ANALYSIS OF DATA

Field observations of precipitation electrical charges have been carried out at the Meteorological Tower at Hanford and at the precipitation scavenging field experimental sites at Skykomish and Quillayute, Washington. Supplemental meteorological measurements were provided by a fast response rainfall rate recording instrument, by ozalid paper exposures to rain (for raindrop size), and by a three-component wind instrument. At Quillayute, surface and upper air data were drawn from weather station records. Charges on individual raindrops were recorded at all three locations and snowflake charges were recorded at Skykomish.

Most of the data were collected in light or calm wind conditions when hydrometeors of all sizes can be assumed to fall vertically and are sampled fairly by the vertical

transducer axis. In windy conditions, however, the "chimney" atop the transducer case apparently prevents the reception of an unbiased size sample. When the axis is vertical, a reduced number of pulses is noted, and the average charge appears higher than in adjacent samples taken in light wind. If the axis is inclined into the wind, more pulses are seen. These pulses, however, may represent smaller hydrometeors with charge magnitudes possibly below the average for all the falling precipitation.

Raindrop Charge

Samples of about 200 pulses each were taken from the records and plotted as statistical distributions (see Figures 2, 3, and 4). The abcissa represents raindrop charge in millipicocoulombs and the ordinate represents the number frequency of charge values in 1 millipicocoulomb intervals.

Table I lists pertinent charge data from analyzed portions of raindrop charge records, including: numbers of positively and negatively

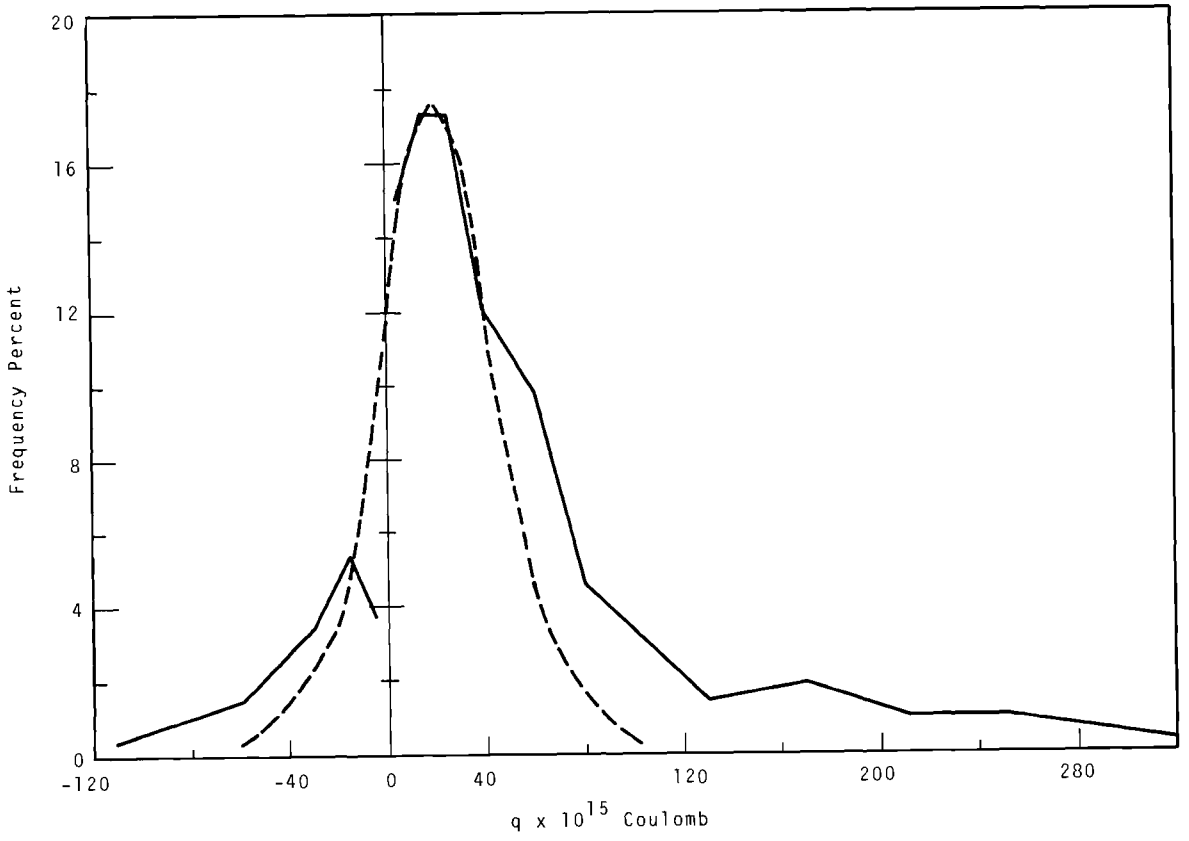

FIGURE 2. Charge Distribution for Sample U (See Table I). Broken Line is Fitted Gaussian Distribution

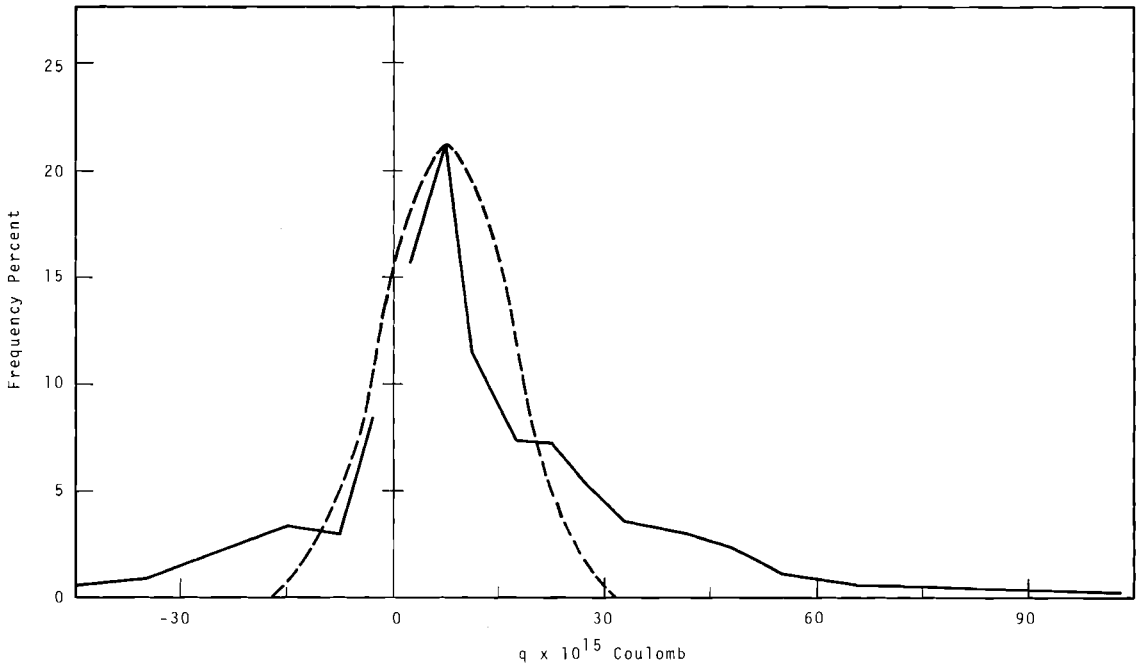

FIGURE 3. Charge Distribution for Sample T (See Table I). Broken Line is Fitted Gaussian Distribution

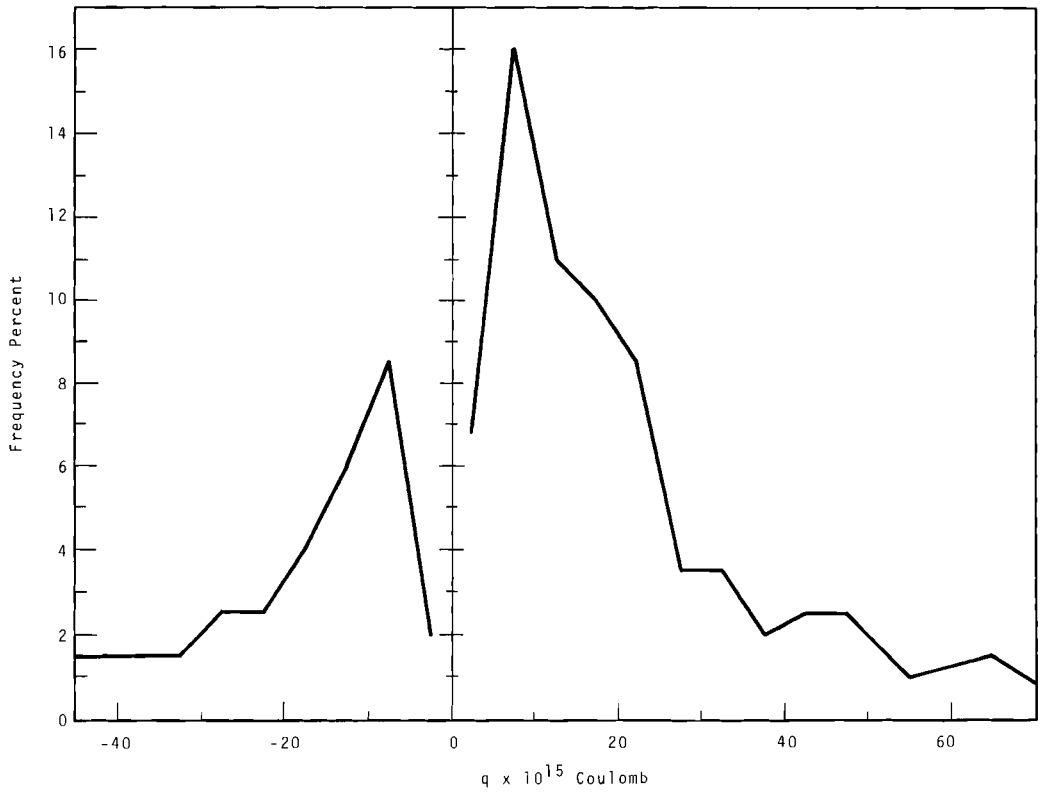

FIGURE 4. Charge Distribution for Sample F (See Table I).

TABLE I. Raindrop Charge Data

Sample	Location	Date	Time, PST	N+	N-	Charge, 10^{-15}C q+	q-	q	q*	q*/m, esu/g	R*, mm/hr
A	Hanford	11-8-67	1337	72	0	+144	0	+144	144	1.09	....
B	Hanford	11-8-67	1351	122	28	+109	- 63	+ 76	100	0.61	....
C	Hanford	11-8-67	1357	178	59	+ 95	-140	+ 37	64	0.53	....
D	Hanford	11-8-67	1407	79	26	+131	-299	+ 25	173	....	....
E	Hanford	11-8-67	1415	124	34	+ 86	- 50	+ 56	78	....	....
F	Skykomish	1-9-68	1132	148	63	+ 22	- 19	+ 10	21	....	....
G	Skykomish	2-20-68	1630	203	14	+ 68	- 39	+ 61	66	0.47	1.5
H	Skykomish	2-21-68	0950	186	32	+ 51	- 23	+ 40	47	....	1.9
I	Skykomish	2-21-68	1449	46	83	+ 36	- 34	- 9	31	0.36	1.1
J	Skykomish	2-21-68	1503	76	141	+537	-708	-272	648	2.19	3.9
L	Skykomish	2-22-68	1257	166	49	+295	-169	+190	267	....	11.5
M	Skykomish	2-22-68	1300	110	72	+287	-211	+ 88	258	....	5.6
N	Skykomish	2-22-68	1307	147	59	+ 66	- 39	+ 36	58	0.82	2.4
O	Skykomish	2-22-68	1313	87	167	+565	-212	+ 54	345	....	5.1
P	Skykomish	2-22-68	1321	18	13	+444	-395	+ 92	423	....	8.4
Q	Skykomish	2-22-68	1324	97	109	+199	-243	- 35	222	....	4.0
R	Skykomish	2-22-68	1332	102	90	+ 65	- 71	+ 4	68	....	1.1
S	Quillayute	3-26-68	1916	527	134	+158	-112	+103	148	0.36	9.1
T	Quillayute	3-28-68	1528	144	42	+ 22	- 17	+ 13	21	0.18	2.2
U	Quillayute	3-28-68	1541	185	31	+ 85	- 35	+ 67	78	....	2.6
V	Quillayute	3-28-68	1648	426	36	+ 93	- 21	+ 91	94	0.69	1.9
W	Quillayute	3-28-68	1341	148	54	+ 36	- 20	+ 21	32	0.18	1.2

charged raindrops (N+, N-) and their average charges (q+, q-) in millipicocoulombs; the average net charge on a drop (q); the average charge on a drop, averaged without respect to sign (q*); and rainfall rate (R*) in millimeters per hour. Table II includes: median and mean mass diameters (d, d_m) in millimeters from available ozalid paper spot distributions; the charge per unit mass ($\frac{q^*}{m}$) esu per gram (computed from the mass mean diameter); and available meteorological details.

The possibility of size bias in the samples taken in windy conditions should be considered in interpreting the charge averages. Sample P, bracketed by samples from relatively calm conditions, includes considerably fewer charge pulses per unit time with higher average magnitudes. All these samples were taken with the transducer axis vertical. It should be noted that larger raindrops (i.e., those falling more vertically) are not necessarily

TABLE II. Raindrop Size and Meteorological Data

Sample	Date	Time, PST	d	d_m	Wind Speed, mph	Temp., °F	R.H., %	Ceiling, ft
A	11-8-67	1337	0.5	0.91	Calm	52	60	....
B	11-8-67	1351	0.7	0.99	4-6	51	....	....
C	11-8-67	1357	0.4	0.88	4-6	47	77	....
D	11-8-67	1407	....	....	4	46	....	7000
E	11-8-67	1415	....	....	4	46	86	....
F	1-9-68	1132	....	....	Calm	34	99	....
G	2-20-68	1630	0.43	0.93	Calm	....	....	....
H	2-21-68	0950	....	....	Calm	42	96	....
I	2-21-68	1449	0.36	0.79	Calm	....	....	....
J	2-21-68	1503	0.28	1.19	Calm	....	....	3000
L	2-22-68	1257	....	....	Calm	44	95	....
M	2-22-68	1300	....	....	Calm	....	....	....
N	2-22-68	1307	0.56	0.74	Calm	....	....	....
O	2-22-68	1313	....	....	Calm	....	....	....
P	2-22-68	1321	....	....	6	....	....	....
Q	2-22-68	1324	....	....	3	....	....	....
R	2-22-68	1332	....	....	Calm	44	97	....
S	3-26-68	1916	0.53	1.24	9	47	100	400
T	3-28-68	1528	0.70	0.87	1	44	85	3000
U	3-28-68	1541	....	....	2	44	93	1800
V	3-28-68	1648	0.65	0.92	4	43	100	1800
W	3-28-68	1341	0.62	1.00	2	45	71	3000

more highly charged. One investigator,[3] simultaneously measuring size and charge of individual thunderstorm raindrops, found no fundamental charge-size relationship. The operation of an automatic raindrop sizer, currently in the planning stage of development in conjunction with the raindrop charge spectrometer, will resolve many such questions about the type of rainfall under study.

The distribution of charges was observed, in all cases with the rain data, to be approximately Gaussian in shape with a peak somewhat near zero charge. With most samples, an apparent dip near zero indicated the limitation of the instrument in measuring small charges. Thus, in the near-zero region, the true number of weakly charged raindrops will usually be in doubt. On one occasion, shown in Figure 3, the maximum sensitivity was attained and this dip was not apparent. This case seems to uphold the assumption that the near-zero magnitudes fit

into the general trend of the distribution. With few exceptions, the distributions have been peaked on the positive side, and fitted Gaussian curves approximate the observed distribution as shown in Figures 2 and 3.

Figure 5 compares the variations of the average positive and negative charge magnitudes, the net (measurable) charge current to the ground, and rainfall rate with time for a 34 min period at Skykomish. These curves illustrate the spread

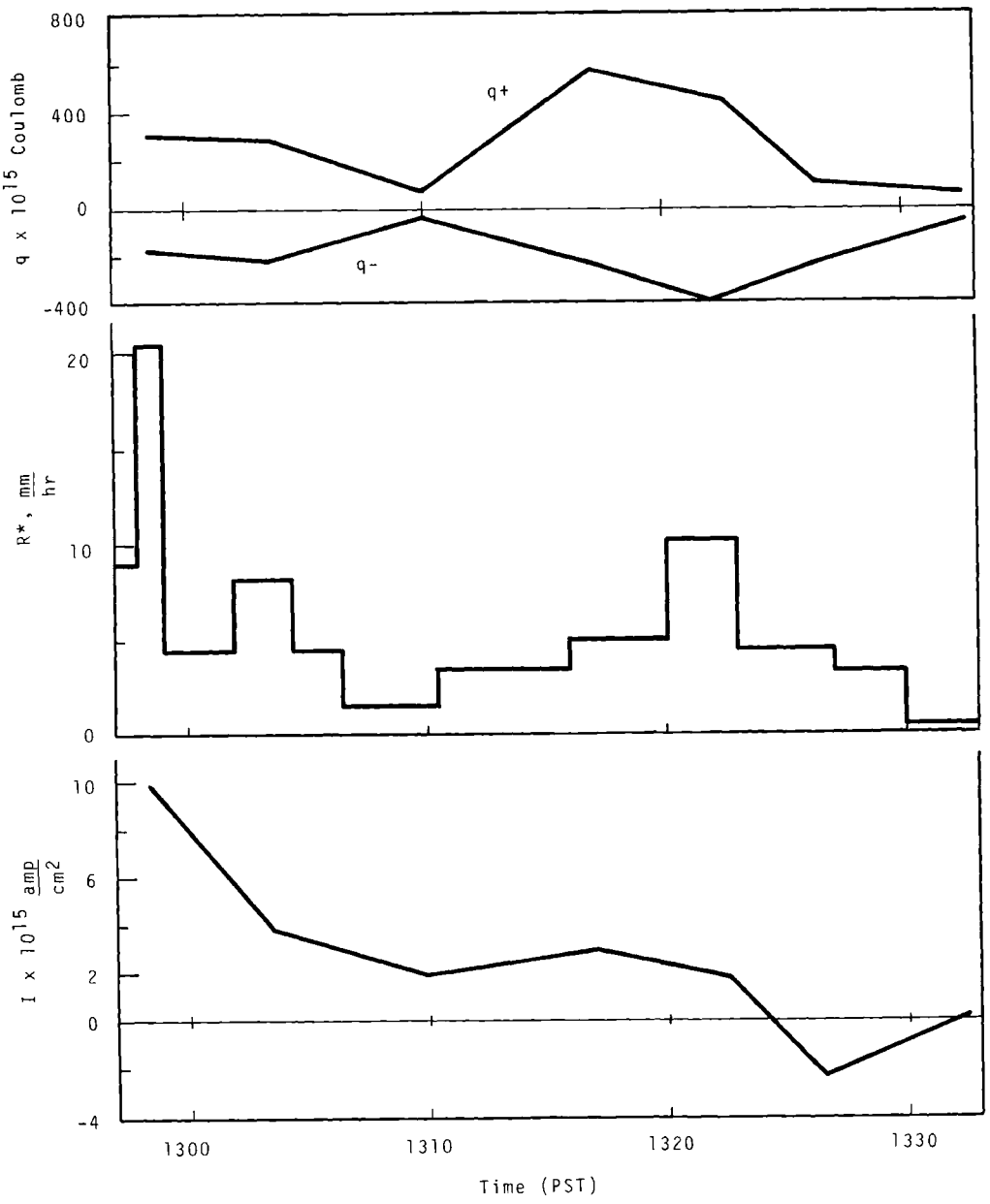

FIGURE 5. Charge Averages, Rainfall Rate, and Current Versus Time for Samples L-R (See Table I).

of the charge distribution with increased rainfall rate. While the average charge, q*, generally increased with rainfall rate, the dependency is apparently a complicated function of the total characteristics of a particular storm or locale. In the case of Figure 5, the current is shown to decrease in value with time without apparent regard for rainfall rate.

Snow Charge

Although a considerable amount of charge data for snowflakes was accumulated at Skykomish, interpretation of the exact nature of the pulses remains a problem. Because the flakes have generally lower and widely variable fall velocities, the pulses are of various widths and shapes, and lack the sharp initial rise characterizing the raindrop pulse. The large size and irregular shape of the snowflake also complicates the nature of the pulse.

A qualitative examination indicates the Skykomish snow charge pulses to be predominantly negative, with magnitudes on the order of the raindrops. Figure 4 is a charge distribution for a sample of raindrops taken at Skykomish. This period of rainfall at near freezing temperature, immediately preceding a change to snow pellets, indicates that the rain most probably had just melted from snow. The range of magnitudes was severely limited, with a mean charge near zero.

COMPARISON TO PRECIPITATION CHARGING THEORY

The most complete precipitation charging theory is that presented by Gunn.[4-10] He points to the vast complexity of possible mechanisms responsible for the polarity and magnitude of individual hydrometeor charges and the character of distributions of them. The predominant initial charging mechanism is the diffusion of cosmic ray-produced ions to cloud droplets. The result of this random process is a Gaussian distribution, the displacement of the peak being dependent on the relative atmospheric conductivities for positive and negative ions. As the droplets fall and combine with other droplets, the random nature of the collision process guarantees the continued Gaussian nature, though the standard deviation will increase. The location of the peak (median charge value) depends on the local ionic conductivity ratio and is limited in magnitude by Coulombic interactions between highly charged drops. A great deal of observation has shown the ionic conductivities at non-thunderstorm rain forming levels to be such that the peak of the charge distribution will be on the positive size of zero charge.

Other charging mechanisms, those dependent upon the presence of significant atmospheric electric fields, include charge separation by non-associating collisions between hydrometeors, and by the effect of a

strong field in separating charge in single drops. The former process results in pairs of oppositely charged drops, while the latter results in highly charged drops all of the same sign. These "influence processes" result, according to Gunn, in charge magnitudes proportional to the value of the field and to the square of a characteristic dimension of the hydrometeors.

The magnitudes tabulated in Table I are substantially higher than those predictable from the ionic diffusion and coagulation mechanisms, while the tendency for the majority of the drops to be positively charged agrees with the findings of Gunn. Charging due to electric fields could vastly outweigh the other mechanisms and potentially change the sign of the majority of the charges separated by them, however. In all the tabulated collection periods, the range of magnitudes increased with rainfall rate, i.e., increased with an increase in the size and/or number of raindrops. It is reasonable to assume that an increase of liquid water in the air would increase the chances of collisions and an increase in size would allow greater charge separation in the presence of electric fields. Sufficiently high electric fields have been reported in non-thunderstorm conditions. Gunn, in fact, has reported that ionic diffusion alone often can separate enough charge to produce these fields. An array of ice contact and change-of-state charge separation theories also may hold true under proper conditions.

RAINDROP CHARGE AND PRECIPITATION SCAVENGING

The effect of electrical charge on both precipitation and atmospheric contaminants has been shown to be of potential importance in the scavenging process, particularly when submicron particulates are involved. The data from Quillayute contained in Tables I and II accompanies precipitation scavenging experiments utilizing both submicron silver iodide and a larger diameter particulate. The charges found even on light rains are sufficient to be of consequence to the washout of charged submicron particulates.*

Future laboratory experiments, utilizing a water drop-contaminant interaction chamber currently under development, will provide better control of the many atmospheric variables encountered in the field. The aim of these experiments will be to measure collection efficiencies as a function of water drop and aerosol characteristics. An important variable in these studies will be the charges on the water drops and aerosol. The results of these experiments, along with a more complete body of charge data from field experiments and the developing theory, will lead to correlations between charge characteristics and the scavenging of atmospheric contaminants by precipitation.

---

* *See "Precipitation Scavenging of Submicron Particles: A Theoretical Analysis" by W. G. N. Slinn, in this report.*

REFERENCES

1. C. A. Ratcliffe and N. C. Hoitink. "Raindrop Charge and Velocity Measurement Techniques," Pacific Northwest Laboratory Annual Report for 1965 in the Physical Sciences, Volume 4: Instrumentation, BNWL-235 4, p. 21. Pacific Northwest Laboratory, Richland, Washington, 1966.

2. C. A. Ratcliffe. "Improvements in Raindrop Charge Measuring Systems," Pacific Northwest Laboratory Annual Report for 1966 to the USAEC Division of Biology and Medicine, Volume II: Physical Sciences, Part I: Atmospheric Sciences, BNWL-481 1, p. 74. Richland, Washington, 1967.

3. L. G. Smith. "The Electric Charge of Raindrops," Quart. J. Roy. Meteorol. Soc., vol. 81, p. 23. 1955.

4. R. Gunn. "The Electrification of Precipitation and Thunderstorms," Proc. I.R.E. vol. 45, p. 1331. 1957.

5. R. Gunn. "The Statistical Electrification of Aerosols by Ionic Diffusion," J. Colloid Sci., vol. 10, p. 107. 1955.

6. R. Gunn. "The Non-Equilibrium Electrification of Raindrops by the Association of Charged Cloud Droplets," J. Meteorol., vol. 14, p. 326. 1957.

7. R. Gunn. "Raindrop Electrification by the Association of Randomly Charged Cloud Droplets," J. Meteorol., vol. 12, p. 562. 1955.

8. R. Gunn. "Droplet Electrification Processes and Coagulation in Stable and Unstable Clouds," J. Meteorol., vol. 12, p. 511. 1955.

9. R. Gunn. "The Hyperelectrification of Raindrops by Atmospheric Electric Fields," J. Meteorol., vol. 13, p. 283. 1956.

10. R. Gunn. "The Systematic Electrification of Mist and Light Rain in the Lower Atmosphere," J. Geophys. Res., vol. 60, p. 23. 1955.

IMPROVEMENTS IN RAINDROP CHARGE MEASURING SYSTEM

C. A. Ratcliffe* and N. C. Hoitink*

Improvements incorporated into the raindrop charge measuring system used in atmospheric studies reduced transducer microphonics, improved charge induction geometry, reduced adverse environmental operating characteristics, and increased the charge sensitivity to approximately 10^{-15} C. The use of an electrostatic pen recording method allowed system operation under adverse climatic conditions. Extensive field tests, on a continuing basis with power obtained by using batteries for the electronics and a portable ac generator for the recording equipment, evidenced marked operational improvement.

DISCUSSION

During the year, selective field tests of the raindrop charge measuring system led to incorporation of specific improvements in design and resulted in considerably enhanced operation. Earlier efforts[1,2] proved satisfactory in the laboratory and under favorable field conditions; however, general performance problems occurred during adverse weather.

The improved transducer previously reported[2] demonstrated partial but inadequate success. Some of the problems concerned microphonics, resulting from the use of long insulators, and minute capacitance changes that introduced extraneous charge signals.

A new ruggedized transducer design (Figure 1) used 0.25 in. aluminum alloy components. This design includes an insulator arrangement that provides high resistance to moisture problems, superior microphonic characteristics, and improved geometry for charge induction.

The electronic portion of the system comprises an amplifier, power supply, and recorder. The present amplifier uses a Philbrick Research Model P2A operational device rather than the more easily damaged MOS field-effect transistor method used in the earlier designs. The approach shown in Figure 2 operates at virtual ground mode by means of the feedback arrangement, which thus reduces amplitude fluctuations caused by changes in capacitance between elements of the transducer. The 1 to 2 pF feedback capacitor determines the charge sensitivity. This amplifier increases the sensitivity by approximately an order of magnitude over that previously reported;[2] thus, charge measurements can be made down to about 10^{-15} C.

The included postamplifier--with gains of 1, 10, and 100--provides signal conditioning to produce signals compatible with the recording system, presently a Brush Mark II, Model RD 2522-20 dual-channel unit with electric writing to

* *Instrumentation Section, Applied Physics and Electronics Department*

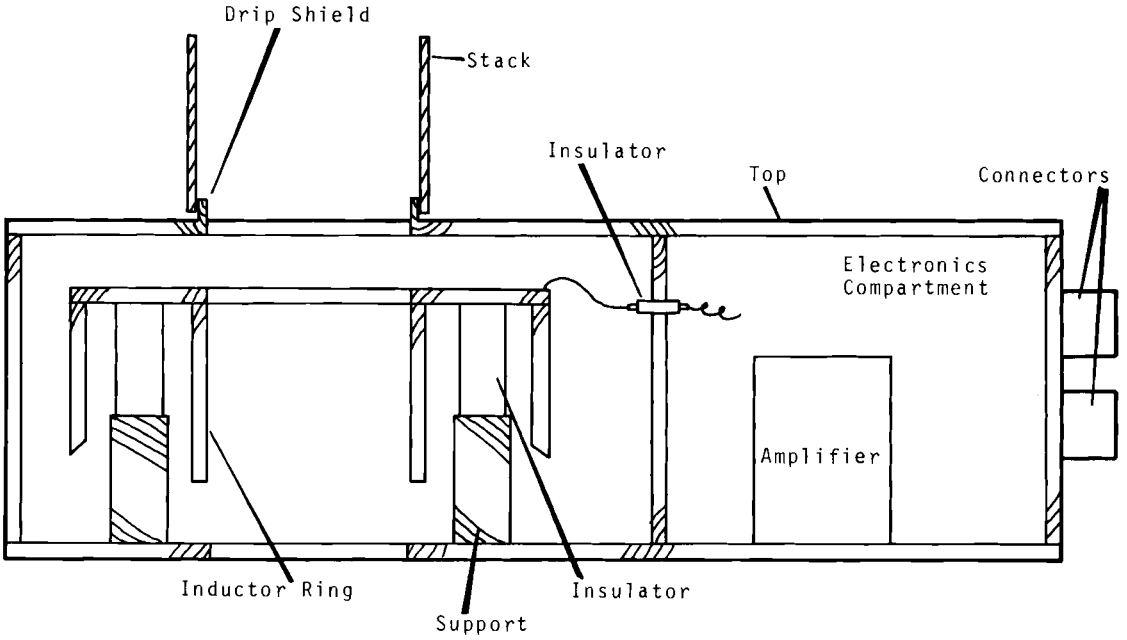

FIGURE 1. Cross Section of Transducer

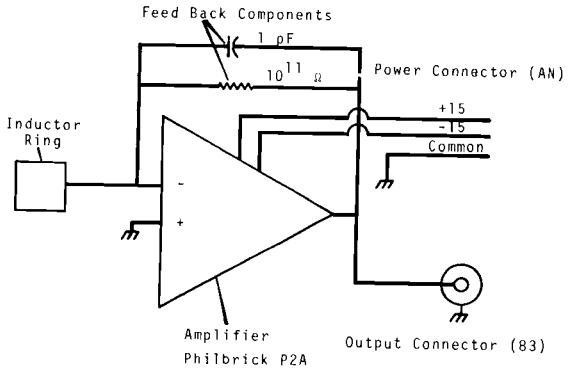

FIGURE 2. Electronic System for Detector

obviate pen inking troubles in outdoor, cold weather operation.

In the field, the amplifier and transducer power supply operate from six lantern batteries of 6 Vdc each and provide regulated outputs of plus and minus 15 Vdc. Battery life during field operation exceeds 50 hr. The recording portion operates from a portable ac generator.

Calibration has been achieved by charging a stream of water drops in the laboratory and noting the response of the measurement system on an oscilloscope. The drop charge, thus determined, completes calibration. Figure 3 shows a satisfactory charging and calibration system. A variable voltage of changeable polarity applied to the ring near the drop generator placed a charge, by induction, on the drop as it forms. The charge remains on the drop as it falls from the generator.

A pulse generator, developed for charged-drop experiments, may be

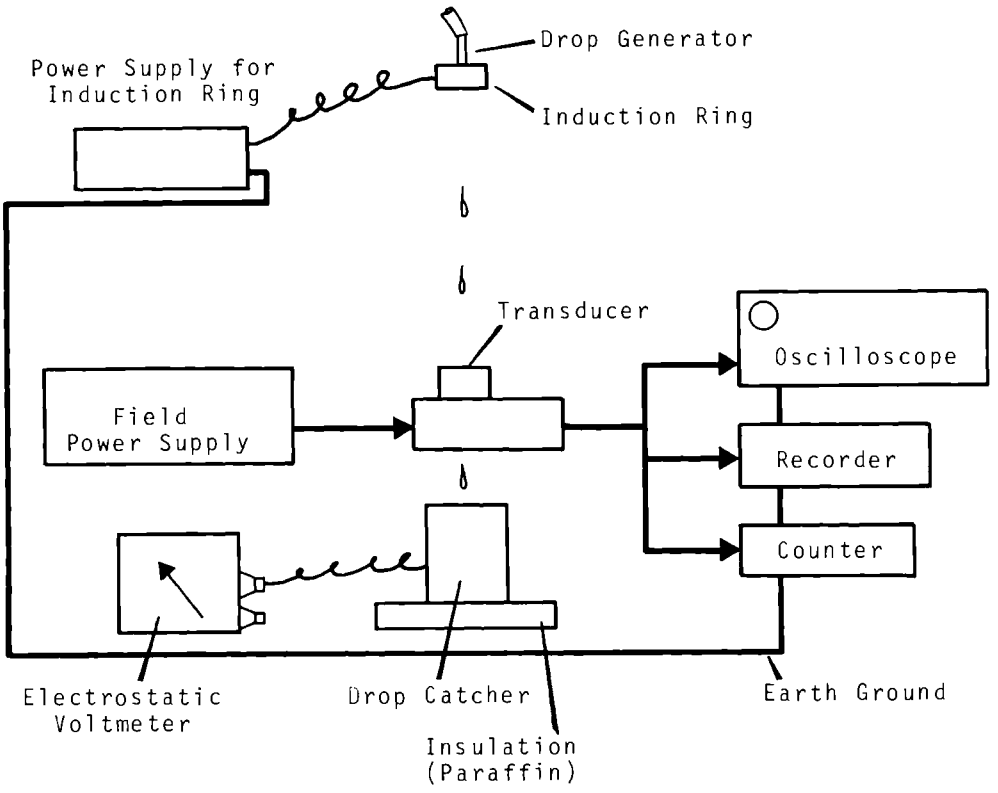

FIGURE 3. Charge Calibration Arrangement

used for calibration purposes. As shown in the schematic of Figure 4, a Unijunction* oscillator sets the pulse repetition rate for the generator and varies, with the setting of the 500 kΩ potentiometer, between about 2 to 20 pulses/sec. The output of the oscillator triggers a monostable multivibrator with a variable-width pulse output, where the 100 kΩ potentiometer controls the pulse width from about 1 msec to about 10 msec. The pulse output of the monostable circuit turns on and saturates the output transistor--chosen for this application because of its relatively high voltage rating. The quiescent output voltage varies from 0 to about 175 V positive with respect to circuit common.

Raindrop charge determination is accomplished by collecting and counting the drops in a system of known capacitance and measurable voltage. From $Q = nq = C(\Delta V)/n$; where n equals the number of drops, C equates to the combined capacitance of the collecting system and electrostatic voltmeter used for measuring ΔV (and varies with the voltmeter reading), and ΔV signifies the voltage increment attained over the period of time needed to collect the n drops. Obviously, the time for

* *Registered General Electric Company trademark.*

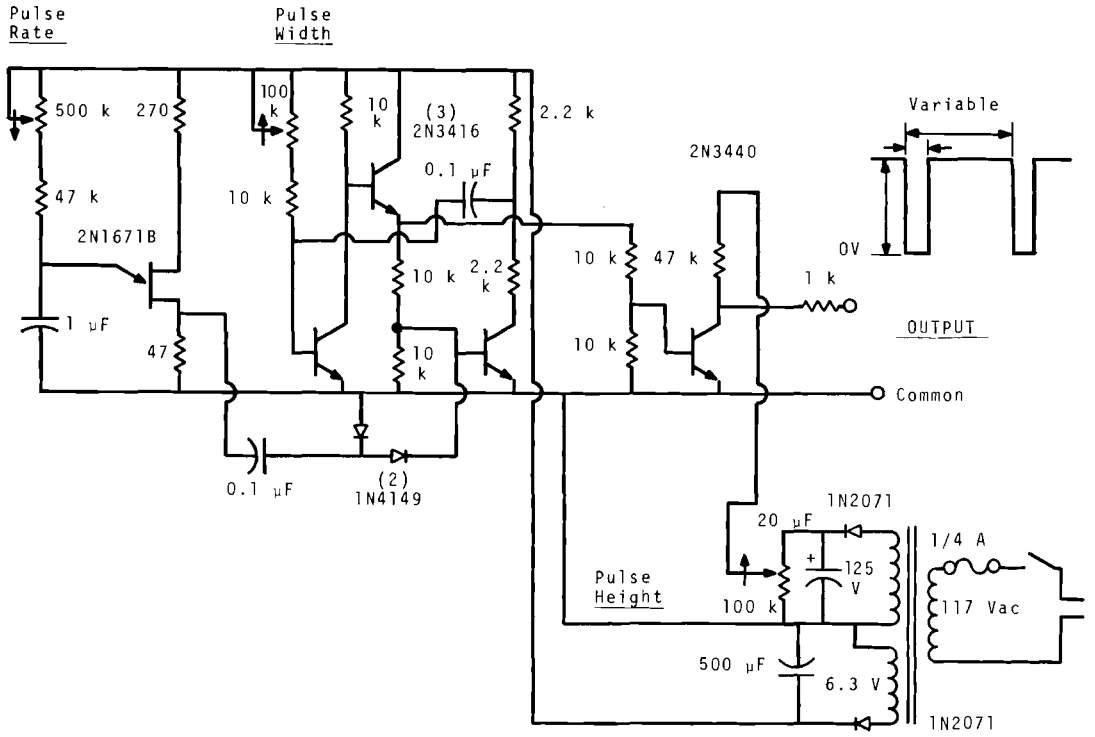

FIGURE 4. Pulse Generator for Charged Drop Experiments

charge to decay (leakage) should be large compared with the measurement time.

Additional improvements to the system will depend on the results achieved through further field testing. Although it would require considerable developmental effort, the capability of measuring drop velocity could also be added in the future if such information would be desirable.

REFERENCES

1. *C. A. Ratcliffe and N. C. Hoitink. "Raindrop Charge and Velocity Measurement Techniques," Pacific Northwest Laboratory Annual Report for 1965 in the Physical Sciences, Volume 4: Instrumentation, BNWL-235, p. 21. Pacific Northwest Laboratory, Richland, Washington. 1966.*

2. *C. A. Ratcliffe. "Improvements in Raindrop Charge Measurement Systems," Pacific Northwest Laboratory Annual Report for 1966 to the USAEC Division of Biology and Medicine, Volume II: Physical Sciences Part 4. Instrumentation, BNWL-481, p. 46. Pacific Northwest Laboratory, Richland, Washington. 1967.*

PRECIPITATION SCAVENGING OF SUBMICRON PARTICLES-A THEORETICAL ANALYSIS

W. G. N. Slinn*

INTRODUCTION

The point of interest is the precipitation scavenging of extremely small particles (radii between 10 and 1000 Å) and how such particles are washed out of the atmosphere by rain of given intensity and of given raindrop size distribution.

The analysis starts from Newton's second law written for a single particle of mass M. The velocity of the particle, $\vec{V}$, is measured from an inertial frame fixed to the raindrop. Because of the minuteness of the particles, their Brownian motion is expected to be significant. This is included in the analysis by introducing a stochastic force, $\vec{F}_s$, in addition to the force from the fluid, $\vec{F}_f$, and an electrical force, $\vec{F}_e$, in the equation of motion:

$$\vec{F}_e + \vec{F}_f + \vec{F}_s = M \frac{d\vec{V}}{dt} \quad .$$

An empirical formula for the drag from the fluid, similar to one used by Millikan,[1] is

$$\vec{F}_f = 6\pi a\rho\nu[\vec{V}_f - \vec{V}]/[1 + A\ell/a + (B\ell/a)\exp(-ba/\ell)]$$

where a is the radius of the particle, ρ, ν, $\vec{V}_f$ are the density, kinematic viscosity and velocity of the fluid, respectively, and A, B, b, ℓ are constants (for $10 < a < 1000$ Å, $A = 0.95$, $B = 0.24$, $b = 1.5$, $\ell = 0.4 \times 10^{-6}$ cm). For convenience, we write this drag as $\vec{F}_f = (M/\tau)[\vec{V}_f - \vec{V}]$. In comparing these two expressions for $\vec{F}_f$, (M/τ) is seen to be mass-independent. Later we will justify writing $(M/\tau) = (kT/D)$, where kT is the thermal energy of the fluid and D is the diffusion constant.

τ is the velocity relaxation time. In a fluid moving at a uniform velocity $\vec{V}_o$, a particle released from rest would have velocity

$$\vec{V} = \vec{V}_o\,[1 - \exp(-t/\tau)] \quad .$$

For the particles of interest, τ is extremely small: $\tau(\mu\text{sec}) \doteq a(\mu)$.

THE SMOLUCHOWSKI EQUATION

The presence of the stochastic force in the equation of motion prohibits us from integrating it directly. The force is known only statistically. We can expect it to be random in direction, with magnitude dependent upon the thermal energy of the air molecules. A reasonable form for the stochastic force was assumed by

* *Analysis Section, Mathematics Department*

Chandrasekhar in his classic review.[2] A derivation of it is given elsewhere in this report.*

Instead of attempting to integrate the equations, we yield on attempting to describe the position and velocity of the particle so exactly. We seek only the probability, $W\, d\vec{r}\, d\vec{V}$, that the particle has velocity $\vec{V}$ (to $\vec{V} + d\vec{V}$) when it is at position $\vec{r}$, at time t, if it had a velocity $\vec{V}_o$ at $\vec{r}_o$ at time t_o. Chandrasekhar shows that the resulting equation for W is the Fokker-Planck equation:

$$\frac{\partial W}{\partial t} + \vec{V}\cdot\nabla_r W + \left(\frac{\vec{F}_e}{M} + \frac{\vec{V}_f}{\tau}\right)\cdot\nabla_V W = \frac{1}{\tau}\left[\nabla_V\cdot(W\vec{V}) + \frac{kT}{M}\nabla_V^2 W\right] .$$

Here, ∇_V is the appropriate operator in velocity space and ∇_r is the familiar operator in physical space.

The Fokker-Planck equation describes the probable location of the particle exactly. Now we approximate it. If we restrict our attention to time intervals $\Delta t >> \tau$, and to distances $\Delta r >> \sqrt{D\tau}$, then the Fokker-Planck equation reduces to the Smoluchowski equation:

$$\frac{\partial w}{\partial t} = \nabla\left[\left(\frac{kT\tau}{M}\right)\nabla w - \left(\frac{\tau}{M}\vec{F}_e + \vec{V}_f\right) w\right] .$$

Here, $w d\vec{r} = w(\vec{r},t;\vec{r}_o,t_o)d\vec{r}$ is the probability that the particle is in $d\vec{r}$ at $\vec{r}$ at time t if it was at $\vec{r}_o$ at time t_o. Notice that w (as opposed to W) contains no reference to the velocity of the particle.

The restrictions $\Delta t >> \tau$ and $\Delta r >> \sqrt{D\tau}$ can be reasonably accepted. The minimum time of interest is the time for a raindrop to fall about 1/100th of its radius, R. Since the terminal velocity of a drop, V_t, is close to 8000 R sec^{-1}, then

$$\Delta t = O(1\mu sec) >> \tau(\mu sec) = O[a(\mu)] ,$$

provided that a << 1 micron. The condition for Δr provides no further restriction.

There are a number of interesting features to the Smoluchowski equation. First, if we identify the diffusion constant $D = (\tau/M)kT$, and recall that τ/M is mass independent, then it is seen that the Smoluchowski equation contains no reference to the mass of the particle. Consequently, for particles of radii a << 1 micron, the contribution to the washout coefficient from inertial effects is negligible. Second, the equation can be interpreted as describing a probability flux $\vec{j}$: $\frac{\partial w}{\partial t} = -\nabla\cdot\vec{j}$ where

$$\vec{j} = -\left[D\nabla w - \left(\frac{\tau}{M}\vec{F}_e + \vec{V}_f\right)w\right] .$$

This will be useful later. Finally, the Smoluchowski equation has a simple physical interpretation.

To obtain this, we assume the fluid to be incompressible, and that no free electrical charge exists in the space between the particle and the drop. Then $\nabla\cdot\vec{V}_f = 0 = \nabla\cdot\vec{F}_e$, and there results

---

* *See, "The Convective Diffusion Equation for the Scavenging of Submicron Particles," by W. G. N. Slinn in this report.*

$\frac{Dw}{Dt} = D\nabla^2 w$ where $\frac{D}{Dt} = \frac{\partial}{\partial t} + \vec{v} \cdot \nabla$ is a substantial derivative taken along the trajectory defined by $\vec{v}$. A uniform density at infinity implies the concentration of aerosol to be constant everywhere. Levin[3] reached a similar conclusion earlier. The full equation describes simple diffusion about these "undiffused" trajectories.

THE CONVECTIVE DIFFUSION EQUATION

The Smoluchowski equation describes the probable location of a single particle at time t when it is known to be at $\vec{r}_o$ at time t_o. However, for our problem, both $\vec{r}_o$ and t_o must be chosen at random. We can simplify the problem. Instead of attempting to describe the intermittent bombardment of the raindrop by particles emanating from random points at random times, we choose to "continuumize" the effect on the raindrop by defining a hypothetical continuous number density of particles, $n(\vec{r},t)$. If, at some arbitrary time, $t = 0$, the density of particles is $n(\vec{r},o)$, then the number of particles in $d\vec{r}$ at time t is

$$n(\vec{r},t)d\vec{r} = \int_{\vec{r}^*} n(\vec{r}^*,0)w(\vec{r},t;\vec{r}^*,0)d\vec{r}^*d\vec{r} \quad .$$

Operating on this equation with $\frac{D}{Dt} - D\nabla^2$, we get $\frac{Dn}{Dt} - D\nabla^2 n = 0$ which has the same form as the equation for w.

The boundary condition at infinity is simply that $n \to n_o$, a constant. Obtaining the boundary condition at the surface of the drop ($r = r_s$) is more difficult. Since the velocity of the fluid is zero at the surface, the probability flux there becomes

$$\vec{j} = -[D\nabla w - (\tau/M)\vec{F}_e w].$$

If the surface is impenetrable, then the flux through it is zero and the boundary condition becomes

$$0 = [D(\nabla w \cdot \hat{p}) - \frac{\tau}{M}(\vec{F}_e \cdot \hat{p}) w]_{\vec{r} = \vec{r}_s},$$

where $\hat{p}$ is a unit vector perpendicular to the surface. At the other extreme, if the raindrop completely absorbs all particles incident upon it, then, as far as the exterior fluid is concerned, the effect is as though no particles are present in the region interior to the drop, i.e., no particles would emerge to repopulate the exterior region. Thus, for perfect absorption, $w(\vec{r} \le \vec{r}_s) = 0$, and the probability flux into the surface becomes

$$\vec{j} \cdot (-\hat{p}) = D(\nabla w) \cdot \hat{p}|_{\vec{r} = |\vec{r}_s}$$

A similar boundary condition is obtained for n.

In summary, for perfect absorption, the steady state convective diffusion problem to be solved is $(\vec{v} \cdot \nabla)n = D\nabla^2 n$, $n \to n_o$ as $r \to \infty$; $n = 0$ at $\vec{r} = \vec{r}_s$.

We shall assume a simple Coulombic force between the particle with charge q and the drop with

charge Q. If distances are nondimensionalized with the radius and velocities normalized with the terminal velocity of a spherical drop, then the equation (using the same symbols for the nondimensional as for the dimensional variables) becomes

$$(\vec{V}_f + \frac{C}{M}\frac{\hat{e}_r}{r^2})\cdot\nabla n = \frac{1}{Pe}\nabla^2 n \quad .$$

Here Pe is the Péclét number, the ratio of the convective transport ($V_t R$) to Brownian diffusion:

$$Pe = V_t R/D = (V_t R/\nu)(\nu/D) = Re\ Sc,$$

where Re is the Reynolds number and Sc is the Schmidt number. C/M is the ratio of the Coulomb force at the surface of the drop, $C = qQ/4\pi\varepsilon_o R^2$ to the order of magnitude of the molecular drag on the particle,

$$M = 6\pi a\rho\nu V_t/[1 + A\ell/a + (B\ell/a)\exp(-ba/\ell)] \quad .$$

An order of magnitude estimate of these quantities is for 10 Å particles in drizzle;

$Pe \doteq 10$, $Re \doteq 1$, $Sc \doteq 10$

and for 1000 Å particles in a cloudburst;

$Pe \doteq 10^8$, $Re \doteq 10^3$, and $Sc \doteq 10^5$.

A discussion of C/M will be given later.

EXACT SOLUTIONS FOR SPECIAL CASES

Solving the convective diffusion equation is extremely difficult because of the presence of the fluid velocity, $\vec{V}_f$. Even in the two limiting cases where it is known (Stokes' flow for $Re \to 0$ and potential flow for $Re \to \infty$), the velocity is a nonlinear function of the coordinates. If there is no fluid velocity and no charges, the dimensional equation becomes $\nabla^2 n = 0$, with $n \to n_o$ as $r \to \infty$, and $n(R) = 0$. The solution is $n = n_o(1 - \frac{R}{r})$. The dimensional flux of particles to the drop, arising solely from the Brownian motion of the particle, is then

$$\dot{n}'' = D\left.\frac{\partial n}{\partial r}\right|_{r=R} = \frac{Dn_o}{R} \quad .$$

Nondimensionalizing this flux, we obtain the Sherwood number (based on the radius) $Sh = \dot{n}''R/Dn_o = 1$.

If there are electrical charges present, but still no fluid motion, the nondimensionalized equation is $E(\hat{e}_r/r^2)\cdot\nabla n = \nabla^2 n$, where $E = (C/M)Pe = CR/kT$. E is a measure of the electrical effect and is the ratio of the particle's electrostatic potential energy if it were at the surface of the drop to the thermal energy kT. The solution is

$$n = n_o(e^{-E/r} - e^{-E})/(1 - e^{-E})$$

and the flux of particles through the surface is $Sh = E/(e^E - 1)$. For $E = 0$ we regain $Sh = 1$, for $E \to +\infty$ (like charges) $Sh \to 0$, and for $E \to -\infty$ (unlike charges) $Sh \to |E|$.

Some useful conclusions can be drawn from this result. For a cloud droplet in the presence of

ions with an excess of charge of one sign, the charging of the droplet will be negligibly small when E climbs to about 10. Therefore, the number of elementary charges on a cloud droplet of radius R is unlikely to climb above 10^4R, R in 0.1 mm. Ziman[4] gives the experimental result for the number of charges as 2×10^3R. Likewise, the number of charges on a falling raindrop is unlikely to climb above 10^5R, R in 0.1 mm, which is considerably below the limit of about 10^8 $R^{3/2}$ set by surface tension.

Although the result Sh = E/(e^E - 1) was derived from a steady state equation, it can provide us with an estimate of the rate of discharge by ions of an object (raindrop, droplet or particle). If the ions of density n_i carry a single elementary charge q_i, then taking Sh = -E for E large and negative, there results

$$E = E(0) \exp [- (n_i q_i^2 D_i/\epsilon_o kT)t] ,$$

that is, in agreement with Gunn,[5] we obtain the decay time

$$\tau_d = (\epsilon_o kT/n_i q_i^2 D_i)$$

which is independent of the size of the object. With normal atmospheric ion densities of around $10^3/cm^3$, the discharge [$\tau_d = O(10^3)$ sec] proceeds very slowly. A drop of 1 mm diam falls about 4 km in this time. At the other extreme, for submicron particles produced in a hydrocarbon flame where ion densities are typically $10^9/cm^3$, the decay time is in the millisecond range.[6]

An estimate of the importance of the electrical effect in precipitation scavenging can be, of course, only as reliable as the estimate of the size of the charges. Even the orders of magnitude of these are in doubt. Raindrops have been observed[7] with charges close to the limit set by surface tension ($10^8 R^{3/2}$, R in 0.1 mm). Smith[8] measured values of the order of 10^6R. Byutner and Gisina[9] use $Q = 10^5$R which we expect to be an upper limit for the charge. Frenkel's theory for the charge on cloud droplets gives $Q = 2 \times 10^4$R, but Ziman[4] argues that the charge on a raindrop will be considerably less than the experimental result for the charge on a cloud droplet, $Q = 2 \times 10^3$, because the drop grows preferentially from the coagulation of droplets of opposite charge. Probably there is no simple charge-to-raindrop size relation useful for all rainstorms. For specific ion concentrations, the prediction of any one of these expressions might be appropriate.

The charge on the particle is also uncertain. Fuchs[1] studied the charge on 100 Å particles that had reached equilibrium with the normal ionization of air at sea level and found that 90% carry no charge, while the other 10% possess only a single charge. In the experiment that we will refer to, the particles of geometric mean radius of about

60 Å are produced in a propane flame and initially may carry a significant charge. However, it is quite possible that they are discharged in a few milliseconds and come to charge equilibrium with the atmosphere during the time (approximately 1 sec) between their formation and collision with the raindrop. Further investigation of this problem is planned.

It is disconcerting to attempt to estimate the importance of the electrical effect from such equivocal data. If Ziman's argument for the charge on a raindrop is appropriate, and if there is a single charge on the particle, then $|C/M| \doteq 1/Pe$. If, as is likely the case, there is an equal probability for attraction or repulsion between the drop and the particle, then the change in the Sherwood number is the arithmetic mean of $(e^1 - 1)^{-1}$ and $(1 - e^{-1})^{-1}$ or 1.08, that is, the correction to the Sherwood number is about 10% of the value for Brownian diffusion. For natural aerosols of about 100 Å radius, this correction is to be applied only to 10% of the particles. The other 90% are uncharged and would be attracted only because of the dipole induced in them by the raindrop's charge. The ratio of this force to the Coulombic force is $O(a^3Q/R^3)$ which, for a 0.1 mm drop and a 100 Å particle, is $O(10^{-9})$. Thus, if the number of charges on the raindrop is 10^3R, R in 0.1 mm, the electrical contribution to the washout of natural aerosols of radius of 100 Å is negligible. However, if raindrops carry 10^5R charges and if all the particles are charged, then the electrical effect can easily be 10 times more important than Brownian motion. The need for more experimental data is obvious.

APPROXIMATE SOLUTIONS

Ignoring the electrical term, the equation to be solved is $\vec{V}_f \cdot \nabla n = Pe^{-1}\nabla^2 n$. Since $Pe >> 1$, a solution might be expected in the form of a perturbation expansion in Pe^{-1}. We have, to the lowest order, $\vec{V}_f \cdot \nabla n = 0$ whose solution is n = constant (as was obtained from the Smoluchowski equation when there was no diffusion). Now there is a dilemma: $n = n_o$ at infinity, and n = 0 at the surface. The lowest order solution, however, can fit only one boundary condition. It is, in fact, a singular pertubation problem[10] with the classic warning that the highest derivative is lost in the lowest order equation. The source of the difficulty is that near the surface of the drop $\vec{V}_f \to 0$ and, consequently, the retained term $\vec{V}_f \cdot \nabla n$ becomes smaller than the ignored term, $Pe^{-1}\nabla^2 n$. Far from the drop, the lowest order solution is $n = n_o$. The density very near the drop would become closer to the solution of $\nabla^2 n = 0$, $n = 0$ at $r = R$; $n = n_o$ at $r = R + \delta$ where δ is an estimate of where the two terms in the full equation become the same order of magnitude.

Determining δ, is not so easy, as Levich demonstrates.[11]

For the problem of interest, $Sc = \nu/D > 10$, which means that the vorticity diffuses farther from the sphere than the region where Brownian motion of the particle is significant. Consequently, the Brownian layer is embedded in a viscous dominated flow, and Stokes' stream function might be expected to be applicable near the surface, even for $Re > 1$. It may be of interest to point out that the second order Stokes' stream function,[10]

$$\psi = \frac{-V_t R^2}{4}\left(\frac{r}{R} - 1\right)^2 \sin^2\theta\left[\left(1 + \frac{3}{8}\,Re\right)\left(2 + \frac{R}{r}\right) + \frac{3}{8}\,Re\left(2 + \frac{R}{r} + \frac{R^2}{r^2}\right)\cos\theta\right] ,$$

describes stationary eddies for $Re < 60$. Here θ is measured from the upstream polar axis. Calculating

$$V_r = \frac{1}{r^2 \sin\theta}\,\frac{\partial\psi}{\partial\theta} , \quad V_\theta = \frac{1}{r \sin\theta}\,\frac{\partial\psi}{\partial r} ,$$

calling the distance from the surface of the sphere $y = r - R$, and substituting into the dimensional convective diffusion equation yields, near the surface,

$$-(3/2)(y^2/R^2)[\cos\theta + Re/8(2\cos\theta - 1)(3\cos\theta + 2)]\;\partial n/\partial r$$

$$+(3/2)(y/R)\sin\theta\,[1 + Re/8(4\cos\theta + 3)]\;1/r\;\partial n/\partial\theta$$

$$= D/V_t\left[\frac{\partial n}{\partial r^2} + \frac{2}{r}\frac{\partial n}{\partial r} + \frac{1}{r^2 \sin\theta}\,\frac{\partial}{\partial\theta}\left(\sin\theta\,\frac{\partial n}{\partial\theta}\right)\right] .$$

We shall work with the case without eddies (take $Re = 0$ in the above equation).

We now attempt to make each term display its order of magnitude by magnifying the distance from the sphere, y, by the amount δ. We define $Y = y/\delta = O(1)$ and then, using $\frac{\partial}{\partial r} = \frac{\partial}{\partial y}$ and $r \doteq R$, we obtain

$$-\frac{3}{2}\,\frac{\delta^2 Y^2 \cos\theta}{R^2\delta}\,\frac{\partial n}{\partial Y} + \frac{3}{2}\,\frac{\delta Y \sin\theta}{R^2}\,\frac{\partial n}{\partial\theta}$$

$$= \frac{D}{V_t}\left[\frac{1}{\delta^2}\,\frac{\partial^2 n}{\partial Y^2} + \frac{2}{R\delta}\,\frac{\partial n}{\partial Y} + \frac{1}{R \sin\theta}\,\frac{\partial}{\partial\theta}\left(\sin\theta\,\frac{\partial n}{\partial\theta}\right)\right] .$$

The assumption by Levich that the derivatives in these strained coordinates are of the same order of magnitude cannot be justified. If this were true, then the left and right hand sides would be equally significant when

$$\frac{\delta}{R^2} = O\left(\frac{D}{V_t \delta^2}\right) \text{ or } \frac{\delta}{R} = O(Pe^{-1/3}) \quad .$$

If $n \doteq n_o$ at this distance, and if we solved $d^2n/dy^2 = 0$ in the region $0 < y < \delta$, then $Sh = \sigma(Pe^{1/3})$. Levich solves essentially

$$3/2 \frac{y \sin\theta}{Rr} \frac{\partial n}{\partial \theta} = \frac{D}{V_t} \frac{\partial^2 n}{\partial r^2} \quad \text{and}$$

obtains $Sh = 0.64\ Pe^{1/3}$.

The error in this method is to assume that $\frac{2}{r}\frac{\partial n}{\partial r} << \frac{\partial^2 n}{\partial r^2}$. If there were no fluid motion, then the equation would be $\nabla^2 n = 0$, or

$$\left|\frac{2}{r} \frac{\partial n}{\partial r}\right| \equiv \left| \frac{\partial^2 n}{\partial r^2}\right| \quad .$$

Neglecting one in comparison to the other leads Levich to the incorrect result that, when there is no fluid velocity, $Sh = 0$. He adds on the zero velocity value as we could here by saying that we should solve

$$\nabla^2 n = \frac{\partial^2 n}{\partial r^2} + \frac{2}{r}\frac{\partial n}{\partial r} = 0 \quad \text{with}$$

$n(R) = 0$, $n(R + \delta) = n_o$ to give $Sh = 1 + O(Pe^{1/3})$. However, if $\frac{2}{r}\frac{\partial n}{\partial r}$ is significant, then we could have assumed in the first place (with equal justification) that

$$\frac{\delta}{R^2} = O\left(\frac{D}{V_t R \delta}\right) \text{ , or } \frac{\delta}{R} = O(Pe^{1/2})$$

which leads to $Sh = 1 + O(Pe^{1/2})$. The resolution of this problem awaits the exact solution.

HEAT TRANSFER ANALOGY

In the meantime, there is a wealth of experimental data apparently not yet applied to the problem of precipitation scavenging of particles.[12] The forced convection heat transfer from an isothermal sphere is governed by almost the same equation and by the same boundary conditions as the mass transfer problem.[13, 14] Therefore, the solution is the same. We need only replace in the heat transfer results the nondimensionalized heat flux (the Nusselt number) by the nondimensionalized mass flux (the Sherwood number), and the Prandtl number, $Pr = k/D$, by the Schmidt number, $Sc = \nu/D$.

Drake[15] recommends for the heat transfer Nusselt number for $10^{-1} < Re < 10^5$, and $2 < Pr < 380$,

$$Nu = 1 + 0.336\ Re^{0.55} Pr^{0.33}.$$

For a similar range, Spalding[16] recommends, and we shall use

$$Nu = 1 + 0.39\ Re^{1/2} Pr^{1/3},$$

that is, we take

$$Sh = 1 + 0.39\ Re^{1/2} Sc^{1/3}.$$

It is interesting to notice how the exponent of $Pe = Re\ Sc$ is neither 1/2 nor 1/3. Both these empirical fits (typically to within 10%) include some mass transfer data and, of course, include the complicated hydrodynamic phenomena from stationary eddies to turbulent wakes. Although the range in Sc is not adequate for our purposes, the exponent is expected to differ very little from 1/3.[17]

Using the preceding expression for the Sherwood number, the total flow to the surface is $(4\pi R^2 D n_o Sh/R)\,sec^{-1}$. The collection

efficiency, E_c, is usually defined by nondimensionalizing this with the flow in the undisturbed fluid to a cross-section πR^2:

$$E_c(a,R) = \frac{4\pi R D n_o Sh}{\pi R^2 n_o V_t}$$

$$= (4/Pe)[1 + 0.39\ Re^{1/2} Sc^{1/3}] \ .$$

Our best estimate of the collection efficiency would be obtained from the preceding expression, which is really the target efficiency, multiplied by the retention efficiency and by the electrical term $E/(e^E-1)$.

Ziman[4] uses for the collection efficiency an interpolation between Levich's solution (Re << 1) and his own boundary layer theory (Re >> 1). Details of the latter were not available. His result is

$$E_c(a,R) = \frac{1}{Pe^{1/2}} \left[\frac{0.24 + 0.64\ Re}{1 + Re}\right] \ .$$

If we use the same rain spectrum and terminal velocity as Ziman:

$$N(R)dR = (10^{-4} J_o/6\pi Rm^7) \cdot R^2 \exp(-2R/Rm)\ dR$$

and

$$V_t = 8000\ R\ sec^{-1},$$

where J_o is the total intensity of rain in cm/sec and Rm is the radius of the drops in the maximum of the spectrum. We then obtain, for the washout coefficient,

$$\Lambda(a) = \int_o^\infty \pi R^2 E_c(a,R)\ V_t\ (R) N(R) dR \ ,$$

$$\Lambda(a) = 25 \times 10^{-6} \frac{J_o(\frac{cm}{hr}) \left[D(a)\ \frac{cm^2}{sec}\right]}{R_m^3\ (cm)} \cdot \left\{1 + \frac{96\ Rm}{D^{1/3}}\right\} hr^{-1} \ .$$

This and Ziman's result are plotted in Figure 1. The error bars on Ziman's curves arise because they were taken from a plot in his paper. His curves begin to climb at $a \doteq 0.1\ \mu$ because he has added the inertial contribution.

A number of observations should be made. The most dramatic of these is that the heat transfer data predict the washout time for submicron particles to be as much as a factor of 10 longer than Ziman predicts. Notice, also, that the curves give the misleading impression that the smaller the raindrop size, the more effective is the scavenging. The reason for this is that the curves are normalized to the same rainfall rate. Finally, the importance of examining the retention efficiency problem is apparent. To ignore it would lead to the ridiculous conclusion that essentially all the "air molecules" ($a \doteq 1$ Å) in the path of a raindrop are collected.

CONCLUSION

This analysis of the precipitation scavenging of submicron particles leads us to conclude that inertial effects are insignificant if the particle radius is less than 0.1 μ. More experimental

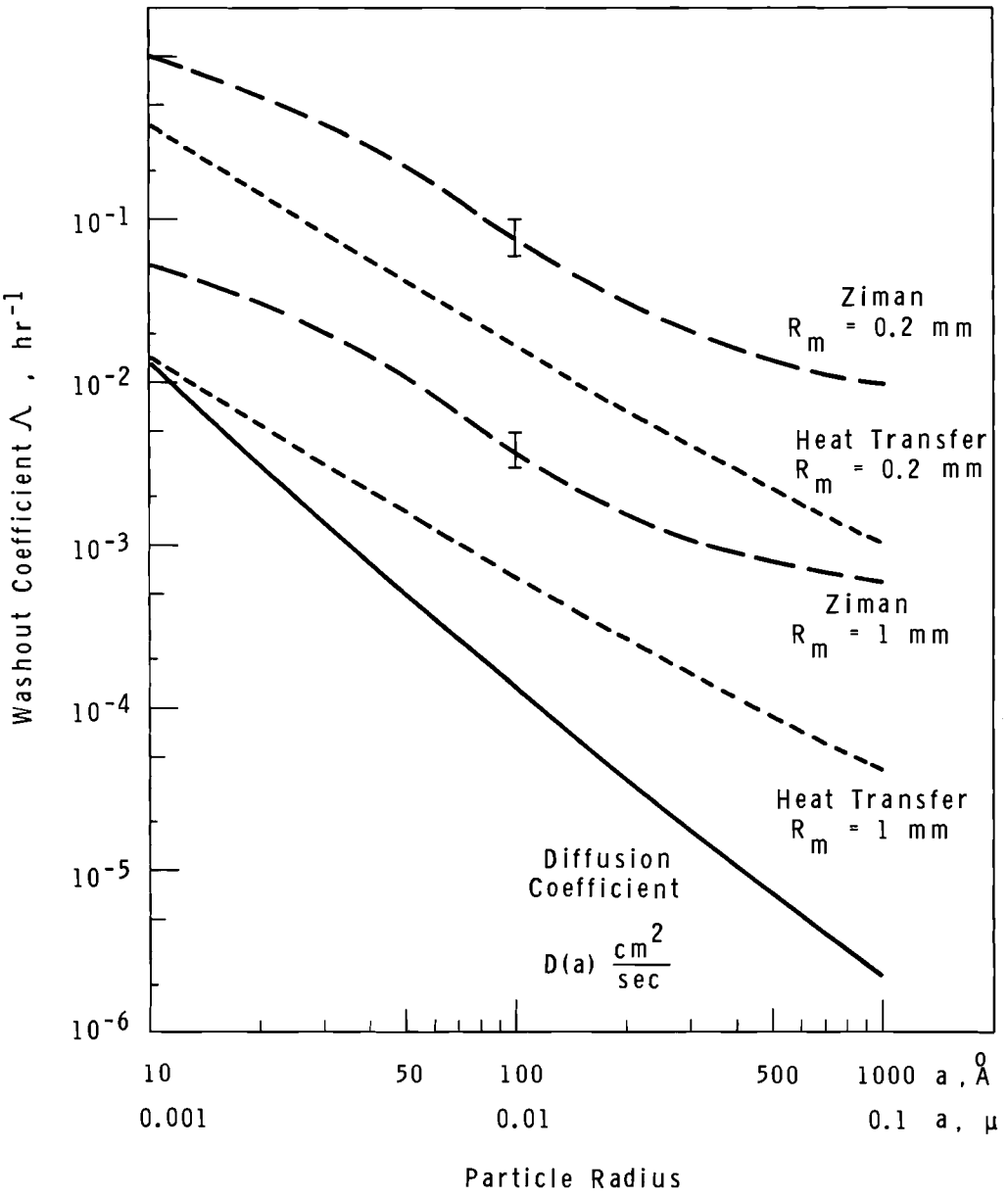

Neg. 0672873-3

FIGURE 1. The Washout Coefficient as a Function of Particle Size with J_o = 1 cm hr^{-1}

data are needed before the contribution of the electrical effects can be reliably evaluated. To within experimental accuracy, heat transfer data are expected to be valuable for calculating the contribution to the washout coefficient from convective diffusion. Comparison with experiment is given in another contribution to this report.*

* *See "Precipitation Scavenging of Submicron Particles: A Comparison of Theory with Field Results" by D. I. Hagen.*

REFERENCES

1. R. Millikan, Phys. Rev., vol. 22, 1. 1923. For a review, see N. A. Fuchs, The Mechanics of Aerosols. Pergamon Press, The MacMillan Co., New York, 1964. p. 27.

2. S. Chandrasekhar. Rev. Mod. Phys., vol. 15, 1. 1943. Reprinted in Noise and Stochastic Processes, edited by N. Wax. Dover Publications, New York, 1954.

3. L. Levin. Izv. Akad. Nauk SSSR, Ser. Geofiz, p. 914. 1957. Or see Fuchs (1), p. 110.

4. A. G. Ziman. Problems of Nuclear Meteorology. Moscow, 1962. (Translation AEC-TR-6128).

5. R. Gunn, J. Meteorol., vol. 11, p. 339 1954.

6. For example, see G. Wortberg, Tenth Symposium (International) on Combustion (The Combustion Institute, Pittsburgh, Penna., 1965.)

7. J. A. Chalmers. Atmospheric Electricity. Pergamon Press, The MacMillan Co., New York, 1957.

8. L. G. Smith. Quart. J. Roy. Met. Soc., vol. 81, p. 23, 1955.

9. E. K. Buytner and F. A. Gisina. Turbulent Diffusion in the Surface Layer of the Earth's Atmosphere. Joint Publications Research Service, Washington, D.C. 20443 1964.

10. M. Van Dyke. Perturbation Methods in Fluid Mechanics, Academic Press, New York, 1964.

11. V. G. Levich. Physicochemical Hydrodynamics. Prentice-Hall, Inc., Englewood Cliffs, N.J., 1962.

12. W. E. Ranz. (Engr. Expt. Sta. Rep. No. 8, U. of Illinois, 1952) has utilized this analog for predicting filtration efficiencies.

13. L. D. Landau and E. M. Lifshitz. Fluid Mechanics. Addison-Wesley Publishing Co., Reading, Massachusetts, 1959. p. 226.

14. W. M. Kays. Convective Heat and Mass Transfer. McGraw-Hill, New York, 1966.

15. R. M. Drake. J. Heat Transfer, vol. 83, p. 170-172, 1961.

16. D. B. Spalding. Convective Mass Transfer. McGraw-Hill, New York, 1963.

17. See Spalding (16) p. 136 or Landau and Lifshitz (13) p. 207.

PRECIPITATION SCAVENGING OF SUBMICRON PARTICLES: A COMPARISON OF THEORY WITH FIELD RESULTS

D. I. Hagen

INTRODUCTION

Descriptions of the washout of gases and of submicron particulates are similar in that diffusion plays a major role, a finding verified theoretically for small particulates in another contribution to this report.* In addition to diffusion, the presence of electric charges on either the drop, the particle, or both can affect the washout by rain. Because of the complex composition and structure of small particulates, particle retention by raindrops and by gases may require different explanations. As particle size increases, all similarity with a gas is lost since Brownian motion becomes neglibible for particles greater than about 0.1 μ, and particle inertia becomes the dominant captive mechanism for sizes greater than about 1 μ.

Little or nothing appears to have been done previously in the experimental study of the rain washout of particles smaller than about 0.1 μ, or of particles roughly between 0.1 μ and 1 μ where neither Brownian diffusion nor inertial impaction effects are large. Consequently, washout coefficients have been measured in the field for the scavenging by rain of silver iodide particles purported to be smaller than 0.1 μ. The field results are compared with values calculated from diffusion theory. It is shown that, by ignoring electrical effects and assuming perfect retention of the particles by the drop, the washout equation becomes similar to that used by Engelmann[1,2] to predict the washout of perfectly soluble gases and, within experimental error, agrees with the field results.

WASHOUT COEFFICIENT EQUATIONS

Experimental Determination

The methods for conduct of the field experiments and for subsequent calculation of washout have been described previously.[3] The equation for determining the washout coefficient from field measurements of wind speed $\bar{u}$, sampler separation ΔY, sampler cross-sectional area A, total quantity of silver iodide released Q, and total quantity of silver iodide recovered (less background) Σc is included below, for convenience, as Equation (1).

$$\Lambda = \bar{u} \frac{\Delta Y}{A} \frac{\Sigma c}{Q} \qquad (1)$$

Theoretical Determination

The washout of particles by rain can be determined also from

---

* *See "Precipitation Scavenging of Submicron Particles: A Theoretical Analysis" by W. G. N. Slinn in this report.*

$$\Lambda = \int_0^\infty \int_0^\infty \pi R^2 E(a,R) \phi(R) f(a) da dR \qquad (2)$$

where a = particle radius
R = raindrop radius
$\phi(R) dR$ = raindrop flux density = number of drops per cm^2 per sec having radii between R and R + dR
E(a,R) = collection efficiency for particle or raindrop
f(a) da = proportion of particles having radii between a and a + da

The collection efficiency is actually the product of the collision efficiency (E_c) and the retention efficiency (E_R). E_c is defined as the ratio of the number of particles that actually collide with the drop to the number in the cylinder swept out by the falling drop. The retention efficiency E_R is simply the fraction of the former that stick to the drop. E_R is taken to be unity.

The collection efficiency E(a,R) suitable for particulates and gases alike, has been obtained from the application of experimental heat transfer results to the problem of mass transfer.* If D(a) is the particle diffusion coefficient, Re, the Reynolds number of the raindrop, ν the viscosity of air, and $V_T(R)$ the raindrop terminal velocity, then the collection efficiency is

$$E(a,R) = 4D(a) V_T^{-1} R^{-1} \left\{1 + 0.39 \, Re^{1/2} \left[\frac{\nu}{D(a)}\right]^{1/3}\right\}$$

where $\left\{1 + 0.39 \, Re^{1/2} \left[\frac{\nu}{D(a)}\right]^{1/3}\right\}$ is the Sherwood number Sh(R,a). Inserting this expression for E(a,R) in Equation (2), we obtain

$$\Lambda = \int_0^\infty \int_0^\infty \frac{4\pi R \, \phi(R) \, D(a) \, Sh(R,a) \, f(a) \, da \, dR}{V_T(R)} \qquad (3)$$

For gases, f(a) da = 1 and D(a) = D so that

$$\Lambda_G = 4\pi D \int_0^\infty \frac{R \, \phi(R) \, dR \, Sh(R)}{V_T} \qquad (4)$$

Equation (4) has been used, as noted earlier, to successfully predict the washout of perfectly soluble gases. Equation (3), then, can be used to calculate the washout coefficient of submicron particles by assuming all effects other than convective diffusion to be negligible.

* *See "Precipitation of Submicron Particles: A Theoretical Analysis" by W. G. N. Slinn in this report.*

Other factors in addition to Brownian diffusion and electrical forces which may influence the washout of submicron particles include:

- Thermophoresis
- Diffusiophoresis
- Stefan flow
- Molecular potential (e.g., van der Waals' forces).

The combined effects of these factors are assumed to be minimal and will not be considered here although a discussion of them can be found in Fuchs[4] and Davies.[5] Their importance may be in the particle size range around 0.1 μ where Brownian diffusion is very small.

RESULTS

Equation (3) is evaluated by using experimental data from rain scavenging tests R18 and R20. The average raindrop flux $\phi(R)$ is unavailable for both runs R18 and R20, and must be estimated from other rainfall spectra taken at different times at the same location. It is assumed that the raindrop flux is, in general, a log-normal distribution of raindrop sizes. This assumption is based on the essentially log-normal behavior of distribution obtained from 16 samples of raindrop spectra, one of which contained on the order of 1600 drops and the other, an average of about 100 drops. However, several of the 100 drop samples had a normal rather than log-normal distribution. Other investigators[1] have observed approximate log-normal distribution for raindrop space density and this should be expected to hold true as well for their flux density. The log-normal distribution is specified when both its geometric mean diameter and standard deviation are known. The estimations of these parameters for experiments R18 and R20, conducted in rain, are as follows. The geometrical mean diameter (D_g) and rainfall rate obtained directly from each spectrum are plotted on log-log paper and a least squares line is fitted to the points as in Figure 1. From this line, geometric mean sizes are obtained for experimentally known average rainfall rates for R18 and R20. Sixty-eight percent confidence intervals are obtained about these points. A similar procedure is followed for estimating the geometric standard deviation σ_g of the size distribution from given values of D_g. These values are shown in the following tabulation.

Test	Rainfall Rate, mm hr^{-1}	Log σg	Log Dg	Dg,mm
R18	1.90	0.449	-0.640	0.527
R20	1.34	0.492	-0.689	0.502

The particle diameter size distribution is approximately log-normal, ranging between 0.002 and 0.05 μ. These values, in agreement with others,[6] have been established from electron microscope grids exposed to the silver iodide plume at a distance of 2 m from the same

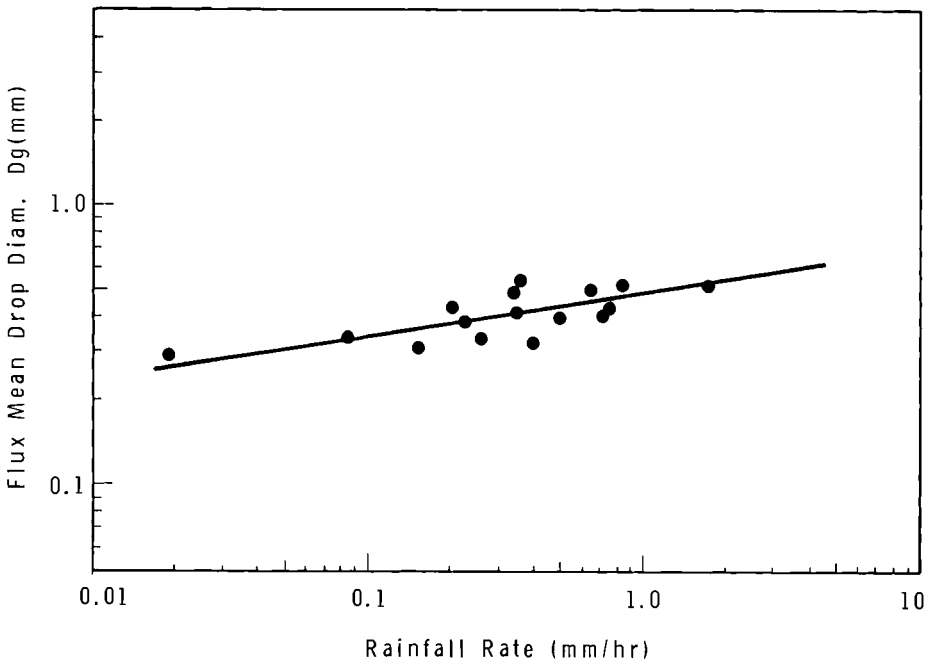

Neg. 0672941-1

FIGURE 1. Geometric Mean Drop Diameters Versus Rainfall Rate from Samples of Raindrop Spectra

generator used in the field experiments. Sizing of 100 particles, from photographs taken under the electron microscope, gave a geometric mean diameter and geometric standard deviation of 0.012 and 1.43 μ, respectively.

The particles are dry when they are sized since any water on them evaporates during examination under the electron microscope. It has been noted by Koenig,[7] however, that silver iodide particles produced by the "skyfire generator" are hygroscopic. Also, it has been shown recently by De Pena and Caimi[8] that, with potassium iodide substituted for sodium iodide, the diameters of the resultant droplets (particle plus condensed water) can significantly exceed the particle diameter. The question relevant to the washout studies described in this report is whether the particles, if generated dry, have sufficient time in the atmosphere (on the order of 10 sec) to condense a significant quantity of water before being scavenged. The resolution of this question is important since the theoretical washout coefficient depends strongly on particle size. In the absence of this information, the measured particle size distribution described above is used in the calculation made here.

Assuming log-normal distribution and valid mean diameters for $\phi(R)$ and $f(a)$, negligible electrical effects and perfect retention efficiency, the theoretical washout coefficients are calculated from

Equation (3). For comparison, these values and the values determined experimentally with Equation (1) are shown in the following tabulation together with the washout coefficient calculated from the theory by A. G. Ziman.[9] Within the limits of expected error, the experimental washout coefficients agree with those predicted theoretically. The close comparison between the experimental result and that using Ziman's theory must be assumed fortuitous in light of the many uncertainties in parametric values, the omission of electrical effects, and the assumption of perfect retention.

Test	Experimental	Calculated (Eqn 2)	Calculated (Ziman)
R18	9.4×10^{-6}	3.64×10^{-6}	8.65×10^{-6}
R20	5.4×10^{-6}	2.44×10^{-6}	5.75×10^{-6}

CONCLUSIONS

Since no measurements have been obtained for either the charging of the silver iodide particles or the rain charges during field tests R18 and R20, an estimation of the electrical effects on scavenging is impossible. Even were information known, calculating the collection efficiency, including charge effects, would be very difficult. No exact solution to this problem is available. It appears that the most profitable approach would be to perform carefully controlled experiments so that, as in the case of heat transfer, empirical relations specifying the collection efficiency as a function of the electrical parameters could be obtained.

Retention efficiencies have been assumed to be equal to 1. While this conclusion is not supported by any direct experimental evidence, theoretical arguments for essentially perfect retention of small particles are presented by Fuch,[4] Davies,[5] and Junge.[10]

Within the experimental and statistical errors in the calculations reported here, it can be concluded that:

- The washout of submicron silver iodide particles may be predicted according to Equation (3) or Ziman's theory. It is believed that the washout of most submicron particulates can be predicted according to these equations except in circumstances resulting from high charges on the raindrops, on particles, or both as, for example, a result of a thunderstorm.
- When electrical effects and imperfect retention efficiencies are ignored, the process of washout of submicron particulates and highly soluble gases is similar, and the same theoretical equation (Equation (3)) may be used to predict either.
- The combined effects of charges and other factors on the washout of submicron particulates are probably smaller than diffusion under normally encountered conditions in the atmosphere.
- Size distributions for both particles and drops must be well defined.

REFERENCES

1. R. J. Engelmann. The Calculation of Precipitation Scavenging, BNWL-77 and BNWL-SA-299. Pacific Northwest Laboratory, Richland, Washington. 1965.

2. R. J. Engelmann, R. W. Perkins, D. I. Hagen, and W. A. Haller. Washout Coefficients for Selected Gases and Particulates, BNWL-SA-657 and APCA 66-11Y. Pacific Northwest Laboratory, Richland, Washington, 1966.

3. R. J. Engelmann, D. I. Hagen, W. A. Haller, and R. W. Perkins. Washout Coefficients for Silver Iodide, BNWL-SA-798. Pacific Northwest Laboratory, Richland, Washington. 1966.

4. N. A. Fuchs. The Mechanics of Aerosols. English edition, Pergamon Press, Oxford. 1964.

5. Aerosol Science, edited by C. N. Davies. Academic Press, London and New York. 1966.

6. N. H. Fletcher. The Physics of Rainclouds. Cambridge University Press, Cambridge, Massachusetts, 1962.

7. L. R. Koenig. "Some Chemical and Physical Properties of Silver Iodide Smokes," J. Appl. Meteor., vol. 3, pp. 307-310. 1964.

8. R. G. DePena and E. A. Caimi. "Hygroscopicity and Chemical Composition of Silver Iodide Smoke Used in Cloud Seeding Experiments," J. Atmos. Sci., vol. 24, pp. 383-386. 1967.

9. A. G. Ziman. "Mechanisms of Capture and Precipitation of Atmospheric Contaminants by Clouds and Precipitation," Problems of Nuclear Meteorology, Moscow, 1962. (Translation AEC-TR-6128 p. 139).

10. C. E. Junge. Air Chemistry and Radioactivity. Academic Press, New York, 1963.

THE CONVECTIVE DIFFUSION EQUATION FOR THE SCAVENGING OF SUBMICRON PARTICLES

W. G. N. Slinn*

INTRODUCTION

In our companion paper[1] which appears in this annual report and which will be referred to as (I), we have studied the precipitation scavenging of submicron particles. Specifically, we discussed the washout by rain of spherical particles of radii between 10 and 1000 Å. The analysis started from Newton's second law

$$\frac{d\vec{V}}{dt} = -\beta(\vec{V} - \vec{V}_f) + \vec{a}_e + \vec{A}(t)$$

where, again, $\vec{V}$ is the velocity of the particle with respect to the raindrop, β is the drag coefficient per unit mass, $\vec{V}_f$ is the velocity of the fluid, $\vec{a}_e$ is the electric force per unit mass on the particle and $\vec{A}$ is the stochastic acceleration.

It is clear in (I) that the entire analysis rests upon the specification of the stochastic acceleration $\vec{A}(t)$. In turn, one can see that the basis for the Fokker-Planck and Smoluchowski equations and for the kinetic derivation of the convective diffusion equation are only as secure as the rational basis for the specification of $\vec{A}(t)$.

It appears that up until now the best available description of the stochastic acceleration was Chandrasekhar's.[2,3] The form he used, was assumed, albeit with superb judgement. We have developed a method to calculate $\vec{A}(t)$. Here the method will be demonstrated by calculating the force on a stationary sphere in an equilibrium environment. The more involved calculation appropriate for a moving particle in a nonequilibrium environment is given in Reference (4). Wider dissemination of the results obtained in (4) is planned.

CHADRASEKHAR'S METHOD

Before presenting a method for calculating $\vec{A}(t)$ let us review Chandrasekhar's analysis. Consider a Brownian particle in an equilibrium environment and suppose that no external forces act on the particle. Then Newton's law becomes

$$\frac{d\vec{V}}{dt} = -\beta\vec{V} + \vec{A}(t).$$

This equation is usually referred to as Langevin's equation. Langevin was the first to suggest separating the total force on the particle into a continuous drag force, $-\beta\vec{V}$, and a fluctuating force, $\vec{A}(t)$. In (4) it is shown that this separation is unnecessary.

If the initial velocity of the particle is $\vec{V}_o$, then the formal solution to the Langevin equation is

* *Analysis Section, Mathematics Department.*

$$\vec{V} = \vec{V}_o e^{-\beta t} + e^{-\beta t} \int_o^t e^{\beta s} \vec{A}(s)\, ds \quad .$$

Because of the stochastic nature of $\vec{A}(t)$, we admit to the practical impossibility of obtaining the solution to this equation in a deterministic form. Instead, we seek only the probability, $W(\vec{V},t;\vec{V}_o,0)d\vec{V}$, that the particle has velocity $\vec{V}$ to $\vec{V} + d\vec{V}$ at time t if it were known to have velocity $\vec{V}_o$ at time t = 0. That is, as $t \to 0$,

$$W(\vec{V},0) \to \delta(\vec{V} - \vec{V}_o) \qquad (t \to 0),$$

where δ is Dirac's delta function.

The core of Chandrasekhar's argument is as follows. Since the particle is assumed to be immersed in an equilibrium environment at temperature T, he requires that $W(\vec{V},t)$ tend to a Maxwellian distribution for the temperature T independent of $\vec{V}_o$ as $t \to \infty$. That is,

$$W(\vec{V},t) \to \left(\frac{M}{2\pi kT}\right)^{3/2} \exp\left\{-\frac{M|\vec{V}|^2}{2kT}\right\} \quad (t \to \infty).$$

In other words, it is required that the particle attains its equipartition value of energy as $t \to \infty$.

To satisfy this requirement, $\vec{A}(t)$ must possess certain statistical properties. In particular, denote by $\vec{B}$ the net change in velocity which a Brownian particle may suffer on a given occasion during an interval of time Δt:

$$\vec{B}(\Delta t) = \int_t^{t+\Delta t} \vec{A}(s)\, ds \quad .$$

Then, to obtain a Maxwellian velocity distribution for the particle as $t \to \infty$, he demonstrates that it is sufficient that the probability of occurrence of different values for $\vec{B}$ be governed by the distribution function

$$W(\vec{B}) = \left(\frac{M}{4\pi kT\beta\Delta t}\right)^{3/2} \exp\left(-\frac{M|\vec{B}|^2}{4kT\beta\Delta t}\right) \quad .$$

Chandrasekhar explains that he was motivated by two separate considerations in postulating this form for $W(\vec{B})$. The first consideration is that, in reality, the change in velocity of the particle is the result of a large number of collisions of molecules with the particle. Since the number is large, one can expect (by the central limit theorem) that the distribution is normal (or Gaussian). The second consideration is that he knows that the β in the expression for W(B) must be the drag coefficient to insure that as $t \to \infty$, the velocity distribution function becomes Maxwellian. This will be seen later.

Although there have been subsequent investigations of the Brownian motion problem it appears that there has been little progress toward a derivation of the stochastic acceleration. Chandrasekhar emphasizes the tenuous nature of his assumption and writes that the correct procedure would be to analyze the problem "based on first principles and without appealing to any 'intuitive' or 'a priori' considerations." We proceed to follow Chandrasekhar's suggestion.

MARKOFF'S METHOD

Since the drag force has been separated from the total force on the particle, we consider a sphere at rest. The objective is to find the distribution function describing the probable amount of momentum delivered to the sphere during a small time interval Δt. If this can be determined then the distribution for the change in velocity of the particle, if it were free to move, can be found easily.

The method which we use, is to obtain first the momentum delivered to one side of a flat plate of area ΔA. Then later, we add the contribution from each such ΔA on a sphere. A polar axis perpendicular to the plate is taken, and any volume element, dV, in the fluid, is located with the usual spherical coordinates (r,θ,ϕ).

Molecules of mass m and speed ξ have momentum whose magnitude is $m\xi$. Although it is not necessary[4] we shall assume that the collisions between the molecules and the plate are elastic and that the mass of the plate is much larger than the mass of a molecule. Then each molecule that collides with the plate transfers to it a momentum $2m\xi \cos\theta\ (-\hat{k})$ where $\hat{k}$ is a unit vector in the z direction. If N molecules hit the plate during Δt, then the total momentum delivered is

$$\vec{P} = \sum_{j=1}^{N} \vec{p}_j = \sum_{j=1}^{N} 2m\xi \cos\theta\ (-\hat{k}).$$

It is not trivial to perform this summation. The speed and location of any molecule is known only statistically, and the total number of molecules that hit the plate is unknown. We have extended Markoff's method[2] to enable us to perform the sum.

The reasoning behind Markoff's method is simple to understand. If a quantity $\vec{\Phi}$ is the sum of N independent quantities $\vec{\phi}_j$:

$$\vec{\Phi} = \sum_{j=1}^{N} \vec{\phi}_j$$

and if the distribution of each $\vec{\phi}_j$ is known then it is expected that the distribution of $\vec{\Phi}$ could be calculated. Markoff's method shows us how.

Specifically, let $\vec{\phi}_j$ depend on s generalized coordinates $q_j^1, q_j^2, \ldots q_j^s$. If the probability that the set $\vec{q}_j$ is between $\vec{q}_j$ to $\vec{q}_j + d\vec{q}_j$ is known to be $\tau(\vec{q}_j)d\vec{q}_j$, then Markoff's result yields the probability that $\vec{\Phi}$ is between $\vec{\Phi}$ to $\vec{\Phi} + d\vec{\Phi}$ is

$$W(\vec{\Phi})d\vec{\Phi} = \frac{1}{(2\pi)^3}\int d\vec{\rho}\ A_N(\vec{\rho})\ e^{-i\vec{\rho}\cdot\vec{\Phi}}$$

where

$$A_N(\vec{\rho}) = \prod_{j=1}^{N}\left[\int d\vec{q}\ \tau(\vec{q})e^{+i\vec{\rho}\cdot\vec{\phi}_j}\right].$$

If $\vec{\phi}_j = \vec{q}_j$, Markoff's result degenerates to a result familiar to statisticians that the characteristic function of a sum is the product of the characteristic function of the elements in the sum.

FLUCTUATING FORCE ON A PLATE

We shall only indicate how Markoff's method can be utilized to determine the distribution of momentum delivered to a flat plate. The details are given in Reference (4). The "coordinates" $\vec{q}_j$ upon which $\vec{p}_j$ depends are the speed, direction of motion, and location of each molecule. If the fluid is in equilibrium, then the distribution of speeds is Maxwellian and the direction of motion is random. Further, although there occur fluctuations in the number density of molecules, n, these are to be consistent with the constraint that the total number of molecules in the hemisphere above the plate must tend to the fixed number $\frac{1}{2}\left(\frac{4}{3}\pi R^3\right)\bar{n}$ as $R \to \infty$, where $\bar{n}$ is the average number density. It is assumed that a specific molecule could be anywhere in the volume. Therefore, the probability that it is in dV is

$$dV/\left[\frac{1}{2}\left(\frac{4}{3}\pi R^3\right)\right].$$

Thus we have

$$\tau_j(\vec{q}_j)\, d\vec{q}_j$$

$$= 4\pi \left(\frac{\gamma}{\pi}\right)^{3/2} \xi^2 e^{-\gamma\xi^2} d\xi \, \frac{d\Omega}{4\pi} \cdot \frac{dV}{\frac{1}{2}\left(\frac{4}{3}\pi R^3\right)}$$

where $\gamma = \frac{m}{2kT}$, in which kT is the thermal energy, and where $d\Omega$ is an infinitesimal solid angle in velocity space. We note that the distribution of the coordinates is the same for all molecules.

We make use of the following result.[4] If the distribution of the coordinates, $\tau_j(\vec{q}_j)$, is the same for all j, then as $N \to \infty$

$$A_N(\vec{\rho}) = \exp\left\{-\, C(\rho)\right\}$$

where

$$C(\vec{\rho}) = N\int d\vec{q}\, [1 - e^{+\, i\vec{\rho}\cdot\vec{\phi}}] \qquad (N \to \infty).$$

To determine the total momentum delivered to the plate we sum over all molecules in the hemisphere above the plate and count "one" or count "zero", depending on whether the molecule can or cannot, respectively, reach the plate during the time interval Δt. That is,

$$\vec{P} = \sum_{j=1}^{N\to\infty} 2m\, \xi \cos\theta(-\hat{k}) \left\{\begin{matrix}1\\0\end{matrix}\right\},$$

where

$$N = \frac{1}{2}\left(\frac{4}{3}\pi R^3\right)\bar{n}\ .$$

To hit the plate during Δt, a molecule must be within the distance $\xi\Delta t$ and must be traveling in a direction within the solid angle $\frac{\Delta A\cos\theta}{r^2}$. It is found to be unnecessary to express this in a mathematically exact form. We write

$$\left\{\begin{matrix}1\\0\end{matrix}\right\} = h(\text{speed})\ h(\text{direction})$$

where h is similar to a Heavyside function but which is to be interpreted as in the above discussion.

Now we apply Markoff's method. The probability that the momentum delivered to a flat plate is between $\vec{P}$ to $\vec{P} + d\vec{P}$ is

$$W(\vec{P})d\vec{P} = \frac{d\vec{P}}{(2\pi)^3}\int d\vec{\rho}\ \exp\ [-C(\vec{\rho})]e^{-i\vec{\rho}\cdot\vec{P}}$$

where

$$C(\vec{\rho}) = \frac{1}{2}\left(\frac{4}{3}\pi R^3\bar{n}\right)\int_0^{R\to\infty} dr\ r^2\int_0^{\pi/2} d\theta\ \sin\theta\int_0^{2\pi} d\phi\int_{\xi=0}^{\infty} d\xi\ \xi^2\int_0^{4\pi} d\Omega x$$

$$\times\ \frac{1}{\frac{1}{2}\left(\frac{4}{3}\pi R^3\right)}\left\{4\pi\left(\frac{\gamma}{\pi}\right)^{3/2} e^{-\gamma\xi^2}\right\}\frac{1}{4\pi}\left[1 - \exp\left\{-i2m\xi\cos\theta\,(\hat{k})\cdot\vec{\rho}\,h(\text{speed})h(\text{direction})\right\}\right] .$$

The integration over the direction of motion of the molecules is simple to perform. If the solid angle is not in $(\Delta A\cos\theta/r^2)$, then h(direction) = 0 and [1 - exp ( )] = [1 - exp (0)] = 0. Otherwise, h(direction) = 1, so that the integrand is not a function of the solid angle and can be taken outside the integral. Similarly, the integral over the speed is zero if the speed is less than $(r/\Delta t)$. Performing the integration on ϕ we are left with

$$C(\vec{\rho}) = 2\pi\bar{n}(\Delta A)\left(\frac{\gamma}{\pi}\right)^{3/2}\int_0^{R\to\infty} dr\int_0^{\pi/2} d\theta\ \sin\theta\ \cos\theta\int_{r/\Delta t}^{\infty} d\xi\ \xi^2 e^{-\gamma\xi^2}$$

$$\times\ [1 - \exp\ (-i2m\rho_z\ \xi\ \cos\theta)] .$$

The remaining integrals are straightforward but rather tedious. The result is[4]

$$C(\vec{\rho}) = i\sqrt{\pi}\ \left(\frac{1}{4}\ \bar{n}\bar{c}\Delta A\Delta t\right)\frac{m\rho_z}{\sqrt{\gamma}}\ w\left(-\frac{m\rho_z}{\sqrt{\gamma}}\right)$$

where $\bar{c}$ is the thermal speed of the molecules, $\bar{c} = \sqrt{\frac{8kT}{\pi m}}$, $\frac{1}{4}\ \bar{n}\bar{c}\Delta A\Delta t) = \bar{M}$ is the familiar expression[5] for the mean number of molecules that hit an area element ΔA during a time interval Δt, and $w(z) = e^{-z^2}\ \text{erfc}\ (-iz)$ is known as the error function with complex argument.[6]

Substituting this result into the expression for the distribution of the total momentum, there is obtained

$$W(\vec{P}) = \frac{1}{(2\pi)3}\int d\vec{\rho}\ \exp\left\{-\ i\sqrt{\pi}\ \bar{M}\ \frac{m\rho_z}{\sqrt{\gamma}}\ w\left(-\frac{m\rho_z}{\sqrt{\gamma}}\right)\right\}\ e^{-i\vec{\rho}\cdot\vec{P}}$$

The integrals over ρ_x and ρ_y are trivial:

$$W(\vec{P}) = \frac{1}{2\pi}\ \delta(P_x)\delta(P_y)\int\ d\rho_z\ \exp\ \left\{-i\sqrt{\pi}\ \bar{M}\ \frac{m\rho_z}{\sqrt{\gamma}}\ w\left(-\frac{m\rho_z}{\sqrt{\gamma}}\right)\right\}\ e^{-i\rho_z P_z} .$$

This result confirms the obvious fact that the amount of momentum delivered to the plate in the x and y directions (in the plane of the plate) is certain to be zero.

Unfortunately, we have not been able to perform the integral over ρ_z. For $\bar{M}$ large (around 10 would probably be adequate),[4] the dominant contribution to the integrand occurs near $\rho_z = 0$. A uniformly convergent power series for $w(z)$ is[6]

$$W(z) = \sum_{n=0}^{\infty} \frac{(iz)^n}{\Gamma(\frac{n}{2}+1)} = 1 + \frac{iz}{\Gamma(3/2)} + \cdots$$

Keeping only the first two terms of this series, there results

$$C(\rho_z) \doteq i\sqrt{\pi}\,\bar{M}\,\frac{m\rho_z}{\sqrt{\gamma}}\left\{1 + \frac{2i}{\sqrt{\pi}}\left(-\frac{m\rho_z}{\sqrt{\gamma}}\right)\right\}.$$

Substituting this into $W(P)$, we obtain the final result, for $\bar{M}$ large:

$$\vec{W}(P) = \frac{\delta(P_x)\,\delta(P_y)}{\sqrt{2\pi(\frac{\pi}{4}\,\bar{n}\bar{c}\Delta A\Delta t)(m\bar{c})^2}} \times \exp\left\{-\frac{(P_z + \bar{n}kT\Delta t\Delta A)^2}{2(\frac{\pi}{4}\,\bar{n}\bar{c}\Delta A\Delta t)(m\bar{c})^2}\right\}.$$

For convenience, we write this result for the distribution of momentum delivered to one side of a flat plate in the form

$$W(P) = \frac{\delta(P_x)\,\delta(P_y)}{\sqrt{2\pi\,\sigma^2}} \times \exp\left\{-\frac{(P_z+\mu)^2}{2\sigma^2}\right\}$$

where $\mu = \bar{n}kT\Delta t\Delta A$ and $\sigma^2 = \pi(\frac{1}{4}\,\bar{n}\bar{c}\Delta A\Delta t)(m\bar{c})^2$.

This normal distribution for the z component is accurate only if the dominant contribution to the integral over ρ_z occurs near $\rho_z = 0$. Essentially, we are requiring that $\bar{M} = \frac{1}{4}\,\bar{n}\bar{c}\Delta A\Delta t$ be large. It is shown in Reference (4) that this restricts the theory to particles of radii greater than about 10 Å.

THE FLUCTUATING FORCE ON A SPHERE - LARGE K_n

Now we have the distribution of momentum delivered to one side of a flat plate. To obtain the distribution of momentum delivered to a sphere of radius a, we imagine the sphere to be divided into L area elements where $L = 4\pi a^2/\Delta A$. Then, using Markoff's method, we determine the total momentum by adding the momenta delivered to each area element.

It is important to notice that Markoff's method is applicable only for the case of adding independent stochastic variables. To obtain the momentum delivered to an area element, its size can be chosen small enough so that the motion of the molecules in its neighborhood can be assumed to be independent. However, if Markoff's method is to be used to sum the momenta delivered to each area element of a sphere, then the impulse on each must be independent. Equivalently, the motion of the molecules about the entire sphere must not influence one another. Consequently, our

result will be applicable only to the case of free molecule flow, that is, when the Knudsen number (the ratio of the mean free path to the radius of the sphere) is large.

Let $\vec{\Phi}$ be the total momentum delivered to the sphere. Then

$$\vec{\Phi} = \sum_{j=1}^{L} \vec{P}_j$$

where, again, the sum is over all area elements of the sphere. Each momentum $\vec{P}_j$ depends on "coordinates" $\vec{q}_j$ which are simply the magnitude and direction of $\vec{P}_j$. The magnitude, P_j, is distributed according to the results of the previous section for the distribution of P_z:

$$W(P_j) = \left(\frac{1}{2\pi\sigma_j^2}\right)^{3/2} \exp\left\{ - \frac{[P_j - \mu_j]^2}{2\sigma_j^2} \right\}.$$

The negative sign appears because now we are considering only the magnitude. The direction of each momentum is not a random variable. It is known to be perpendicular to the appropriate area element.

Let us determine the component, in some arbitrary direction Z, of the total momentum delivered to the sphere. The components in mutually orthogonal directions X and Y will be identical. Thus we desire

$$\Phi_z = \sum_{j=1}^{L} P_j \cos\theta_j$$

where θ_j is the polar angle from Z to the jth area element. Since $\cos\theta_j$ is not a stochastic variable, it is relatively easy to see that the distribution of $P_j \cos\theta_j$ is[4]

$$\tau(P_j \cos\theta_j) = \left(\frac{1}{2\pi\sigma_j^2 \cos^2\theta_j}\right)^{3/2} \exp\left\{ - \frac{[P_j \cos\theta_j - \mu \cos\theta_j]^2}{2\sigma_j^2 \cos^2\theta_j} \right\}.$$

Now we apply Markoff's method:

$$W(\Phi_z) = \frac{1}{2\pi} \int d\rho\, A_L(\rho) e^{-i\rho\Phi_z} \quad \text{where} \quad A_L(\rho) = \prod_{j=1}^{L} \int dq_j\, \tau(q_j) \exp(i\rho\phi_j).$$

Here $q_j = \phi_j = P_j \cos\theta_j$.

The integral over q_j is simple to perform and we obtain

$$A_L(\rho) = \prod_{j=1}^{L} \exp\left(\mu_j \cos\theta_j\, i\rho - \frac{1}{2}\sigma_j^2 \cos^2\theta_j \rho^2\right)$$

$$= \exp\left\{ i\rho \sum_{j=1}^{L} \mu_j \cos\theta_j - \frac{1}{2}\rho^2 \sum_{j=1}^{L} \rho_j^2 \cos^2\theta_j \right\}.$$

For large L, the first summation in the above expression becomes

$$\sum_{j=1}^{L} \mu_j \cos\theta_j = \bar{n}kT\Delta t \sum_{j=1}^{L} \cos\theta_j \Delta A_j$$

$$= \bar{n}kT\Delta t \int_0^{\pi} \int_0^{2\pi} a^2 \cos\theta a^2 \sin\theta d\theta d\omega$$

which is zero. Physically, this corresponds to the obvious result that the sum of the mean values of the momentum delivered to each area element of a stationary sphere is zero. In a similar manner, the other term in the exponent becomes

$$-\frac{\pi}{2}\rho^2 \frac{1}{4} \bar{n}\bar{c}\Delta t \,(m\bar{c})^2 \frac{4}{3}\pi a^2.$$

Substituting the resulting expression for $A_L(\rho)$ into the equation for $W(\Phi_z)$ and utilizing the observation that the distribution of the Φ_x and Φ_y will be the same, we obtain the result

$$W(\vec{\Phi})\, d\vec{\Phi} = \frac{d\vec{\Phi}}{(2\pi\sigma^{-2})^{3/2}} \left\{ \exp - \frac{|\vec{\Phi}|^2}{2\bar{\sigma}^2} \right\}$$

where $\bar{\sigma}^2 = \frac{\pi}{3} \frac{1}{4} \bar{n}\bar{c}\Delta A \Delta t \,(4\pi a^2)\,(m\bar{c})^2$.

THE DRAG AND DIFFUSION COEFFICIENTS

We have obtained the distribution function describing the momentum $\vec{\Phi}$, delivered to a sphere at rest. If the sphere were free to move, it would acquire the velocity $\vec{B} = \vec{\Phi}/M$ where M is the mass of the particle. Thus we have derived for the probability that, during Δt, a sphere attains velocity between $\vec{B}$ to $\vec{B} + d\vec{B}$, the result

$$W(\vec{B})d\vec{B} = \frac{d\vec{B}}{\left(4\pi \frac{kT}{M} \frac{\Delta t}{\tau}\right)^{3/2}} \exp\left\{ - \frac{|\vec{B}|^2}{4\frac{kT}{M}\frac{\Delta t}{\tau}} \right\},$$

where we have used

$$\bar{c}^2 = \frac{8kT}{\pi m} \quad \text{and defined}$$

$$\tau = \frac{3m}{m\bar{n}\bar{c}4\pi a^2} .$$

Chandrasekhar assumed that

$$W(\vec{B})d\vec{B} = \frac{d\vec{B}}{\left(4\pi \frac{kT}{M} \beta\Delta t\right)^{3/2}} \times \exp\left\{ - \frac{|\vec{B}|^2}{4 \frac{kT}{M} \beta\Delta t} \right\}$$

where β is the drag coefficient per unit mass. These two forms for $W(\vec{B})$ are strikingly similar. Our first result, then, is that we have justified the form of Chandrasekhar's expression, at least for the case when the Knudsen number is large, and we are aware of its limitations.

We can now obtain the consequences of our derivation of τ. The Langevin equation for a free Brownian particle was integrated to

$$\vec{V} - \vec{V}_o e^{-\beta t} = e^{-\beta t} \int_o^t e^{\beta s} \vec{A}(s)ds.$$

Suppose that the time interval is divided into a large number of sub-intervals, each of duration Δt. Then

$$\vec{V} - \vec{V}_o e^{-\beta t} = e^{-\beta t} \sum_{j=1}^{J=t/\Delta t} e^{-\beta(j\Delta t)} \int_{j\Delta t}^{(j+1)\Delta t} \vec{A}(s)\, ds.$$

But $\int_{j\Delta t}^{(j+1)\Delta t} \vec{A}(s)\, ds$ is the change, during Δt, in the velocity of the Brownian particle arising from random impulses from the molecules. This is the quantity whose distribution we have calculated.

Then for sufficiently large Δt, the problem of determining the probable velocity of a free Brownian particle is reduced to finding the distribution of

$$\vec{\psi} \equiv \vec{V} - \vec{V}_o e^{-\beta t} = \sum_{j=0}^{J} e^{-\beta(t-j\Delta t)} \vec{B}_j(\Delta t) = \sum_{j=1}^{J} \vec{\psi}_j .$$

If it is assumed that the changes in velocity occurring during each Δt are statistically independent, Markoff's method can be used once again. The result is[4]

$$W(\vec{V},t;\vec{V}_o,0) = \left[\frac{1}{2\pi \frac{kT}{M}\frac{1}{\tau\beta}\left(1 - e^{-2\beta t}\right)}\right]^{\frac{3}{2}} \times \exp\left\{-\frac{|\vec{V} - \vec{V}_o e^{-\beta t}|^2}{2\frac{kT}{M}\frac{1}{\tau\beta}\left(1 - e^{-2\beta t}\right)}\right\}$$

It is seen in this expression describing the velocity of the particle, that as $t \to \infty$, the particle will attain a Maxwellian velocity distribution only if $\tau\beta = 1$. Here we have an alternative. We can either accept that the particle does attain a Maxwellian velocity distribution and predict that $\beta = 1/\tau$ or we can accept $\tau\beta = 1$ and predict the asymptotic form of the distribution function. Both choices are rewarding, but neither is completely satisfactory.

Accepting that the velocity distribution function becomes Maxwellian, the heretofore unspecified drag coefficient per unit mass must be given by $\beta = 1/\tau$, where, again, τ is the coefficient that has been derived in the calculation of the fluctuating force on a sphere at rest. Thus with this choice it can be said that we have derived the drag coefficient per unit mass, for a sphere in free molecule flow, from information that is available when the sphere is stationary! Specifically,

$$\beta = \frac{1}{\tau} = \frac{4}{3\pi}\frac{a^2 m \bar{n} \bar{c}}{M}$$

This is exactly Epstein's drag formula.[7]

Alternatively it could have been accepted that the drag coefficient, β, was given by Epstein's formula Then it can be claimed that we have demonstrated that equipartition is a consequence of the dynamics and randomness of the process. It need not be a postulate.

The reason why there exists the indeterminancy at this point in the analysis is because our basic equation is the Langevin equation and not Newton's second law. This deficiency is removed in Reference 4 and, in addition, the effect of diffuse reflections of the molecules is investigated.

The description of the position of the particle and thereby the diffusion coefficient can be obtained in a similar manner.[2,4] The position of the particle, $\vec{R}$, is governed by $\frac{d\vec{R}}{dt} = \vec{V}$, or $\vec{R} - \vec{R}_o = \int_o^t \vec{V}(s)\, ds$. Once again Markoff's method is applied. The result for the diffusion coefficient is (at STP)

$$D = \frac{kT}{M}\tau = \frac{3\bar{c}}{32\, a^2} = \frac{1.41}{a^2}\ \frac{cm^2}{sec}\ (a \text{ in } \mathring{A}).$$

this is in satisfyingly close agreement with experimental results. For the calculation in (I) we used the empirical formula[8]

$$D = \frac{1.3}{a^2}\ \frac{cm^2}{sec}\ (a \text{ in } \mathring{A}).$$

Even this slight numerical discrepancy can be removed by changing our assumption about the nature of the molecule-particle collision term.[4]

That we have determined the diffusion coefficient and, especially, the drag coefficient from a calculation of the fluctuating force on a sphere at rest permits a new outlook on a result usually referred to as the fluctuation-dissipation theorem.[9] This theorem expresses a general relation between irreversible response and equilibrium fluctuations. Einstein's result,[10] $D = kT/M\beta$, relating the diffusion coefficient (diffusion being a manifestation of equilibrium fluctuations) to the drag coefficient (an irreversible response) is considered to be the first illustration of the theorem. Another is Nyquist's result[9] relating the electrical resistance with spontaneous charge fluctuations in electrical systems.

The new outlook that we have gained is the following. Einstein used Stokes' drag law to obtain the diffusion coefficient. We have calculated the diffusion coefficient and thereby have obtained Epstein's drag law. An attempt has been made to derive Stokes' drag law in this manner. The difficulty in obtaining it is that, for small Knudsen number, it cannot be assumed that the molecules move independently. Then Markoff's method is not applicable. We have obtained a drag law in the continuum regime, which is within a numerical factor of Stokes' law, by introducing correlations between the fluctuations of the momentum delivered to the different area elements of a sphere. Further discussion is given in Reference 4.

THE CONVECTIVE DIFFUSION EQUATION

Our final objective at this time is to indicate how the convective diffusion equation can be obtained once the stochastic acceleration is known. A complete description of the motion of the particle in the

precipitation scavenging problem is given by the Fokker-Planck equation.[4] In the interest of space, we will bypass this equation and proceed directly to the convective diffusion equation.

The motion of a Brownian particle in a force field $M\vec{f}$ is governed by

$$\frac{d\vec{V}}{dt} = -\frac{1}{\tau}\vec{V} + \vec{A} + \vec{f}$$

in which we have used the result $\tau\beta = 1$.

For a moment, let us ignore the stochastic acceleration, $\vec{A}$. If τ and $\vec{f}$ are constants, then the solution to the equation is

$$\vec{V} = \vec{V}_o e^{-t/\tau} + \vec{f}\,\tau\,(1 - e^{-t/\tau}) .$$

Thus in a time of order τ the effect of the initial velocity, $\vec{V}_o$, disappears and the particle reaches its terminal or drift velocity $(\vec{f}\tau)$.

For the problem of the precipitation scavenging of particles of radii near 100 Å, $\tau \doteq 10^{-7}$ sec. Suppose that the minimum time of interest, Δt, is larger than τ. If τ and $\vec{f}$ change only by negligible amounts in distances of order $V_o\Delta t$ or $(f\tau)\Delta t$, whichever is larger, then we can say that the mean velocity of the particle is the local terminal velocity. For an uncharged particle of 100 Å radius, $V_o\tau \doteq (\sqrt{kT/M})\,\tau \doteq 100$ Å and $f\tau^2 \doteq V_f\tau \doteq 10^{-3}R_D$, where R_D is the radius of the raindrop. Clearly, the restriction of insignificant spatial variations in these distances is not a stringent requirement.

In addition to this mean motion, the particle moves in response to the stochastic acceleration. It can be seen[2,4] that in a time Δt, of order τ, a free Brownian particle attains a Maxwellian velocity distribution and has mean square displacement of $2D\Delta t$. Thus the following picture emerges. The transition probability, which describes the probability that a Brownian particle at position $\vec{R}$ at time $\vec{t}$, is displaced a distance $\Delta\vec{R}$ during Δt, is

$$\chi(\vec{R},t;\Delta\vec{R}) = \left[\frac{1}{2\pi(2D\Delta t)}\right]^{3/2} \exp\left\{-\frac{|\Delta\vec{R} - \vec{f}\tau\Delta t|^2}{2(2D\Delta t)}\right\} .$$

Let $W(\vec{R},t;\vec{R}_o t_o)d\vec{R}$ be the probability that the particle is in the volume element $d\vec{R}$ at $\vec{R}$ at time t if the particle is known to be at $\vec{R}_o$ at time t_o. Then

$$W(\vec{R},t + \Delta t) = \int W(\vec{R} - \Delta\vec{R},t)\,\chi(\vec{R} - \Delta\vec{R},t;\Delta\vec{R})\,d(\Delta\vec{R}) .$$

This expression is a restricted form of the Chapman-Kolmogorov equation.[11] Expanding all quantities in Taylor Series about their values at $\vec{R}$ and t, and utilizing

$$\langle\Delta\vec{R}\rangle = \int\chi\,\Delta\vec{R}\,d(\Delta\vec{R}) = \vec{f}\tau\Delta t \quad \text{and}$$

$$\langle\Delta\vec{R}^2\rangle = 2D\Delta t + 0(\Delta t)^2,$$

we obtain, to first order in Δt, the Smoluchowski equation

$$\frac{\partial w}{\partial t} = \nabla\cdot\left(\frac{kT}{M\tau}\nabla w - \vec{f}\tau w\right).$$

Proceeding as in (I), we define a number density of particles as

$$n(\vec{r},t)d\vec{r} = d\vec{r} \int_{\vec{r}^*} n(\vec{r}^*,0)\, w(\vec{r},t;\vec{r}^*,0)\, d\vec{r}^* \ .$$

Thus n gives the probability that a particle is in $d\vec{r}$ without regard to its initial position. Operating on the equation for n with

$$\frac{\partial}{\partial t} - \nabla\cdot\left(\frac{kT}{m\tau}\nabla - \vec{f}\tau\right) \ ,$$

and using $\nabla \circ \vec{V}_f = 0 = \nabla \circ \vec{E}$, we obtain the convective diffusion equation

$$\frac{\partial n}{\partial t} + (\vec{V}_f + \mu_e\vec{E})\cdot\nabla n = \nabla\cdot(D\nabla n) \ .$$

Here we have used that the terminal velocity is $\vec{f}\tau = \vec{V}_f + \mu_e\vec{E}$, where $\vec{E}$ is the electric field, and the mobility is defined as $\mu_e = (q/M)\tau$, with q denoting the charge on the particle.

It should be mentioned that we have obtained here, as well as the convective diffusion equation, two other important results. First, we have an independent derivation of Einstein's formula relating the diffusion coefficient to the mobility:

$$\mu_e = \frac{q}{M}\tau = q\,\frac{D}{kT} \ .$$

Second, although we set out to derive no more than the fluctuating force on a sphere at rest, we have calculated not only the drag on a sphere if it were in motion, but now we have the result that if it were charged and in the presence of an electric field, its mobility would be

$$\mu_e = \frac{q}{M}\tau = q\,\frac{3}{4\pi a^2 m\bar{n}\bar{c}} \ .$$

This agrees exactly with the expression for the mobility obtained by alternate methods[5,12] for the case when the mass of the particle is much larger than the mass of a molecule.

SUMMARY

In summary, we have described a method by which the stochastic force on a Brownian particle can be calculated. The technique used was Markoff's method. This limited the results to the regime Kn > 1. Although it was assumed here that the particle was stationary and in an equilibrium environment these are not essential assumptions.

Having derived the description of the fluctuating force on a stationary sphere it was apparent that we had obtained Epstein's drag coefficient from information that is available when the sphere is at rest. Alternatively, if the drag coefficient is assumed to be known, then we have demonstrated that for specular reflection of the molecules, equipartition is a consequence of and need not be a postulate for the motion of a Brownian particle. In addition to the drag coefficient, the diffusion coefficient and the mobility for a particle were obtained. All are in agreement with experimental results or with results obtained by alternate theoretical analysis.

The method developed here provides the framework within which the following question can be

answered. What is the diffusion coefficient appropriate for the description of the motion of a particle in a nonequilibrium environment? Previously, the effects of heat flux and viscous stress on the diffusion of a submicron particle in air were unknown. As this report goes to press, the answer to this question has been found and is given in Reference 4.

REFERENCES

1. W. G. N. Slinn. "Precipitation Scavenging of Submicron Particles." Included in this annual report.

2. S. Chandrasekhar, "Stochastic Problems in Physics and Astronomy," Rev. Mod. Phys., vol. 15, p. 1, 1943.

3. E. Nelson, Dynamical Theories of Brownian Motion. Princeton University Press, Princeton, New Jersey, 1967.

4. W. G. N. Slinn, Brownian Diffusion of Submicron Particles in Air Under Nonequilibrium Conditions. Ph.D. Dissertation, Cornell University, Ithaca, New York, 1969.

5. E. H. Kennard, Kinetic Theory of Gases. McGraw-Hill Book Co., New York, 1938.

6. N.B.S. Handbook of Mathematical Functions, edited by M. Abramowitz and I. A. Stegun. U.S. Printing Office, Washington, D.C., 1964.

7. P. W. Epstein, "On the Resistance Experienced by Spheres in Their Motion Through Gases," Phys. Rev. vol. 23, p. 710, 1924.

8. N. A. Fuchs, The Mechanics of Aerosols. Pergamon Press, The MacMillan Co., New York, 1964.

9. H. B. Callen, "Thermodynamic Fluctuations," Nonequilibrium Thermodynamics, Variational Techniques and Stability. University of Chicago Press, Chicago, Illinois, 1966.

10. A. Einstein, Brownian Movement. Dover Publishing Co., New York, 1956.

11. A. N. Kolmogorov, Foundations of the Theory of Probability. Chelsea Publishing Co., New York, 1950.

12. L. B. Loeb, Fundamental Processes of Electrical Discharges in Gases. John Wiley & Sons, Inc., New York, 1939.

SOME ENVIRONMENTAL CONSEQUENCES OF SHADING IN SHRUB COMMUNITIES

W. T. Hinds

INTRODUCTION

The manifold interactions of vegetation with the underlying soil and with the overlying atmosphere have been the subject of considerable investigation for many years. The emphasis, however, has usually been placed on uniform vegetation cover, particularly for meteorological and climatological studies. In most cases, surfaces under study are defined as uniform to permit reasonable analytical approximations for a mathematical treatment of the interaction between surface, plants, and atmosphere. In careful micrometeorological work, the passion for uniformity of terrain can lead to remarkable searches for suitable sites, especially in attempting to avoid advective effects. Perhaps the best example is reported by Swinbank[1] where, in describing his experimental site, he stated that "the only obstacle within a distance of several miles was a small group of trees two miles SSW."

Climatological studies, particularly the standardized climatic measurements recommended by the United States Weather Bureau, likewise emphasize the benefits of a uniform surface. The aim in this case, of course, is to assure that properties of the air, not those of a particular plant community, are measured. To this end, the standard shelter is best placed by each user over a (hopefully) standard size plot of short grass.

The existence of a discontinuous plant cover leads to a rather complex set of interacting edge effects. A most striking example is the mosaic of shade pools and sunlit surface. Strong contrasts are commonly formed, particularly if the vegetation causing the shade is multi-stemmed. Many semi-arid plant communities have the characteristic widely spaced shrubs, with a more or less continuous understory of grasses and forbs. The shrub communities of a desert steppe thus are excellent focal points for the study of discontinuous cover effects.

SHADING BY INDIVIDUAL SHRUBS

During the spring of 1966, a series of soil temperature measurements was carried out near a typical multi-stemmed desert-steppe shrub, spiny hopsage (Grayia spinosa). Temperatures were measured at 18 points around the shrub at a depth of 3 cm, so a good estimate of the diurnal cycle of surface temperature was possible. A detailed discussion of the results by Hinds and Rickard[2] pointed out that

the shaded area appeared to duplicate a virtual depth environment several centimeters deeper than the unshaded areas. The time and magnitude of the daily maxima and minima, for instance, were 2 to 4 hr later than for the sunlit area. As expected, the maximum temperature in the shade pool was much lower than in the sunlit area and the minimum temperatures were essentially the same in the two areas.

Patterns of isotherms around the shrub are shown in Figure 1, where it can be readily seen tnat temperature differences of 20 or 30 °F are induced within a few decimeters. Furthermore, the integral of temperature at a point with respect to time (i.e., the thermal exposure of a point) is significantly reduced over a large portion of the surface near the shrub, as indicated by Figure 2. This may be ecologically significant for two reasons:

- Typically, because desert steppe shrubs are long-lived, any alteration in environmental character is quasi-permanent.
- Any temperature-dependent physiological process taking place in plants growing in the shaded region must be affected. Therefore, associated chemical reactions may well reflect the sensitivity of chemical reaction rate to temperature.

A direct example of plant process dependence upon the plant root location was provided by following the phenology of cheatgrass (Bromus tectorum) growing around the hopsage chosen for study. The cheatgrass growing in the shade pool was 7 to 10 days slower in flowering and seed set than the cheatgrass growing in sunlit sites. Since the cheatgrass in both sites germinated at the same time (in

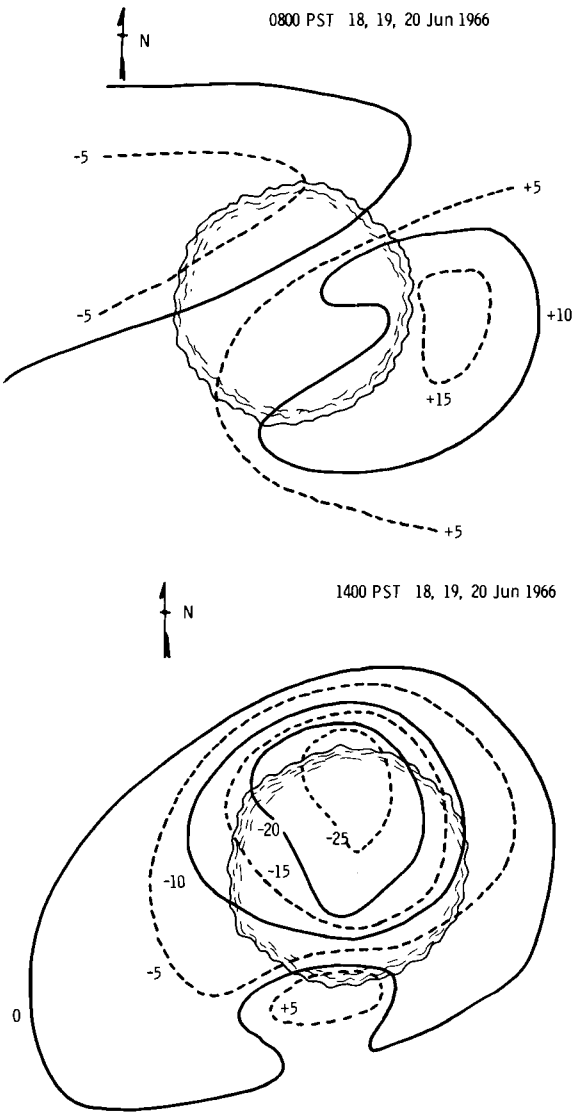

Neg. 0671580-1

FIGURE 1. Isotherm Patterns Around a Hopsage, Averaged over Three Days at 0800 and 1400 hrs

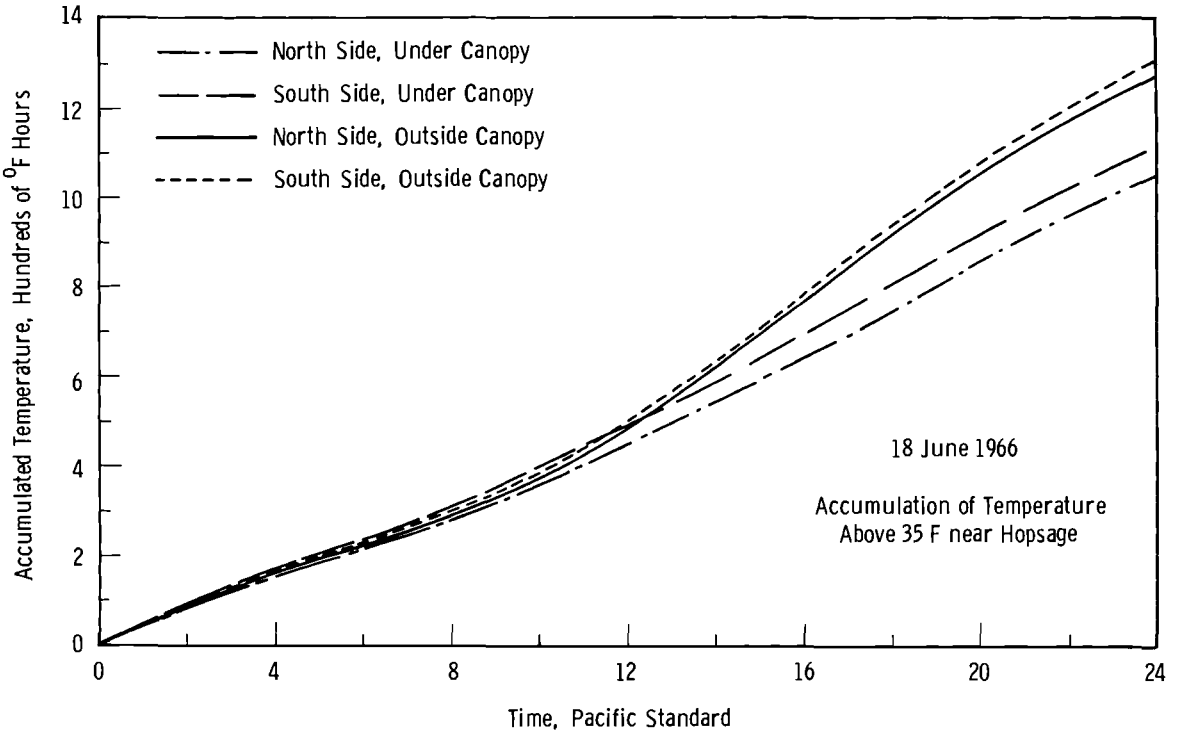

Neg. 0671580-3

FIGURE 2. Accumulated Temperature at Shaded and Sunlit Points. June 18, 1966

response to soil moisture increases due to winter rains), the lag in flowering shown by the shaded cheatgrass corresponds to about a 10% increase in growing season from germination to death.

SHADING BY SHRUB COMMUNITIES

The intensity of the localized shade pools in shrub communities, as typified by the measurements shown in Figure 1, allows some speculation concerning the effects of community-scale modification of surface temperature. Examination of the shade pool (Figure 1) for 1400 hr shows that a substantial part of the desert floor near a shrub is really quite cool compared to the sunlit areas. The total effect of shading shrubs sufficiently numerous to provide a significant canopy cover in a given community must be to reduce the average temperature of the soil surface in that community, thereby providing a link between plant community characteristics and the overlying atmosphere. A simple averaging technique applied to a uniform stand of shrubs indicates the expected magnitude of the community-scale cooling.

Let T be the temperature at a point

$\bar{T}$ be the average temperature of the surface over the shrub stand

T_o be the temperature of the unobstructed (sunlit) surface

A be the fractional area covered by shrub canopy in the community (determined usually by line transect)

About 1/2 the canopy area of this shrub (Figure 2) is characterized by surface temperatures about 0.7 that of the unobstructed surface, and about 1.5 times the shrub canopy area is characterized by temperatures about 0.9 that of the unobstructed surface.* Thus,

$$\bar{T} = 0.5A(0.7T_o) + 1.5A(0.9T_o) + (1 - 2A)T_o$$
$$= (1 - 0.3A)\, T_o \quad . \qquad (1)$$

Equation 1 assumes that the shrubs are widely enough spaced so that no interaction of shading occurs, and that the shading effect is approximately a linear function of T_o.

Hopsage is distributed over the Hanford reservation in rather a non-uniform fashion. Large areas have no hopsage at all while in special areas, hopsage is the only shrub extant. However, even within a pure hopsage stand, canopy cover is not uniform from one section to another. Whatever the causes of the variation in canopy cover, the environmental effect of canopy variation can be estimated from Equation 1. Figure 3 is a composite photograph of two sections of a hopsage stand growing on what apparently is a playa. To an observer strolling through the two sections, little if any difference is discernible. However, line transect measurements of canopy cover showed the section pictured on the left hand side of Figure 3 to have a canopy cover of 35%, while the section on the right hand side had a canopy cover of 22%. Thus, from Equation 1, the average surface temperature on a warm spring day (with T_o = 120 °F) would be about 107 °F for section "a" and about 112 °F for section "b".

DISCUSSION

Some interesting implications follow from the previously noted variety of thermal environments in shrub stands. Clearly, on a sunny day with a generally super-adiabatic lapse rate in existence over most of the steppe region, any local areas with superficially warmer surface air must act as centers for convection because, at some height not too far removed from the surface, the underlying surface character loses its local importance--the air at that height "feels" an average surface which is perforce cooler than the

---

* *The unobstructed surface temperature (averaged over three days at 1400 hours) was about 115 °F. See Hinds and Rickard, 1968.*

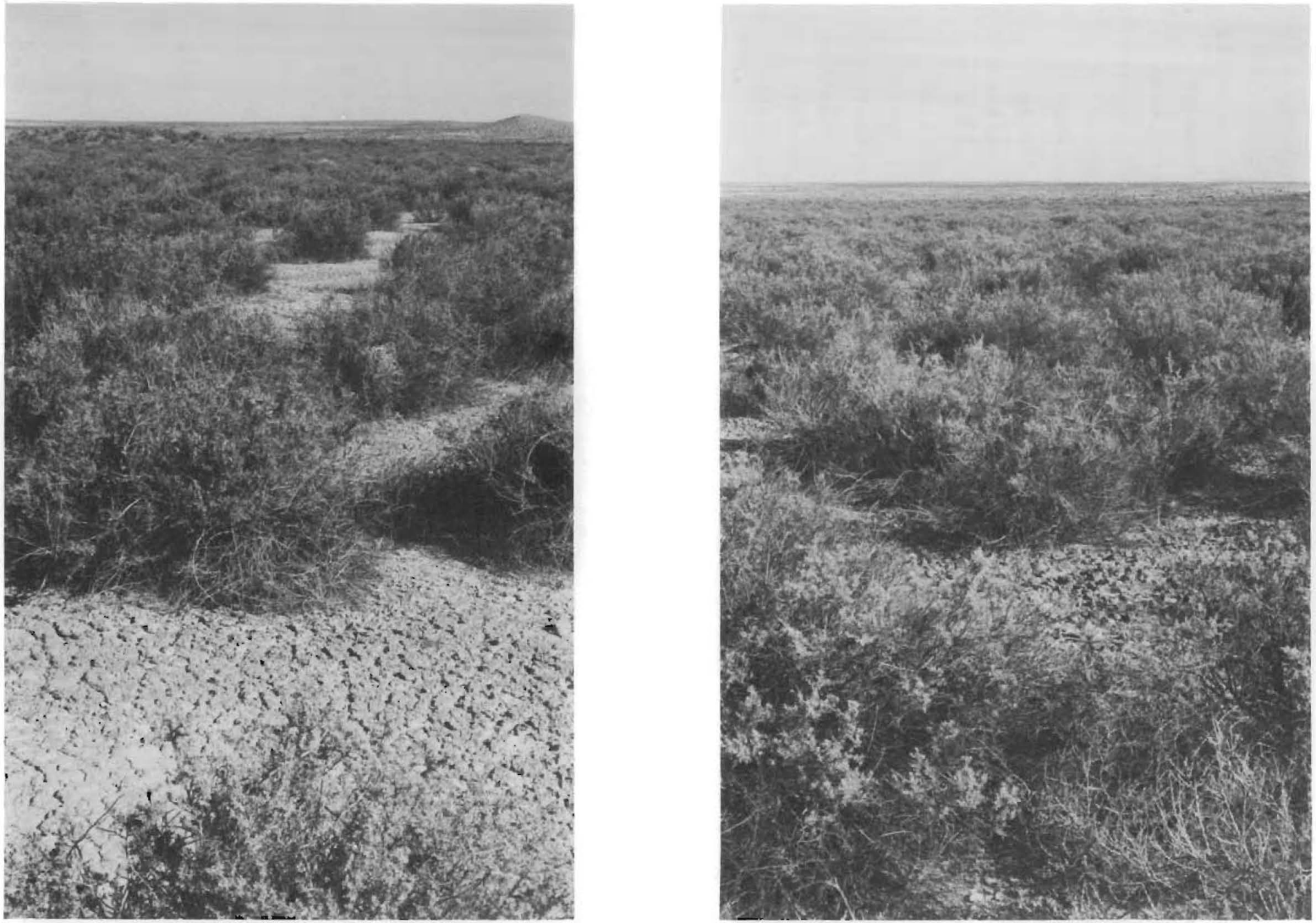

Neg. 0681787

FIGURE 3. Hopsage Community on Project ALE, Hanford Reservation

local warm region. Therefore, the local lapse rate over the warm region must be more unstable than over surrounding regions, leading to somewhat more vigorous convective activity at that point which may, after establishment, lead to air motion along the surface from the cooler regions toward the warmer region. Consequently, convective plumes may be preferentially located over areas of a steppe which are in no way different than the surroundings other than a difference in fractional canopy cover.

In general, though, the most important aspects of shrub shading in a shrub community are bound up in the intense local differences in environmental factors due to shading by a single shrub. The variation in microenvironments due to the presence of a shrub is considerable, ranging from a relatively warm area on the sunward side (Figure 1) to the cool shade pool. The incident solar radiation no doubt is both qualitatively and quantitatively different on the two sides, with the shrub acting as a micro-mountain insofar as local factors are concerned. Likewise, net radiation must show a considerable variation between the sunny and the shaded sides. Furthermore, the mean temperature of the two regions surrounding the shrub are significantly different. Since the minimum temperature on both sides of the shrub is about the same, but the maximum on the shaded side is only about 0.7 that on the sunlit side, the mean temperature of the shaded portion of the steppe floor must be less than that of the sunlit portion. An estimate of the mean temperature reduction can be made as follows:

$$T_{\text{mean sun}} = 1/2T_{max} + 1/2T_{min}$$

$$T_{\text{mean shade}} = 1/2(0.7T_{max}) + 1/2T_{min}$$

$$\frac{T_{\text{mean sun}} - T_{\text{mean shade}}}{T_{\text{mean sun}}}$$

$$= \frac{0.15T_{max}}{1/2T_{max} + 1/2T_{min}}$$

$$= \frac{0.15}{0.5 + 0.5(T_{min}/T_{max})}$$

Typically, the warm spring weather during which temperature measurements are taken yield readings ranging from maximums of about 120 °F to minimums of approximately half this value, or 60 °F. Thus,

$$\frac{T_{\text{mean sun}} - T_{\text{mean shade}}}{T_{\text{mean sun}}} = \frac{0.15}{0.75} = 20\%$$

Therefore local reductions in mean temperature of the order of 20% may be induced by localized shrub shading.

In sum, then, shrubs induce a wide variety of alterations in their immediate environment and may provide a community-scale alteration

in the earth-air energy exchange mechanism. A great deal remains to be done in identifying the important alterations in energy and moisture transfers resulting from shrub shading, and a comparable effort remains in determining the ecological importance of the microenvironment diversity so introduced.

REFERENCES

1. *W. C. Swinbank. "The Exponential Wind Profile." Quart. Jour. Roy. Meteor. Soc., vol. 40, p. 119. 1964.*

2. *W. T. Hinds and W. H. Rickard. "Soil Temperatures Near a Desert Steppe Shrub." Northwest Science, vol. 42, no. 1, pp. 5-13. 1968.*

A PORTABLE LABORATORY

H. G. Rieck and N. A. Wogman

Concentrations of short half-life cosmic-ray and naturally produced isotopes are being measured in atmospheric physics and fallout studies.[1] When these experiments are conducted at sites remote from the home laboratory, the time element prohibits return of the sample to the counting laboratory for a successful measurement. In other investigations, the samples must be reduced in volume or, as in studies of uranium ore inhalation,[2] the subjects must be counted at their home site. A portable laboratory, designed for use at the experimental site where the sample would be collected and rapidly processed in the chemical section, was fabricated. Chemical processes might include separation, volume reduction, drying, sample mounting, etc. The concluding step would be the measurement of radioactivity in a low background gamma-ray spectrometer system[3] located in the adjoining counting room. A minimum time delay between sample collection and counting would allow determination of isotopes such as ^{38}Cl (37.3 min), ^{39}Cl (55 min), and ^{214}Bi (19.7 min). In addition, studies of these isotopes in real time to follow any experimental condition could be conducted.

A 15 ton rated, tandem axle, semi-trailer was used as the laboratory shell. The basic trailer, 30 ft long by 8 ft wide by 12 ft-9 in. high was equipped with a curbside door, a full opening rear door, and 3 in. fiberglass insulation. A plywood partition containing 3 in. fiberglass insulation was installed near the curbside door to isolate the rear portion of the trailer as the counting room. The chemistry laboratory was located in the forward section. A floor plan of the laboratory is shown in Figure 1.

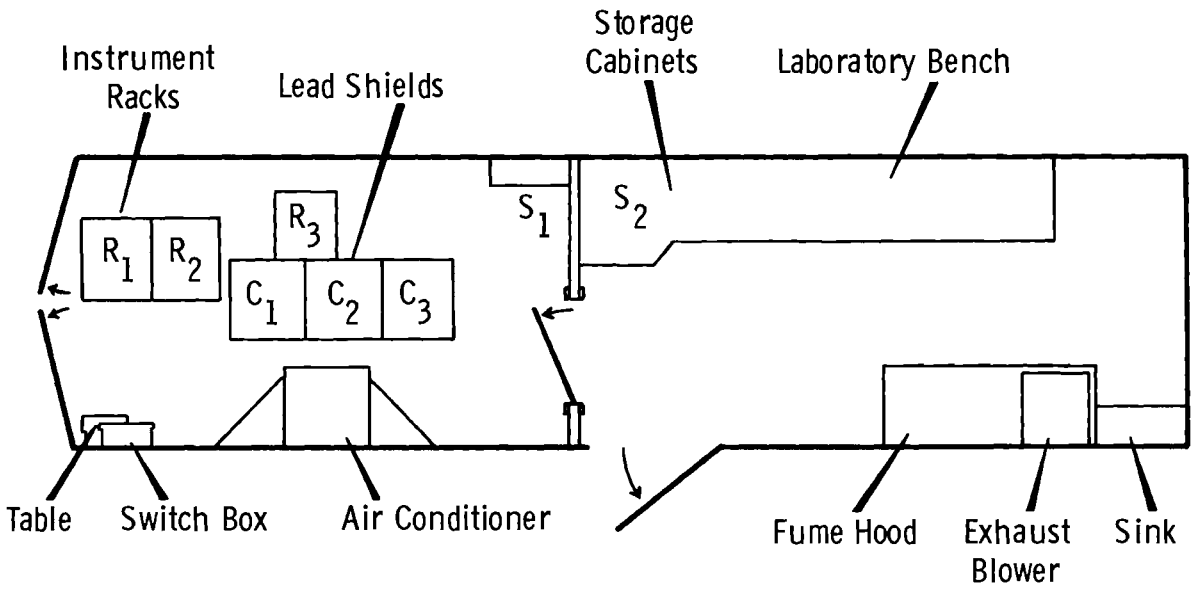

FIGURE 1. Portable Laboratory Floor Plan

A stable ambient counting room temperature is provided by a 15,000 Btu commercial air conditioning unit equipped with 4000 W of resistive heating. This unit was installed in the right wall of the counting room as shown in the trailer side view, Figure 2. Resistive heat is supplied on demand from a thermostat located in the counting room. Room cooling is supplied by the air conditioner on demand from a thermostat located in the air conditioning unit. Counting room air is continuously circulated through the unit during counting operations and the room temperature can be maintained to ±1 °F.

Counting instrumentation is installed in shock-mounted racks near the rear of the trailer. Lead bricks, used in shield fabrication, are stacked during transit in several layers on the floor over the trailer axles. Caster equipped frames are used to move the heavy detector assemblies. During transit, the upper detectors of the three low-level, multi-dimensional gamma-ray spectrometers are stored in specially padded containers located in the counting room. The lower NaI(Tl) crystals, ranging in size from 6 in. diam by 4 in. thick to 13 1/2 in. diam by 6 in. thick are positioned in permanent lead caves and are shock mounted for travel.

For operation, the detectors are moved from the storage boxes into position above the rear axles, and the top halves of the lead shields are built up around them (see Figure 3).

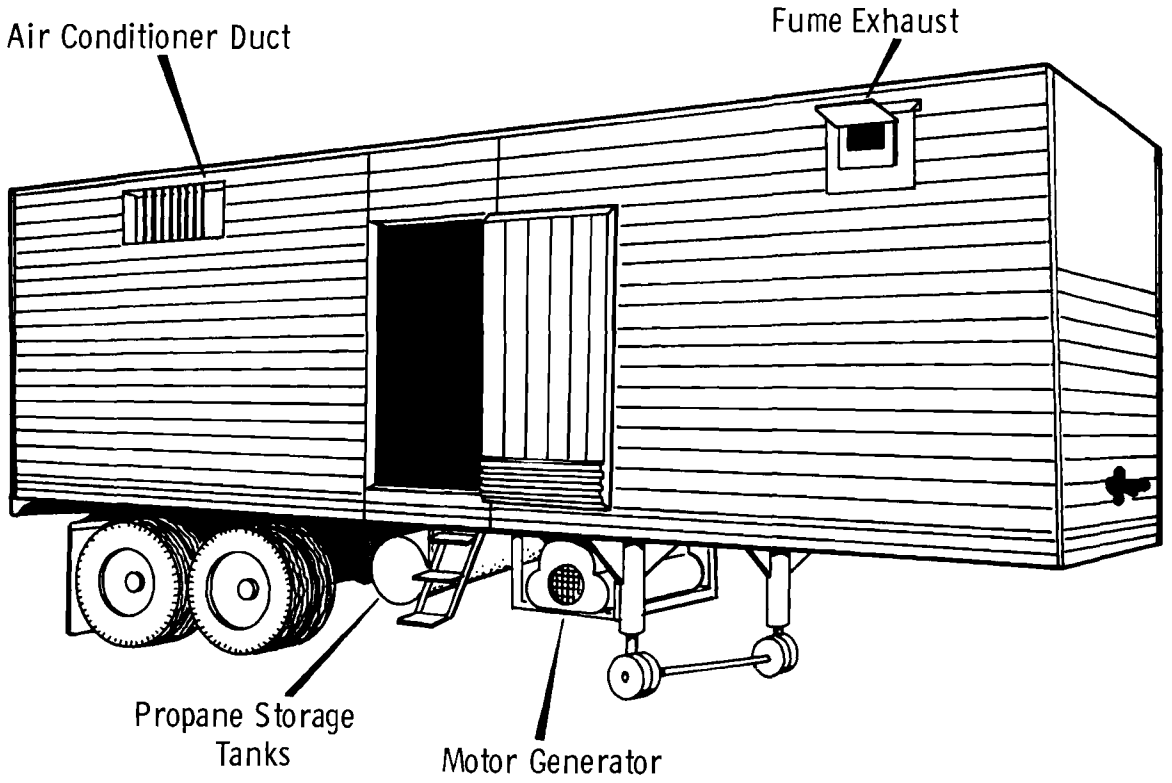

FIGURE 2. Portable Laboratory Trailer

Sample evaporation equipment, five propane hot plates and a 2 ft x 3 ft propane grill are located on the right wall of the forward or chemistry laboratory. A stainless steel fume hood attached to a 1/3 HP squirrel caged blower exhausts the vapors through the trailer wall. A standard 10 ft long by 20 in. wide laboratory bench with drawers is located on the left wall. Figure 4 shows the laboratory in use handling large rain water samples in a rapid separation of short-lived emitters from the atmosphere. The mobility of the counting laboratory system has and will facilitate the conduct of study in atmospheric physics, biology, oceanography, and other environmental sciences with the ultra low backgrounds and high sensitivities provided by gamma-ray multidimensional analyses.

Electrical power for heating, cooling, lighting, and instrumentation is supplied by a 5 kW, 220 V, single phase, 60 cycle propane motor-generator located under the trailer. Provision is made by external plug and switching to use available commercial power. The motor generator is operated during transit to maintain stable counting room temperatures. Propane for sample evaporation equipment and motor operation is stored in two 50 gal tanks located under the trailer.

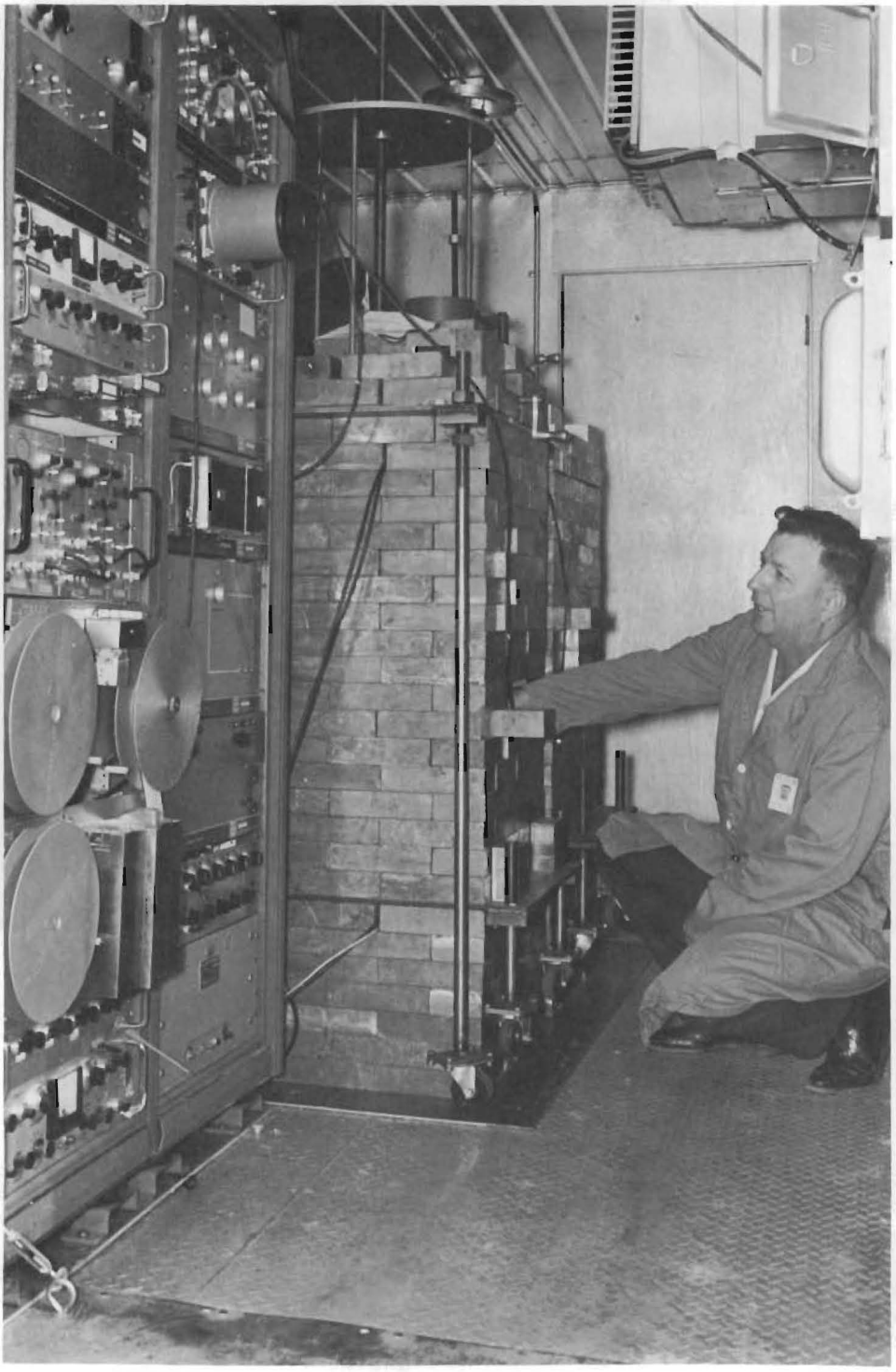

Neg. 0680785-18

FIGURE 3. Mobile Multidimensional Gamma Ray Spectrometer Counting Room

Neg. 0680785-12

FIGURE 4. Laboratory Preparation of Precipitation Samples at Quillayute, Washington

REFERENCES

1. N. A. Wogman, C. W. Thomas, J. A. Cooper, R. J. Engelmann, and R. W. Perkins. "Cosmic Ray Produced Radionuclides as Tracers of Atmospheric Precipitation Processes," Science, vol. 159, p. 189. 1968.

2. H. E. Palmer, R. W. Perkins, and B. O. Stuart. "The Distribution and Deposition of Radon Daughters Attached to Dust Particles in the Respiratory System of Humans Exposed to Uranium Mine Atmospheres," Health Phys. vol. 10, pp. 1129-1135. 1964.

3. N. A. Wogman, D.E. Robertson, and R. W. Perkins. "A Large Detector, Anticoincidence Shielded Multidimensional Gamma-Ray Spectrometer," Nucl. Instr. Methods, vol. 50, pp. 1-10. 1967.

DISTRIBUTION

No. of Copies

2 AEC, Chicago Patent Group
- G. H. Lee
- R. K. Sharp

8 AEC Richland Operations Office
- L. C. Brazley
- N. W. Fraser
- W. E. Lotz
- C. L. Robinson
- M. W. Tiernan
- D. G. Williams
- Technical Information Library (2)

2 AEC, RDT Site Representative-PNL
- P. G. Holsted

1 AIF Task Force
- MPR Associates, Inc.
- 815 Connecticut Ave. NW
- Washington, D. C. 20006

1 Air Force Cambridge Research Laboratory
- Bellford, Massachusetts
- D. A. Haugen

2 Air Resources Laboratory
- Environmental Science Services Administration
- 8060 - 13th Street
- Silver Spring, Maryland 20910
- D. Pack
- I. Van der Hoven

1 Argonne National Laboratory
- J. Loeding
- H. Moses

3 ARHCO
- D. J. Brown
- R. E. Tomlinson
- Files

2 ARL, ESSA
- 5710 Wooster Pike
- Cincinnati, Ohio 45227
- C. R. Hosler
- R. A. McCormick

No. of Copies

1 Atomic Energy of Canada Limited
- Chalk River, Ontario
- C. A. Mawson

2 Atomic Energy Establishment Trombay
- Bombay 73, India
- P. N. Krishnamoorthy
- K. T. Thomas

2 Atomic Energy Research Establishment
- Harwell, Berks, England
- R. H. Burns
- E. Glueckauf

1 Atmospheric Turbulence and Diffusion Laboratory
- Environmental Science Services Administration
- P. O. Box E
- Oak Ridge, Tennessee 37830
- F. A. Gifford

1 Australian AEC
- Post Office Coogee
- New South Wales, Australia
- A. W. R. Wilson

3 Battelle Memorial Institute

1 Brookhaven National Laboratory
- L. P. Hatch
- M. E. Smith

5 Commissariat a l'Energie Atomique
- Centre d' Etudes Nucleaires de Cadarache (1)
- BP n° 1, 13- St Paul lez Durance
- C. Gailledreau

- Centre d' Etudes Nucleaires de Saclay (4)
- P.O. Box 2, Saclay
- Gif-sur-Yvette (S & O), France
- A. Barbreau
- F. Duhamel
- A. Menoux
- P. Slizewicz

No. of Copies

1 Comision Nacional de Energia Atomica
Buenos Aires, Argentina
E. Vander Elst

2 Commonwealth Scientific and Industrial Research Organization
Aspendal, Victoria, Australia
B. B. Hicks

1 Division of Naval Reactors
R. S. Brodski

1 Division of Production
W. L. Lennemann

1 Division of Reactor Development and Technology
W. G. Belter

269 Division of Technical Information Extension

4 Douglas United Nuclear
T. W. Ambrose
P. C. Jerman
M. Lewis
Files

2 du Pont Company
Aiken, South Carolina
B. C. Rusche
W. B. Scott

1 du Pont Company
Wilmington, Delaware
V. R. Thayer

1 ENEA (OECD) Health and Safety Office
38, Blvd. Suchet,
Paris XVI, France
E. Wallauschek

2 Eureochemic Library
Mol, Belgium

1 Geological Survey of the United Kingdom
Water Division
Stevenson Buchan, Chief Geologist

No. of Copies

2 Geological Survey of the United States
Washington 25, D.C.
M. King Hubbert
C. V. Theis

1 George Washington University
Washington, D.C.
C. R. Naeser

1 Geotechnical Corporation
Box 28277,
Dallas 28, Texas
W. B. Heroy

1 Gesellschaft Kernforschung mbH
Karlsruhe 5, West Germany
H. Krause

2 Hanford Occupational Health Foundation
G. H. Crook
P. A. Fuqua

1 Health and Safety Laboratory
New York City
John Harley

2 International Atomic Energy Agency
Vienna 1, Kaerntnerring 11,
Austria
H. Seligman
J. Servant

1 Johns Hopkins University
Baltimore, Maryland
W. A. Patrick

2 Lawrence Radiation Laboratory
Livermore, California
G. H. Higgins
J. B. Knox

1 Los Alamos Scientific Laboratory
J. W. Healy

No. of Copies

2 National Institute of Radiological Sciences
250, Kurosuna-Cho,
Chiba-shi, Japan

M. Saiki
M. Suzuki

2 N. V. Belchim
200 Boeretang
Mol, Belgium

Leo H. Baetsle
Paul Dejonghe

2 Oak Ridge National Laboratory

K. Z. Morgan
E. G. Struxness

1 University of Arizona
Tucson, Arizona
Department of Geology

E. S. Simpson

1 University of California
Berkeley, California
Department of Civil Engineering

W. J. Kaufman

1 University of Illinois
Department of Agronomy

M. B. Russell

1 University of North Carolina
Chapel Hill, N.C.
Department of Chemistry

H. C. Thomas

1 University of Wisconsin
Department of Chemistry

H. Gladys Swope

No. of Copies

14 U.S. Atomic Energy Commission
Washington, D.C.
Division of Biology and Medicine

N. F. Barr
H. D. Bruner
W. W. Burr
W. D. Claus
J. J. Davis
C. W. Edington
J. Z. Holland
J. S. Kirby-Smith
A. W. Klement
S. A. Lough
J. R. Totter
J. N. Wolfe
R. W. Wood

Division of Space Nuclear Systems

J. A. Powers

1 U.S. Atomic Energy Commission
Savannah River Operations Office

K. K. Brown

1 U.S. Public Health Service
Division of Health Mobilization
Washington, D.C.

J. J. Lang, Research Branch

1 World Health Organization
Geneva, Switzerland

R. L. Dobson

1 World Meteorological Organization
Geneva, Switzerland

No. of Copies

206 Battelle Northwest

F. W. Albaugh
G. J. Alkire
W. J. Bair
J. H. Bender
C. A. Bennett
R. J. Brouns
R. E. Brown
W. J. Clarke
G. M. Dalen
R. F. Dickerson
R. L. Dillon (2)
W. L. Dotson
C. E. Elderkin
R. F. Foster
J. J. Fuquay (75)
W. A. Haney (5)
K. M. Harmon
A. J. Haverfield
J. F. Honstead
F. P. Hungate
R. T. Jaske
R. L. Junkins
D. R. Kalkwarf
H. A. Kornberg
C. R. Lagergren
H. V. Larson
K. H. Larson
R. E. Nakatani
C. E. Newton, Jr.
J. M. Nielsen
T. P. O'Farrell
R. F. Palmer
H. M. Parker
D. W. Pearce
R. W. Perkins
E. H. Phinney
W. C. Roesch
P. T. Santilli
G. A. Sawyer
L. C. Schwendiman
W. G. Spear
C. L. Simpson (75)
R. J. Sorenson
A. J. Stevens
M. F. Sullivan
W. L. Templeton
R. C. Thompson
C. R. Tipton, Jr.
C. J. Touhill (5)
C. M. Unruh
E. E. Voiland
W. E. Wilson
D. C. Worlton
Biology Library (2)
Technical Information Files (5)
Technical Publications (2)